

COLD GAS IN HIGH REDSHIFT GALAXIES

A Thesis

Submitted to the

Tata Institute of Fundamental Research
(A Deemed University)

for the degree of Doctor of Philosophy
in Physics

by

J. N. H. S. Aditya



National Centre for Radio Astrophysics
Tata Institute of Fundamental Research

2016

అమ్మ, నాన్న, గురువులకు అంకితం.

Acknowledgements

It is hard to believe that the ripples of time have flown so fast. Five years at NCRA have passed so swiftly. And, today I am in a position to conclude my work done in these years, and submit my Ph.D. thesis. I consider this as a moment of beginning my career as a researcher. An extensive effort by many people, directly and indirectly, has gone into helping me produce this thesis, and here I wish to sincerely thank everyone. Although it is not possible to mention everyone who has contributed in my journey this far, I sincerely acknowledge them.

Foremost, my advisor Nissim Kanekar has played a tremendous role in mentoring me throughout this time, and in moulding my career. I am always thankful to him, and grateful for his effort. He introduced me to radio astronomy, and made me realize the relevance of this subject, although I was wavering regarding my fields of interest, initially. Further, I am always inspired by his unprecedented commitment towards his job, and his bluntly honest personality. These qualities are easy to notice in every interaction with him. I try hard to soak-in at least a fraction of these, and hope that I would come up to his expectations in the near future. On a lighter note, the phrase “I don’t know what you are doing with your life”, used intermittently by my respectable advisor, will always strike my mind whenever I am in doubt.

Next, I sincerely thank my committee members Jayaram Chengalur, Tirthankar Roy Choudhury, and Divya Oberoi, for their valuable suggestions and comments that they have provided throughout the course of my Ph.D. These have really helped in fine tuning the direction of my work. I particularly thank Tirth for being my advisor for my MSc project. I could ‘taste’ the theoretical aspects of astrophysics during this period, which I

always cherish. I wish to thank Ishwar, Dharam, Poonam, Nimisha, Subhashis, Yogesh W. and Swarna, for all my interaction, both academically and socially. Further, I like to thank Paddy, Gulab, Ajit, Anand, Kandu, Dipanjan, Ramprakash, Tarun and Durgesh, all of whom have taught me courses during the graduate school.

I would especially like to thank Hemant and Reena for their constant cooperation in all administrative affairs. Gole and VVS have always been supportive and helpful in solving software and hardware related problems, I would like to extend my sincere thanks to them. I further like to convey my thanks and regards to the NCRA and the canteen staff for their constant help and support. All these guys have made my stay at NCRA feel like home, all these years.

Further, I like to thank all the staff of the GMRT who have made the observations for my thesis possible. Particularly, I like to thank Pramod and Surender, long chat sessions with them helped pass the time easily during the observing runs. Importantly, Pramod was very helpful on a particular occasion when I got ill at an odd time at the night, things would have been really difficult for me without his help.

Next, I always cherish the time spent with my friends/colleagues/partners in crime, Rohit, Prakash, Vishal, Naidu, Naren, Yogesh, Sambit, Ujjwal, Aritra, Rahul, Avishek, Preetish, Omkar, Raghu, Peter, Ruta, Atul, Nayana, Sushma, Biny, Sravani, Vikram and others. Rohit's music albums have made my life at office quite pleasurable, thanks Rohit. A large fraction of the coding required for my work was done with the help (read just 'done' here !!) of Prakash, so one can estimate his contribution for my thesis. Discussions with Naren have been quite informative regarding the 'tricks' in AIPS. All in all, my stay at NCRA has been made pleasurable because of all these wonderful guys. Thank you, friends !!

My thesis uses a lot of data obtained from the online sources NASA ads, NED, Vizier etc., and also utilizes softwares like latex, Supermongo, ASURV etc., to name a few. I extend my sincere thanks to all the organizations which develop and maintain these data systems and softwares. I would also

like to sincerely thank NCRA-TIFR for providing me with all the infrastructure through the research fellowship, to support my research.

A special thanks to my family. My parents, Padmavati and Prabhakar, and my brother Seshu, have been my pillars of strength. I like to thank them for all their love and encouragement, and will always be indebted to them.

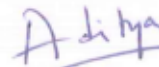
J. N. H. S. Aditya

23 October, 2016

Declaration

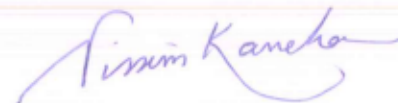
This thesis is a presentation of my original research work. Wherever contributions of others are involved, every effort is made to indicate this clearly, with due reference to the literature, and acknowledgement of collaborative research and discussions.

The work was done under the guidance of Nissim Kanekar, at the Tata Institute of Fundamental Research, Mumbai.



(J. N. H. S. Aditya)

In my capacity as supervisor of the candidate's thesis, I certify that the above statements are true to the best of my knowledge.



(Nissim Kanekar)

Date: 29th September, 2016

Abstract

The neutral hydrogen gas, HI, present in the local environments of Active Galactic Nuclei (AGNs), can be probed through HI 21 cm absorption studies. Both the distributional and the kinematical properties of the gas can be studied through this technique. Such studies can help us understand the physics of the centrally located AGN, since the surrounding gas may be the source of the fuel for the AGN activity. The gas may be supplied to the central regions either by slow accretion or by the triggering of gas infall by galaxy mergers, after which it can get consumed by the central black hole. Conversely, the centrally located AGN may also play an active role in regulating the star formation and the growth of its host galaxy through the effects of mechanical feedback. The AGN heats the gas present in the nuclear regions and drives it out, causing outflows of gas from the central areas. These outflows result in the quenching of star formation in the central regions and may even end the active state of the nucleus in some cases. Associated HI 21 cm absorption studies can be used to detect inflows and outflows of neutral hydrogen gas, relative to the central AGN. For example, HI 21 cm absorption lines that are redshifted relative to the AGN indicate infalling gas, while blueshifted absorption lines indicate the presence of outflowing gas.

Studies of associated HI 21 cm absorption can also be used to test AGN unification schemes. These models argue that the various observational classifications of AGNs arise due to orientation effects, and the different lines of sight to the nucleus. For example, these schemes predict that the line of sight towards broad-line AGNs is perpendicular to the plane of the dusty torus, while that towards narrow-line AGNs is close to the plane of the torus and the thick disk. The central region and the active nucleus

itself are typically obscured in the latter case. As such, in AGN unification schemes, detections of associated HI 21 cm absorption are expected to be systematically more common in sightlines towards narrow-line AGNs, as compared to those towards broad-line systems.

There are more than a hundred searches for associated HI 21 cm absorption in the literature, with ≈ 50 detections, mostly at low redshifts, and with only 4 detections at high redshifts, $z > 1$. The first sample of reasonable size was that of van Gorkom et al. (1989) who searched for absorption in 29 AGNs in the local Universe, detecting absorption in four systems. They found that all the four detections showed evidence for infalling neutral gas. However, at intermediate redshifts, $0.2 < z < 0.7$, Vermeulen et al. (2003) found that outflows were more common than inflows, in their sample of 57 sources with 19 detections. While the two results suggest a redshift evolution in the nuclear environment, it is difficult to interpret the results due to the small number statistics. Later studies have not been able to shed much light on this issue.

The typical reported detection fraction of associated HI 21 cm absorption at $z < 1$ is $\gtrsim 30\%$ (e.g. Gupta et al., 2006; Vermeulen et al., 2003). Conversely, at $z > 1$ there have been 25 searches with just 4 known detections of associated HI 21 cm absorption. The detection fraction at $z > 1$ is thus $16_{-8}^{+13}\%$. While the detection fraction at $z > 1$ is just half the value at $z < 1$, suggesting redshift evolution in the strength of associated HI 21 cm absorption, the difference between the detection rates at low and high redshifts is not significant due to the large uncertainty in the detection fraction at $z > 1$. This is because only a small number of sources have so far been targetted at high redshifts in searches for associated HI 21 cm absorption.

Moreover, most of the studies in the literature at all redshifts have targetted highly heterogeneous samples. The samples typically include AGNs with different radio morphologies, and different characteristics (e.g. blazars, radio galaxies, compact steep spectrum sources, etc.). The heterogeneity of

the sample makes it difficult to separate redshift evolution from differences in the AGN samples at different redshifts.

Recently, Curran and Whiting (2010) proposed that the reason for a lower strength of HI 21 cm absorption at high redshifts might be that high- z AGN samples typically contain sources with high radio and/or UV luminosities. A high AGN luminosity in the UV and/or radio wavebands can lead to a lower HI 21 cm optical depth, either by ionizing the HI in the AGN environment and thus reducing the HI column density, or by altering the HI hyperfine level populations, and thus increasing the spin temperature. However, the sample of AGNs used by the authors to test the above hypothesis was also highly heterogeneous, containing all the AGNs that had been searched for associated HI 21 cm absorption till then. The heterogeneity of the sample makes it difficult to interpret their results.

In this thesis, we have targetted a large and uniformly selected AGN sample, with a large number of sources at high redshifts, $z > 1$, to probe the dependence of the strength of associated HI 21 cm absorption on redshift, UV and radio luminosity, AGN colour, etc., as well as to study any redshift evolution in the gas kinematics (e.g. infall versus outflow, line widths, etc.). We have used source compactness as our primary selection criterion in choosing our target sample. This is because compact radio sources are more likely to be fully covered by an intervening medium than extended sources. The apparent (i.e. measured) optical depth of the absorbing medium would hence be similar to its true optical depth for a compact source, while it may be much smaller than its true optical depth for an extended source. Thus, at a given *apparent* optical depth sensitivity, the chances of detecting HI 21 cm absorption are much higher for compact AGNs. Our use of source compactness as the main selection criterion thus significantly improves the probability of our detecting HI 21 cm absorption towards our target sources. Flat-spectrum and Gigahertz-Peaked-Spectrum (GPS) radio sources are two classes of compact AGNs. The typical spectrum of an AGN is “steep” at low radio frequencies, with a higher flux density at lower frequencies; the emission is presumed to be synchrotron radiation from ultra-relativistic

electrons. However, the radio spectra of flat-spectrum sources and GPS sources are either flat or inverted at low frequencies, due to synchrotron self-absorption in a compact and optically thick medium. We have hence chosen flat-spectrum and GPS sources as our targets for the survey for associated HI 21 cm absorption. Our primary survey targetted flat-spectrum sources, as these typically have a somewhat higher flux density at the low frequencies of the redshifted HI 21 cm line than GPS sources, and hence yield a higher optical depth sensitivity.

The targets for our primary survey for associated HI 21 cm absorption were chosen from the Caltech-Jodrell Bank Flat-spectrum (CJF) sample (e.g. Taylor et al., 1996). The sources in the CJF sample have the following characteristics: (1) they have flat radio spectra, with a spectral index $\alpha > -0.5$ (for $S_\nu \propto \nu^\alpha$) between 1.4 and 4.8 GHz, (2) the redshifts for most CJF sources are available in the literature (e.g. Lawrence et al.), and (3) the sample is nearly complete, comprising of all sources north of a declination of $+35^\circ$ and with 4.8 GHz flux density ≥ 350 mJy. 29 sources of the CJF sample, mostly at $z < 0.7$, have searches for associated redshifted HI 21 cm absorption in the literature. In this thesis, we used the GMRT to search for HI 21 cm absorption from 74 new CJF sources whose redshifts are such that their redshifted HI 21 cm absorption line lies at frequencies covered by the GMRT 325 MHz, 610 MHz, or 1420 MHz receivers, i.e. 300 – 360 MHz, 570 – 670 MHz, and 1000 – 1437 MHz. 21 of these sources are at $z < 0.4$, 46 sources at $1.1 < z < 1.5$, and 7 at $3.0 < z < 3.6$. Including the 29 CJF sources with literature searches for associated HI 21 cm absorption, our full flat-spectrum target sample consists of 103 sources. The sensitivity of the GMRT observations was chosen so as to at least match the sensitivity of the observations of the literature sample.

Further, in a second survey for redshifted associated HI 21 cm absorption, we targetted a sample of GPS sources, selected from the literature (e.g. Labiano et al., 2007), at declinations observable with the GMRT and whose redshifted HI 21 cm line frequencies lie in the above GMRT bands. 23 sources of this sample, mostly at $z < 0.7$, have searches for associated HI 21

cm absorption in the literature. During this thesis, we carried out searches for redshifted HI 21 cm absorption in 12 new GPS sources of this sample, 9 at $z < 0.4$, and 3 at $1.1 < z < 1.5$. Again, the sensitivity of the new observations was chosen to match the sensitivity of the observations of the literature sample.

We used the GMRT 1420 MHz, 610 MHz and 327 MHz receivers, respectively, for AGNs in the redshift ranges $z < 0.4$, $1.1 < z < 1.5$, and $3.0 < z < 3.6$. The GMRT hardware correlator was used for the observations of the initial pilot survey of 24 CJF sources, while all remaining sources were observed using the GMRT software correlator. The typical velocity resolution was $\approx 10\text{--}30\text{ km s}^{-1}$ for all observations, while the velocity coverage was $\approx 4000\text{--}16000\text{ km s}^{-1}$, depending on the observing band and correlator. This provided both good sensitivity to narrow HI 21 cm absorption components, as well as sufficient coverage to detect wide absorption, with line widths $\lesssim 1000\text{ km s}^{-1}$. The total GMRT observing time for the CJF and GPS samples was ≈ 200 hours, with 75 hours in the 1420 MHz band, 90 hours in the 610 MHz band, and 45 hours in the 327 MHz band.

We used the Astronomical Image Processing System (AIPS) software package to analyse all our GMRT data, following standard procedures for low-frequency imaging and spectroscopy. The data on 11 sources of the CJF sample and 5 sources of the GPS sample were found to be affected by radio frequency interference (RFI); these sources were hence excluded from our analysis. We obtained clean spectra for 63 sources of the CJF sample, and 7 sources of the GPS sample, allowing deep searches for HI 21 cm absorption towards these AGNs. This yielded a total of five confirmed, and one tentative, new detections of redshifted HI 21 cm absorption. Three of the confirmed detections are at $z \approx 1.2$, while the tentative detection is at $z \approx 3.5$. We have thus roughly doubled the number of detections of HI 21 cm absorption at $z > 1$ in this thesis.

We used the uniformly-selected sample of 92 flat-spectrum AGNs (63 sources observed by us and 29 sources from the literature) to test the dependence of the strength of associated HI 21 cm absorption on redshift,

low-frequency spectral index, rest-frame 1216 Å UV luminosity, rest-frame 1.4 GHz radio luminosity, and AGN (R-K) colour. We find no evidence that the strength of HI 21 cm absorption depends on the radio spectral index (within the flat-spectrum AGN population) or on the (R-K) colour. We find, for the first time, statistically significant evidence for redshift evolution in the strength of the HI 21 cm absorption in a uniformly-selected sample. However, we also find statistically significant evidence that the strength of the HI 21 cm absorption is anti-correlated with AGN luminosity at both rest-frame UV and rest-frame 1.4 GHz frequencies. Since the high- z AGNs of our sample also have high UV/radio luminosities, it is not at present possible to separate between the two possible scenarios of redshift evolution in, or luminosity dependence of, the strength of the HI 21 cm absorption. Similar results (at higher statistical significance) were obtained on combining the CJF and GPS samples together to obtain a large sample of compact radio sources with HI 21 cm absorption studies. Observations of a sample at intermediate redshifts and luminosities would be critical to break the degeneracy between the two possible effects. We have already carried out some of these observations during this thesis using the Green Bank Telescope, and plan to continue this project with the new 550 – 900 MHz receivers of the upgraded GMRT.

The individual chapters of the thesis are summarised below.

In Chapter 1, we give a brief introduction to AGNs and their classification, gas infall and outflow, and finally, discuss the physics of the HI 21 cm line. We then describe studies of associated HI 21 cm absorption and provide details of the previous work done in this field.

In Chapter 2, we discuss the relation between HI 21 cm absorption and radio source compactness, the main selection criterion that was used to choose our target samples. We initially describe the physics of synchrotron self-absorption, which is believed to be the cause for the flat and inverted nature of the spectra of radio sources. We explain why such sources with flat and inverted spectra are likely to be compact, and hence, to have strong associated HI 21 cm absorption. We next list the characteristics of the Caltech-Jodrell

Flat-spectrum (CJF) sample (e.g. Taylor et al., 1996), from which we chose targets for our primary survey for redshifted HI 21 cm absorption. We then move to our secondary sample, consisting of Gigahertz-Peaked Spectrum (GPS) sources, and describe the GPS source characteristics that were used to select our targets from the GPS literature (e.g. Labiano et al., 2007). We finally list the sources of our two target samples that were searched for associated HI 21 cm absorption during this thesis, and also provide details of the sources belonging to the two samples that already have HI 21 cm absorption searches in the literature.

In Chapter 3, we describe the observational details of the CJF and GPS samples and the techniques that were employed to analyse the data. We initially explain our sensitivity goals, which were based on the sensitivities of earlier HI 21 cm absorption studies of similar sources in the literature. We then describe the observational strategy, including details of the observing frequency, the bandwidth, the velocity resolution, the velocity coverage and the on-source time. We then describe the data analysis procedure that was followed for all sources, in the AIPS package, and that was used to obtain the final HI 21 cm absorption spectra. This includes the details of data editing, calibration, imaging, self-calibration, and spectroscopy. Finally, we provide details of the 11 CJF and 5 GPS sources where strong RFI prevented us from obtaining clean HI 21 cm absorption spectra.

In Chapter 4, we provide the details of all sources with usable HI 21 cm absorption spectra, obtained from our analysis. We obtained 5 confirmed new detections and one new tentative detection of associated HI 21 cm absorption from our analysis of the CJF and GPS samples. Of these, two detections are at $z < 0.4$, 3 are at $z \approx 1.2$, while one (tentative) detection is at $z = 3.530$. In total, our analysis has yielded associated HI 21 cm absorption spectra for 63 sources (4 detections and 59 non-detections) from the CJF sample, and 7 sources (2 detections and 5 non-detections) from the GPS sample.

In Chapter 5, we discuss the properties of the six AGNs with detections of associated HI 21 cm absorption. The confirmed detections are towards

TXS 0003+380 at $z = 0.229$, B3 1456+375 at $z = 0.333$, TXS 1945+513 at $z = 1.223$, TXS 1200+045 at $z = 1.226$, and TXS 1245-197 at $z = 1.275$, while the single tentative detection is towards TXS 0604+728 at $z = 3.530$. Before our survey, only 4 associated HI 21 cm absorbers were known at $z > 1$; we have thus nearly doubled this number.

The source B3 1456+375 is classified as a red quasar in the literature (e.g. Glikman et al., 2012); the detection of HI 21 cm absorption towards this source is consistent with the hypothesis that the red colour in the optical band is caused due to dust extinction, although the derived HI column density is not particularly high.

The GMRT image of TXS 1954+513 at 640 MHz shows a triple structure, with a prominent core and two extended lobes, that are aligned nearly perpendicular to the VLBI-scale core-jet structure (e.g. Xu et al., 1995). The misalignment could arise either due to a twisted radio jet or due to restarted AGN activity with a spin-flip of the central supermassive black hole. We find that the HI 21 cm absorption is blueshifted from the AGN redshift by $\approx 330 \text{ km s}^{-1}$, indicating outflowing neutral gas, possibly being driven out due to the ram pressure from the radio jet. We find that this AGN has a high intrinsic 1216 Å UV luminosity of $\approx \text{few} \times 10^{23} \text{ W Hz}^{-1}$, demonstrating that neutral hydrogen gas can indeed survive in AGN environments in the presence of high UV luminosities, contrary to suggestions in the literature.

We find that the HI 21 cm absorption towards TXS 1200+045 is also significantly blueshifted from the AGN redshift. The spectrum shows a strong narrow component, along with a weak wide feature with a span of $\approx 600 \text{ km s}^{-1}$, suggesting the presence of disturbed gas. Again, the absorption appears to arise in outflowing neutral gas possibly being pushed by the radio jet to high velocities.

We detect wide HI 21 cm absorption towards the source TXS 1245-197, with a span of $\approx 328 \text{ km s}^{-1}$ between the 20% points of the line. The source is classified as a Compact Symmetric Object in the literature (Sokolovsky et al., 2011). The large velocity width in the HI 21 cm absorption profile

could arise due to absorption against both VLBI-scale radio lobes, or due to disturbed gas that is interacting with the AGN jets.

Finally, if the tentative detection at $z = 3.530$ towards TXS 0604+728 is confirmed, this would be the highest redshift at which HI 21 cm absorption has ever been detected.

In Chapter 6, we use the 92 flat-spectrum sources, including 63 sources observed by us and 29 sources from the literature, to test the dependence of the strength of HI 21 cm absorption on redshift, and AGN radio/UV luminosity, spectral index and colour. The tests were based on both the fraction of HI 21 cm detections, and two-sample Peto-Prentice tests, in subsamples obtained by dividing the full sample at the median value of the parameter under consideration (e.g. redshift, luminosity, etc.).

Upon dividing the sample of 92 flat-spectrum AGNs at the median redshift, we find, using a Peto-Prentice test, that the strength of HI 21 cm absorption is weaker (at $\approx 3\sigma$ significance) in the high- z sample than in the low- z sample. This is the first statistically significant evidence for redshift evolution in the strength of HI 21 cm absorption in a uniformly-selected sample.

However, we also find that the HI 21 cm absorption strength is higher in AGNs with low rest-frame UV or rest-frame radio luminosities, at $\approx 3.5\sigma$ significance. The strength of the HI 21 cm absorption thus depends on both redshift and AGN luminosity, being weaker at high redshifts and high AGN luminosities. Unfortunately, most of the AGNs of our sample with high radio/UV luminosities also lie at high redshifts, and it is hence not possible to break the degeneracy between AGN luminosity and redshift evolution as the primary cause, if any, of the weaker HI 21 cm absorption at high redshifts and high luminosities.

We find no evidence that the strength of HI 21 cm absorption depends on the low-frequency spectral index (a proxy for radio source compactness, and thus, the covering factor), indicating that it is unlikely that the low strength of HI 21 cm absorption in the high- z sample has arisen due to the low-frequency radio emission being dominated by extended, steep-spectrum

structure, and hence, a low covering factor. We also do not find any significant difference in the distributions of the spectral index in the low- z and high- z sub-samples, implying that it is unlikely that the high- z AGNs in our sample have systematically low covering factors.

Finally, we have included 27 GPS sources (7 observed by us and 20 from the literature) to construct a large sample of 119 compact AGNs with searches for associated HI 21 cm absorption. This is by far the largest sample of compact AGNs that has been searched for associated HI 21 cm absorption till date. We continue to find a statistically significant dependence of the strength of HI 21 cm absorption on both redshift and AGN luminosity. Again, it is currently not possible to break the degeneracy to identify the primary cause, since most of the high luminosity AGNs in our sample lie at high redshifts.

On dividing either the sample of 92 flat-spectrum AGNs or the full sample of 119 compact AGNs at the median (R-K) colour, we find no evidence that the strength of the HI 21 cm absorption depends on AGN colour. We thus do not find evidence to support the hypothesis that the red AGN colour might arise due to dust reddening and a high HI column density.

Contents

List of Figures	xxiii
List of Tables	xxvii
1 Introduction	1
1.1 Supermassive black holes	2
1.2 Active Galactic Nuclei	2
1.2.1 Radio-Quiet AGNs	6
1.2.2 Radio-Loud AGNs	6
1.3 Inflow mechanisms	8
1.3.1 Cold gas accretion	8
1.3.2 Galaxy mergers	9
1.3.3 Accretion of hot X-ray emitting gas	9
1.4 Outflows and feedback	10
1.5 Physics of the HI 21 cm line	11
1.6 Associated HI 21 cm absorption studies	13
1.7 Previous Associated HI 21 cm absorption studies	14
1.8 Outline of the thesis	16
2 The Target Samples: Flat-Spectrum and Gigahertz-Peaked Spectrum Sources	19
2.1 Radio-source compactness	19
2.2 Synchrotron self-absorption	20
2.3 GPS and Flat-spectrum sources	22
2.4 The target samples	23

CONTENTS

3	Observations and Data Analysis	33
3.1	The GMRT observations	33
3.1.1	CJF sources	33
3.1.2	GPS sources	37
3.2	Data Analysis	39
3.3	Sources affected by RFI	48
4	Results	53
4.1	The Caltech-Jodrell Flat Spectrum sample	53
4.1.1	HI 21 cm detections in the CJF Sample	56
4.1.2	Results for the CJF sample	58
4.2	The Gigahertz-Peaked Spectrum sample	73
4.2.1	HI 21 cm detections in the GPS sample	73
4.2.2	Results for the GPS sample	74
5	Detections	79
5.1	Detections in the CJF sample	79
5.1.1	TXS 0003+380, $z = 0.229$	79
5.1.2	B3 1456+375, $z = 0.333$	81
5.1.3	TXS 1954+513, $z = 1.223$	83
5.1.4	TXS 0604+728, $z = 3.530$	87
5.2	HI 21 cm absorption detections in the GPS sample	89
5.2.1	TXS 1200+045, $z = 1.226$	89
5.2.2	TXS 1245-197, $z = 1.275$	89
6	Discussion	93
6.1	The Caltech-Jodrell Bank Flat-Spectrum sample	93
6.1.1	A uniformly-selected flat-spectrum sample	93
6.1.2	Redshift evolution	96
6.1.3	Dependence on the radio spectral index	103
6.1.4	Dependence on ultraviolet and radio luminosity	107
6.1.5	Effects of varying covering factor	111
6.1.6	Dependence on the R-K colour	116
6.2	The Gigahertz Peaked Spectrum sample	119

6.3	The combined sample of 119 compact AGNs	125
7	Summary and Future Work	143
7.1	GMRT surveys for associated HI 21 cm absorption	143
7.2	AGNs with detections of HI 21 cm absorption	144
7.3	Redshift evolution and AGN luminosity dependence	146
7.4	Future Work	148
A		151
	Bibliography	153

CONTENTS

List of Figures

1.1	Schematic illustration of an AGN.	4
1.2	AGN classification.	5
2.1	Radio spectrum of a compact source undergoing synchrotron self-absorption.	21
3.1	The velocity-integrated HI 21 cm optical depths of the CJF sources from literature studies, plotted against redshift.	36
3.2	The velocity-integrated HI 21 cm optical depths of the GPS sources from literature studies, plotted against redshift.	38
4.1	The GMRT continuum images of TXS 0344+405 and TXS 1954+513.	55
4.2	The GMRT HI 21 cm absorption spectra for the 63 CJF sources.	59
4.3	The GMRT HI 21 cm absorption spectra for the 7 GPS sources.	76
5.1	The GMRT HI 21 cm absorption spectrum towards TXS 0003+380, at $z = 0.229$	80
5.2	The GMRT HI 21 cm absorption spectrum towards B3 1456+375, at $z = 0.333$	82
5.3	The GMRT 640 MHz continuum image and HI 21 cm absorption spectra of the source TXS 1954+513.	85
5.4	The optical depth spectra towards TXS 1954+513.	86
5.5	The GMRT HI 21 cm absorption spectrum towards TXS 0604+728, at $z = 3.530$	88
5.6	The GMRT HI 21 cm absorption spectrum towards TXS 1200+045, at $z = 1.226$	90

LIST OF FIGURES

5.7	The GMRT HI 21 cm absorption spectrum towards TXS 1245-197, at $z = 1.275$	92
6.1	The integrated HI 21 cm optical depths of the full sample of 92 CJF sources, plotted as a function of redshift.	104
6.2	The detection rates of HI 21 cm absorption for the sub-samples with $z < z_{med}$ and $z > z_{med}$	105
6.3	The integrated HI 21 cm optical depth of the 92 CJF sources plotted against the low-frequency spectral index, $\alpha_{21\text{ cm}}$	106
6.4	The rest-frame 1216 Å UV luminosities of 87 CJF sources of the sample plotted, in logarithmic units, against the AGN redshifts.	108
6.5	The rest-frame 1.4 GHz radio luminosities of the full sample of 92 CJF sources plotted, in logarithmic units, against the AGN redshifts.	109
6.6	The rest-frame 1.4 GHz radio luminosities of 87 CJF sources of the sample plotted, in logarithmic units, against the rest-frame 1216 Å UV luminosities, in logarithmic units.	110
6.7	The integrated HI 21 cm optical depths of 87 sources of the CJF sample plotted against the rest-frame 1216 Å UV luminosities.	112
6.8	The integrated HI 21 cm optical depths of the full CJF sample of 92 sources plotted against the rest-frame 1.4 GHz radio luminosities.	113
6.9	The low-frequency spectral index, $\alpha_{21\text{ cm}}$, plotted as a function of redshift.	117
6.10	The HI 21 cm optical depth, in logarithmic units, plotted against (R-K) colour.	118
6.11	The integrated HI 21 cm optical depths of the sample of 30 GPS sources, plotted as a function of redshift.	126
6.12	The integrated HI 21 cm optical depths plotted against rest-frame 1216 Å UV luminosities, for the sample of 30 GPS sources.	127
6.13	The integrated HI 21 cm optical depths plotted against rest-frame 1.4 GHz radio luminosities, for the sample of 30 GPS sources.	128
6.14	The integrated HI 21 cm optical depths, in logarithmic units, plotted against the low-frequency spectral indices, for the sample of 30 GPS sources.	129

LIST OF FIGURES

6.15	The low-frequency spectral index, $\alpha_{21\text{ cm}}$, plotted as a function of redshift, for the 30 GPS sources.	130
6.16	The HI 21 cm optical depth, in logarithmic units, plotted against (R-K) colour, for the 30 GPS sources.	131
6.17	The integrated HI 21 cm optical depths of the sample of 119 compact sources, plotted as a function of redshift.	134
6.18	The rest-frame 1216 Å UV luminosities of 114 compact sources of the full sample plotted, in logarithmic units, against the AGN redshift. . . .	135
6.19	The rest-frame 1.4 GHz radio luminosity of the full sample of 119 compact sources, plotted against the redshift.	136
6.20	The integrated HI 21 cm optical depth of the 114 compact AGNs of our full sample, plotted as a function of rest-frame 1216 Å UV luminosity. . .	137
6.21	The integrated HI 21 cm optical depth plotted as a function of rest-frame 1.4 GHz radio luminosity, for the full sample of 119 compact AGNs. . .	138
6.22	The integrated HI 21 cm optical depth plotted as a function of low-frequency spectral index, for the full sample of 119 compact AGNs. . .	139
6.23	The low-frequency spectral index, $\alpha_{21\text{ cm}}$, plotted as a function of redshift for the full sample of 119 compact AGNs.	140
6.24	The integrated HI 21 cm optical depth, in logarithmic units, plotted against (R-K) colour.	141

LIST OF FIGURES

List of Tables

2.1	The 29 CJF sources with associated HI 21 cm absorption searches available in the literature.	26
2.2	The 74 CJF sources whose HI 21 cm line frequencies redshift into the GMRT bands.	27
2.3	The 23 GPS sources with searches for associated HI 21 cm absorption available in the literature.	30
2.4	The 12 GPS sources whose HI 21 cm line frequencies redshift into the GMRT bands.	31
2.5	The sources from the CJF and GPS samples with low inferred flux densities at the redshifted HI 21 cm line frequencies.	32
3.1	Observational details of the 74 CJF sources.	44
3.2	Observational details of the 12 GPS sources.	51
4.1	The 63 target sources selected from the CJF sample.	71
4.2	The 7 GPS sources.	75
6.1	The 63 CJF sources observed using the GMRT.	97
6.2	The 29 CJF sources with HI 21 cm absorption searches available in the literature.	101
6.3	The 7 GPS sources observed using the GMRT.	121
6.4	The 23 GPS sources with HI 21 cm absorption searches available in the literature.	123

GLOSSARY

1

Introduction

The Interstellar Medium (ISM) of a galaxy consists of a variety of ingredients like dark matter particles, interstellar gas, interstellar dust, cosmic rays, electromagnetic radiation, interstellar magnetic field and gravitational field. The interstellar gas is primarily composed of hydrogen (H) and helium (He) persisting from the Big Bang, with atomic hydrogen (HI) being one of the most important components. Further, it is known that in the Milky Way approximately 60% of the gas is in HI regions – regions where the hydrogen is predominantly atomic (e.g. Draine, 2011). Many researchers are particularly interested in understanding the physical properties of HI gas. This is mainly because HI forms the main reservoir for star formation in a galaxy, and thus has an important influence on the evolution of the galaxy with cosmic time. It is hence worthwhile to study neutral hydrogen gas to get insights regarding the structural properties and evolution of galaxies.

This thesis investigates the distribution and kinematical properties of the neutral hydrogen gas present in the surrounding environments of active galactic nuclei (AGNs; see section 1.2). It mainly tries to test whether these properties evolve with redshift. In this chapter, we provide a brief description of supermassive black holes, describe the structure of AGNs, the various classifications of AGNs, interaction of the gas with the black hole in the form of inflows and outflows, the physics of HI 21 cm absorption, and previous absorption studies of neutral hydrogen gas associated with the AGNs using the HI 21 cm line, and finally, give an outline of the current thesis.

1. INTRODUCTION

1.1 Supermassive black holes

Many galaxies have very bright nuclei, so bright that the central tiny region is more luminous than the rest of the galaxy. Emission from the nuclear region is bright at all wavelengths and the spectrum is not like that observed from stars. The luminosity is known to vary on short time scales, even shorter than a day in some cases. The centres of such galaxies are assumed to be powered by Supermassive Black Holes (SMBHs; e.g. Ferrarese and Merritt, 2000). This is because the most efficient conversion of mass to energy occurs during the accretion of matter onto a black hole. A black hole is a mass condensation which forms a singularity (e.g. Raine and Thomas, 2014) in space, and from which not even light can escape if it crosses the event horizon. Black holes can be indirectly “seen” by observing mass and light that are affected by its strong gravitational field.

Observational work indicates that SMBHs with masses in the range ($10^6 < M_{BH} < 10^{9.5} M_{\odot}$) exist in the centres of all massive galaxies (e.g. Ferrarese and Merritt, 2000; Kormendy and Gebhardt, 2001; Kormendy and Richstone, 1995). Many studies have found tight scaling relations between the mass of the SMBH and various parameters of the host galaxy, including the stellar bulge mass, the stellar velocity dispersion and the stellar concentration index (e.g. Ferrarese and Merritt, 2000; Gebhardt et al., 2000; Graham and Driver, 2007; Häring and Rix, 2004; Hopkins et al., 2007; Magorrian et al., 1998; Marconi and Hunt, 2003). These relations suggest that the SMBH and the host galaxy have a common evolutionary process, with the SMBH mass growing during the galaxy’s evolution. The SMBH is believed to grow in two main ways: one is by coalescence with another SMBH, and the second through the accretion of gas and dust onto the black hole. The accretion process by the black hole is believed to be radiatively efficient (e.g. Marconi et al., 2004; Merloni and Heinz, 2008; Shankar et al., 2004).

1.2 Active Galactic Nuclei

Supermassive black holes that are located in the central regions of galaxies and that actively accrete gas and dust, producing copious amounts of radiation, are known as active galactic nuclei. Due to the conservation of angular momentum, the accreting mass forms a flattened structure around the black hole, a so-called accretion disc. The size of this disc is expected to be small ($\sim 10^{-3}$ pc, e.g., Peterson, 1997), and it

rotates at high speeds, emitting large amounts of radiation at all wavelengths (see, e.g., Magorrian et al., 1998; Peterson, 1997; Rees, 1984). Moving radially outward from the centre of the AGN, fast moving clouds exist at a distance of ≈ 100 light days from the black hole. The circumnuclear region consisting of these fast moving clouds is known as the ‘broad-line region’ (BLR; see Fig. 1.1). These clouds produce the broad emission lines seen in some AGN spectra (e.g. Baldwin, 1997).

According to the standard model of AGNs (e.g. Antonucci, 1993; Urry and Padovani, 1995), a torus consisting of dust and gas surrounds the black hole and the accretion disk (see Fig. 1.1). The size of this torus is $\approx 1 - 10$ pc. These dusty toroidal structures have been directly imaged recently, due to the advancements in technology (e.g. Jaffe et al., 2004; Tristram et al., 2009; van der Wolk et al., 2010). Models of infrared spectral energy distributions from AGN-heated dust (e.g. Nenkova et al., 2008; Privon, 2009) provide further evidence for the existence of AGN tori. At a distance of ≈ 100 light years from the central black hole, projected in directions perpendicular to the accretion disk, narrow-line regions (NLRs) exist. These regions comprise of small, low-density gas clouds moving at lower velocities than the gas in the broad-line region and producing the narrow emission lines seen in some AGN spectra. On larger scales (tens of parsecs), clouds of ionized, atomic and molecular gas have been detected in a few sources (e.g. Hicks et al., 2009; Lo, 2005; Peck and Taylor, 2001; Schinnerer et al., 2000).

In about 15 – 20% (e.g. Kellermann et al., 1989) of the AGN population, material around the black hole is found to escape and form jets in directions perpendicular to the accretion disk. These jets are sometimes seen to extend out to Mpc scales, far larger than the size of the AGN host galaxies (tens of kpc). The jets are composed of a plasma of relativistic electrons. The relativistic electrons follow a magnetic field helix created by the differential rotation of the black hole and the accretion disk (e.g. Meier et al., 2001). These electrons emit radiation at radio wavelengths. Black holes with strong radio emission are called “radio-loud” AGNs and the ones with weak or no radio emission are referred to as “radio-quiet” AGNs. The radio-loud and radio-quiet AGNs are differentiated based on the radio to optical flux-density ratio, R . Radio-loud AGNs have $R > 10$, whereas radio-quiet AGNs have $R < 10$ (Kellermann et al., 1989). The following description and Fig. 1.2 provide further details regarding the classification of the two types of AGNs (Peterson, 1997).

1. INTRODUCTION

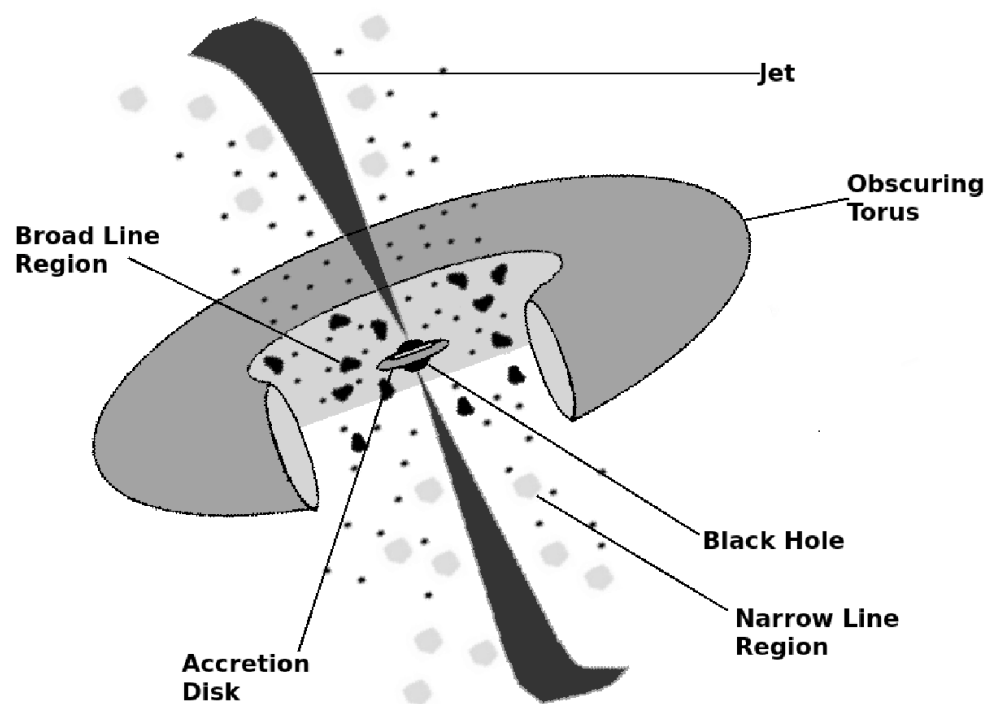


Figure 1.1: Schematic illustration of an AGN, adapted from Urry and Padovani (1995).

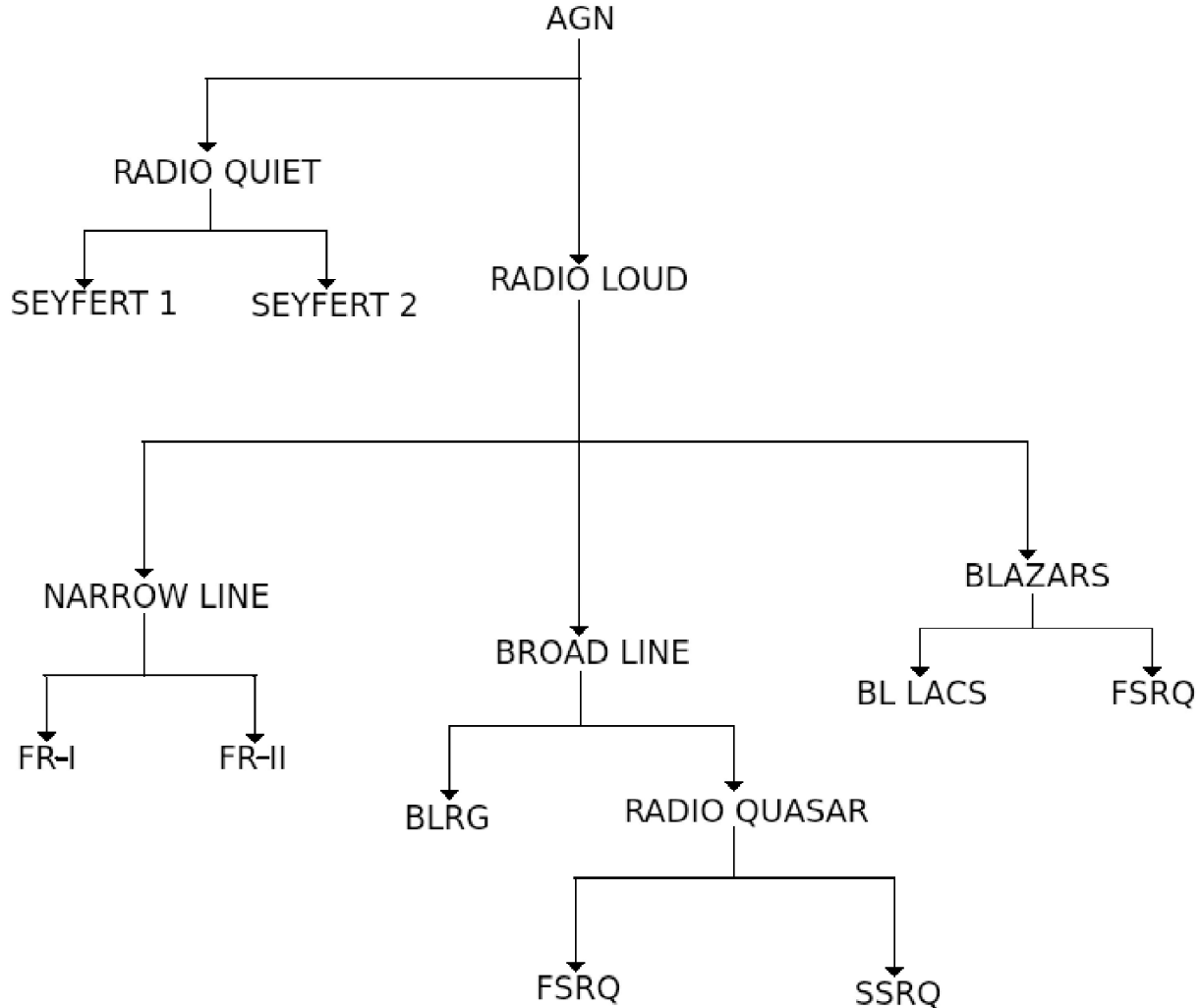


Figure 1.2: AGN classification. The abbreviations used in the figure are (1) AGN, the active galactic nucleus, (2) RADIO QUIET, the class of radio-quiet AGNs (see section 1.2.1), (3) SEYFERT 1, the Seyfert type 1 galaxies, (4) SEYFERT 2, the Seyfert type 2 galaxies, (5) RADIO LOUD, the class of radio-loud AGNs (see section 1.2.2), (6) NARROW LINE, the class of narrow line radio galaxies, (7) FR-I, the Fanaroff-Riley I radio galaxies, (8) FR-II, the Fanaroff-Riley II radio galaxies, (9) BROAD LINE, the class of broad line radio galaxies and radio quasars, (10) BLRG, the broad-line radio galaxies, (11) FSRQ, the flat-spectrum radio quasars, (12) SSRQ, the steep-spectrum radio quasars.

1. INTRODUCTION

1.2.1 Radio-Quiet AGNs

The most common radio-quiet galaxies are classified as “Seyfert galaxies”; here, the AGN host galaxy has the morphology of a spiral disk (e.g. Peterson, 1997).

Seyfert Type 1: These are radio-quiet galaxies that have a bright star-like nucleus and strong continuum emission over far-infrared (FIR) to X-ray wavelengths. The spectra of these sources contain broad emission lines of width ~ 1000 km/s.

Seyfert Type 2: These are radio-quiet galaxies with weak continuum emission and narrow emission lines, with widths of ≈ 100 km/s.

Seyfert galaxies with properties intermediate between type 1 and type 2 are labelled as type 1.2, 1.5 and so on.

1.2.2 Radio-Loud AGNs

The classification of radio-loud AGNs is based on their morphology and optical/ultraviolet properties.

Narrow Line Radio Galaxies (NLRGs): The Fanaroff-Riley I and Fanaroff-Riley II radio galaxies are together referred to as narrow-line radio galaxies. These objects have emission-line widths similar to those of Seyfert 2 galaxies.

Fanaroff-Riley I (FR-I) radio galaxies: These sources have extended morphology, with a core, radio jet and radio lobes. They often have symmetrical jet structures that become fainter as one approaches the outer extremes. Because of this feature, they are also called edge-darkened sources. The spectra of these sources contain narrow emission line features.

Fanaroff-Riley II (FR-II) radio galaxies: These sources are more luminous than FR-I radio galaxies. The jets are knotty with bright lobes and hot-spots at the ends. In contrast to the FR-I counterparts, the luminosity of these sources falls off towards the nucleus. The jets in these sources are often well collimated and one-sided. Their spectra also contain narrow-line emission features.

Broad-Line Radio Galaxies: The continua and the emission line regions of these sources resemble those of Seyfert 1 galaxies.

Radio Quasars: These sources are mainly characterised by high UV, radio and X-ray luminosities, outshining the rest of the galaxy. Many of these systems are

located at high redshifts, $z > 1$. The luminosities of these sources are known to be highly time-variable, with changes on time scales of a few days to a few years. These sources are often compact in size or observed to have one-sided jets. Radio quasars are further classified as Steep-Spectrum Radio Quasars (SSRQs) and Flat-Spectrum Radio Quasars (FSRQs), based on their radio spectral indices of $\alpha < -0.5$ and $\alpha > -0.5$, respectively (where the flux density S_ν at a frequency ν is given by $S_\nu \propto \nu^\alpha$).

BL Lacs: These sources have strong continuum emission along with rapid flux variability and high polarization. The continuum extends from radio to γ -ray frequencies. The emission lines are either weak or absent.

BL Lacs and a group of FSRQs which have very strong optical variability are collectively classified as blazars. The jet originating from the AGN is assumed to be oriented towards the observer in this class of objects, which accounts for the rapid variability and high polarization of the optical emission.

Various authors have tried to unify the various AGN types by invoking its asymmetric structure (see Figure 1.1; e.g. Urry, 2004). The different AGN classes are interpreted as the manifestations of different orientations of the AGN towards the line-of-sight. For example, when the line-of-sight is aligned close to the axis of the radio jet, then the central broad-line region is unobscured by the torus and the thick galactic disk. Such systems are classified as broad-line radio galaxies. In the case of BL Lacs and blazars, the line-of sight is within few degrees of the direction of the axis of the jet. In the case of the narrow-line radio galaxies, the line-of-sight is likely to be oriented close to the plane of the torus, and the thick disk. In such a case, the narrow-line regions that are projected in directions normal to the plane of the torus are visible. FR-I and FR-II radio galaxies are examples of narrow-line radio galaxies, in which the narrow-line regions and the radio lobes are oriented close to the plane of the sky.

Despite the current understanding of the physical properties and structure of AGNs, several critical questions still remain unanswered. How does the SMBH that is located in the centre of the galaxy accrete mass and dust, and what constitutes the material which is fueling the AGN? The circumnuclear gas clouds could provide the necessary mass to trigger and fuel the centrally located AGN, but the exact accretion mechanism and the geometries of these cloud structures remain ambiguous till date. The follow-

1. INTRODUCTION

ing section sheds light on some of the prominent accretion mechanisms and processes studied so far.

1.3 Inflow mechanisms

The angular momentum of the ambient gas in a galaxy must be reduced by several orders of magnitude before it is ‘fit’ for consumption by the black hole. In particular, the specific angular momentum of the matter located at a radius of a few kpc must be reduced by ≈ 4 orders of magnitude before it is consumed by the SMBH (Jogee, 2006). There is no known universal accretion mechanism that operates efficiently from scales of several kpc down to the last orbit of the black hole. Gravitational torques, dynamical friction (acting on massive circumnuclear gas clumps), hydrodynamic torques, and viscous torques are some of the mechanisms that remove the angular momentum from the gas component and channel it to small scales. These different mechanisms are of different relative importance at different radii in a galaxy. Their relative importance also differs when dealing with a strongly interacting galaxy versus an isolated one. Following is a brief description of the prominent scenarios in which these mechanisms come into play.

1.3.1 Cold gas accretion

Gallagher et al. (1977), Ekers (1978) and Gunn (1979) have suggested that the radio activity of the AGN might be associated with the presence of cold gas. This was further tested using larger samples by Walsh et al. (1989). Kotanyi and Ekers (1979) showed that the rotation axis of the cold gas is usually aligned with the radio axis. Further, van Gorkom et al. (1989) used the Very Large Array to search for HI 21 cm absorption in a well-defined sample of radio galaxies. They found that gas inflows are more common than outflows in local AGNs. There has been an increasing consensus that cold gas might be the main component of the gas mass which fuels the central AGN.

Binney (1977) pointed out the possible significance of cold gas accretion from the intergalactic medium (IGM), necessary for the formation of galaxies. Several recent simulations have shown that galaxies can indeed accrete cold gas from the IGM along filaments, without being shock heated (e.g. Brooks et al., 2009; Kaufmann et al., 2006; Kereš and Hernquist, 2009; Kereš et al., 2005; Peek et al., 2008). Further, the amount

of gas mass required to switch on a quiescent black hole is relatively small. Gas masses as little as $\approx 10^3 - 10^5 M_{\odot}$ could be sufficient to trigger an AGN (e.g. van Gorkom et al., 1989) over its maximum lifetime of $\approx 10^8$ yrs (Leahy et al., 1989). Considering that only small amounts of gas are required to trigger black holes, the slow accretion of cold gas from larger scales to the central regions of the galaxy may be a relevant mechanism to cause nuclear activity.

1.3.2 Galaxy mergers

Mergers and galaxy interactions disturb the galaxy potential and can channel the gas to the central regions. For example, mergers can cause tidal interactions, which may enhance cloud-cloud collisions, and hence, remove angular momentum from the gas. The low angular momentum gas can get stirred to the nuclear regions and eventually fuel the AGN. The orbits of interacting galaxies play an important role; direct collisions are more efficient in channeling gas to the central regions than retrograde encounters (e.g. Di Matteo et al., 2008).

A number of studies have searched for signatures of disturbances in radio galaxies. Signs of disturbance have been found mainly in optical and infrared bands; signs of interaction include tails, fans, bridges, shells and dust lanes (e.g. Canalizo et al., 2007; Heckman et al., 1986; Lin et al., 1988; Smith and Heckman, 1989; Tasse et al., 2008; Wu et al., 1998). Most radio galaxies ($\sim 85\%$) indeed show signatures of disturbances, in the form of merging and/or interaction (e.g. Heckman et al., 1986; Roche and Eales, 2000). Interestingly, however, a one-to-one correspondence between galaxy mergers and AGN activity does not seem to exist. This indicates that mergers are unlikely to be the primary mechanism for initiating AGN activity (e.g. Struve et al., 2010). Thus, while interactions of gas-rich objects may cause nuclear activity, galaxy mergers are not a necessary condition to trigger AGN activity.

1.3.3 Accretion of hot X-ray emitting gas

It is believed that most early-type galaxies are embedded in a hot X-ray emitting halo (see, e.g., Mo et al., 2010). The hot X-ray emitting gas can directly accrete into the vicinity of the black hole and can feed the central engine. Evidence for such accretion have been found in a few cases (e.g. Balmaverde et al., 2008; Best et al., 2006). Allen et al. (2006) have recently found a correlation between the jet power and the accretion

1. INTRODUCTION

rate of the hot gas, which implies that the hot X-ray emitting gas could be an important component of the fuel that powers the central AGN. Recent simulations also support the result that galaxies can efficiently accrete hot gas. In particular, the accretion is predicted to be more efficient in massive ($M_{halo} > 3 \times 10^{11} M_{\odot}$) galaxies (e.g. Croton et al., 2006).

1.4 Outflows and feedback

For a long time, the active nucleus was thought to be ‘inert’, in the sense that it has no impact on the host galaxy. It was believed that gas and dust could get accreted onto the AGN, and the gas could escape and form jets, without significant effects on the growth of the galaxy. However, recent simulations have shown that AGNs can regulate the growth of galaxies through the effects of mechanical feedback (e.g. Croton et al., 2006; Hopkins et al., 2005; Springel et al., 2005). Feedback is the process of transferring energy back to the IGM, and hence regulating gas collapse and star formation in the AGN host galaxy. The AGN heats the gas present in the nuclear region and drives it out, causing outflows of neutral, warm and/or hot gas (e.g. de Vries et al., 2002). These outflows result in the quenching of star formation in the central regions and possibly even end the active state of the nucleus (e.g. Fabian, 2012). This feedback effect due to the nuclear activity has gained prominence in recent years due to the discovery of massive gas outflows in a growing number of galaxies with AGNs. Many questions are still open, in particular with regard to the driving mechanism of these outflows. These questions have implications for understanding how ubiquitous the AGN-related feedback is, and whether it is linked to specific phases in the life of an AGN or is a recurrent phenomenon.

The kinetic interaction of the radio jet with gas in the ISM provides a possible mechanism for driving gas outflows. However, this mechanism has been criticized on the grounds that the opening angle of the jet is quite narrow and hence it is likely to affect only a small fraction of the ISM (e.g. Loeb and Furlanetto, 2013). However, recent simulations (e.g. Wagner and Bicknell, 2011; Wagner et al., 2012) have shown that this mechanism is indeed effective, especially when the radio source is in its initial phase and surrounded by a porous clumpy medium. This is because a large cocoon

of disturbed and outflowing gas is created around the radio jet due to the interaction with the radio plasma, thus affecting a much larger region of the galaxy.

Feedback from massive stellar outbursts which drive galactic superwinds is also believed to be critical to the evolution of galaxies. The cosmological models of galaxy evolution which do not implement the effect of stellar feedback have been found to show star formation rates (SFRs) ≈ 10 times the SFRs observed in galaxies (e.g. Hopkins et al., 2012; Katz et al., 1996; Somerville and Primack, 1999; Springel and Hernquist, 2003). The necessity for stellar feedback also arises due to the fact that the amount of baryons in real galactic discs is much lower than the amount of cool gas found in cosmological simulations (e.g. White and Frenk, 1991). This is especially found to be true in low-mass galaxies.

However, galactic winds seem to have a complex multi-phase structure (e.g. Hopkins et al., 2012). The physical structures in these winds seem to depend on the interactions between winds caused by multiple feedback mechanisms operating on different spatial and temporal scales. Any single feedback mechanism incorporated in the simulations fails to reproduce the observed winds (e.g. Hopkins et al., 2012). Hence, despite its acknowledged importance, the effect of feedback on galaxy evolution is sparsely understood. Also, it is unclear which of the two prominent mechanisms, AGN-induced feedback and supernovae outbursts, dominates the regulation of star formation. Blueshifted absorption features indicate gas outflows from the AGN. Detections of such blueshifted features can be used to trace the importance of feedback at different redshifts, and in different AGN types. Very long baseline interferometry (VLBI) in the redshifted HI 21 cm line (see section 1.5) can be used for follow-up observations of the detected absorption features. Such studies may be used to determine the location of gas outflows, and hence to determine whether they are likely to arise from AGNs or supernovae (e.g. Morganti et al., 2013).

1.5 Physics of the HI 21 cm line

The physical properties of atomic hydrogen present in galaxies can be probed via a hyperfine transition in the ground state of the H atom. This transition gives rise to radio emission or absorption at a wavelength of 21.1 cm. The transition occurs when the electron reverses its spin relative to that of the proton. Here, the higher energy

1. INTRODUCTION

state is the one in which the two spins are parallel, and the lower energy state is the one in which the two spins are anti-parallel. van de Hulst (1944) predicted that this transition should be observable in astronomical objects, and in 1951 two groups (Ewen and Purcell, 1951; Muller and Oort, 1951) reported the detection of emission from interstellar neutral hydrogen. The frequency of this transition has been determined in the laboratory to be 1420.405752 MHz (Kerr, 1968).

The number of atoms present in the upper and lower states, in a gas cloud that is in thermodynamic equilibrium, are related to the gas temperature by the Boltzmann distribution law,

$$\frac{n_1}{n_0} \equiv \frac{g_1}{g_0} e^{-(h\nu/kT)}, \quad (1.1)$$

where n_1 and n_0 are the number of atoms in the upper and lower states respectively, g_1 and g_0 are the statistical weights of the upper and lower levels, respectively, ν is the transition frequency, h and k are the Planck and Boltzmann constants, respectively, and T is the excitation temperature. While equation 1.1 applies to gas in thermodynamic equilibrium, which is not the case for astrophysical systems, we can use this relation to *define* a quantity with dimensions of temperature that describes the distribution of atoms in the two hyperfine states. This line excitation temperature is called the spin temperature, T_s , of the HI 21 cm line.

The spin temperature of the gas is influenced by a number of factors, including the gas kinetic temperature and the temperature of the radiation field at the 21 cm line frequency and at the Lyman- α frequency (e.g. Field, 1958; Liszt, 2001). In gas clouds of high density and far away from radio or ultraviolet sources, collisions dominate over the other effects, and the spin temperature is approximately equal to the kinetic temperature. This is the situation in cold gas clouds in normal galaxies. However, the timescale of collisions is much longer in low-density regions, and spin temperatures here are typically somewhat lower than the gas kinetic temperature (e.g. Liszt, 2001).

The spin temperature is related to the neutral hydrogen column density N_{HI} along the path by the equation (e.g. Kerr, 1968; Spitzer, 1968)

$$N_{\text{HI}} = 1.823 \times 10^{18} \times T_s \times \int \tau dv, \quad (1.2)$$

where $\int \tau dv$ is the velocity integral of the HI 21 cm optical depth τ . Here, N_{HI} is in cm^{-2} , T_s is in K, dv in km s^{-1} .

1.6 Associated HI 21 cm absorption studies

The spin temperature is a quantity of much interest as it provides information on the temperature of the HI gas. However, it should be emphasized that, for a multi-phase medium, the spin temperature is the column-density-weighted harmonic mean of the spin temperatures of different HI phases along the line of sight. T_s hence contains the information about the fraction of gas in cold and warm phases. Furthermore, T_s is biased towards cold gas: for example, the inferred T_s is only ≈ 200 K, if the gas is equally distributed between two phases of temperature ≈ 100 K and $\approx 10^4$ K.

Studies in the past have tried to estimate the spin temperatures of clouds in the galaxy using HI 21 cm emission and absorption spectroscopy. More than 80% of the measurements in the Milky Way yield $T_s < 350$ K (see, e.g., Braun and Walterbos, 1992). Dickey (1995) studied a few nearby spiral galaxies, and found the average spin temperatures to be 155 K for M31, 335 K for M33 and 180 K for the Large Magellanic Clouds. Other studies of nearby galaxies (e.g. Carilli et al., 1992; Reeves et al., 2015) have also obtained T_s values in the range 100 – 200 K. In the case of damped Lyman- α absorbers (DLAs), a class of quasar absorbers which have $N_{\text{HI}} \geq 2 \times 10^{20} \text{ cm}^2$, Kanekar et al. (2014) found that there is a statistically significant difference between the spin temperature distributions in their high- z and low- z DLA samples, and an even more significant difference between the spin temperature distributions in DLAs and in the Milky Way. However, there are also a few high- z DLAs with low spin temperatures, in the 100 – 300 K range (e.g. Kanekar et al., 2014; York et al., 2007).

1.6 Associated HI 21 cm absorption studies

Studies of the kinematics of gas present in and around AGN host galaxies can provide insights into the physics of active nuclei. Understanding the distribution and kinematics of different components of the circumnuclear gas is important both to study the fuelling of the radio activity and to probe AGN feedback.

Atomic gas in the host galaxies of radio-loud AGNs can be probed through absorption studies in the HI 21 cm line. An important advantage of using HI 21 cm absorption studies (as compared to HI 21 cm emission studies) is that the detectability of the absorption depends only on the strength of the background source. Therefore, HI 21 cm absorption can probe neutral gas in systems present at high redshifts, where it is not possible to detect the gas in emission (e.g. Kanekar and Briggs, 2004; Morganti,

1. INTRODUCTION

2012). For the same reason, HI 21 cm absorption can also be detected with high spatial resolution observations, which is again not possible for HI 21 cm emission. This makes HI 21 cm absorption suitable to study atomic gas in the circumnuclear environments of AGNs, particularly for systems at high redshifts. But, as a downside, it gives a view of the distribution of HI which is limited to the regions covering a background continuum source.

An estimate of the gas spin temperature T_s is required in order to compute the HI column densities of AGNs with searches for HI 21 cm absorption. In the vicinity of an AGN, the bright radio continuum source can change the hyperfine level populations, and hence alter the spin temperature, yielding values as high as $T_s \approx 8000$ K (e.g. Bahcall and Ekers, 1969; Maloney et al., 1996). This is far larger than spin temperatures in the Milky Way or nearby galaxies, and comparable to values seen in high- z DLAs. Unfortunately, we do not have any direct estimates of the spin temperature of the HI in AGN environments. Typical assumed spin temperatures in the literature are 100 K or 1000 K, implying a range of at least an order of magnitude in the N_{HI} estimates from this assumption alone. It would hence be more appropriate to work with the measured HI 21 cm optical depths, rather than the inferred HI column densities. While we will follow this practice in this thesis, we will also provide inferred HI column densities for all our targets, assuming a spin temperature of 100 K, for comparisons with the literature.

Associated HI 21 cm absorption studies can be used to probe the kinematics of gas relative to the AGN. The immediate surroundings of AGN are characterized by extreme physical conditions, where the interplay between the enormous amounts of energy released from the nucleus and the ISM takes place. Hence, it is critical to probe the kinematical properties of the gas present in these regions. Absorption features which are redshifted from the systemic velocity indicate the presence of inflowing gas, whereas blueshifted features are the signatures of gas outflows.

Associated HI 21 cm studies can also be used to probe AGN unification schemes (e.g. Barthel, 1989). These schemes try to unify various AGN classes by proposing that the properties of the different AGN types arise due to their different orientations to the line of sight (see the discussion in Section 1.2). For example, if the line of sight towards the central nucleus is parallel to the plane of the disk, we tend to observe the narrow-line regions, since these regions are projected in directions normal to the plane of the

1.7 Previous Associated HI 21 cm absorption studies

disk. Conversely, if the line of sight is close to the axis of the jet, the centrally located broad-line region is likely to be visible, since this region is not obscured by the torus or the thick disk along such a sightline. In such a scenario, detections of associated HI 21 cm should be systematically more common in narrow-line radio galaxies since the line of sight is close to the gaseous disk. Tentative evidence for this effect has been obtained by Morganti et al. (2001), but for a relatively small sample of AGNs at low redshifts ($z < 0.5$).

1.7 Previous Associated HI 21 cm absorption studies

At present, more than fifty radio sources have been detected with associated HI 21 cm absorption. Most of the target sources in these studies are limited to low or intermediate redshifts ($z < 1$) and have flux densities > 100 mJy. Sources with high flux densities are usually targeted, to maximize the sensitivity to HI 21 cm absorption. The detection rate is $\approx 15 - 20\%$ in extended radio galaxies (e.g. Emonts et al., 2010; Gupta et al., 2006; Morganti et al., 2001), and is higher ($\approx 30 - 40\%$) in the more compact gigahertz-peaked spectrum (GPS) and compact steep spectrum (CSS) sources (e.g. Gupta et al., 2006; Vermeulen et al., 2003). There appears to be a tendency for the compact sources to be more often detected in HI 21 cm absorption. Finally, only a small fraction of the sources detected in HI 21 cm absorption have been followed up using high-resolution VLBI observations (e.g. Morganti et al., 2013). Such VLBI observations are the key to identifying the location of the absorbing gas in the AGN host galaxy.

Searches for associated HI 21 cm absorption have been carried out for the past three decades, but physical conditions in neutral gas in AGN environments are still unclear. The first systematic search for HI 21 cm absorption in radio galaxies was performed by van Gorkom et al. (1989), as mentioned earlier. The authors obtained detections in 4 out of 29 observed sources. Absorption lines in all four sources were found to be redshifted from the systemic velocities. This preponderance of redshifted HI 21 cm absorption has been interpreted as evidence of cold gas falling into the nucleus (van Gorkom et al., 1989). However, in more recent years, HI 21 cm absorption has been detected in several samples of radio galaxies, out to intermediate redshifts, $z \approx 0.9$, and with detection rates $\lesssim 40\%$ (e.g. Gupta et al., 2006; Morganti et al., 2000, 2005; Pihlström et al., 2003; Vermeulen et al., 2003). Blueshifted absorption against the

1. INTRODUCTION

nucleus was detected at least as frequently as redshifted absorption in these samples. These results indicate that both infall and outflow may be important in AGN environments. Later searches for HI 21 cm absorption in larger but heterogeneous samples (e.g. Curran et al., 2008; Geréb et al., 2015) have been unable to shed much light on whether or not inflowing neutral gas is the main component of the AGN fuel.

The aforementioned studies of associated HI 21 cm absorption have found a wide range of absorption line profiles, ranging from narrow ($< 100 \text{ km s}^{-1}$) to broad ($\approx 1000 \text{ km s}^{-1}$) line widths. The features are also found to have a wide range of velocity offsets from the respective systemic velocities. The absorption profiles indicate that the gaseous structures around the central nucleus have complex morphologies (e.g. Geréb et al., 2015; Gupta et al., 2006). For example, narrow lines with widths $\lesssim 100 \text{ km s}^{-1}$ and small velocity offsets from the systemic redshifts would indicate gas clouds with low velocity dispersion, probably rotating in the circumnuclear disk. Conversely, broader absorption features indicate the presence of unsettled gas, probably interacting with the central radio source. Interactions between the neutral gas and the radio jet are likely to produce absorption lines with the largest widths. Such wide absorption features are typically found to be blueshifted from the systemic velocity and most commonly detected in compact sources (e.g. Geréb et al., 2015; Gupta et al., 2006; Pihlström et al., 2003). This indicates that compact sources might be the best targets to search for radio source-gas interactions and AGN-driven outflows.

Morganti et al. (2001) observed a sample of extended radio galaxies selected from the 2-Jy sample of Wall and Peacock (1985), to test AGN unification schemes. They observed the following trends in their sample. HI 21 cm absorption was detected in only one FR-I source out of an observed sample of 10 FR-I radio galaxies. In the case of FR-II radio galaxies, they detected HI 21 cm absorption in three out of four NLRGs, while absorption was not detected in any of four BLRGs. These findings are largely consistent with the predictions of the unified scheme (see, e.g., Pihlström et al., 2003; van Ojik et al., 1997). They also found that the detections of HI 21 cm absorption in two out of three NLRGs were blueshifted from the systemic velocity. This means that it would be too simplistic to attribute the neutral gas just to the torus. The gas could be widely distributed in the thick disk and its dynamics could be resulting in blueshifted and redshifted absorption features.

HI 21 cm absorption studies provide a useful probe to test the redshift evolution of the distribution of neutral hydrogen gas in AGN environments (e.g. Kanekar and Briggs, 2004). Unfortunately, most of the previous surveys of associated HI 21 cm absorption are limited to low redshifts ($z \leq 1$) (e.g. Gupta et al., 2006; Morganti et al., 2001; Vermeulen et al., 2003), and with only a handful of such searches at $z > 1$ (e.g. Curran et al., 2013; Gupta et al., 2006) present in the literature. Some of these searches have fairly low sensitivities. In fact, there are only four known associated HI 21 cm absorbers at $z > 1$; these are 3C190 at $z \approx 1.2$ (Ishwara-Chandra et al., 2003), J1545+4751 at $z \approx 1.3$ (Curran et al., 2013), MG J0414+0534 at $z \approx 2.6$ (Moore et al., 1999), and TXS 0902+343 at $z \approx 3.4$ (Uson et al., 1991). Most of these searches, particularly the ones at high redshifts (e.g. Curran et al., 2013; Gupta et al., 2006), have targeted heterogeneous samples. The main barrier to using HI 21 cm absorption studies to probe redshift evolution in AGN environments is the dearth of such studies, and detections of absorption, at higher redshifts. Also, the heterogeneous samples in the literature make it difficult to separate redshift effects in the AGN environment from differences in the AGN types observed at different redshifts. We have hence chosen to carry out a survey for redshifted associated HI 21 cm absorption in a large, uniformly-selected AGN sample, distributed over a wide redshift range, in the present thesis.

1.8 Outline of the thesis

Despite the wide range of studies, our understanding of the distribution and kinematics of neutral gas in AGN environments at high redshifts, and the redshift evolution of these quantities, is still quite poor. Presently, there are ≈ 25 searches for associated HI 21 cm absorption available at $z > 1$, but only four known associated HI 21 cm absorbers. An important question that arises when we examine the searches at high redshifts is why the number of associated HI 21 cm absorbers at $z \gtrsim 1$ is so small, while there are ≈ 50 known absorbers at low redshifts, $z < 1$. Even in the samples searched at $z < 1$, the detection fraction appears to be significantly higher at low redshifts, $z \lesssim 0.4$, compared to that at intermediate redshifts ($0.4 \lesssim z \lesssim 1$). Do the apparent differences in the number of detections and the detection rate imply a real phenomenon, indicating redshift evolution in the AGN environment? Or, are these just a manifestation of heterogeneous sample selection?

1. INTRODUCTION

The main objective of this thesis is to test whether the properties of the neutral hydrogen gas in AGN environments, including the detection fraction, the kinematics (e.g. infall versus outflow), the profile characteristics (e.g. broad versus narrow lines), etc., show any evolution with redshift. We have used a uniformly selected, large sample of AGNs for this purpose. The following is a chapter-wise outline of this thesis.

In Chapter 2, I explain the criteria used to obtain a uniform AGN target sample, as well as to maximize the detection rate of HI 21 cm absorption, based on previous studies. I then provide a detailed listing of the AGNs of our sample, along with their various characteristics. In Chapter 3, I describe the Giant Metrewave Radio Telescope (GMRT) observations that were carried out to acquire the data on which this thesis is based. Besides the observational details, this chapter also discusses the procedures that were used in the analysis of the GMRT data. In Chapter 4, I summarize the results from our observational programme. This chapter presents the final HI 21 cm absorption spectra for all our targets, discusses the routes used to confirm the detections of HI 21 cm absorption, describes the sources that did not yield usable spectra due to radio frequency interference, and provides the final observational results, including the flux density, the root-mean-square (RMS) spectral noise, the HI 21 cm optical depth (or limits on this quantity) and the derived HI column density (or limits on this quantity) for all the sources of our sample. In Chapter 5, I discuss in detail the new detections of associated HI 21 cm absorption that were obtained in this thesis, including the nature of the HI 21 cm absorption profiles and the AGN characteristics. Chapter 6 describes the results from a detailed statistical analysis of the strength of redshifted HI 21 cm absorption in different sub-samples of our full sample. This includes the dependence of the HI 21 cm opacity on redshift, AGN radio and ultraviolet luminosity, AGN spectral index, etc.. Finally, in Chapter 7, I provide a summary of the thesis and comment on future avenues for research in this field.

2

The Target Samples: Flat-Spectrum and Gigahertz-Peaked Spectrum Sources

In this chapter, we discuss the criterion of radio-source compactness which was used to select the sources in our sample. We briefly describe the physics of synchrotron emission and synchrotron self-absorption. We then discuss the inverted spectra and flat spectra characteristics, that were used to identify compact AGNs. Finally, we give the details of the Caltech-Jodrell Bank Flat-spectrum (CJF) source catalogue and the Gigahertz Peaked Spectrum (GPS) samples from the literature, from which the target sources were selected.

2.1 Radio-source compactness

A large fraction of the known radio sources at high redshifts ($z > 1$) remain unsearched for associated HI 21 cm absorption. Searches for HI 21 cm absorption in AGNs over a wide range of redshifts are essential to probe possible redshift evolution in the neutral gas in AGN environments. The problem with using samples which have been searched earlier in the literature is that the samples are highly heterogeneous, making it difficult to distinguish redshift evolution from differences in AGN type. We hence aimed to

2. THE TARGET SAMPLES: FLAT-SPECTRUM AND GIGAHERTZ-PEAKED SPECTRUM SOURCES

put together a large, uniformly-selected sample of AGNs, out to high redshifts $z \gtrsim 1$. The primary selection criterion is targeted at maximizing the detection rate of HI 21 cm absorption in the sample. This would enable us to trace the distribution and kinematical properties of the neutral hydrogen in and around AGN hosts.

A number of studies, mostly targetting AGNs at $z \lesssim 1$, have established that the integrated HI 21 cm optical depth ($\int \tau dv$) is anti-correlated with the spatial extent of the radio emission (e.g. Gupta et al., 2006; Pihlström et al., 2003). For example, Pihlström et al. (2003) found that the smaller Gigahertz Peaked-Spectrum (GPS) sources (with sizes < 1 kpc) have larger HI 21 cm optical depths compared to the larger Compact Steep-Spectrum (CSS) sources (with sizes > 1 kpc). Gupta et al. (2006) found that the detection rate of HI 21 cm absorption is highest for compact sources and lowest for the sources with extended continua in their sample of 96 sources. Such an inverse correlation between the integrated optical depth and the linear source size is expected because, when the linear size of the source is small, the foreground obscuring gas is likely to cover a larger fraction of the radio flux density. This will result in a larger covering factor, f , which takes values between 0 and 1. When $f \ll 1$, for extended sources, the apparent optical depth, τ_{app} , is much less than the true optical depth,

$$\tau_{app} = -\ln(1 - f + fe^{-\tau}), \text{ for } 0 < f \leq 1, \tau_{app} \ll 1 \quad (2.1)$$

Here τ is the true optical depth of the intervening medium. Compact radio sources have covering factors $f \approx 1$ and their apparent optical depth is hence very similar to the true optical depth. At a fixed optical depth sensitivity, the chances of detecting associated HI 21 cm absorption are thus higher towards compact radio sources. We have hence used source compactness as the principal criterion for selecting our target AGN sample.

2.2 Synchrotron self-absorption

Compact AGNs can be identified by examining their radio spectra. The steep-spectrum nature, with a higher flux density at low radio frequencies, of the typical radio spectra of AGNs implies that the radio emission is non-thermal in nature (see, e.g., Shu, 1991). The emission is presumed to be synchrotron radiation from ultra-relativistic electrons with energies of typically about 1 GeV, moving in weak magnetic fields of

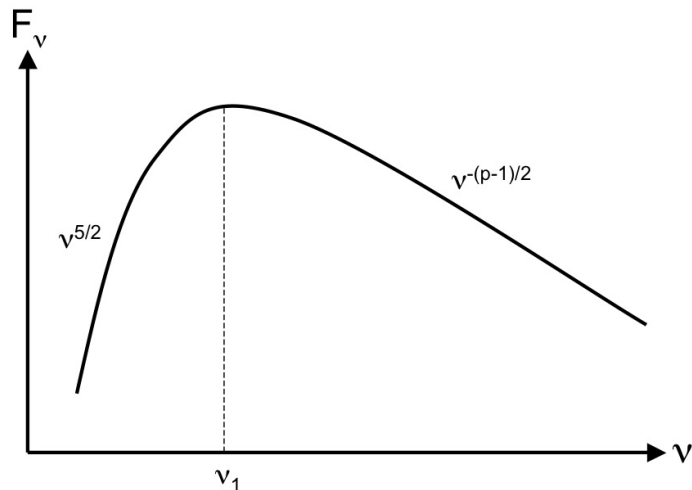


Figure 2.1: Radio spectrum of a compact source undergoing synchrotron self-absorption. ν_1 represents the turnover frequency.

about 10^{-4} gauss (e.g. Kellermann and Owen, 1988). For a power-law electron energy distribution, $\propto E^{-p}$, the spectrum follows a power-law ($S \propto \nu^\alpha$) shape at radio frequencies (e.g. Shu, 1991). The radio spectrum has a spectral index of $\alpha = -(p-1)/2$ (refer Fig. 2.1). However, at low radio frequencies, the relativistic electrons themselves absorb the emitted synchrotron photons; this is referred to as synchrotron self-absorption. Synchrotron self-absorption causes a turn-over in the spectrum, and results in lower flux densities at low radio frequencies. The self-absorbed spectrum has a positive spectral index, $\alpha = 5/2$, at frequencies below the turnover frequency; note that this is independent of the power-law index of the electron energy distribution (see Fig. 2.1 and Shu, 1991).

The turnover frequency represents a boundary in the frequency domain, between the optically thick and optically thin regimes of the emitting source. Compact and dense emitting regions can absorb synchrotron photons up to higher frequencies, compared to extended regions. Thus, compact sources are optically thick to synchrotron emission at higher frequencies than sources with extended radio emission. The turnover frequency thus depends on the compactness of the emitting source. In fact, the turnover frequency for a homogeneous, self-absorbed, incoherent synchrotron radio source with a power-law electron energy distribution depends on the angular extent of

2. THE TARGET SAMPLES: FLAT-SPECTRUM AND GIGAHERTZ-PEAKED SPECTRUM SOURCES

the radio source as $\nu_{max} \propto B^{1/5} S^{2/5} \theta^{-4/5} (1+z)^{1/5}$, where B is the magnetic field in gauss, the flux density at the peak S is in Jy, z is the redshift, and the angular size θ is in milli-arcsec (e.g. Kellermann and Pauliny-Toth, 1981). This means that compact regions would have higher turnover frequencies, whereas radio sources with larger linear extents would have turnovers at low radio frequencies. In extremely compact sources, synchrotron self-absorption can occur up to very high radio frequencies, giving rise to spectral turnovers in the GHz range. These sources are classified as Gigahertz Peaked Spectrum (GPS) sources (e.g. O’Dea, 1998). Some of these sources peak at tens of GHz, which are further classified as High-Frequency Peakers (HFPS) (e.g. Dallacasa et al., 2002; Edge et al., 1998). An inverse relation between the turnover frequency and the linear extent of the radio source can be inferred from these studies. Accordingly, O’Dea (1998) found the relation $\nu_{max} \propto l^{-0.65}$ between the turnover frequency ν_{max} and the largest linear extent l of the radio source for his sample of GPS sources.

2.3 GPS and Flat-spectrum sources

GPS sources are known to be extremely compact, with sizes $\lesssim 1$ kpc. It is now widely agreed that these sources correspond to the early stages of the evolution of powerful radio sources (e.g. Fanti et al., 1995; Readhead et al., 1996; Snellen et al., 2000). The radio emitting region grows and expands within the interstellar medium of the host galaxy, before breaking out to become a powerful radio source. It is thus interesting to study the gaseous environments in which these sources are engulfed. The ambient gas reservoirs could provide the necessary fuel to the central AGN for its activity.

Flat-spectrum radio sources are another class of compact sources, which are characterized by a spectral index of $\alpha \approx 0$ at low radio frequencies, up to ≈ 5 GHz. At higher frequencies the spectra bend to steeper power-laws. The flattening at low frequencies results from the superposition of the emission from several synchrotron-self-absorbed regions, each of which peaks at different frequencies (e.g. Cotton et al., 1980; Kellermann and Pauliny-Toth, 1969). Hence, the radio emission arises from multiple emitting components lying within a spatially compact region. The low-frequency radio spectrum

of these sources is typically complex, sometimes showing multiple weak peaks and dips, and a simple power-law form does not provide a good representation of the spectrum. However, a power-law with a small value of α (≈ 0) provides a good identifier of such sources.

We chose the flat-spectrum criterion to choose the target sample for our primary survey for associated HI 21 cm absorption in high-redshift AGNs, for the following reasons. First, the flat-spectrum criterion implies that the sources are relatively compact. Second, the low-frequency flux densities of flat-spectrum sources are typically higher than those of typical GPS sources, due to the flat spectra of the former class and the inverted spectra of the latter class. Since typical flat-spectrum sources have higher flux densities than typical GPS sources at their redshifted HI 21 cm line frequency, they require shorter integration times to achieve the same optical depth sensitivity. The selection of flat spectrum sources thus provides a balance between source compactness and low-frequency radio flux density, both critical for searches for redshifted HI 21 cm absorption

Besides the above primary survey in flat-spectrum sources, we also undertook a secondary survey for associated HI 21 cm absorption in GPS sources. There have been a few surveys in the past that searched for associated HI 21 cm absorption in GPS sources, but these searches were at fairly low redshifts, $z \lesssim 1.0$ (e.g. Gupta et al., 2006; Pihlström et al., 2003). It has been shown by Gupta et al. (2006) that, at low redshifts, GPS sources have the highest detection rate of associated HI 21 cm absorption, $\approx 60\%$. However, there are almost no searches in GPS sources at high redshifts, $z \gtrsim 1$, in the literature. We hence chose to target GPS sources at high redshifts, $z > 1$, in our secondary survey, aiming to study the detection rates and kinematic properties of associated neutral gas in the environments of GPS sources as a function of redshift.

2.4 The target samples

The Caltech-Jodrell Bank Flat-spectrum (CJF) sample (Henstock et al., 1995; Pearson and Readhead, 1988; Polatidis et al., 1995; Taylor et al., 1996) was used to select the target flat-spectrum AGNs for our primary survey. The following are the properties of the sources in the CJF sample which are important for the associated HI 21 cm absorption search: (1) All the sources have declinations (δ) $> 35^\circ$ and hence can be

2. THE TARGET SAMPLES: FLAT-SPECTRUM AND GIGAHERTZ-PEAKED SPECTRUM SOURCES

observed using the GMRT, (2) All the sources in the sample have flat spectra, with $\alpha_{1400}^{4850} > -0.5$ ($S_\nu \propto \nu^\alpha$), implying that the sources are compact, (3) accurate redshifts are available for most of the sources in the CJF sample, from the follow-up optical spectroscopy (e.g. Henstock et al., 1997), (4) the CJF sources are all relatively bright at radio frequencies, with 4.85 GHz flux densities ≥ 350 mJy (e.g. Taylor et al., 1996), (5) VLBI information is available for all CJF sources, at frequencies of $\approx 1 - 5$ GHz, providing additional details of their spatial structure (e.g. Polatidis et al., 1995; Taylor et al., 1996), and (6) low-frequency flux density estimates are available for all CJF sources from the 327 MHz Westerbork Northern Sky Survey (WENSS) (Rengelink et al., 1997) or the 365 MHz Texas survey (Douglas et al., 1996), and, from the 1.4 GHz Faint Images of the Radio Sky at Twenty-cm (FIRST) survey (Becker et al., 1995) or the NRAO VLA Sky Survey (NVSS) (Condon et al., 1998). The 1.4 GHz and 327/365 MHz flux densities can be used to infer the flux densities of the CJF sources at their redshifted HI 21 cm line frequencies, and (7) prior to this thesis, the detection rate of HI 21 cm absorption in the CJF sample was ≈ 40 %, mostly for sources at $z < 1$ (e.g. Gupta et al., 2006; Vermeulen et al., 2003).

The CJF sources appear to form a complete radio-selected sample, since they all have 4.85 GHz flux densities ≥ 350 mJy. However, the CJF flux density measurements extend over multiple observing epochs, so it is possible that AGN variability might cause a few sources to fall out of the CJF sample and others to be part of the sample. As such, the CJF sample is a “nearly-complete”, radio-selected sample.

There are a total of 293 sources in the CJF sample, distributed over redshifts $0 \lesssim z \lesssim 4.0$. 29 sources of the sample have been searched earlier in the literature for associated HI 21 cm absorption (see Table 2.1). We decided to cover all the remaining CJF sources that could be observed with the GMRT. We have compiled a sample of 74 CJF sources, out of which 21 lie at redshifts < 0.4 , 46 are in the redshift range $1.0 < z < 1.5$ and 7 are in the redshift range $3.0 < z < 3.6$. These sources could be observed using the GMRT’s 1420 MHz, 610 MHz and 325 MHz receivers to search for associated HI 21 cm absorption. Table 2.2 lists these sources in order of increasing redshift.

Our full flat-spectrum sample thus consists of 103 sources, including 29 sources from the literature and 74 sources that were observed during the course of this thesis. The distribution of this full sample of sources is as follows: 40 sources at redshifts

< 0.4 , 8 sources in the redshift range $0.4 < z < 1.0$, 48 sources in the redshift range $1.1 < z < 1.5$ and 7 sources in the redshift range $3.0 < z < 3.6$. It should be noted that we have not observed 8 CJF sources whose redshifted HI 21 cm line frequencies lie in the GMRT bands, five at $1.1 < z < 1.5$ and three at $3.0 < z < 3.6$, due to their low flux densities that would require large integration times to achieve good optical depth sensitivity. These eight sources are listed in Table 2.5. All remaining CJF sources with redshifted HI 21 cm line frequencies lying in the GMRT bands have been included in our survey.

For our second survey, we have put together a sample of 58 GPS sources at declinations observable with the GMRT, and whose HI 21 cm line frequencies redshift into the GMRT bands, from the GPS literature (de Vries et al., 2007; Labiano et al., 2007; Randall et al., 2011; Stanghellini et al., 1998). The selection criteria are that the sources should have inverted spectra, with the turn-over frequency lying between 300 MHz and 5 GHz, which is the definition of a GPS source (e.g. Labiano et al., 2007). Out of the 58 sources, 23 sources either have earlier searches for HI 21 cm absorption in the literature or have been included in the CJF target sample (refer Table 2.3). Of the remaining 35 sources, 10 have redshifts < 0.4 , 4 are in the range $1.1 < z < 1.5$ and 21 sources lie at redshifts $1.9 < z < 4.0$. We have observed 12 sources at redshifts < 0.4 and $1.1 < z < 1.5$ using GMRT. These sources are listed in Table 2.4. Two sources have been excluded from the sample since these have low flux densities (see Table 2.5).

In the next chapter, we discuss the details of the observations carried out for this thesis, and the data analysis techniques that were used to produce the HI 21 cm absorption spectra.

2. THE TARGET SAMPLES: FLAT-SPECTRUM AND GIGAHERTZ-PEAKED SPECTRUM SOURCES

Table 2.1: The 29 CJF sources with associated HI 21 cm absorption searches available in the literature, listed in order of increasing redshift.

Source	z	$\nu_{21\text{ cm}}^{\text{a}}$ MHz	Ref. ^b
TXS 1146+596	0.011	1405.2	1
TXS 0316+413	0.018	1395.8	2
B3 0651+410	0.022	1389.8	3
TXS 1101+384	0.030	1379.0	4
TXS 1744+557	0.030	1379.0	5
TXS 1652+398	0.034	1373.7	4
TXS 1254+571	0.042	1363.2	6
TXS 1807+698	0.051	1351.5	4
TXS 0402+379	0.055	1346.4	7
TXS 1144+352	0.063	1336.2	5
TXS 2200+420	0.069	1328.7	4
TXS 1946+708	0.101	1290.1	8
TXS 0309+411	0.134	1252.6	5
IVS B1622+665	0.201	1182.7	3
S5 1826+79	0.224	1160.5	9
TXS 2021+614	0.227	1157.6	9
TXS 2352+495	0.238	1147.3	9
TXS 0831+557	0.241	1144.6	9
TXS 1943+546	0.263	1124.6	9
TXS 1031+567	0.459	973.5	9
TXS 1355+441	0.646	862.9	9
S4 0108+38	0.669	851.1	10
TXS 1504+377	0.672	849.8	10
TXS 0923+392	0.695	838.0	9
S5 0950+74	0.695	838.0	9
TXS 1642+690	0.751	811.2	9
S4 1843+35	0.764	805.2	9
TXS 1543+480	1.277	623.8	11
TXS 0248+430	1.311	614.6	1

Notes:

^aThe column shows the redshifted HI 21 cm line frequencies.

^bThe column shows the literature references for associated HI 21 cm absorption searches.

References: (1)Gupta et al. (2006); (2)De Young et al. (1973); (3)Orienti et al. (2006); (4)van Gorkom et al. (1989); (5)Chandola et al. (2013); (6)Dickey (1982); (7)Morganti et al. (2009); (8)Peck et al. (1999); (9)Vermeulen et al. (2003); (10)Carilli et al. (1998b); (11)Curran et al. (2013).

2.4 The target samples

Table 2.2: The 74 CJF sources whose HI 21 cm line frequencies redshift into the GMRT bands.

Source	z	$\nu_{21 \text{ cm}}^{\text{a}}$ MHz	Band ^b MHz	$S_{1.4 \text{ GHz}}^{\text{c}}$ mJy	$S_{325 \text{ MHz}}^{\text{d}}$ mJy	$S_{\nu_{21 \text{ cm}}}^{\text{e}}$ mJy
TXS0344+405	0.039	1367.1	1420	496.3	1628.0	505.8
TXS0733+597	0.041	1365.1	1420	560.6	814.0	564.1
S5 2116+81	0.084	1310.3	1420	286.5	351.0	289.1
TXS1418+546	0.153	1232.4	1420	787.9	745.0	784.1
S4 0749+54	0.200	1183.7	1420	803.3	271.0	709.2
TXS0003+380	0.229	1155.7	1420	572.2	589.0	574.3
S4 1356+47	0.230	1154.8	1420	693.3	111.0	544.8
TXS0010+405	0.255	1131.8	1420	1650.9	3932.0	1873.1
TXS1719+357	0.263	1124.6	1420	819.2	680.0	796.7
B3 0251+393	0.289	1101.9	1420	230.4	227.0	229.8
TXS0716+714	0.300	1092.6	1420	726.6	1647.0	834.8
TXS1700+685	0.301	1091.8	1420	338.0	602.0	372.9
S5 1928+73	0.302	1090.9	1420	3950.2	4628.0	4058.9
JVASJ1010+8250	0.322	1074.4	1420	503.4	684.0	532.1
TXS0424+670	0.324	1072.8	1420	696.1	1460.0	796.7
JVAS J1458+3720	0.333	1065.2	1420	214.6	238.0	218.7
JVASJ2005+7752	0.342	1058.4	1420	1059.6	806.0	1005.6
TXS0035+367	0.366	1039.8	1420	843.6	2094.0	1015.0
TXS0954+658	0.368	1038.3	1420	729.4	630.0	707.9
JVASJ0929+5013	0.370	1036.5	1420	522.0	246.0	447.2
TXS0110+495	0.389	1022.6	1420	666.8	1174.0	753.1
TXS1030+415	1.117	671.0	610	473.2	805.0	618.3
TXS0249+383	1.122	669.4	610	662.7	1153.0	877.0
TXS 0600+442	1.136	665.0	610	948.6	1844.0	1418.0
JVASJ1048+7143	1.150	660.7	610	736.3	678.0	705.9
8C1305+804	1.183	650.7	610	784.8	2158.0	1334.2
TXS 2356+390	1.198	646.2	610	420.6	1231.0	558.5
TXS 0821+394	1.216	641.1	610	1480.8	3415.0	2061.1
TXS1954+513	1.223	639.8	610	1587.6	3092.0	2270.2
TXS1105+437	1.226	638.1	610	300.4	403.0	352.0
TXS1015+359	1.228	637.5	610	615.2	517.0	560.2
TXS1432+422	1.240	634.1	610	308.1	328.0	318.7
TXS 0945+408	1.249	631.6	610	1599.5	2711.0	2002.7
JVASJ1153+8058	1.250	631.3	610	1343.1	1388.0	1367.9
TXS1020+400	1.254	630.2	610	1122.6	2102.0	1582.0
JVASJ1044+8054	1.260	628.5	610	828.0	634.0	715.7
TXS 0641+392	1.266	626.8	610	442.8	510.0	852.7

Continued on next page

2. THE TARGET SAMPLES: FLAT-SPECTRUM AND GIGAHERTZ-PEAKED SPECTRUM SOURCES

Source	z	$\nu_{21\text{ cm}}^a$ MHz	Band ^b MHz	$S_{1.4\text{ GHz}}^c$ mJy	$S_{325\text{ MHz}}^d$ mJy	$S_{\nu_{21\text{ cm}}}^e$ mJy
TXS 0537+531	1.275	624.4	610	651.9	920.0	925.9
TXS1656+571	1.281	622.7	610	939.6	2837.0	1734.3
TXS 0707+476	1.292	619.7	610	1018.9	1232.0	1119.3
TXS0833+416	1.301	617.3	610	412.0	421.0	444.0
TXS2138+389	1.306	616.0	610	614.1	611.0	612.5
TXS2319+444	1.310	614.9	610	364.0	471.0	421.0
TXS 0850+581	1.318	612.9	610	1101.7	2122.0	1802.2
TXS1240+381	1.318	612.7	610	550.2	419.0	471.8
TXS2007+659	1.325	610.9	610	508.4	967.0	732.7
S5 2353+81	1.344	606.0	610	520.5	571.0	411.7
JVAS J2236+7322	1.345	605.7	610	267.6	341.0	307.7
TXS1342+663	1.351	604.2	610	638.5	284.0	400.9
TXS 0035+413	1.353	603.7	610	691.7	567.0	702.6
TXS1739+522	1.375	598.1	610	806.9	1251.0	1042.1
TXS1442+637	1.380	596.8	610	689.1	364.0	474.8
TXS 1030+611	1.401	591.6	610	461.9	736.0	591.0
TXS1010+350	1.410	589.4	610	355.5	443.0	405.0
TXS2229+695	1.413	588.7	610	508.5	512.0	510.7
TXS 0820+560	1.418	587.3	610	1449.4	1807.0	1551.7
TXS 0805+410	1.418	587.3	610	584.0	514.0	522.1
TXS 0804+499	1.436	583.1	610	1114.5	602.0	720.2
TXS0145+386	1.442	581.7	610	344.7	160.0	217.4
TXS 0917+624	1.446	580.7	610	945.7	1682.0	1463.0
JVAS J2311+4543	1.447	580.5	610	378.2	229.0	279.6
JVASJ1101+7225	1.460	577.4	610	1245.0	3044.0	2142.1
TXS 0859+470	1.470	575.1	610	1754.9	3373.0	2962.3
TXS 2253+417	1.476	573.7	610	1894.7	1165.0	1378.9
TXS 0340+362	1.484	571.8	610	513.2	585.0	541.3
JVAS J1747+4658	1.484	571.8	610	304.7	417.0	369.3
TXS0859+681	1.499	568.4	610	550.5	409.0	458.4
TXS1427+543	3.013	353.9	325	1028.3	2495.0	2372.0
TXS 0800+618	3.033	352.2	325	828.2	686.0	683.4
S5 0014+81	3.366	325.3	325	692.5	688.0	688.3
TXS 0642+449	3.396	323.1	325	452.4	716.0	712.8
TXS 0620+389	3.469	317.8	325	808.0	1558.0	1573.1
TXS 0604+728	3.530	313.6	325	1041.0	1933.0	1964.0
TXS 0749+426	3.589	309.5	325	710.0	539.0	534.2

Notes:

^aThe column shows the redshifted H I 21 cm line frequencies.

^bThe column shows the GMRT receiver band used to search for associated H I 21 cm absorption.

2.4 The target samples

^c The column lists the 1.4 GHz flux densities, from the FIRST or NVSS surveys (Becker et al., 1995; Condon et al., 1998).

^d The column lists the 325 MHz or 365 MHz flux densities from the WENSS or Texas surveys (Douglas et al., 1996; Rengelink et al., 1997).

^e The column lists the inferred flux density at the redshifted H I 21 cm line frequency, obtained by interpolating between the flux densities at 1.4 GHz and 325/365 MHz.

2. THE TARGET SAMPLES: FLAT-SPECTRUM AND GIGAHERTZ-PEAKED SPECTRUM SOURCES

Table 2.3: The 23 GPS sources with searches for associated HI 21 cm absorption available in the literature, listed in order of increasing redshift.

Source	z	$\nu_{21\text{ cm}}$ ^a MHz	Ref. ^b
TXS 0116+319	0.060	1340.0	3
B3 1315+415	0.066	1332.5	4
TXS 1404+286	0.077	1318.9	5
TXS 0902+468	0.085	1309.1	4
TXS 1946+708	0.101	1290.1	3
TXS 0729+562	0.104	1286.6	4
GB6 J1247+6723	0.107	1283.1	2
TXS 1345+125	0.122	1266.0	3
TXS 1601-222	0.141	1244.9	7
PKS 1934-63	0.181	1202.7	6
S3 0428+20	0.219	1165.2	1
TXS 2021+614	0.227	1157.6	1
TXS 0941-080	0.228	1156.7	1
TXS 0554-026	0.235	1150.1	1
TXS 2352+495	0.238	1147.3	1
TXS 2050+364	0.354	1049.0	1
TXS 1117+146	0.362	1042.9	1
TXS 1323+321	0.368	1038.3	1
8C 2342+821	0.735	818.7	1
TXS 2149+056	0.740	816.3	9
TXS 1518+046	1.296	618.6	7
TXS 2055+055	1.381	596.6	7
TXS 1351-018	3.707	301.8	8

Notes:

^aThe column shows the redshifted HI 21 cm line frequencies.

^bThe column shows the literature references for associated HI 21 cm absorption searches.

References: (1)Vermeulen et al. (2003); (2)Saikia et al. (2007); (3)Pihlström et al. (2003); (4)Chandola et al. (2011); (5)van Gorkom et al. (1989); (6)Véron-Cetty et al. (2000); (7)Gupta et al. (2006); (8)Curran et al. (2008); (9)Carilli et al. (1998b)

2.4 The target samples

Table 2.4: The 12 GPS sources whose HI 21 cm line frequencies redshift into the GMRT bands.

Source	z	$\nu_{21 \text{ cm}}^{\text{a}}$ MHz	Band ^b MHz	$S_{1.4 \text{ GHz}}^{\text{c}}$ mJy	$S_{325 \text{ MHz}}^{\text{d}}$ mJy	$S_{\nu_{21 \text{ cm}}}^{\text{e}}$ mJy
B3 0801+437	0.123	1264.8	1420	346.0	89.0	322.4
TXS 1540-077	0.172	1211.9	1420	1509.1	1650.0	1525.9
TXS 0320+053	0.179	1204.7	1420	2794.3	7130.0	3159.9
TXS 1819+671	0.221	1163.3	1420	301.3	454.0	317.9
TXS 1151-348	0.258	1129.0	1420	6440.0	1090.0	4650.6
TXS 1108+201	0.299	1093.4	1420	1195.3	681.0	1082.2
TXS 0019-000	0.305	1088.4	1420	265.0	287.0	2985.7
TXS 0240-217	0.314	1080.9	1420	1254.9	1120.0	1229.9
TXS 0507+179	0.416	1003.1	1420	704.7	1700.0	898.7
TXS 2121-014	1.158	658.2	610	1087.1	1780.0	1467.2
TXS 1200+045	1.226	638.1	610	1146.6	1390.0	1292.7
TXS 1245-197	1.275	624.3	610	5136.1	8890.0	7199.0

Notes:

^aThe column shows the redshifted HI 21 cm line frequencies.

^bThe column shows the GMRT receiver band used to search for associated HI 21 cm absorption.

^cThe column lists the 1.4 GHz flux densities, from the FIRST or NVSS surveys (Becker et al., 1995; Condon et al., 1998).

^dThe column lists the 325 MHz or 365 MHz flux densities from the WENSS or Texas surveys (Douglas et al., 1996; Rengelink et al., 1997).

^eThe column lists the inferred flux density at the redshifted HI 21 cm line frequency, obtained by interpolating between the flux densities at 1.4 GHz and 325/365 MHz.

2. THE TARGET SAMPLES: FLAT-SPECTRUM AND GIGAHERTZ-PEAKED SPECTRUM SOURCES

Table 2.5: The sources from the CJF and GPS samples with low inferred flux densities at the redshifted HI 21 cm line frequencies.

Source	z	$\nu_{21\text{ cm}}^{\text{a}}$ MHz	Band ^b MHz	$S_{1.4\text{ GHz}}^{\text{c}}$ mJy	$S_{325\text{ MHz}}^{\text{d}}$ mJy	$S_{\nu_{21\text{ cm}}}^{\text{e}}$ mJy
NGC 3468 ^h	0.025	1385.5	1420	45.1	–	45.1 ^f
CJ2 1534+501	1.121	669.7	610	212.9	59.0	111.4
7C 1550+5815	1.324	611.2	610	190.0	80.0	116.3
CJ2 1308+471	1.113	672.2	610	130.5	119.0	124.6
S5 0454+84	1.340	607.0	610	294.5	137.0	190.1
TXS 1851+488	1.250	631.3	610	238.2	186.0	208.2
S4 0636+68	3.180	339.8	325	192.4	58.0	58.0
BZQ J1526+6650	3.020	353.3	325	87.7	–	– ^g
B3 1839+389	3.095	346.9	325	142.7	73.0	73.0
PKS 2126-15 ^h	3.268	332.8	325	590.1	97.0	100.5

Notes:

^aThe column shows the redshifted HI 21 cm line frequencies.

^bThe column shows the GMRT receiver band used to search for associated HI 21 cm absorption.

^cThe column lists the 1.4 GHz flux densities, from the FIRST or NVSS surveys (Becker et al., 1995; Condon et al., 1998).

^dThe column lists the 325 MHz or 365 MHz flux densities from the WENSS or Texas surveys (Douglas et al., 1996; Rengelink et al., 1997).

^eThe column lists the inferred flux density at the redshifted HI 21 cm line frequency, obtained by interpolating between the flux densities at 1.4 GHz and 325/365 MHz.

^fThe flux density at 325 MHz is not available in the literature. However, since the redshifted HI 21 cm line frequency is close to 1.4 GHz, we have assumed that the flux density at the redshifted HI 21 cm line frequency is the same as that at 1.4 GHz.

^gThe flux density at ≈ 325 MHz is not available in the literature.

^hThese are GPS sources.

3

Observations and Data Analysis

In this chapter, we discuss the details of the observations that were carried out as part of our two GMRT surveys for associated HI 21cm absorption from neutral gas associated with compact AGNs, selected from the CJF and GPS samples. We then describe in detail the data analysis techniques that were employed in analysing the observed data.

3.1 The GMRT observations

3.1.1 CJF sources

The GMRT was used to observe the 74 sources of the CJF sample that did not have earlier searches for associated HI 21 cm absorption. GMRT's 327 MHz, 610 MHz and 1420 MHz receivers were used to observe the sources at $3.0 < z < 3.6$, $1.1 < z < 1.5$ and $z < 0.4$, respectively. The first 24 sources of the sample were observed in an initial, pilot GMRT survey in November 2008 in GMRT Cycle 15. Out of these 24 sources, 6 were in the redshift range $3.0 < z < 3.6$ and 18 were in the range $1.1 < z < 1.5$. The GMRT hardware correlator (the "GHB") was used as the backend for these observations. The observations used a bandwidth of 4.0 MHz for the 327 MHz band observations and 8.0 MHz for the observations in the 610 MHz band. Each 4/8 MHz band was centred at the redshifted HI 21 cm line frequency of the target source, and was subdivided into 256 channels using the GHB. The velocity resolution was $\sim 14.1 - 16.5 \text{ km s}^{-1}$ and the velocity coverage was $\sim 3600 - 4200 \text{ km s}^{-1}$ for the sources at redshifts $1.1 < z < 1.5$. For the sources at redshifts $3.0 < z < 3.6$, the velocity resolution was $\sim 13.3 - 15.5 \text{ km s}^{-1}$ and the velocity coverage was $\sim 3400 - 3900 \text{ km s}^{-1}$.

3. OBSERVATIONS AND DATA ANALYSIS

Another 37 sources of the full sample were observed in GMRT Cycle 26 in the period April–September 2014. 19 of these 37 sources have redshifts $1.1 < z < 1.5$, 17 are at $z < 0.4$, and the last source is at $z = 3.013$. The GMRT software correlator (“GSB”) was used as the backend for these observations. Bandwidths of 16.7 MHz or 33.3 MHz were used for all observations, centred at the redshifted HI 21 cm line frequency. The observing bands were divided into 512 channels each, using the high-resolution mode of the GMRT software correlator. For the sources at redshifts $z < 0.4$, the velocity resolution and coverage were $\sim 7.1\text{--}9.6\text{ km s}^{-1}$ and $\sim 3600\text{--}4900\text{ km s}^{-1}$, respectively, when a bandwidth of 16.7 MHz was used. The velocity resolution and coverage were $\sim 14.3\text{--}19.0\text{ km s}^{-1}$ and $\sim 7300\text{--}9700\text{ km s}^{-1}$, respectively, when a bandwidth of 33.3 MHz was used. For the sources at redshifts $1.1 < z < 1.5$, the velocity resolution and coverage were $\sim 14.5\text{--}17.3\text{ km s}^{-1}$ and $\sim 7400\text{--}8900\text{ km s}^{-1}$, respectively, when a bandwidth of 16.7 MHz was used. The values were $\sim 29.1\text{--}34.4\text{ km s}^{-1}$ and $\sim 14900\text{--}17600\text{ km s}^{-1}$ when a bandwidth of 33.3 MHz was used. Finally, the single source at $z = 3.013$ was observed using a bandwidth of 16.7 MHz; this yielded a velocity resolution of $\approx 13.8\text{ km s}^{-1}$ and a velocity coverage of $\approx 7050\text{ km s}^{-1}$.

The remaining 13 sources of the CJF sample were observed in GMRT Cycle 28, during the period May–August 2015. 4 of the 13 sources have redshifts $z < 0.4$, while the remaining 9 sources are at $z \approx 1.1$. The GSB was again used as the backend for these observations. All observations used a bandwidth of 16.7 MHz, centred at the expected redshifted HI 21 cm line frequency of each source, and sub-divided into 512 channels. The resolution and coverage were, respectively, $\approx 7.5\text{--}9.2\text{ km s}^{-1}$ and $\approx 3600\text{--}4900\text{ km s}^{-1}$, for sources at $z < 0.4$, and $\approx 15.2\text{--}16.7\text{ km s}^{-1}$ and $\approx 7400\text{--}8900\text{ km s}^{-1}$, respectively, for sources at $1.1 < z < 1.5$.

The sources with tentative HI 21 cm absorption detections were followed up with re-observations, to confirm the reality of the absorptions. The GSB was used as the backend for these observations. A bandwidth of 4.2 MHz, centred at the expected redshifted HI 21 cm line frequency of each source, and sub-divided into 512 channels, was used for observing the sources TXS 0003+380, TXS B3 1456+375 and TXS 1954+513. This provided higher velocity resolution of 2.1 km s^{-1} , 2.3 km s^{-1} and 3.8 km s^{-1} , respectively, and coverage of $\approx 1075\text{ km s}^{-1}$, $\approx 1178\text{ km s}^{-1}$ and $\approx 1946\text{ km s}^{-1}$, respectively, for the sources TXS 0003+380, B3 1456+375 and TXS 1954+513. The source TXS 0604+728 was re-observed two times using a bandwidth of 16.7 MHz,

3.1 The GMRT observations

sub-divided into 512 channels, and centred at the redshifted HI 21 cm line frequency. However, the data from the follow-up observations were strongly affected by RFI (see Section 4.1.1); we have hence listed the observational details from the first observation, for the source TXS 0604+728 in Table 3.1.

For most sources, the velocity coverage was sufficient to detect wide (FWHM $\lesssim 1000 \text{ km s}^{-1}$) absorption features, while the velocity resolution allowed good sensitivity to even relatively narrow ($\approx 20 \text{ km s}^{-1}$) spectral components. The velocity resolution was poorest for 8 sources, at $z \approx 1.1 - 1.5$, that were observed with a bandwidth of 33.3 MHz sub-divided into 512 channels, yielding a resolution of $\approx 30 \text{ km s}^{-1}$. For these sources, the search for absorption was carried out without smoothing the spectra; this is discussed in more detail later.

Our sensitivity goals were set based on the known distribution of HI 21 cm optical depths in the CJF sources with HI 21 cm absorption studies in the literature; these are plotted versus redshift in Fig. 3.1. It is clear from the figure that the lowest integrated HI 21 cm optical depth amongst detections in the literature is $\approx 0.59 \text{ km s}^{-1}$. We hence aimed to detect HI 21 cm absorption of this strength in all our targets at $\gtrsim 5\sigma$ significance. This implies a required HI 21 cm optical depth RMS noise of ≈ 0.015 per $\sim 8 \text{ km s}^{-1}$ and ≈ 0.008 per $\sim 15 \text{ km s}^{-1}$ channel. The estimates of the source flux densities at the redshifted HI 21 cm line frequencies, listed in Table 3.1, were used to compute the on-source times.

The source flux densities at the respective redshifted HI 21 cm line frequencies were inferred by interpolating between the measured flux densities at 1.4 GHz (from the FIRST or NVSS surveys; Becker et al. (1995); Condon et al. (1998)) and at 325 MHz or 365 MHz (from the WENSS and Texas surveys; Douglas et al. (1996); Rengelink et al. (1997)). The typical on-source times were ≈ 1 hour for sources observed with the 610 MHz and 1420 MHz receivers, ≈ 3 hours for sources observed with the 327 MHz receivers.

The data were recorded by following the usual pattern of observing a standard flux calibrator at the start or end of each run, and with long observations (scans of $\approx 30 - 40$ minutes) of the target source bracketed by short observations (scans of $\approx 5 - 6$ minutes) on a nearby phase calibrator. One or more of the flux calibrators 3C48, 3C147 and 3C286 were used for all observations, with scans of ≈ 7 -minute duration. Nearby compact sources, within $\approx 10^\circ$ of the target source, were chosen from

3. OBSERVATIONS AND DATA ANALYSIS

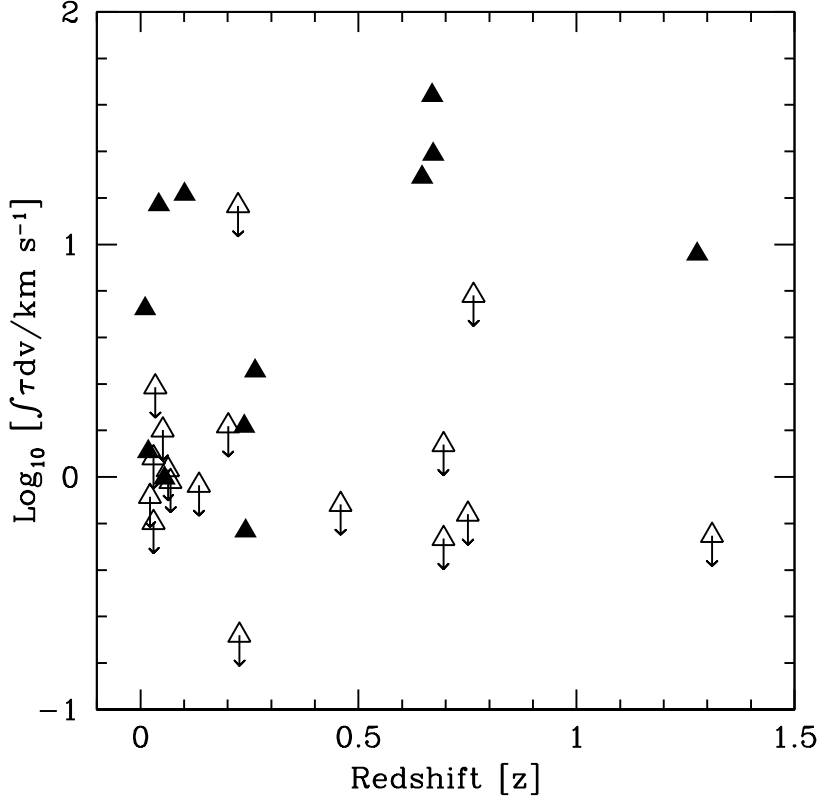


Figure 3.1: The figure shows the velocity-integrated HI 21 cm optical depths of the CJF sources from literature studies, plotted against redshift. Detections and non-detections of HI 21 cm absorption are shown as filled and hollow triangles, respectively.

the VLA calibrator manual for phase calibration. The flux and/or phase calibrators were also used to calibrate the system passband; no additional observations of bandpass calibrators were carried out.

The details of the observations of the 74 sources of the CJF sample are summarized in Table 3.1, in order of increasing source redshift. The columns of the table are (1) the source name, (2) the right ascension, RA, (3) the declination, DEC, (4) the redshift of the source, z , (5) the redshifted HI 21 cm frequency, $\nu_{21 \text{ cm}}$, in MHz (6) the estimated flux density at $\nu_{21 \text{ cm}}$, S_ν , in mJy (7) the date of observation, (8) the correlator that was used for the observations, GSB/GHB, (9) the bandwidth, BW, in MHz (10) the resolution, in kHz, (11) the velocity coverage, in km/s, (12) the velocity resolution, in km/s, and (13) the on-source time, in minutes.

3.1.2 GPS sources

12 GPS sources (from our full sample of 58 systems) that did not have earlier searches for redshifted HI 21 cm absorption were observed using the GMRT during this thesis. The observations were carried out in the period October–December 2015, in GMRT Cycle 29, using the GSB as the backend. 9 sources of the sample are at $z \lesssim 0.4$ and were observed with the 1420 MHz receivers, while 3 sources lie at $1.1 < z < 1.5$ and were observed with the 610 MHz receivers. A bandwidth of 16.7 MHz was used for all observations, centred at the expected redshifted HI 21 cm line frequency of each source, and sub-divided into 512 channels. This yielded a velocity coverage of $\approx 3900 - 5000 \text{ km s}^{-1}$ and a velocity resolution of $\approx 7.7 - 9.8 \text{ km s}^{-1}$ for sources at $z \lesssim 0.4$, and of $\approx 14.9 - 15.6 \text{ km s}^{-1}$ and $\approx 7600 - 8000 \text{ km s}^{-1}$, respectively, for sources at $1.1 < z < 1.5$. The two sources TXS 1200+045 and TXS 1245-197 showed tentative detections of HI 21 cm absorption in their spectra. Hence, these sources were re-observed, using the GSB as the backend, to confirm the reality of the absorptions. Again, a bandwidth of 16.7 MHz was used for the observations, centred at the expected HI 21 cm line frequency of each source, and sub-divided into 512 channels. The velocity resolution and velocity coverage were, respectively, $\approx 15.5 \text{ km s}^{-1}$ and $\approx 7800 \text{ km s}^{-1}$. Again, for all sources, the velocity coverage was sufficient to ensure good sensitivity to even wide absorption, while the velocity resolution was sufficient to detect narrow absorption components.

Our sensitivity requirements were based on the known distribution of the HI 21 cm optical depths in the GPS sources with HI 21 cm absorption studies in the literature. For these sources, the integrated HI 21 cm optical depths are plotted as a function of redshift in Figure 3.2. It is clear from the figure that the lowest detected integrated HI 21 cm optical depth and the most stringent 3σ upper limit on the integrated optical depth are a factor of $\approx 5 - 10$ lower than the second-lowest 3σ upper limit on the integrated optical depth ($\approx 0.15 \text{ km s}^{-1}$). Since the former two quantities are likely to be outliers of the present distribution, we chose to use the second lowest 3σ upper limit on the HI 21 cm optical depth in the literature GPS sample, i.e. 0.15 km s^{-1} , to set our sensitivity goals. We aimed to detect HI 21 cm absorption of this strength in all our targets at $\geq 5\sigma$ significance. This implies a required HI 21 cm optical depth RMS noise of ≈ 0.0037 per $\approx 8 \text{ km s}^{-1}$ channel and ≈ 0.0022 per $\approx 15 \text{ km s}^{-1}$ channel.

3. OBSERVATIONS AND DATA ANALYSIS

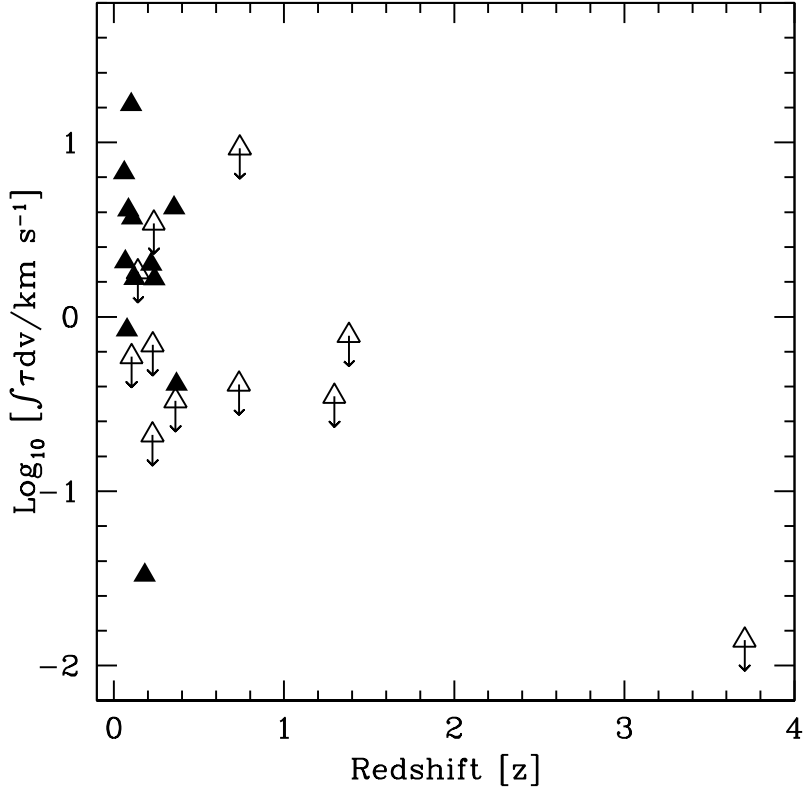


Figure 3.2: The figure shows the velocity-integrated HI 21 cm optical depths of the GPS sources from literature studies, plotted against redshift. Detections and non-detections of HI 21 cm absorption are shown as filled and hollow triangles, respectively.

The source flux densities at the respective redshifted HI 21 cm line frequencies were inferred by interpolating between the measured flux densities at 1.4 GHz (from the FIRST or NVSS surveys; Becker et al. (1995); Condon et al. (1998)) and at 325 MHz or 365 MHz (from the WENSS and Texas surveys; Douglas et al. (1996); Rengelink et al. (1997)). These flux densities are listed in Table 3.2 and were used to estimate the on-source integration times (≈ 1 hour in all cases). The observing procedure was the same as that for the CJF sample, described in Section 3.1.1.

The details of the observations of our 12 GPS targets are summarized in Table 3.2, in order of increasing AGN redshift. The columns of this table are the same as those of Table 3.1, listed at the end of Section 3.1.1.

3.2 Data Analysis

The GMRT measures the complex visibilities arising from radiation from some region of the sky, usually centred on the source of interest. The data are recorded by the correlator in the Long Term Accumulated (LTA) data format. We used the Astronomical Image Processing System (AIPS) software package to analyse all our GMRT data. The data were first converted from the LTA format to the Flexible Image Transport System (FITS) format, which can be read by AIPS programs, using the GMRT programs “listscan” and “gvfits”. Each FITS file was then imported into AIPS using the task FITLD, which yields a multi-source, multi-channel visibility dataset. The U-V datafile was initially indexed, using the task INDXR; this indexing speeds up the access to the actual data.

The first step in the data analysis is editing of the data to remove corrupted visibilities, arising due to non-working antennas, radio frequency interference (RFI), correlator effects, etc. The calibrator data from a single frequency channel of each data set were initially inspected to identify antennas that were “dead” throughout the observing session, or times at which individual antennas were not working. In the case of the observations with the hardware correlator from 2008, all data were inspected, baseline by baseline, to remove baseline-specific data affected by correlator errors (known to be common with the GHB). The AIPS tasks VPLOT and UVPLT were used to examine the data and identify antennas or time ranges with systematic problems. A list of such “bad” antennas, time ranges, or baselines were specified in an ASCII file in a format that could be read with the AIPS task UVFLG. Later, the flags for a single channel were applied to all channels of the dataset. The data editing was done independently for the two polarizations.

For a radio interferometer, the measured complex visibilities must be calibrated to obtain the true visibilities, before one carries out the 2-D Fourier transform to obtain the sky image. In general, the complex gains $G_{ij}(\nu, t)$ depend on baseline, frequency, and time. The calibration of radio interferometers is based on two critical simplifying assumptions, first that the complex gain on any baseline can be factored into the product of two antenna-based gains, i.e. $G_{ij}(\nu, t) = f_i(\nu, t) \times f_j(\nu, t)$, where i and j denote antenna numbers, and second, that the antenna-based gains themselves can be factored into the product of two functions, one of which [denoted by $g_i(t)$] depends

3. OBSERVATIONS AND DATA ANALYSIS

solely on time and the other of which [denoted by $B_i(\nu)$] depends solely on frequency. The time-dependent part, $g_i(t)$, is usually referred to as the antenna-based system gain, while the frequency-dependent part, $B_i(\nu)$, is referred to as the antenna-based system bandpass. The two functions are estimated separately, via the procedure below.

The first step in determining the antenna-based gains, $g_i(t)$, is to set the flux density scale by estimating the flux density of the primary calibrators (3C48, 3C147 or 3C286) at the observing frequency. This was done using the task SETJY on the above single-channel dataset, using the Perley-Butler flux scale (Perley and Butler, 2013). The task CALIB was then used to solve for the antenna-based complex gains for both the primary (i.e. flux) and secondary (i.e. phase) calibrators, using a typical solution interval of 2 minutes. Next, the task GETJY was used to estimate the flux density of the phase calibrator, scaling from the known flux density of the primary calibrator. Finally, the task CLCAL was used to interpolate between phase calibrator scans to obtain the antenna-based complex gains on the target source. The calibrated data were then again inspected for time-specific intermittent RFI or other baseline-dependent effects, using the tasks VPLOT, UVPLT and TVFLG, and corrupted data were further edited out. This calibration and editing procedure was carried out iteratively until no bad calibrator data remained. The final flag and calibration tables were then copied over to the multi-channel visibility data set.

Next, we determined the antenna-based system bandpass, $B_i(\nu)$, from the multi-channel visibility data sets. We typically used the flux calibrator to derive the bandpass solutions, due to the high signal-to-noise here. In some cases, the phase calibrator was sufficiently bright to be used to calibrate the bandpass, and this allowed us to also track any changes in the bandpass shape with time. The antenna-based bandpasses $B_i(\nu)$ were derived by normalizing the function at one channel (i.e. setting the visibility amplitude of this channel to unity and the phase to zero), chosen to be in a line-free part of the spectrum and also somewhat distant from the falling edges of the bandpass. We also divided the visibilities at all channels by the visibility at this channel (referred to as “channel-0”), as this has been found to provide more stable bandpass solutions.

After solving for the bandpass, the solutions were inspected using the task POSSM, for the RR and LL polarizations separately. In some cases, antenna-based RFI was seen, or large oscillations were observed in the bandpass shapes. In such situations, additional flagging was carried out to remove the affected data (in some cases, by

removing the antenna itself), and we then again solved for the bandpass solutions. The process was carried out iteratively until clean bandpass solutions were obtained for all antennas.

The antenna-based complex gain and bandpass solutions were then applied to the data of the target source using the task `SPLIT`. The bandpass calibration was carried out using the nearest bandpass solutions (in time). This yielded a calibrated multi-channel visibility dataset on the target source. An initial spectrum was obtained by vector averaging the visibilities using `POSSM`, to test for strong absorption, RFI, or other systematic patterns.

The next step in the analysis procedure is to self-calibrate the data on the target source and also produce a good continuum image of the field. For this purpose, and to reduce the data size, a number of line- and RFI-free channels were averaged together to produce a “channel-0” dataset. Before the averaging, the task `CLIP` was used to remove strong RFI from the channels that were to be averaged together. The task `AVSPC` was then used to carry out the averaging; in this process, care was taken to retain sufficient frequency resolution so that the images would not be affected by bandwidth smearing at the edges of the GMRT primary beam. This produced a channel-averaged visibility dataset consisting of typically 10 – 20 channels, of resolution ≈ 0.5 MHz, ≈ 1 MHz, and ≈ 2 MHz, for observations in the 327 MHz, 610 MHz and 1420 MHz bands, respectively. These channel-0 datasets were used for the purpose of imaging and self-calibration.

The task `IMAGR` was used to carry out the imaging procedure: we typically imaged a region out to the first null of the GMRT primary beam at the observing frequency. A 3-D imaging procedure was used, based on faceting of the 3-D sky into multiple 2-D planes. This is to avoid the large errors that arise when the small-field approximation is used to produce the image through a simple 2-D Fourier inversion. In the 3-D imaging technique, the field is split into a number of facets, where each facet is imaged by shifting the phase centre to the centre of the facet. The facet size is chosen so that the small field approximation holds true for each facet. The task `SETFC` was used to choose the facets for each target source, with care being taken to ensure sufficient overlap of the facets for accurate imaging of sources at the facet edges.

The imaging procedure used a “robust” weighting scheme (`ROBUST=1` in `AIPS`), under which the visibilities were given intermediate weights between “natural” weighting (in which the weights are the reciprocals of the variance of the error in the visibili-

3. OBSERVATIONS AND DATA ANALYSIS

ties) and “uniform” weighting (where the weights are the reciprocals of the local density of the visibilities). This provides a reasonable balance between the higher sensitivity that is obtained in natural weighting and the better point spread function and imaging characteristics that are obtained in uniform weighting.

Finally, the shortest baselines (typically, within 500 metres) were excluded from the imaging and self-calibration procedure to reduce the effect of RFI. Further, the sidelobes of the synthesized beam were reduced by tapering the data at long UV distances and before holes in the UV coverage, so as to avoid sharp breaks in the UV coverage.

The task IMAGR was used to “CLEAN” and deconvolve the image, assuming that sources in the sky can be represented by delta functions. The CLEAN’ing was typically stopped when the peak image residual (after subtracting CLEAN components) was about three times the root-mean-square noise on the image. The resulting image was then used to self-calibrate the UV visibilities, using the task CALIB, again excluding the short baselines. CLEAN components up to the first negative in each facet were used for the self-calibration, to ensure that only real sources are used. The typical solution interval was 2 minutes. The self-calibrated data were then again imaged, using IMAGR, and the new image further used for self-calibration. This procedure was carried out iteratively, typically involving 3 rounds of phase-only self-calibration and 2 rounds of amplitude-and-phase self-calibration, until the final image did not improve on further self-calibration. The CLEAN components of the final image (again, up to the first negative component in each facet) were then subtracted from the calibrated visibilities using the task UVSUB, and the residuals inspected for systematic effects with the tasks UVPLT and VPLOT. Any data showing systematic features were removed, using a combination of CLIP and UVFLG. The iterative self-calibration procedure was then re-run until the final image did not improve on further self-calibration and data editing.

Most of the target sources were found to be unresolved by the GMRT synthesized beam. Their flux densities were measured by fitting a single-Gaussian model to a small region of the image plane around the target, using the task JMFIT.

Next, the calibration and flag tables that were obtained from the above self-calibration procedure were copied back and applied to the original calibrated multi-channel, single-source UV visibility dataset. All CLEAN components of the final continuum image were then subtracted out from this calibrated multi-channel dataset, using the task UVSUB. Any residual continuum emission was further subtracted via a linear

baseline fit to line- and RFI-free spectral regions, using the task UVLIN. A final round of baseline-by-baseline flagging, to edit out intermittent RFI, was then done using the task SPFLG (again for RR and LL polarizations separately). The residual visibilities were then shifted to the heliocentric frame using the task CVEL (note that the GMRT does not do online Doppler tracking). The final, multi-channel, continuum-subtracted visibilities in the heliocentric frame were then imaged in all channels using IMAGR, with natural weighting to increase the sensitivity, to obtain a three-dimensional spectral cube. A spectrum was extracted from this cube by taking a cut along the frequency axis at the location of the AGN. The final spectrum was then obtained by subtracting out a second-order polynomial fit to line- and RFI-free regions, to compensate for any residual bandpass effects.

Table 3.1: Observational details of the 74 CJF sources. Sources are listed in the order of increasing redshift.

Name	RA	DEC	z	$\nu_{21 \text{ cm}}^{\text{a}}$ MHz	$S_{\nu_{21 \text{ cm}}}^{\text{b}}$ mJy	Date	Cor. ^c	BW MHz	Res. kHz	Vel. cov. km/s	Res. km/s	Time ^d min
TXS 0344+405	03h48m00.0s	+40d43m59s	0.039	1367.1	505.8	3-7-2014	GSB	33.3	65.1	7321.6	14.3	75
TXS 0733+597	07h37m30.1s	+59d41m03s	0.041	1365.1	564.1	28-7-2014	GSB	33.3	65.1	7321.6	14.3	60
S5 2116+81	21h14m01.2s	+82d04m48s	0.084	1310.3	289.1	28-5-2015	GSB	16.7	32.6	3840.0	7.5	60
TXS 1418+546	14h19m46.6s	+54d23m15s	0.153	1232.4	784.1	20-5-2014	GSB	33.3	65.1	8140.8	15.9	60
S4 0749+54	07h53m01.4s	+53d53m00s	0.200	1183.7	709.2	28-7-2014	GSB	33.3	65.1	8448.0	16.5	60
TXS 0003+380	00h05m57.2s	+38d20m15s	0.229	1155.7	574.3	3-7-2014	GSB	33.3	65.1	8642.6	16.9	90
TXS 0003+380 ^e	00h05m57.2s	+38d20m15s	0.229	1155.7	547.3	19-10-2015	GSB	4.2	8.1	1075.2	2.1	60
S4 1356+47	13h58m40.6s	+47d37m58s	0.230	1154.8	544.8	19-5-2014	GSB	33.3	65.1	8652.8	16.9	60
TXS 0010+405	00h13m31.1s	+40d51m37s	0.255	1131.8	1873.1	20-5-2014	GSB	33.3	65.1	8857.6	17.3	60
TXS 1719+357	17h21m09.5s	+35d42m16s	0.263	1124.6	796.7	20-5-2014	GSB	33.3	65.1	8908.8	17.4	60
B3 0251+393	02h54m42.6s	+39d31m35s	0.289	1101.9	229.8	30-5-2015	GSB	16.7	32.6	4556.8	8.9	60
TXS 0716+714	07h21m53.4s	+71d20m36s	0.300	1092.6	834.8	21-6-2014	GSB	33.3	65.1	9164.8	17.9	60
TXS 1700+685	17h00m09.3s	+68d30m07s	0.301	1091.8	372.9	28-5-2015	GSB	16.7	32.6	4556.8	8.9	60
S5 1928+73	19h27m48.5s	+73d58m02s	0.302	1090.9	4058.9	20-5-2013	GSB	33.3	65.1	9164.8	17.9	60
S5 1003+83	10h10m15.8s	+82d50m14s	0.322	1074.4	532.1	19-5-2014	GSB	33.3	65.1	9318.4	18.2	60
TXS 0424+670	04h29m06.0s	+67d10m17s	0.324	1072.8	796.7	21-6-2014	GSB	33.3	65.1	9318.4	18.2	60
B3 1456+375	14h58m44.8s	+37d20m22s	0.333	1065.2	218.7	28-5-2015	GSB	16.7	32.6	4710.4	9.2	75
B3 1456+375 ^e	14h58m44.8s	+37d20m22s	0.333	1065.2	148.4	19-10-2015	GSB	4.2	8.1	1177.6	2.3	90
S5 2007+77	20h05m30.9s	+77d52m43s	0.342	1058.4	1005.6	20-5-2014	GSB	33.3	65.1	9472.0	18.5	75
TXS 0035+367	00h37m46.1s	+36d59m11s	0.366	1039.8	1015.0	21-6-2014	GSB	33.3	65.1	9625.6	18.8	60
TXS 0954+658	09h58m47.2s	+65d33m55s	0.368	1038.3	707.9	28-7-2014	GSB	33.3	65.1	9625.6	18.8	60
CJ2 0925+504	09h29m15.4s	+50d13m36s	0.370	1036.5	447.2	28-7-2014	GSB	33.3	65.1	9676.8	18.9	60
TXS 0110+495	01h13m27.0s	+49d48m24s	0.389	1022.6	753.1	3-7-2014	GSB	33.3	65.1	9779.2	19.1	60
TXS 1030+415	10h33m03.7s	+41d16m06s	1.117	671.0	618.3	28-4-2014	GSB	16.7	32.6	7475.2	14.6	60

Continued on next page

Name	RA	DEC	z	$\nu_{21\text{ cm}}^{\text{a}}$ MHz	$S_{\nu_{21\text{ cm}}}^{\text{b}}$ mJy	Date	Cor. ^c	BW MHz	Res. kHz	Vel. cov. km/s	Res. km/s	Time ^d min
TXS 0249+383	02h53m08.9s	+38d35m25s	1.122	669.4	877.0	31-8-2014	GSB	33.3	65.1	14950.4	29.2	60
TXS 0600+442	06h04m35.6s	+44d13m59s	1.136	665.0	1418.0	17-11-2008	GHB	8.0	31.3	3609.6	14.1	45
S5 1044+71	10h48m27.6s	+71d43m36s	1.150	660.7	705.9	15-5-2014	GSB	16.7	32.5	7577.6	14.8	60
8C 1305+804	13h06m05.7s	+80d08m21s	1.183	650.7	1334.2	28-6-2014	GSB	33.3	65.1	15411.2	30.1	60
TXS 2356+390	23h58m59.9s	+39d22m28s	1.198	646.2	558.5	25-11-2008	GHB	8.0	31.3	3712.0	14.5	60
TXS 0821+394	08h24m55.5s	+39d16m42s	1.216	641.1	2061.1	25-11-2008	GHB	8.0	31.3	3737.6	14.6	30
TXS 1954+513	19h55m42.7s	+51d31m49s	1.223	639.8	2270.2	28-4-2014	GSB	16.7	32.6	7833.6	15.3	60
TXS 1954+513 ^e	19h55m42.7s	+51d31m49s	1.223	639.8	1514.3	13-5-2015	GSB	4.2	8.1	1945.6	3.8	90
TXS 1105+437	11h08m23.5s	+43d30m54s	1.226	638.1	352.0	9-8-2015	GSB	16.7	32.6	7833.6	15.3	60
TXS 1015+359	10h18m11.0s	+35d42m39s	1.228	637.5	560.2	28-4-2014	GSB	16.7	32.6	7833.6	15.3	60
TXS 1432+422	14h34m05.7s	+42d03m16s	1.240	634.1	318.7	24-8-2015	GSB	16.7	32.6	7884.8	15.4	60
TXS 0945+408	09h48m55.3s	+40d39m45s	1.249	631.6	2002.7	25-11-2008	GHB	8.0	31.3	3814.4	14.9	45
S5 1150+81	11h53m13.0s	+80d58m29s	1.250	631.3	1367.9	28-6-2014	GSB	33.3	65.1	15820.8	30.9	60
TXS 1020+400	10h23m11.5s	+39d48m15s	1.254	630.2	1582.0	28-4-2014	GSB	16.7	32.6	7936.0	15.5	60
S5 1039+81	10h44m23.0s	+80d54m39s	1.260	628.5	715.7	28-6-2014	GSB	33.3	65.1	15923.2	31.1	60
TXS 0641+392	06h44m53.7s	+39d14m48s	1.266	626.8	852.7	25-11-2008	GHB	8.0	31.3	3814.4	14.9	60
TXS 0537+531	05h41m16.2s	+53d12m25s	1.275	624.4	925.9	25-11-2008	GHB	8.0	31.3	3840.0	15.0	60
TXS 1656+571	16h57m20.7s	+57d05m54s	1.281	622.7	1734.3	14-5-2014	GSB	16.7	32.6	8038.4	15.7	60
TXS 0707+476	07h10m46.1s	+47d32m11s	1.292	619.7	1119.3	19-9-2014	GSB	33.3	65.1	16128.0	31.5	100
TXS 0833+416	08h36m36.9s	+41d25m55s	1.301	617.3	444.0	31-8-2014	GSB	33.3	65.1	16179.2	31.6	60
TXS 2138+389	21h40m16.9s	+39d11m45s	1.306	616.0	612.5	15-5-2014	GSB	16.7	32.6	8140.8	15.9	60
TXS 2319+444	23h22m20.3s	+44d45m42s	1.310	614.9	421.0	24-8-2015	GSB	16.7	32.6	8140.8	15.9	60
TXS 0850+581	08h54m42.0s	+57d57m30s	1.318	612.9	1802.2	25-11-2008	GHB	8.0	31.3	3916.8	15.3	45
TXS 1240+381	12h42m51.4s	+37d51m00s	1.318	612.7	471.8	28-4-2014	GSB	16.7	32.6	7833.6	15.3	60
TXS 2007+659	20h07m28.8s	+66d07m23s	1.325	610.9	732.7	28-4-2014	GSB	16.7	32.6	8140.8	15.9	60

Continued on next page

Name	RA	DEC	z	$\nu_{21\text{ cm}}^{\text{a}}$ MHz	$S_{\nu_{21\text{ cm}}^{\text{b}}}$ mJy	Date	Cor. ^c	BW MHz	Res. kHz	Vel. cov. km/s	Res. km/s	Time ^d min
S5 2353+81	23h56m22.8s	+81d52m52s	1.344	606.0	411.7	25-11-2008	GHB	8.0	31.3	3968.0	15.5	60
JVAS J2236+7322	22h36m38.6s	+73d22m53s	1.345	605.7	307.7	16-8-2015	GSB	16.7	32.6	8243.2	16.1	60
TXS 1342+663	13h44m08.7s	+66d06m12s	1.351	604.2	400.9	9-8-2015	GSB	16.7	32.6	8294.4	16.2	60
TXS 0035+413	00h38m24.8s	+41d37m06s	1.353	603.7	702.6	17-11-2008	GHB	8.0	31.3	3968.0	15.5	60
TXS 1739+522	17h40m37.0s	+52d11m43s	1.375	598.1	1042.1	15-5-2014	GSB	16.7	32.6	8345.6	16.3	60
TXS 1442+637	14h43m58.6s	+63d32m26s	1.380	596.8	474.8	28-6-2014	GSB	33.3	65.1	16742.4	32.7	60
TXS 1030+611	10h33m51.4s	+60d51m07s	1.401	591.6	591.0	17-11-2008	GHB	8.0	31.3	4070.4	15.9	60
TXS 1010+350	10h13m49.6s	+34d45m51s	1.410	589.4	405.0	9-8-2015	GSB	16.7	32.6	8499.2	16.6	60
TXS 2229+695	22h30m36.5s	+69d46m28s	1.413	588.7	510.7	15-5-2014	GSB	16.7	32.6	8499.2	16.6	30
TXS 0820+560	08h24m47.2s	+55d52m43s	1.418	587.3	1551.7	17-11-2008	GHB	8.0	31.3	4070.4	15.9	40
TXS 0805+410	08h08m56.7s	+40d52m45s	1.418	587.3	522.1	17-11-2008	GHB	8.0	31.3	4070.4	15.9	60
TXS 0804+499	08h08m39.7s	+49d50m37s	1.436	583.1	720.2	17-11-2008	GHB	8.0	31.3	4121.6	16.1	60
TXS 0145+386	01h48m24.4s	+38d54m05s	1.442	581.7	217.4	16-8-2015	GSB	16.7	32.6	8601.6	16.8	90
TXS 0917+624	09h21m36.2s	+62d15m52s	1.446	580.7	1463.0	17-11-2008	GHB	8.0	31.3	4147.2	16.2	60
JVAS J2311+4543	23h11m47.4s	+45d43m56s	1.447	580.5	279.6	24-8-2015	GSB	16.7	32.6	8601.6	16.8	60
S5 1058+72	11h01m48.8s	+72d25m37s	1.460	577.4	2142.1	14-5-2014	GSB	16.7	32.6	8652.8	16.9	60
TXS 0859+470	09h03m04.0s	+46d51m04s	1.470	575.1	2962.3	17-11-2008	GHB	8.0	31.3	4172.8	16.3	30
TXS 2253+417	22h55m36.7s	+42d02m53s	1.476	573.7	1378.9	25-11-2008	GHB	8.0	31.3	4172.8	16.3	60
TXS 0340+362	03h43m29.0s	+36d22m12s	1.484	571.8	711.3	17-11-2008	GHB	8.0	31.3	4224.0	16.5	60
B3 1746+470	17h47m26.6s	+46d58m51s	1.484	571.8	369.3	9-8-2015	GSB	16.7	32.6	8755.2	17.1	30
TXS 0859+681	09h03m53.1s	+67d57m23s	1.499	568.4	458.4	31-8-2014	GSB	33.3	65.1	17561.6	34.3	45
TXS 1427+543	14h29m21.9s	+54d06m11s	3.013	353.9	2372.0	5-5-2014	GSB	16.7	32.6	7065.6	13.8	90
TXS 0800+618	08h05m18.2s	+61d44m23s	3.033	352.2	683.4	22-11-2008	GHB	4.0	15.6	3404.8	13.3	180

Continued on next page

Name	RA	DEC	z	$\nu_{21\text{ cm}}^{\text{a}}$ MHz	$S_{\nu_{21\text{ cm}}}^{\text{b}}$ mJy	Date	Cor. ^c	BW MHz	Res. kHz	Vel. cov. km/s	Res. km/s	Time ^d min
S5 0014+81	00h17m08.5s	+81d35m08s	3.366	325.3	688.3	22-11-2008	GHB	4.0	15.6	3686.4	14.4	180
TXS 0642+449	06h46m32.0s	+44d51m17s	3.396	323.1	712.8	23-11-2008	GHB	4.0	15.6	3712.0	14.5	120
TXS 0620+389	06h24m19.0s	+38d56m49s	3.469	317.8	1573.1	23-10-2013	GHB	4.0	15.6	3788.8	14.8	180
TXS 0604+728	06h10m48.9s	+72d48m53s	3.530	313.6	1964.0	23-10-2013	GHB	4.0	15.6	3814.4	14.9	210
TXS 0749+426	07h53m03.3s	+42d31m31s	3.589	309.5	534.2	23-11-2008	GHB	4.0	15.6	3891.2	15.2	180

Notes:

^a $\nu_{21\text{ cm}}$ is the redshifted H I 21 cm line frequency.

^b $S_{\nu_{21\text{ cm}}}$ is the flux density of the source at the redshifted H I 21 cm line frequency. This was estimated by interpolating between the 1.4 GHz and 325/365 MHz flux densities from the literature.

^c The column shows the correlator that was used for the observation, GSB/GHB.

^d The on-source times are rounded to the nearest multiple of 15m.

^e These details are for the follow-up observations.

3.3 Sources affected by RFI

From our data analysis, we found that the data on 11 sources from the CJF sample were strongly affected by RFI. Clean RFI-free spectra could not be obtained for these sources, and we have hence excluded them from the sample, and our subsequent analysis. Below, we provide a few details on the spectra of these sources, and the reasons for their exclusion.

1. S4 1356+47, $z = 0.230$: This source was observed using the 1420 MHz receivers, using a bandwidth of 16.7 MHz centred at 1154.80 MHz and sub-divided into 512 channels, with the GSB as the correlator. Strong RFI features spanning $\gtrsim 50$ channels, near the redshifted HI 21 cm line frequency, were found to be present in the data, affecting $\approx 70\%$ of the baselines. Other channel ranges were found to be affected by strong narrow-band RFI, in $\approx 60\%$ of the baselines. Since even the remaining baselines are likely to be affected by low-level RFI, it is very difficult to obtain a reliable RFI-free spectrum; we hence chose to exclude this source from the sample.

2. B3 0251+393, $z = 0.289$: The 1420 MHz receivers were used for these observations, with a bandwidth of 16.7 MHz centred at 1101.94 MHz and sub-divided into 512 channels, with the GSB as the correlator. The data were found to be corrupted by multiple broadband and narrowband RFI features in all baselines and throughout the observing time.

3. TXS 0716+714, $z = 0.300$: This source was observed with the 1420 MHz receivers, with a 16.7 MHz band centred at 1092.62 MHz, and sub-divided into 512 channels, with the GSB as the correlator. Three strong and broad (width ≈ 70 channels) RFI features were visible in the data, affecting all baselines, and present throughout the observing period.

4. TXS 1700+685, $z = 0.301$: The source was observed with the 1420 MHz receivers, with a 16.7 MHz band centred at 1091.77 MHz and sub-divided into 512 channels, with the GSB as the correlator. The data of all baselines were found to be corrupted by wideband RFI features spanning ≈ 120 channels, and present throughout the observations.

5. S5 1928+73, $z = 0.302$: The source was observed with the 1420 MHz receivers, with a 33.3 MHz band centred at 1090.86 MHz and sub-divided into 512 channels, with the GSB as the backend. Multiple RFI patterns, each extending over ≈ 40 channels,

were evident in the data, in all baselines and observing times.

6. JVAS J1010+8250, $z = 0.322$: The 1420 MHz receivers were used for these observations, with a central frequency of 1074.44 MHz, and a bandwidth of 33.3 MHz sub-divided into 512 channels, and the GSB as the correlator. Multiple wideband RFI features spanning ≈ 1520 channels were visible on all baselines, and at all observing times. Broadband RFI covering a large number of channels was also visible in $\approx 80\%$ of the data.

7. TXS 0249+383, $z = 1.122$: The observations used the 610 MHz receivers, with a 33.3 MHz band centred at 669.37 MHz and sub-divided into 512 channels, with the GSB as the correlator. Broadband RFI was found to be present in all channels and throughout the observation, on all baselines. Strong narrowband RFI was also seen in individual channels.

8. 8C 1305+804, $z = 1.183$: The source was observed using the 610 MHz receivers, with a bandwidth of 33.3 MHz centred at 650.67 MHz and sub-divided into 512 channels, with the GSB as the correlator. Wideband patchy RFI features were seen on all baselines during most of the observing times, with the worst data arising at the higher frequencies of the band. Some individual channels were also affected by strong narrowband RFI.

9. TXS 2138+389, $z = 1.306$: The source was observed with the 610 MHz receivers, using a 16.7 MHz bandwidth centred at 615.96 MHz and sub-divided into 512 channels, and the GSB as the correlator. The final Stokes-I spectrum showed a wide absorption feature spanning ≈ 180 channels, but there were clear differences in the strength of the absorption in the RR and LL polarizations: the absorption was not visible in the LL polarization. Attempts were made to salvage the spectrum by careful data editing, but no strong patterns were visible on inspecting the time-frequency plane in SPFLG. It is clear that the data are affected by RFI that is either causing the strong absorption in the RR polarization or suppressing it in the LL polarization. Since we cannot separate between these possibilities, we chose to exclude this source from the sample.

10. TXS 0859+681, $z = 1.499$: The source was observed with the 610 MHz receivers, using a 33.3 MHz bandwidth, centered at 568.39 MHz and sub-divided into 512 channels, with the GSB as the correlator. Wideband RFI patterns covering all channels were visible in the data, on all baselines and at all observing times, strongly affecting the lower frequency channels. Some of the individual channels were also affected by

3. OBSERVATIONS AND DATA ANALYSIS

strong narrowband RFI, in all the baselines.

11. TXS 0014+813, $s = 3.033$: This source was observed on multiple occasions using the 325 MHz receivers. Bandwidths of 4 MHz and 16 MHz, sub-divided into 256 (GHB) and 512 (GSB) channels, respectively, and centered at 352.20 MHz, were used for the observations. All data were severely affected by RFI, on all baselines.

Finally, the spectra of 5 sources from the GPS sample, TXS 1540-077 at $z = 0.172$, TXS 0320+053 at $z = 0.179$, TXS 1151-348 at $z = 0.258$, TXS 0019-000 at $z = 0.305$, and TXS 0240-217 at $z = 0.314$, show a clear ripple across the observing band. This may have arisen due to time variability in the antenna bandpass shapes that was not calibrated out. Attempts to excise these ripples by careful data editing were unsuccessful. Wide-band RFI features, spanning $\approx 50 - 80$ channels, were visible in $\approx 70\%$ of the data in these sources, making it impossible to obtain clean spectra. These 5 GPS sources were hence excluded from our sample and from later discussion.

Table 3.2: Observational details of the 12 GPS sources.

Name	RA	DEC	z	$\nu_{21\text{ cm}}^{\text{a}}$ MHz	$S_{\nu_{21\text{ cm}}}^{\text{b}}$ mJy	Date	Cor. ^c	BW MHz	Res. kHz	Vel. cov. km/s	Res. km/s	Time ^d min
B3 0801+437	08h04m54.9s	+43d35m37s	0.123	1264.8	322.4	27-10-2015	GSB	16.7	32.6	3942.4	7.7	120
TXS 1540-077	15h43m01.7s	-07d57m07s	0.172	1211.9	1525.9	6-12-2015	GSB	16.7	32.6	4147.2	8.1	90
TXS 0320+053	03h23m20.3s	+05d34m12s	0.179	1204.7	3159.9	21-10-2015	GSB	16.7	32.6	4147.2	8.1	45
TXS 1819+671	18h19m44.4s	+67d08m47s	0.221	1163.3	317.9	6-12-2015	GSB	16.7	32.6	4300.8	8.4	390
TXS 1151-348	11h54m21.8s	-35d05m29s	0.258	1129.0	4650.6	23-10-2015	GSB	16.7	32.6	4454.4	8.7	60
TXS 1108+201	11h11m20.1s	+19d55m36s	0.299	1093.4	1082.2	22-10-2015	GSB	16.7	32.6	4556.8	8.9	90
TXS 0019-000	00h22m25.4s	+00d14m56s	0.305	1088.4	2985.7	21-10-2015	GSB	16.7	32.6	4608.0	9.0	60
TXS 0240-217	02h42m35.9s	-21d32m26s	0.314	1080.9	1229.9	22-10-2015	GSB	16.7	32.6	4659.2	9.1	60
TXS 0507+179	05h10m02.4s	+18d00m42s	0.416	1003.1	898.7	22-10-2015	GSB	16.7	32.6	5017.6	9.8	60
TXS 2121-014	21h23m39.1s	-01d12m35s	1.158	658.2	1467.2	12-12-2015	GSB	16.7	32.6	7628.8	14.9	30
TXS 1200+045	12h03m21.9s	+04d14m19s	1.226	638.1	1292.7	11-12-2015	GSB	16.7	32.6	7833.6	15.3	60
TXS 1200+045 ^e	12h03m21.9s	+04d14m19s	1.226	638.1	1675.2	15-08-2016	GSB	16.7	32.6	7833.6	15.3	105
TXS 1245-197	12h48m23.9s	-19d59m19s	1.275	624.3	7199.0	11-12-2015	GSB	16.7	32.6	7987.2	15.6	60
TXS 1245-197 ^e	12h48m23.9s	-19d59m19s	1.275	624.3	8302.2	16-08-2016	GSB	16.7	32.6	7987.2	15.6	135

Notes:

^a $\nu_{21\text{ cm}}$ is the redshifted HI 21 cm line frequency.

^b $S_{\nu_{21\text{ cm}}}$ is the flux density of the source at the redshifted HI 21 cm line frequency. This was estimated by interpolating between the 1.4 GHz and 325/365 MHz flux densities from the literature.

^c The column shows the correlator that was used for the observation, GSB/GHB.

^d The on-source times are rounded off to the nearest multiple of 15m.

^e These details are for the follow-up observations.

3. OBSERVATIONS AND DATA ANALYSIS

4

Results

In this chapter, we present the results of our data analysis. We display the spectra of all sources of the CJF and GPS samples that had reliable RFI-free data. We discuss in detail all sources with detections of HI 21 cm absorption. Finally, we provide a tabular summary of our results, which include the integrated HI 21 cm optical depths (or limits on this quantity), and the equivalent HI column density (or limits).

4.1 The Caltech-Jodrell Flat Spectrum sample

Except for two sources, TXS 0344+405 and TXS 1954+513, all sources in the CJF sample are compact and unresolved in the GMRT images at the respective redshifted HI 21 cm line frequencies. Hence, we have fitted a single Gaussian component to a small region around the target source, using the task JMFIT, to measure the source flux densities. Our measured flux densities are listed in Table 4.1. TXS 0344+405 and TXS 1954+513 both show extended radio structures, consisting of a central core and two extended emission components, with a typical FR-II morphology (see Figure 4.1). Since our aim is to search for neutral gas in the environments of compact AGNs, we have considered only the core components of these two sources in our analysis.

We have obtained three new confirmed detections and one new tentative detection of associated HI 21 cm absorption from our analysis of the 74 CJF sources. Out of the 74 target sources, the spectra of 59 sources were consistent with noise, with no evidence for any significant absorption. The GMRT data towards the remaining 11 sources were severely affected by RFI around the redshifted HI 21 cm line frequency, and it

4. RESULTS

was not possible to obtain reliable, RFI-free spectra for these sources (see Section 3.3 for details). The GMRT HI 21 cm absorption spectra of the 63 sources (3 confirmed detections, 1 tentative detection, and 59 non-detections) with usable data are displayed in Figure 4.2, in order of increasing redshift. For the two sources TXS 0344+405 and TXS 1954+513, we have provided absorption spectra at the peaks of the core and the extended emission components, in the figure. We did not detect any absorption in the spectra towards the source TXS 0344+405, against either the core or the radio lobes. In the case of TXS 1954+513, strong HI 21 cm absorption was detected in the spectrum towards the radio core, while no absorption was detected in the spectra towards the two lobes.

For all sources, the panels of the figure show flux density (in mJy) plotted against velocity (in km/s) relative to the source redshift. Except for the four detections, and the sources that were observed using a velocity resolution of $\approx 30 \text{ km s}^{-1}$, all the spectra have been Hanning-smoothed and re-sampled, to reduce the effect of Gibbs ringing. The shaded regions in the spectra indicate channels that were corrupted by RFI. Note that the RMS noise values on the final spectra were obtained over the RFI-free and line-free channels. The final spectra of two sources, TXS 0954+658 and S5 2007+77, show a clear ripple across the observing band that may have arisen due to time variability in the antenna bandpass shapes that could not be calibrated out. Attempts to excise these ripples by data editing were unsuccessful. Since the peak-to-peak spread of the ripple is relatively low, the spectra may still be used to constrain the presence of strong absorption. Hence, for these two sources, we conservatively computed our limits on the HI 21 cm optical depth (and thence, on the HI column density) as $3 \times$ the peak-to-peak spread in the optical depth.

4.1 The Caltech-Jodrell Flat Spectrum sample

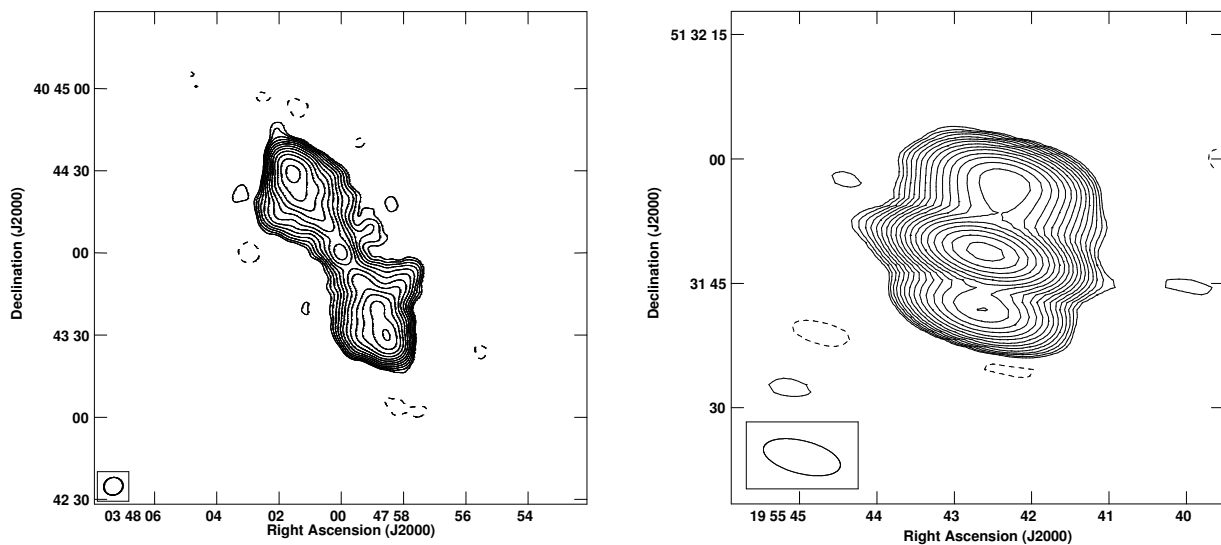


Figure 4.1: The left panel shows the GMRT 1367.1 MHz continuum image of the source TXS 0344+405, showing the core, and two radio lobes extended towards north-west and south-east directions. The positive contour levels extend from 1.8 mJy/Bm to 921.6 mJy/Bm, in steps of $\sqrt{2}$, while the single negative (dashed) contour is at -1.8 mJy/Bm. The right panel shows the GMRT 638.9 MHz continuum image of the source TXS 1954+513, displaying the core, and two radio lobes extended in the north and south directions. The positive contour levels extend from 2.0 mJy/Bm to 1024.0 mJy/Bm, in steps of $\sqrt{2}$, while the single negative (dashed) contour is at -2.0 mJy/Bm.

4. RESULTS

4.1.1 HI 21 cm detections in the CJF Sample

1. TXS 0003+380, $z = 0.229$:

This source was initially observed on 3/7/2014, using the 1420 MHz receivers. A bandwidth of 16.7 MHz, centered at 1155.74 MHz, and sub-divided into 512 channels was used for the observations, with the GSB as the backend. 3C48 was used for flux calibration, while 0029+349 was used for phase calibration. The on-source time was ≈ 94 minutes. A narrow absorption line with $\approx 18\sigma$ significance was detected in the initial spectrum. To confirm the reality of the line, we re-observed the source on 19/10/2015, using a bandwidth of 4.2 MHz split into 512 channels. This provided a finer velocity resolution of 2.1 km/s. Again, the source 3C48 was used as the flux calibrator, and 0029+349 was used for phase calibration. The on-source time was ≈ 62 minutes in the second run. The absorption line was again detected in the spectrum. The peak of the absorption profile in both the spectra is blueshifted by ≈ 40 km/s from the source redshift. The absorption line was detected with $> 10\sigma$ significance in both the observing runs, suggesting that the absorption is likely to be real.

The radio source in the continuum image is compact, with no extended structure. A single gaussian was fitted to the source using the task JMFIT. The peak flux density of the source is 547.3 ± 0.2 mJy. The integrated optical depth of the line is 1.943 ± 0.057 km/s.

2. B3 1456+375, $z = 0.333$:

The initial observations of this source were carried out on 28/5/2015, using the 1420 MHz receivers. A bandwidth of 16.7 MHz, sub-divided into 512 channels, and centred at a frequency of 1065.23 MHz, was used for the observations, with the GSB as the software backend. The standard calibrator 3C286 was observed to calibrate the flux density scale and the system passband, and the source 1416+347 was observed to calibrate the phases. The on-source time was ≈ 75 minutes. A narrow absorption line with $\approx 14\sigma$ significance was detected in the initial spectrum. We hence re-observed the radio source on 19/10/2015 to confirm the reality of the absorption. We used a bandwidth of 4.2 MHz, split into 512 channels, for this observation, which provided a finer velocity resolution of 2.3 km/s. Again, the sources 3C286 and 1416+347 were used for flux and phase calibration. The on-source time in the second observing run was ≈ 92 minutes. The absorption line was again detected in the second observing run.

4.1 The Caltech-Jodrell Flat Spectrum sample

The peak of the absorption line is blueshifted from the source redshift by ≈ 62 km/s in both spectra. The detection of the absorption line in both observing runs, separated by few months, suggests that the absorption is likely to be real.

The continuum radio source is compact and unresolved in the GMRT image at 1065 MHz. The peak flux density of the source is estimated to be 148.4 ± 0.1 mJy. The integrated optical depth of the line is 3.834 ± 0.079 km/s.

3. TXS 1954+513, $z = 1.223$:

The source was first observed on 28/04/2014, using the 610 MHz receivers. A bandwidth of 16.7 MHz, centred at 639.82 MHz and sub-divided into 512 channels, was used for the observations, with the GSB as the correlator. The standard flux calibrators 3C286 and 3C295 were observed to calibrate the flux density scale and the system passband. No phase calibrator was used since the target source is known to be compact at low radio frequencies. The on-source time was ≈ 60 minutes. A narrow absorption feature with $\approx 8\sigma$ significance was detected in this initial spectrum. To confirm the reality of the absorption feature, we re-observed this source on 13/5/2015. A bandwidth of 4.2 MHz, sub-divided into 512 channels, was used for the second observing run, to obtain a finer spectral resolution of 3.8 km/s. 3C286 was again used to calibrate the flux density scale and the system bandpass. The on-source time was ≈ 90 minutes in this second observing run. The absorption line was re-detected in the spectrum obtained from the second observation. The peak of the absorption line is blueshifted from the source redshift by ≈ 325 km/s in both the spectra. Since the absorption line was detected in both the observing runs, it is likely that the absorption is real.

The GMRT 640 MHz continuum image of the source shows extended emission structure, with three distinguishable components: a central core and two extended lobes in north and south directions. We fitted a 3-component Gaussian model to the source (using the task JMFIT), to estimate the flux densities. The peak and the integrated flux densities of the core are 1221.3 ± 0.6 mJy/Bm and 1254.1 ± 1.2 mJy respectively. The peak and integrated flux densities of the northern and the southern lobes are 247.9 ± 0.7 mJy/Bm and, 403.4 ± 1.6 mJy, and, 184.0 ± 0.7 mJy/Bm and, 198.1 ± 1.3 mJy, respectively. The core appears to be marginally resolved since the peak and the integrated flux densities have slightly different values. We have used the peak core flux to compute the integrated HI 21 cm optical depth. The integrated optical

4. RESULTS

depth of the detected HI 21 cm absorption feature is $0.716 \pm 0.037 \text{ km s}^{-1}$.

4. TXS 0604+728, $z = 3.530$:

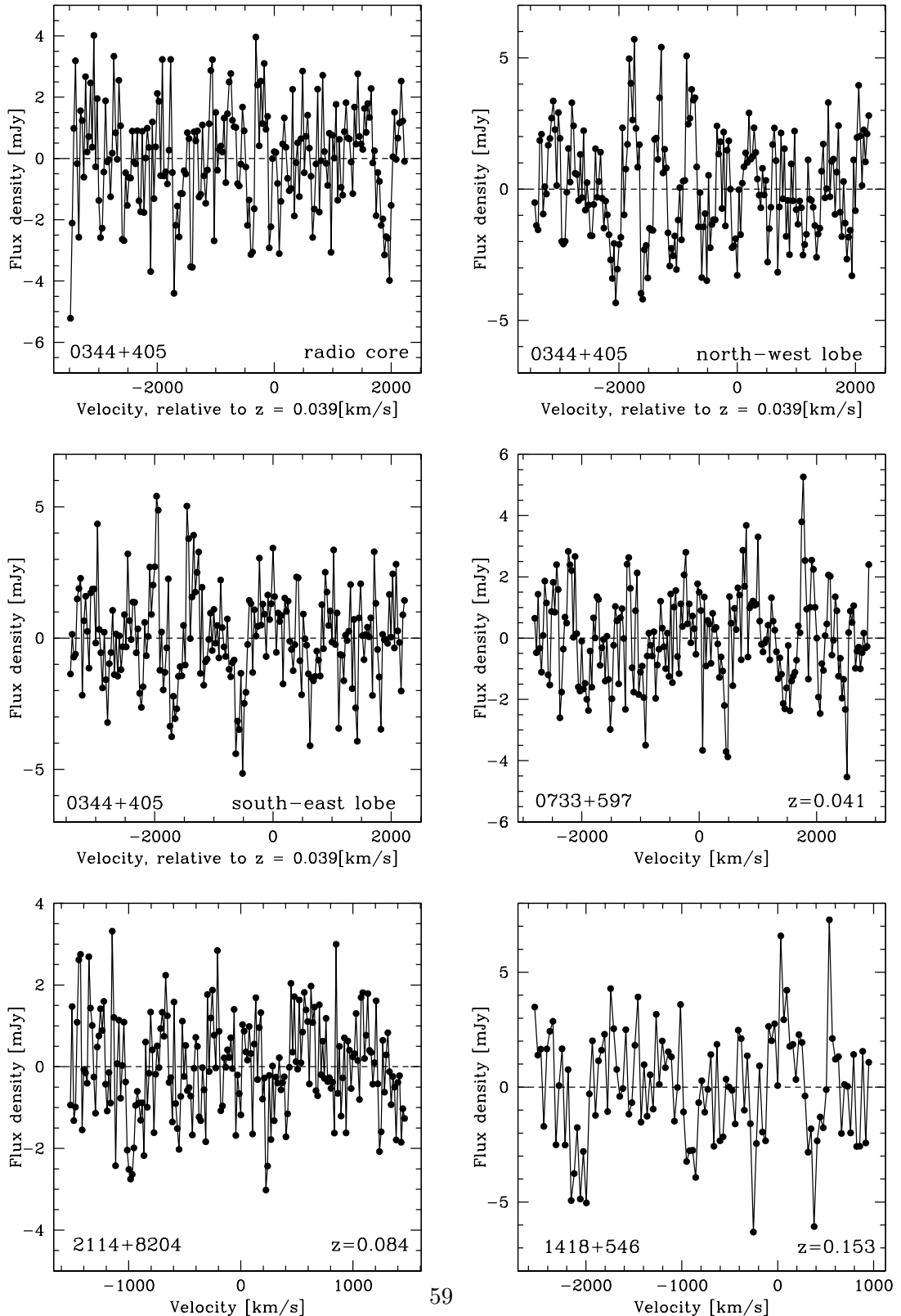
The radio source was observed three times using the GMRT 327 MHz receivers. The first observations, on 23/11/2008, used a bandwidth of 4 MHz, centred at 313.55 MHz and sub-divided into 256 channels, with the GHB as the correlator. 3C147 was used as the flux calibrator, and 0739+703 as the phase calibrator. The total on-source time was ≈ 220 minutes. A strong and wide absorption feature was detected in this observing run, with $> 20\sigma$ statistical significance after integrating over the full absorption profile. The feature was seen in the two independent polarizations, with consistent strengths in both the cases. Follow-up observations to confirm the reality of the feature were carried out on 23/10/2013, and on 08/02/2015. The follow-up observations were carried out using the GSB as the correlator, with a bandwidth of 4.2 MHz, sub-divided into 512 channels. No phase calibrator was observed, as it was possible to self-calibrate the UV data with the earlier GMRT image of the field. The data from the follow-up observing runs were strongly affected by RFI, and it was not possible to either confirm or rule out the reality of the absorption feature. The detection towards this source will hence be referred to as a tentative detection in our further discussions.

4.1.2 Results for the CJF sample

Table 4.1 summarizes the results from the GMRT observations of the CJF sample, with the sources ordered in increasing redshift. The listed velocity resolutions are for the Hanning-smoothed and re-sampled spectra. Note that the quoted velocity resolutions and RMS noise values for S5 1150+81, S5 1039+81, TXS 0707+476, TXS 0833+416 and TXS 1442+637 are without Hanning-smoothing and re-sampling. These sources were observed using a bandwidth of 33.3 MHz, yielding velocity resolutions of $\approx 30 \text{ km s}^{-1}$. Also, the sources with detections were observed using better velocity resolutions in the confirming observation runs. We have hence listed the velocity resolutions and RMS noise values from the higher resolution spectra, without Hanning-smoothing and re-sampling. All the upper limits on the integrated HI 21 cm optical depths for the sources in the literature assumed a line FWHM of 100 km s^{-1} . For consistency with the literature, we smoothed the spectra of all our non-detections to a resolution of 100 km s^{-1} before computing the 3σ limits on the integrated HI 21 cm optical depths.

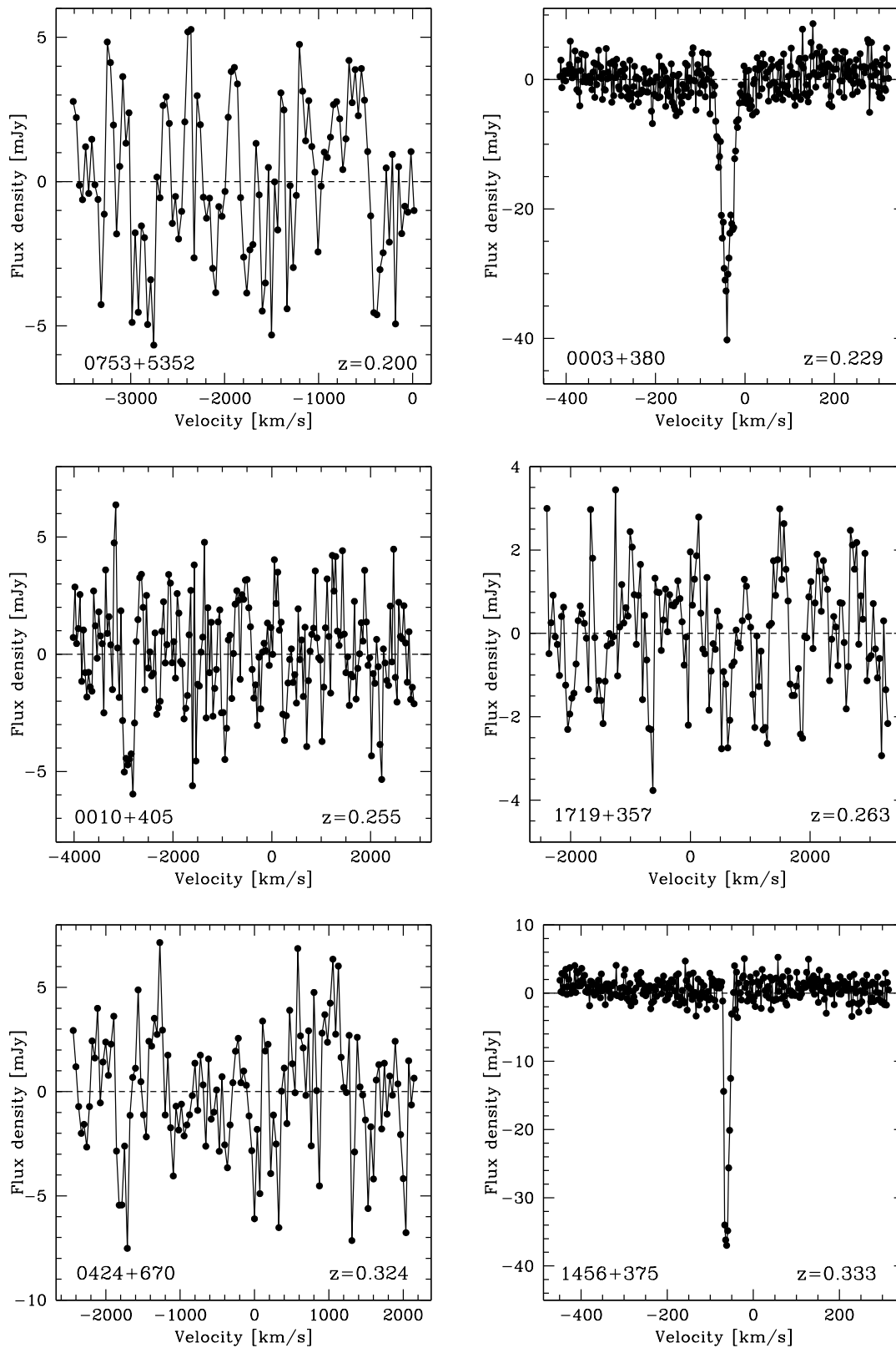
4.1 The Caltech-Jodrell Flat Spectrum sample

Figure 4.2: The GMRT Hi 21 cm spectra for the 63 CJF sources with usable data. All spectra have been Hanning-smoothed and re-sampled. The shaded channels in the spectra are corrupted by RFI.



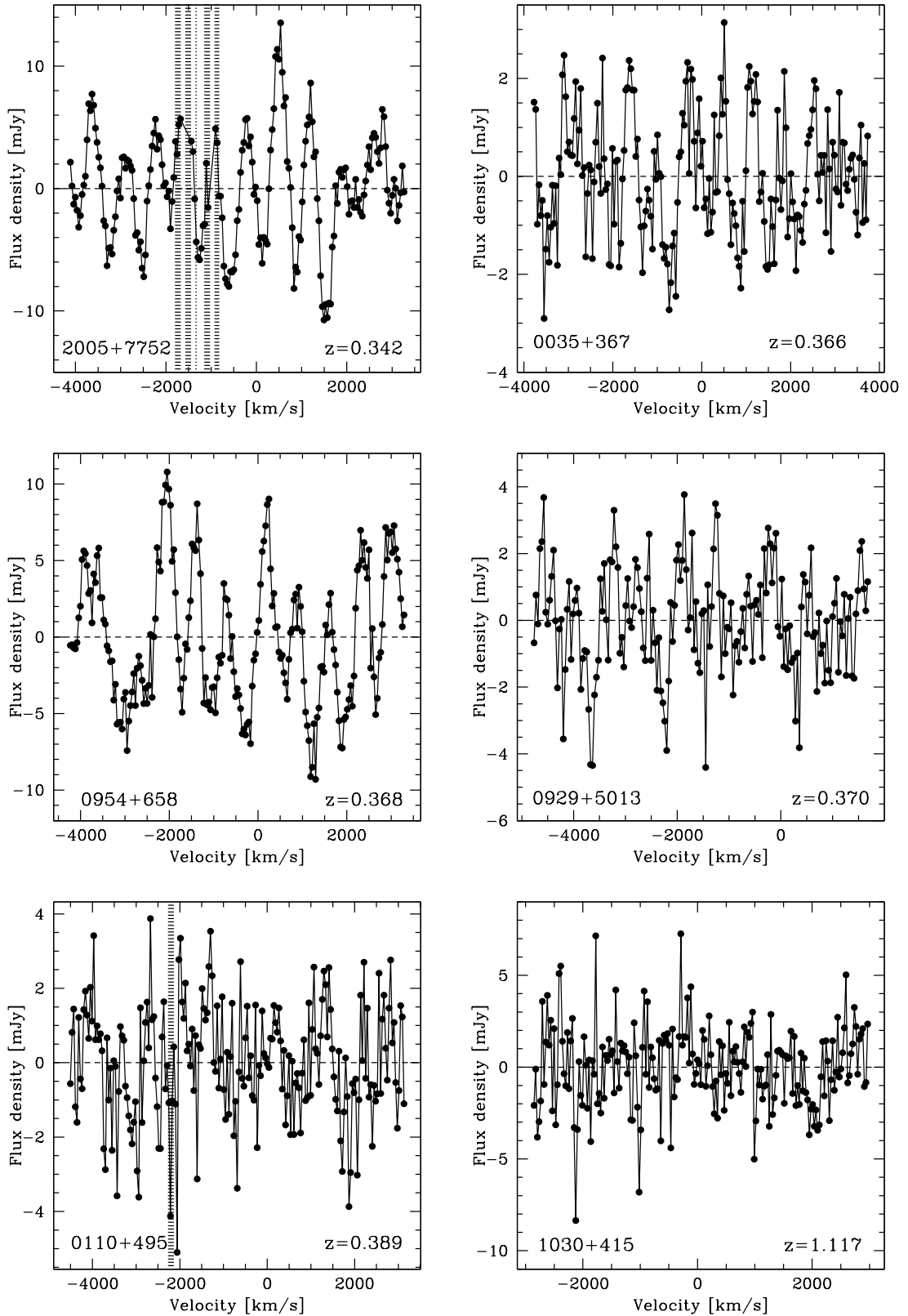
4. RESULTS

The GMRT HI 21 cm spectra for the 63 CJF sources (continued).



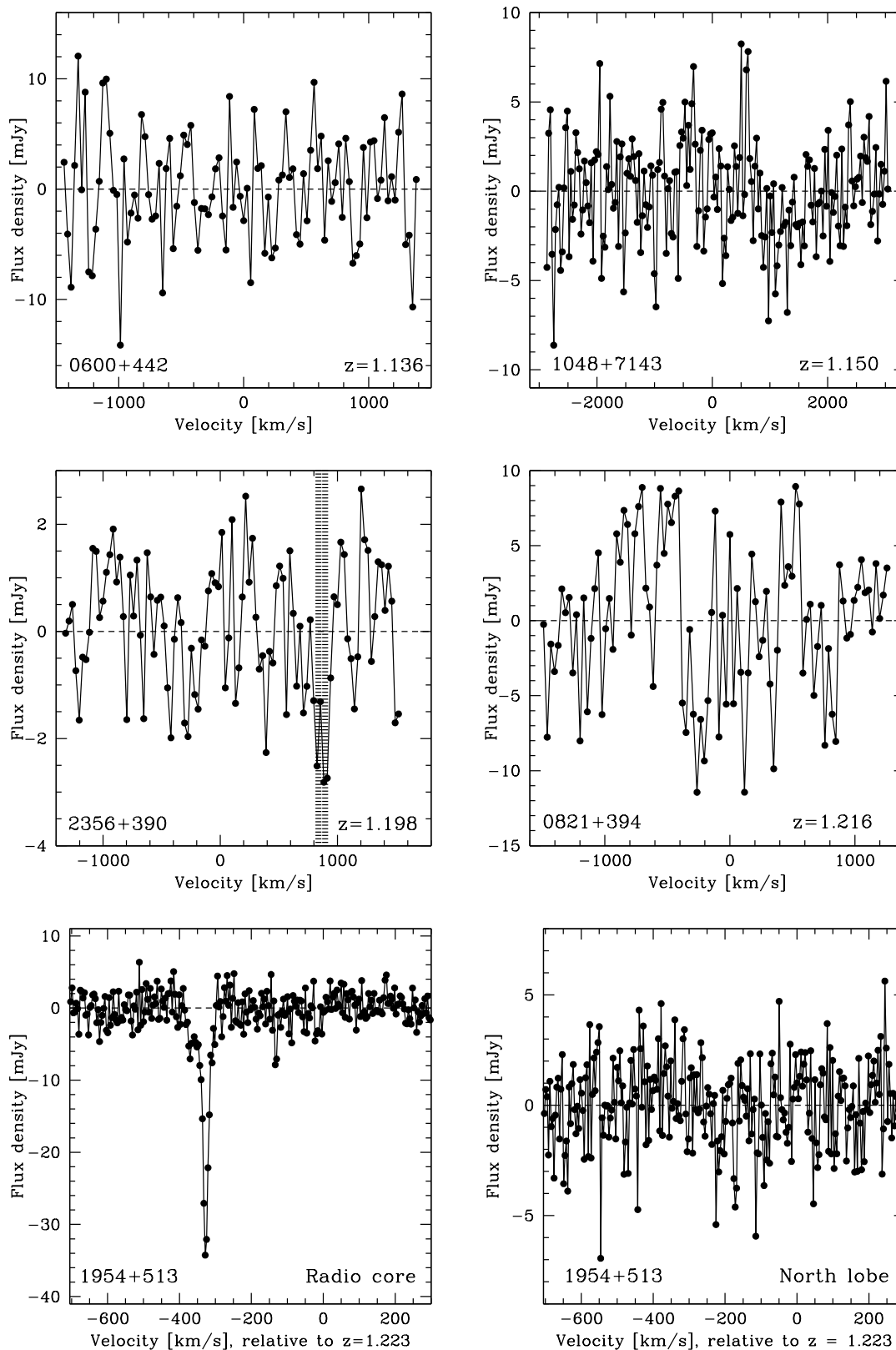
4.1 The Caltech-Jodrell Flat Spectrum sample

The GMRT H_i 21 cm spectra for the 63 CJF sources (continued).



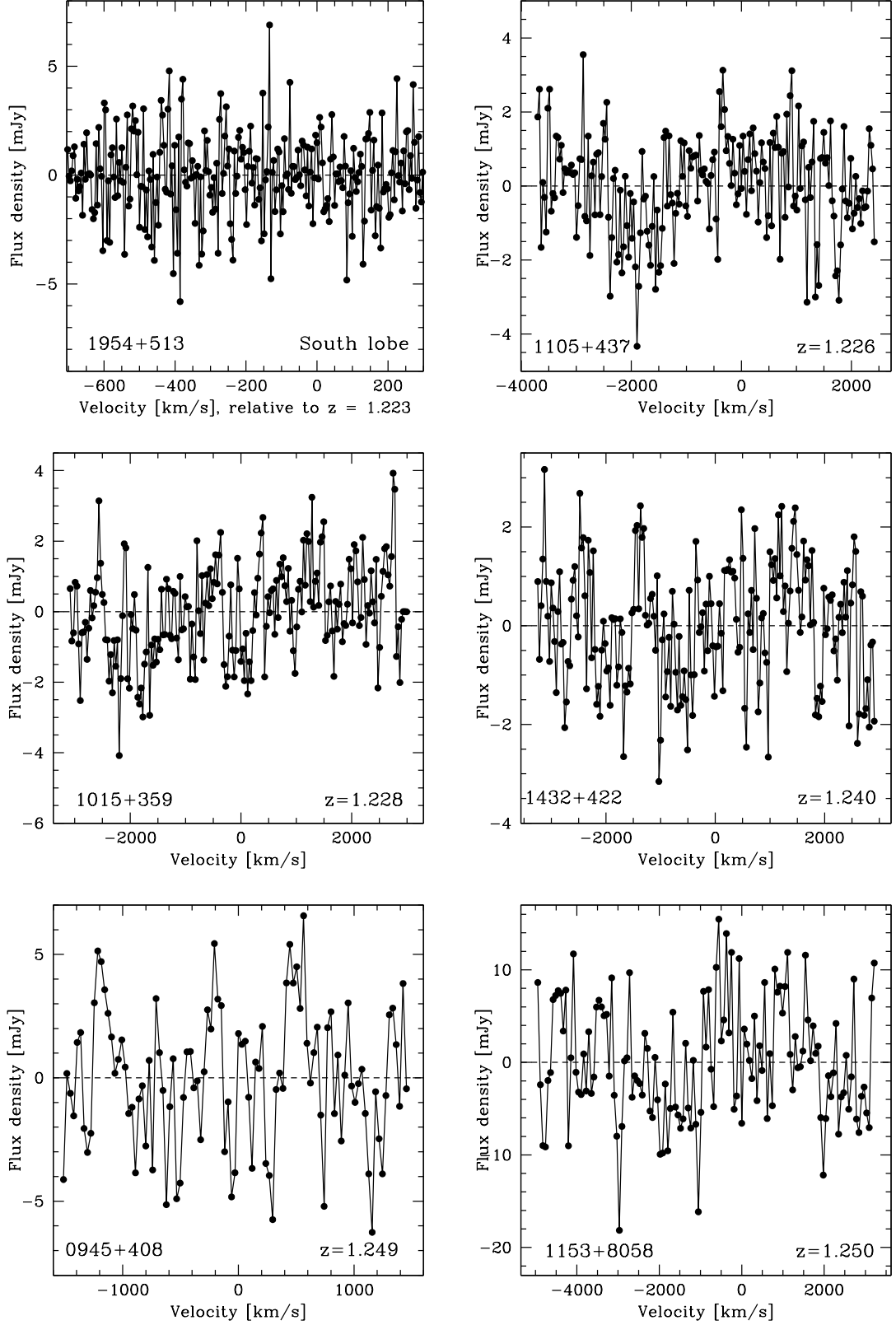
4. RESULTS

The GMRT Hi 21 cm spectra for the 63 CJF sources (continued).



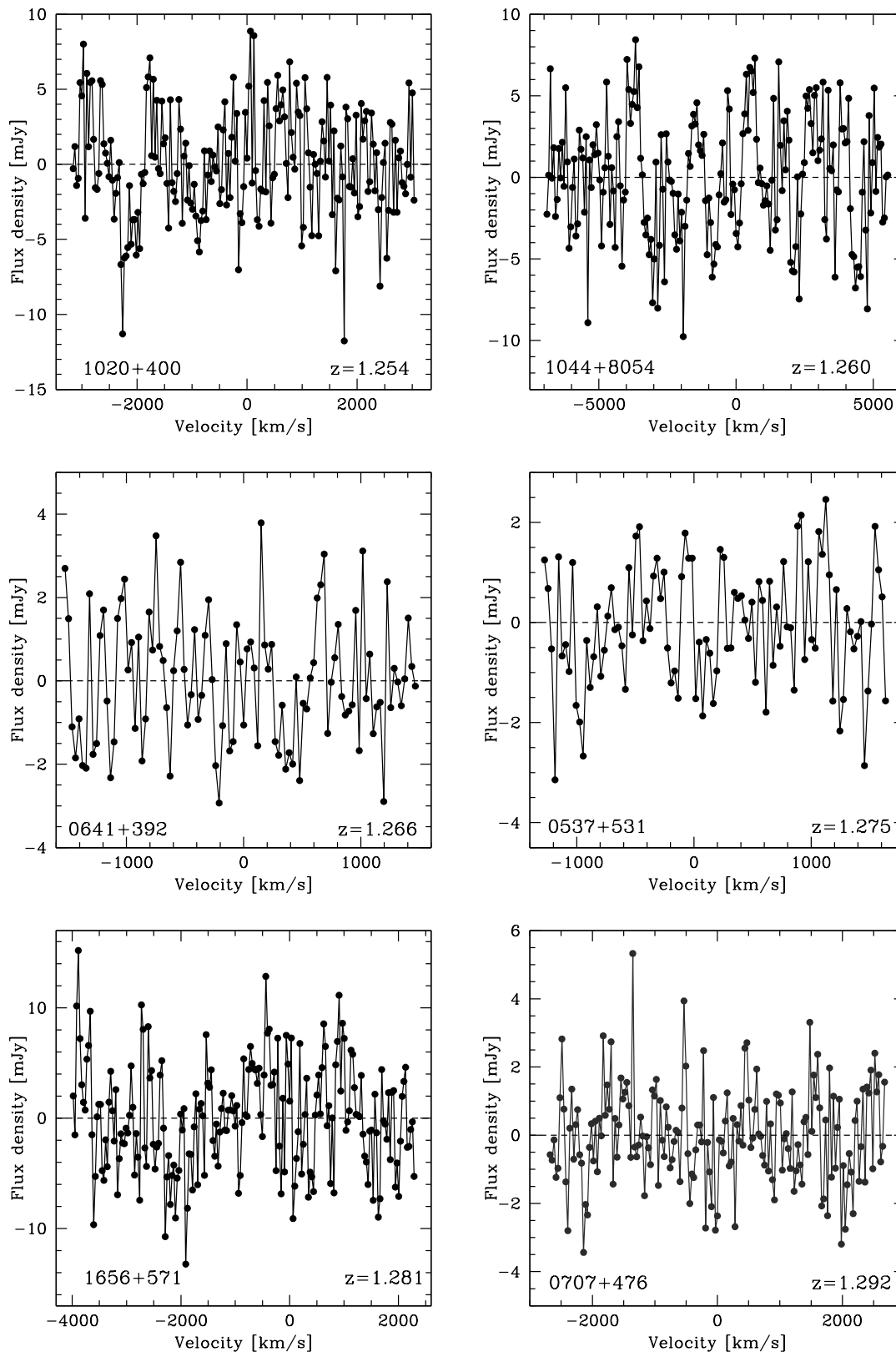
4.1 The Caltech-Jodrell Flat Spectrum sample

The GMRT H_i 21 cm spectra for the 63 CJF sources (continued).



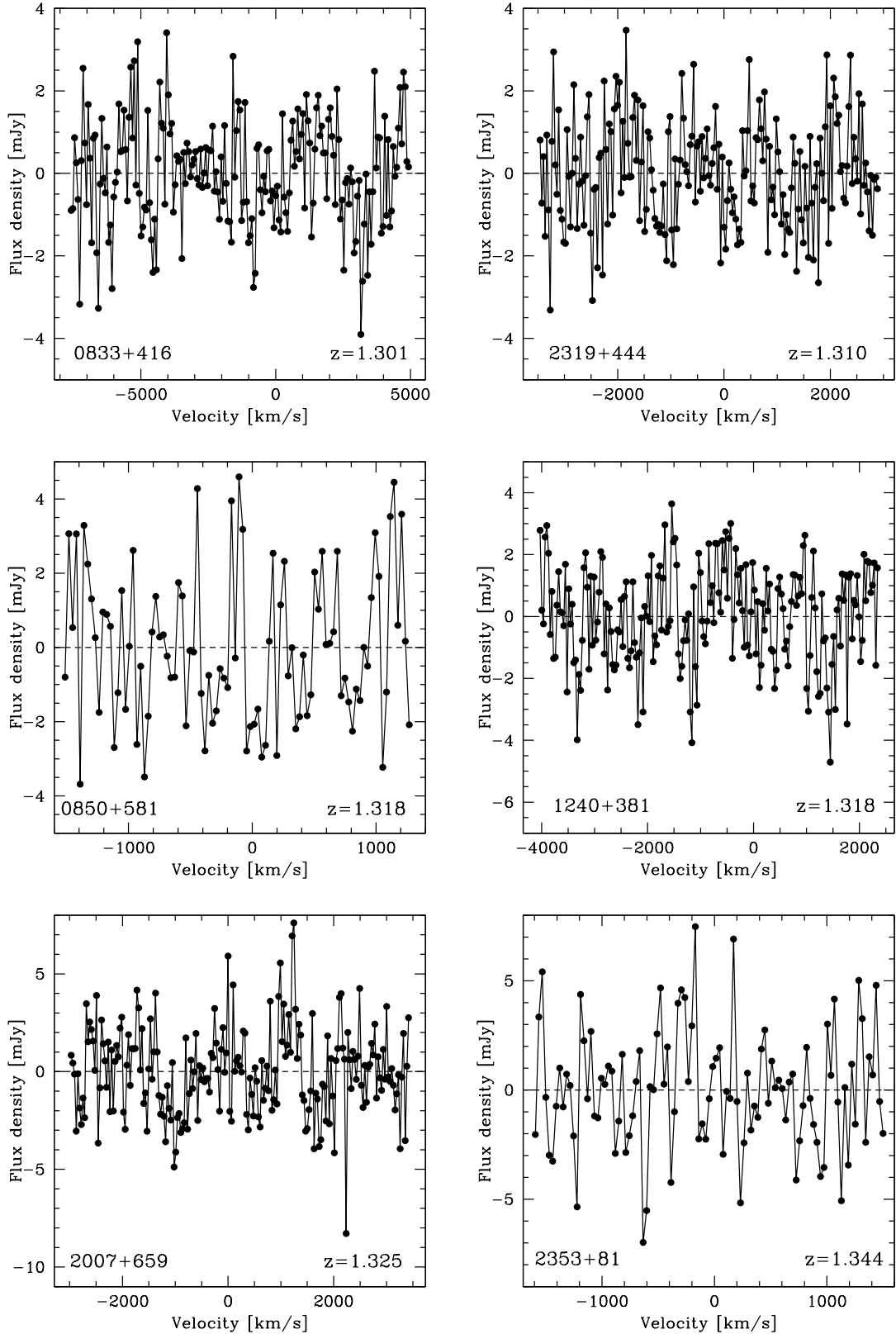
4. RESULTS

The GMRT HI 21 cm spectra for the 63 CJF sources (continued).



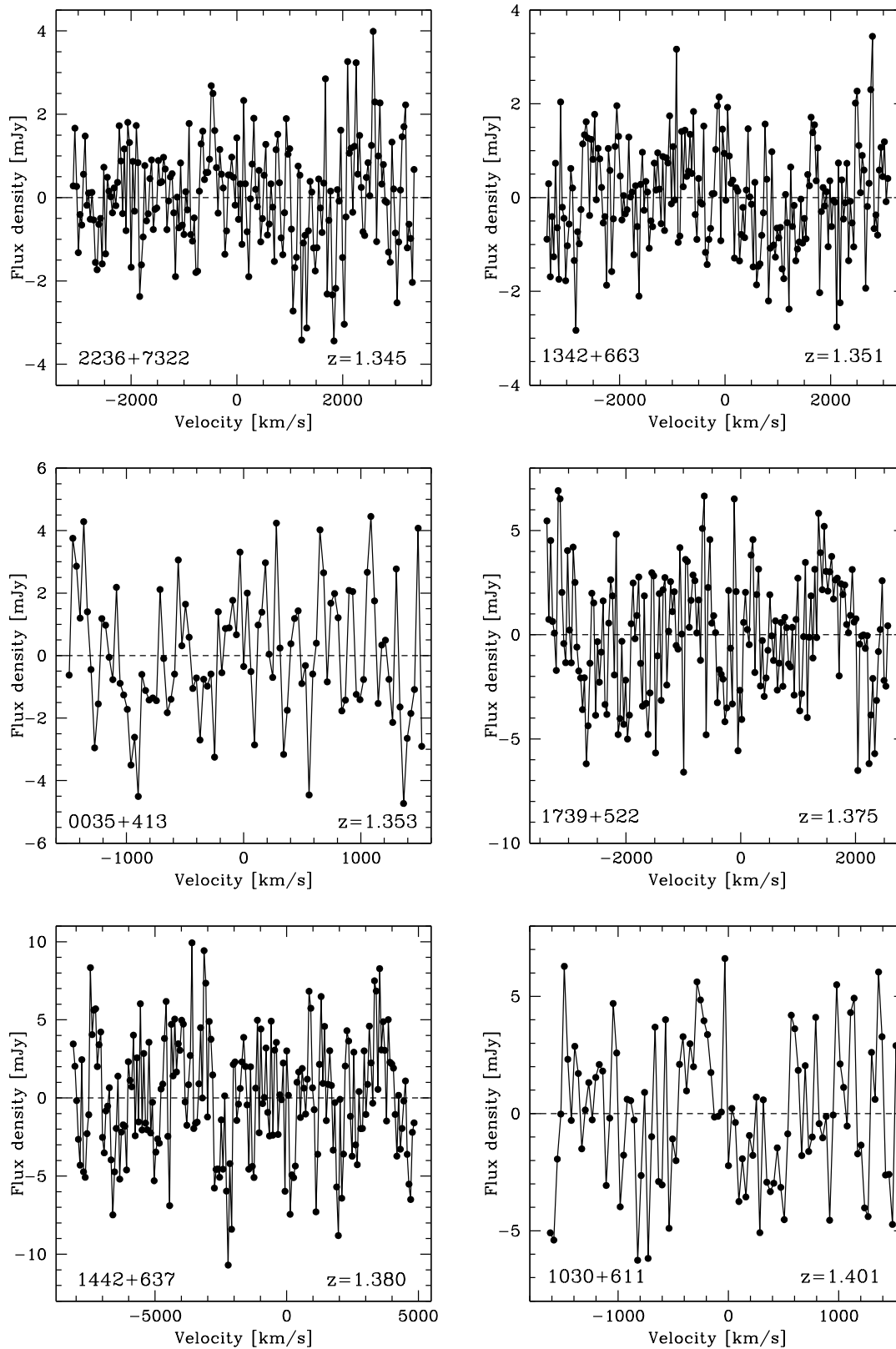
4.1 The Caltech-Jodrell Flat Spectrum sample

The GMRT HI 21 cm spectra for the 63 CJF sources (continued).



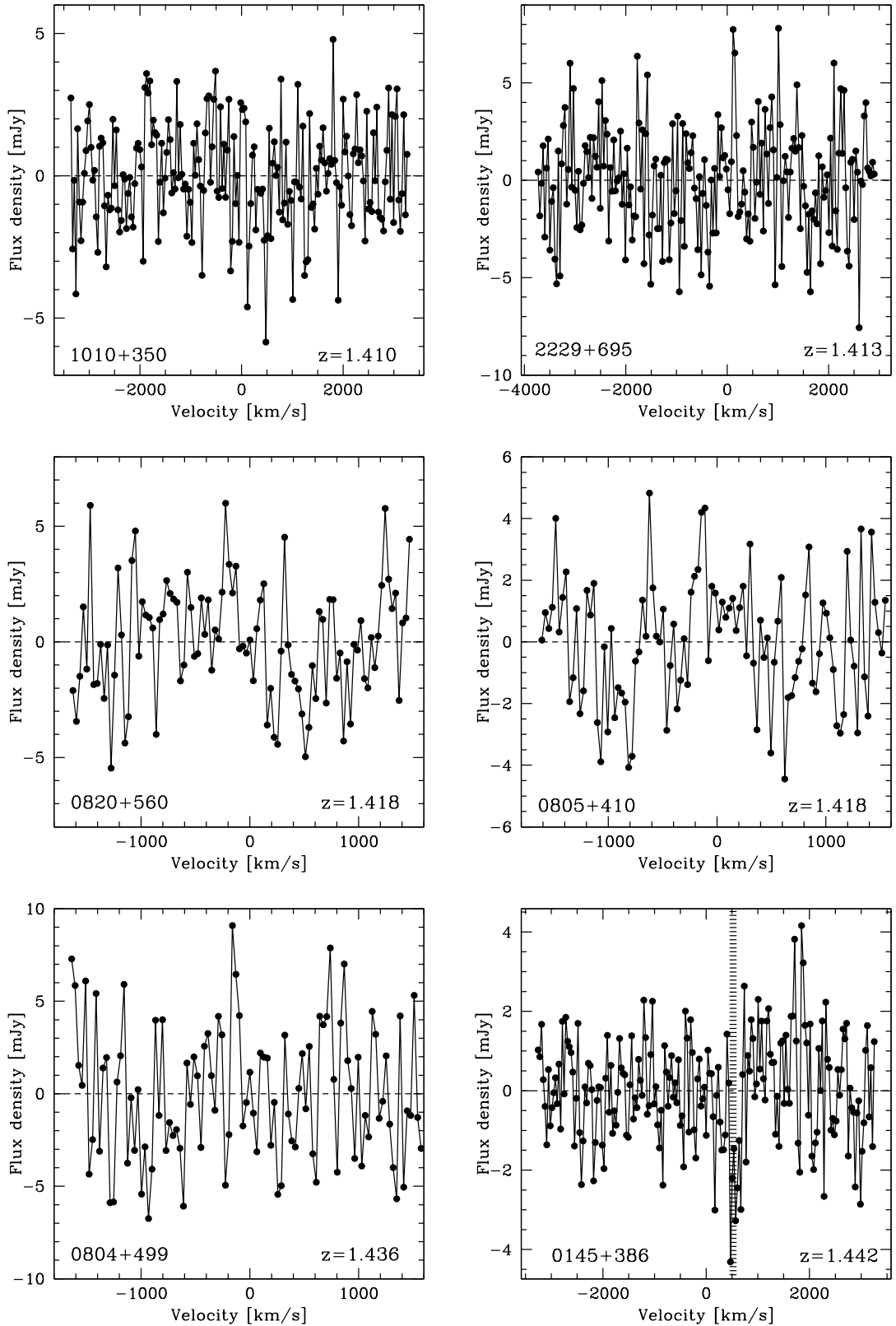
4. RESULTS

The GMRT HI 21 cm spectra for the 63 CJF sources (continued).



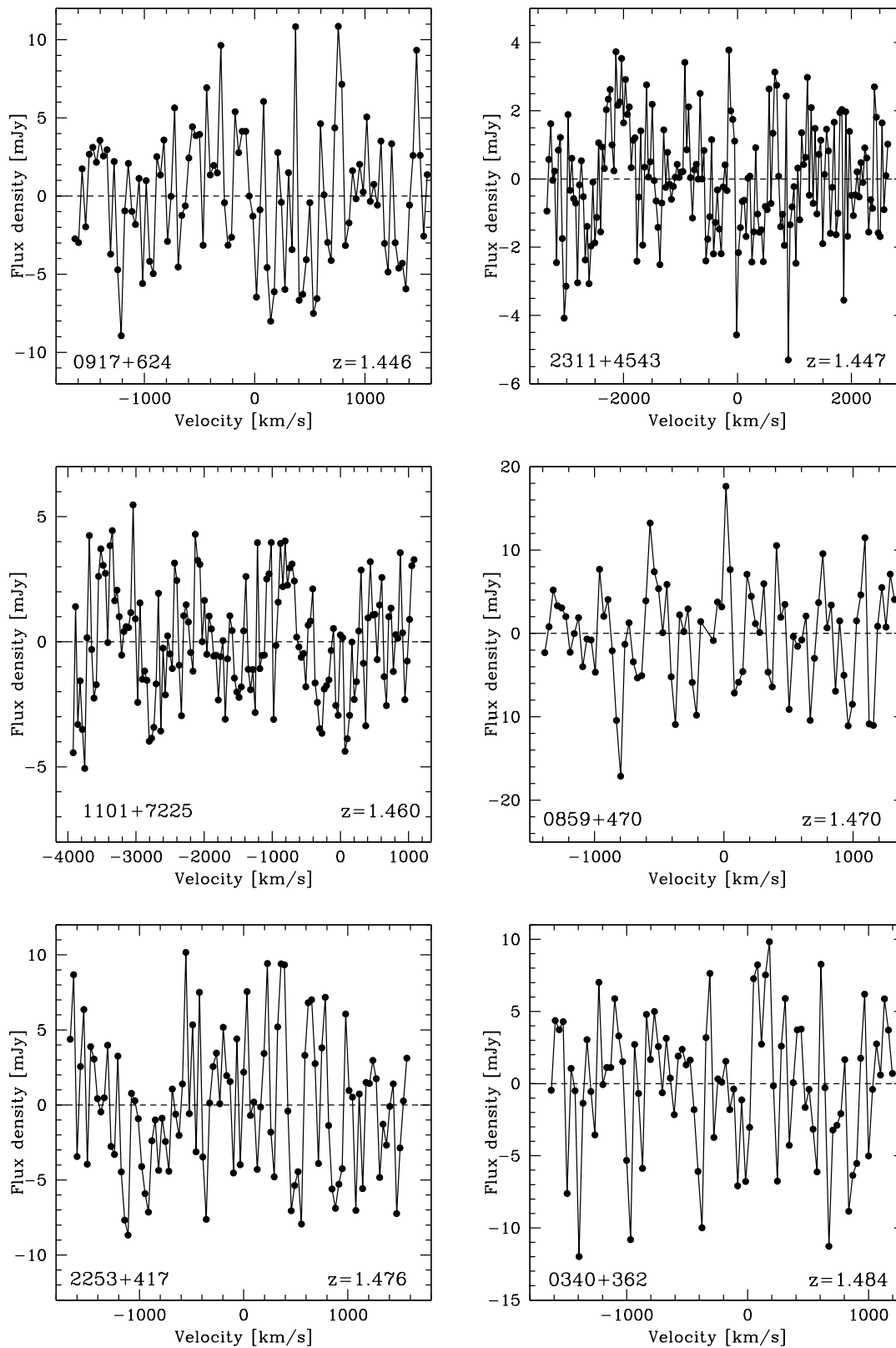
4.1 The Caltech-Jodrell Flat Spectrum sample

The GMRT H_i 21 cm spectra for the 63 CJF sources (continued).



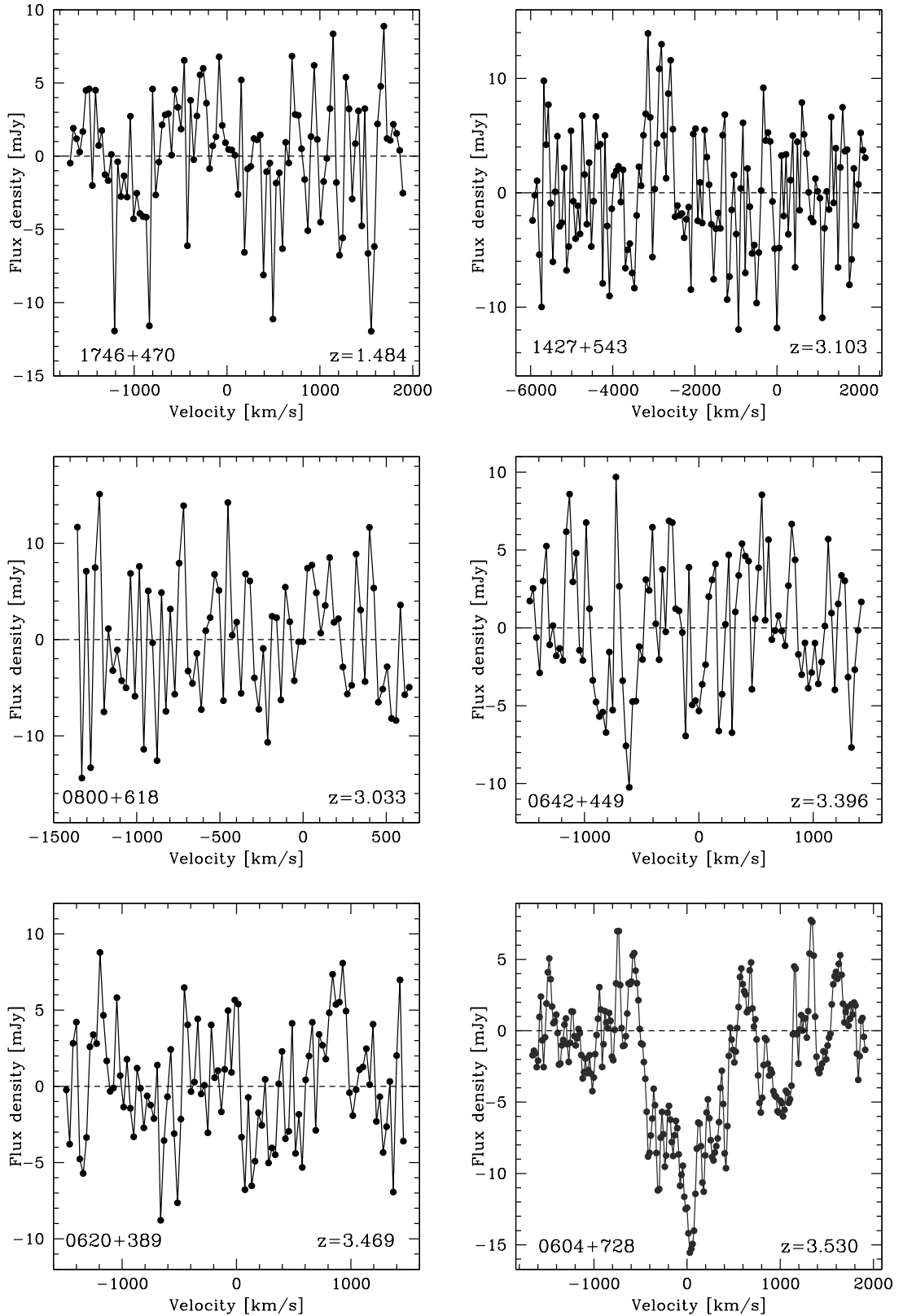
4. RESULTS

The GMRT Hi 21 cm spectra for the 63 CJF sources (continued).



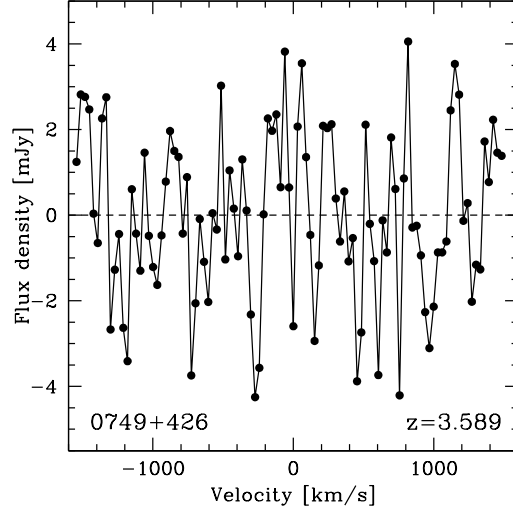
4.1 The Caltech-Jodrell Flat Spectrum sample

The GMRT H_i 21 cm spectra for the 63 CJF sources (continued).



4. RESULTS

The GMRT HI 21 cm spectra for the 63 CJF sources (continued).



Finally, we assumed a spin temperature of 100 K to estimate the HI column densities for all target sources.

The columns of Table 4.1 are (1) the source name, (2) the source redshift, z (3) the observing frequency, ν_{21cm} , in MHz, (4) the source flux density, S_ν , measured using JMFIT, in mJy, (5) the velocity resolution Δv of the final spectrum, in km/s, (6) the RMS noise ΔS on the final spectrum at the velocity resolution listed in column (5), in mJy, (7) the integrated HI 21 cm optical depth $\int \tau dv$ in km s^{-1} , or, for non-detections, the 3σ upper limit on $\int \tau dv$, assuming a FWHM of 100 km s^{-1} , (8) the column density N_{HI} in cm^{-2} , or, for non-detections, the 3σ upper limit on N_{HI} assuming a line FWHM of 100 km s^{-1} .

4.1 The Caltech-Jodrell Flat Spectrum sample

Table 4.1: The 63 target sources, selected from the CJF sample, in order of increasing redshift.

Source	z	ν_{21cm} MHz	S_ν^b mJy	$\Delta\nu$ km s ⁻¹	ΔS mJy	$\int \tau dv^c$ km s ⁻¹	N_{HI}^d $\times 10^{20}$ cm ⁻²
TXS 0344+405 ^{CR}	0.039	1367.08	24.3 ± 0.4	28.6	1.7	< 14	< 26
TXS 0344+405 ^{SE}	0.039	1367.08	82.4 ± 0.4	28.6	1.8	< 4.9	< 8.9
TXS 0344+405 ^{NW}	0.039	1367.08	89.1 ± 0.4	28.6	2.0	< 5.5	< 10
TXS 0733+597	0.041	1364.46	502.8 ± 0.1	28.6	1.5	< 0.67	< 1.2
S5 2116+81	0.084	1310.33	137.2 ± 0.5	14.9	1.2	< 1.4	< 2.5
TXS 1418+546	0.153	1231.92	595.6 ± 0.1	31.7	2.4	< 1.5	< 2.7
S4 0749+54	0.200	1183.67	533.3 ± 0.2	32.9	2.7	< 1.8	< 2.1
TXS 0003+380	0.229	1155.74	547.3 ± 0.2	2.1 ^a	1.7	1.943 ± 0.057	3.54 ± 0.11
TXS 0010+405	0.255	1131.79	358.9 ± 0.2	34.5	2.3	< 1.4	< 2.5
TXS 1719+357	0.263	1124.62	262.4 ± 0.2	34.7	1.4	< 1.2	< 2.2
TXS 0424+670	0.324	1072.81	719.1 ± 0.3	36.4	2.9	< 0.89	< 1.6
B3 1456+375	0.333	1065.57	148.4 ± 0.1	2.3 ^a	3.8	3.834 ± 0.079	6.98 ± 0.15
S5 2007+77	0.342	1058.42	660.0 ± 0.2	36.9	24.3	< 9.9	< 18
TXS 0035+367	0.366	1039.82	581.2 ± 0.2	37.5	1.2	< 0.51	< 0.93
TXS 0954+658	0.368	1038.30	1104.8 ± 0.2	37.6	20.1	< 5.8	< 11
CJ2 0925+504	0.370	1036.79	310.4 ± 0.1	37.7	1.6	< 1.2	< 2.2
TXS 0110+495	0.389	1022.61	615.4 ± 0.2	38.2	1.6	< 0.43	< 0.78
TXS 1030+415	1.117	670.95	636.6 ± 0.4	29.1	2.2	< 0.69	< 1.3
TXS 0600+442	1.136	664.98	1260.7 ± 0.6	28.2	4.9	< 0.71	< 1.3
S5 1044+71	1.150	660.65	1522.9 ± 0.5	29.5	2.9	< 0.38	< 0.69
TXS 2356+390	1.198	646.22	643.0 ± 0.5	28.9	1.2	< 0.42	< 0.76
TXS 0821+394	1.216	640.97	2532.8 ± 0.4	29.2	5.1	< 0.44	< 0.80
TXS 1954+513 ^{CR}	1.223	639.82	1221.3 ± 0.6	3.8 ^a	2.3	0.716 ± 0.037	1.271 ± 0.064
TXS 1954+513 ^S	1.223	639.82	184.0 ± 0.7	3.8 ^a	1.9	< 0.33	< 0.60
TXS 1954+513 ^N	1.223	639.82	247.9 ± 0.6	3.8 ^a	1.9	< 0.56	< 1.0
TXS 1105+437	1.226	638.09	406.5 ± 0.3	30.6	1.3	< 0.70	< 1.3
TXS 1015+359	1.228	637.52	702.7 ± 0.3	30.5	1.3	< 0.43	< 0.78
TXS 1432+422	1.240	634.10	286.1 ± 0.3	30.8	1.2	< 0.95	< 1.7
TXS 0945+408	1.249	631.57	2026.0 ± 0.5	29.7	2.8	< 0.30	< 0.55
S5 1150+81	1.250	631.29	1788.1 ± 0.6	30.9 ^a	8.8	< 1.1	< 2.0
TXS 1020+400	1.254	630.17	1496.5 ± 0.5	30.9	3.6	< 0.51	< 0.93
S5 1039+81	1.260	628.49	726.5 ± 0.3	31.1 ^a	5.2	< 1.5	< 2.8
TXS 0641+392	1.266	626.83	417.7 ± 0.3	29.9	1.5	< 0.68	< 1.2
TXS 0537+531	1.275	624.35	711.3 ± 0.5	30.0	1.2	< 0.32	< 0.59
TXS 1656+571	1.281	622.71	1456.3 ± 0.5	31.3	4.9	< 0.74	< 1.4
TXS 0707+476	1.292	619.72	1022.5 ± 0.2	31.5 ^a	1.4	< 0.30	< 0.54
TXS 0833+416	1.301	617.29	432.2 ± 0.1	31.6 ^a	1.8	< 0.63	< 1.1
TXS 2319+444	1.310	614.89	378.4 ± 0.2	31.7	1.3	< 0.65	< 1.9

continued on the next page

4. RESULTS

Source	z	ν_{21cm} MHz	S_ν^b mJy	Δv km s ⁻¹	ΔS mJy	$\int \tau dv^c$ km s ⁻¹	N_{HI}^d $\times 10^{20}$ cm ⁻²
TXS 0850+581	1.318	612.77	998.6 ± 0.5	30.6	2.0	< 0.37	< 0.68
TXS 1240+381	1.318	612.77	547.2 ± 0.3	31.8	1.6	< 0.63	< 1.1
TXS 2007+659	1.325	610.92	631.1 ± 0.4	31.9	2.3	< 0.76	< 1.4
S5 2353+81	1.344	605.97	581.6 ± 0.6	30.9	2.7	< 0.87	< 1.6
JVAS J2236+7322	1.345	605.71	270.7 ± 0.3	32.2	1.3	< 0.97	< 1.8
TXS 1342+663	1.351	604.17	231.8 ± 0.2	32.3	1.1	< 0.98	< 1.8
TXS 0035+413	1.353	603.65	541.8 ± 0.6	31.0	2.1	< 0.76	< 1.4
TXS 1739+522	1.375	598.06	1006.7 ± 0.5	32.6	2.9	< 0.58	< 1.1
TXS 1442+637	1.380	596.80	656.6 ± 0.5	32.7 ^a	5.4	< 1.3	< 2.3
TXS 1030+611	1.401	591.58	692.1 ± 0.5	31.7	3.1	< 0.87	< 1.6
TXS 1010+350	1.410	589.37	520.1 ± 0.4	33.1	1.8	< 0.67	< 1.2
TXS 2229+695	1.413	588.64	291.4 ± 0.2	33.1	2.7	< 1.7	< 3.1
TXS 0820+560	1.418	587.43	1507.7 ± 0.1	31.9	2.5	< 0.34	< 0.62
TXS 0805+410	1.418	587.43	512.3 ± 0.8	31.9	2.0	< 0.69	< 1.3
TXS 0804+499	1.436	583.08	682.6 ± 0.5	32.1	3.6	< 0.95	< 1.7
TXS 0145+386	1.442	581.65	207.4 ± 0.2	33.6	1.3	< 1.2	< 2.2
TXS 0917+624	1.446	580.70	975.6 ± 0.5	32.3	4.2	< 0.79	< 1.4
JVAS J2311+4543	1.447	580.46	156.4 ± 0.2	33.6	1.7	< 2.2	< 3.9
S5 1058+72	1.460	577.40	1499.7 ± 0.5	33.8	2.3	< 0.31	< 0.57
TXS 0859+470	1.470	575.06	2819.5 ± 0.4	32.6	6.2	< 0.43	< 0.78
TXS 2253+417	1.476	573.66	1255.2 ± 0.5	32.6	4.5	< 0.71	< 1.3
TXS 0340+362	1.484	571.82	291.4 ± 0.5	33.0	4.7	< 3.0	< 5.5
B3 1746+470	1.484	571.82	187.9 ± 0.5	34.1	4.2	< 4.5	< 8.2
TXS 1427+543	3.013	353.95	2402.7 ± 0.7	27.6	7.4	< 0.44	< 0.81
TXS 0800+618	3.033	352.19	858.5 ± 0.5	26.6	6.7	< 1.2	< 2.1
TXS 0642+449	3.396	323.11	310.6 ± 1.1	29.0	4.2	< 2.9	< 5.2
TXS 0620+389	3.469	317.83	1318.6 ± 1.3	29.5	3.7	< 0.20	< 0.37
TXS 0604+728	3.530	313.55	1890.9 ± 1.9	29.9 ^a	3.5	4.29 ± 0.28	7.82 ± 0.51
TXS 0749+426	3.589	309.52	537.5 ± 0.6	30.3	2.0	< 0.76	< 1.4

Notes:

^aThe Spectrum has not been Hanning-smoothed and re-sampled.

^bFlux densities are measured using the task JMFIT.

^cThe upper limits on the integrated HI 21 cm optical depth assuming a line FWHM of 100 km s⁻¹.

^dThe HI column density is calculated for an assumed spin temperature of 100 K.

For the sources TXS 0344+405 and TXS 1954+513, CR corresponds to the core, SE to the south-east lobe, NW to the north-west lobe, S to the south lobe, and N to the north lobe.

4.2 The Gigahertz-Peaked Spectrum sample

The seven GPS sources with RFI-free spectra were found to be compact in the GMRT continuum images at the respective redshifted HI 21 cm line frequencies. We have hence fitted a single Gaussian model to a small region around each source, to estimate their flux densities. Table 4.2 lists the measured flux densities of the seven sources. We have obtained two new detections and 5 non-detections of associated HI 21 cm absorption from our analysis. Figure 4.3 displays the GMRT HI 21 cm absorption spectra of the 7 GPS sources, in order of increasing redshift. For all sources, the panels of the figure show flux density (in mJy) plotted against velocity (in km s^{-1}), relative to the source redshift. Except for the two detections, all spectra have been Hanning-smoothed and re-sampled. Note that the RMS noise values on the final spectra were obtained over RFI- and line-free channels.

4.2.1 HI 21 cm detections in the GPS sample

The two new detections of associated HI 21 cm absorption are towards TXS 1245-197 at $z = 1.275$, and TXS 1200+045 at $z = 1.226$. We briefly discuss the observations and results for these sources below.

1. TXS 1200+045, $z = 1.226$:

The source was initially observed using the GMRT 610 MHz receivers on 10/12/2015, using the GSB as the correlator. A bandwidth of 16.7 MHz, sub-divided into 512 channels, and centred at 638.13 MHz, was used for the observations. The source 3C147 was used for flux calibration and bandpass calibration, while 1150-003 was used for phase calibration. The total on-source time was $\approx 46\text{m}$ in the initial observing run. A strong and narrow absorption line, with $\approx 12\sigma$ significance, was detected in the spectrum. Along with this, a wide weak feature was also visible, at low significance.

To confirm the reality of the absorption, we re-observed the source on 15/8/2016 with the 610 MHz receivers, with an on-source time of ≈ 105 minutes. These observations used a bandwidth of 16.7 MHz, sub-divided into 512 channels and centred at 644.33 MHz, again with the GSB as the correlator. Both the narrow absorption feature and the wide, weak absorption (spanning $\approx 500 \text{ km s}^{-1}$) were clearly detected in the

4. RESULTS

new spectrum, in both polarizations. It is hence likely that both the narrow and the wide absorption features in the spectra are likely to be real.

The continuum source is compact in the GMRT image, and its 640 MHz flux density was measured to be 1675.2 ± 0.4 mJy. The integrated HI 21 cm optical depth of the absorption line is 2.52 ± 0.12 km/s.

2. TXS 1245-197, $z = 1.275$:

The source was initially observed using the GMRT 610 MHz receivers on 10/12/2015, using the GSB as the correlator. A bandwidth of 16.7 MHz, sub-divided into 512 channels, and centred at 624.35 MHz, was used for the observations. The standard calibrator 3C147 was observed to calibrate the flux scale and the system passband. A separate phase calibrator was not observed since the target is itself a phase calibrator for the VLA. The on-source time was ≈ 55 minutes in the initial observing run. The data analysis yielded a strong narrow absorption feature, along with a weak, wide wing. We hence re-observed the source on 16/8/2016 to confirm the tentative detections, using the same settings and a total on-source time of ≈ 130 minutes. The strong narrow feature was clearly detected in the second observing run; however, a combination of low sensitivity and intermittent weak RFI meant that it was not possible to confirm the reality of the wide absorption feature. We conclude that the narrow absorption feature is definitely real, but that the weak feature will require additional observations to confirm its reality. The continuum source is compact and shows no signatures of extended emission. The peak flux density of the source was measured to be 8302.2 ± 0.6 mJy, via a single-Gaussian fit. The integrated HI 21 cm optical depth is 3.477 ± 0.083 km s⁻¹.

4.2.2 Results for the GPS sample

Table 4.2 summarizes the results for the 7 GPS sources which had reliable data. The columns of this table are the same as those of Table 4.1. The quoted velocity resolutions correspond to the Hanning-smoothed and re-sampled spectra. The upper limits on the integrated HI 21 cm optical depths assume a line FWHM of 100 km s⁻¹, while the HI column densities are computed for an assumed spin temperature of 100 K.

4.2 The Gigahertz-Peaked Spectrum sample

Table 4.2: The 7 GPS sources, in order of increasing redshift.

NAME	z	ν_{21} MHz	S_ν ^a mJy	Δv ^b km s ⁻¹	ΔS mJy	$\int \tau dV$ ^c km s ⁻¹	N_{HI} ^d $\times 10^{20}$ cm ⁻²
B3 0801+437	0.123	1264.83	407.7 ± 0.1	15.4	1.42	< 0.58	< 1.1
TXS 1819+671	0.221	1163.31	434.1 ± 0.2	16.8	1.74	< 0.85	< 1.5
TXS 1108+201	0.299	1093.46	1448.7 ± 0.2	17.9	3.93	< 0.44	< 0.81
TXS 0507+179	0.416	1003.11	504.2 ± 0.3	19.5	1.11	< 0.41	< 0.75
TXS 2121-014	1.158	658.20	2095.2 ± 0.4	29.7	3.56	< 0.38	< 0.69
TXS 1200+045	1.226	638.09	1675.2 ± 0.4	15.3	2.32	2.52 ± 0.12	4.59 ± 0.22
TXS 1245-197	1.275	624.35	8302.2 ± 0.6	15.6	7.88	4.530 ± 0.062	8.26 ± 0.11

Notes:

^aFlux densities are measured using the task JMFIT.

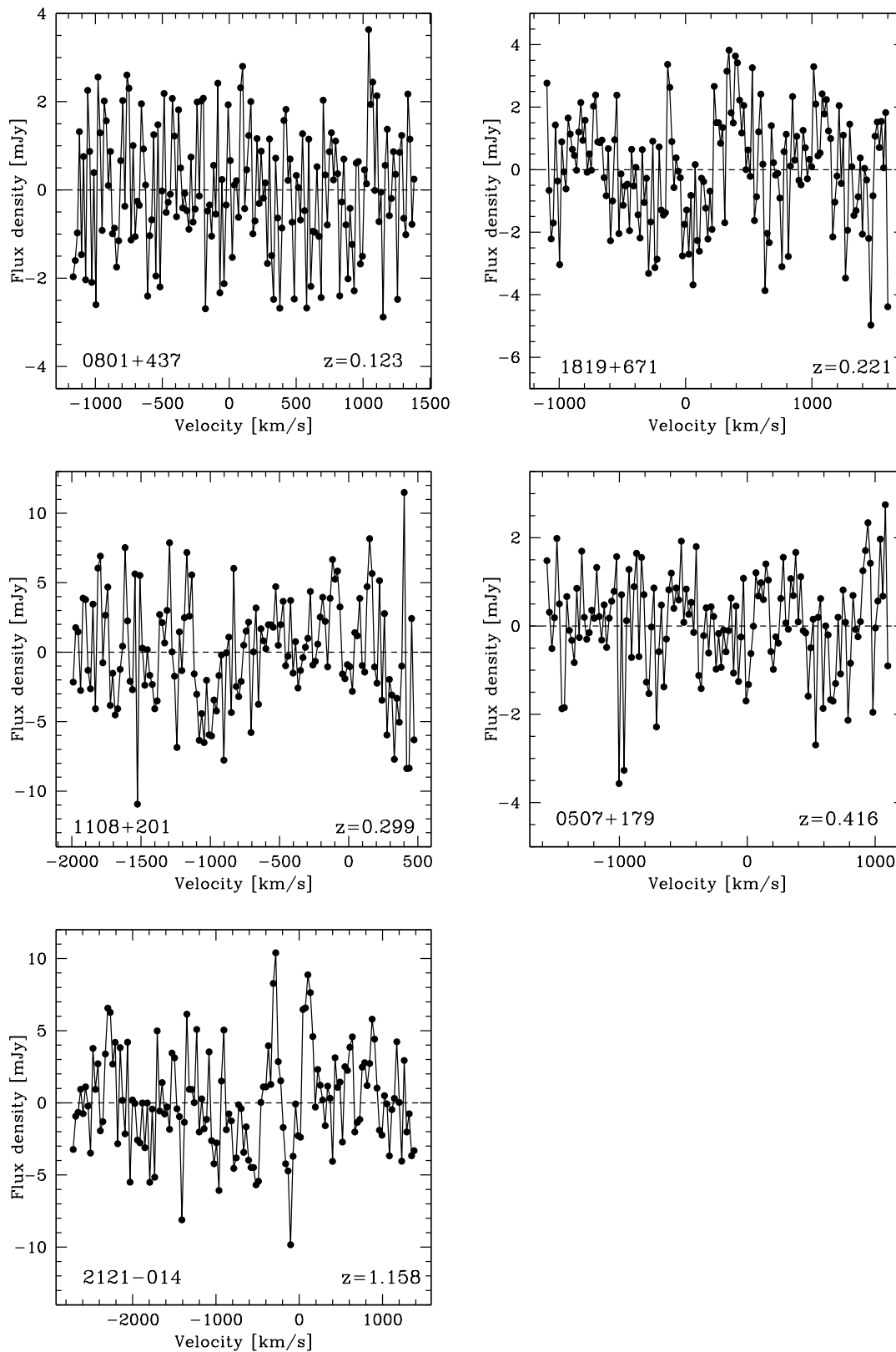
^bThe quoted velocity resolutions are for the Hanning-smoothed and re-sampled spectra.

^cThe upper limits on the integrated HI 21 cm optical depth assume a line FWHM of 100 km s⁻¹.

^dThe HI column density is calculated for an assumed spin temperature of 100 K.

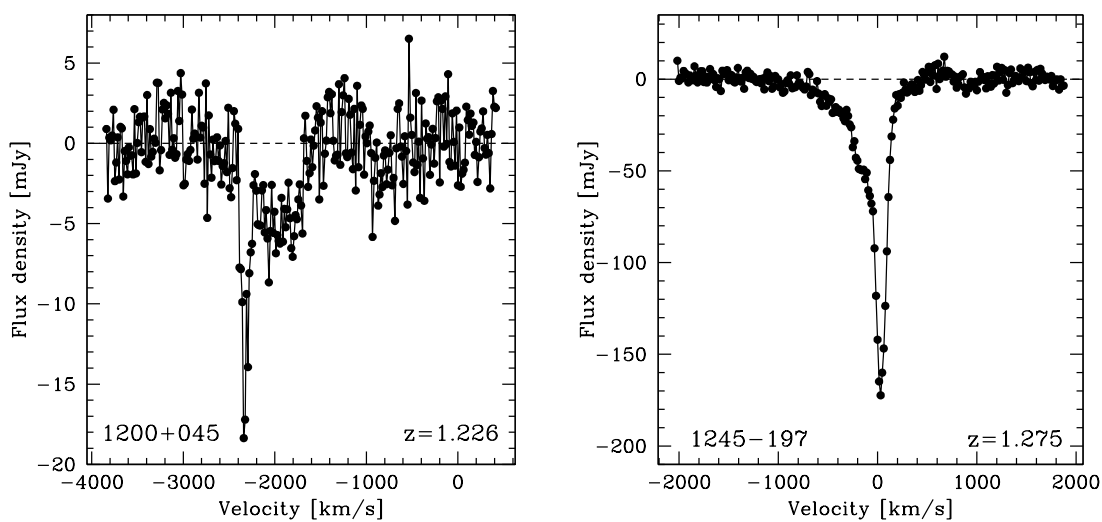
4. RESULTS

Figure 4.3: The GMRT HI 21 cm absorption spectra of the 7 GPS sources with usable data.



4.2 The Gigahertz-Peaked Spectrum sample

The GMRT HI 21 cm absorption spectra of 7 GPS sources (continued).



4. RESULTS

5

Detections

In this chapter, we will discuss the characteristics of the six AGNs with new detections of redshifted H I 21 cm absorption.

5.1 Detections in the CJF sample

5.1.1 TXS 0003+380, $z = 0.229$

The radio source is extremely compact in the GMRT continuum image at 1156 MHz, with no evidence of any extended emission. The milli-arcsec scale VLBI map at 2.32 GHz shows a prominent core, along with a weak signature of a jet projected towards the south-west (Fey and Charlot, 2000). The spectrum is extremely flat at low radio frequencies, with a spectral index of $\alpha = -0.03$ between 1.4 GHz and 4.8 GHz (Condon et al., 1998; Gregory and Condon, 1991). The flux density of the source at radio wavelengths is known to vary rapidly, over a time-scale of 2–20 days (Heeschen, 1984). A possible reason for such ‘flickering’ is that the radiation is beamed towards the observer (Ghisellini et al., 1993). Optical and X-ray studies of this source also find evidence for strong blazar characteristics (e.g. Massaro et al., 2009).

The GMRT H I 21 cm absorption spectrum towards TXS 0003+380 is shown in Figure 5.1. The absorption could be occurring either against the radio core or against beamed emission from the components in the radio jet. The absorption line is relatively narrow, with a full width of 44 km s^{-1} between the 20% points. While the H I 21 cm absorption appears blueshifted from the source redshift of $z = 0.229$ (Stickel and Kuehr, 1994), we note that the latter authors do not quote an uncertainty on the AGN redshift.

5. DETECTIONS

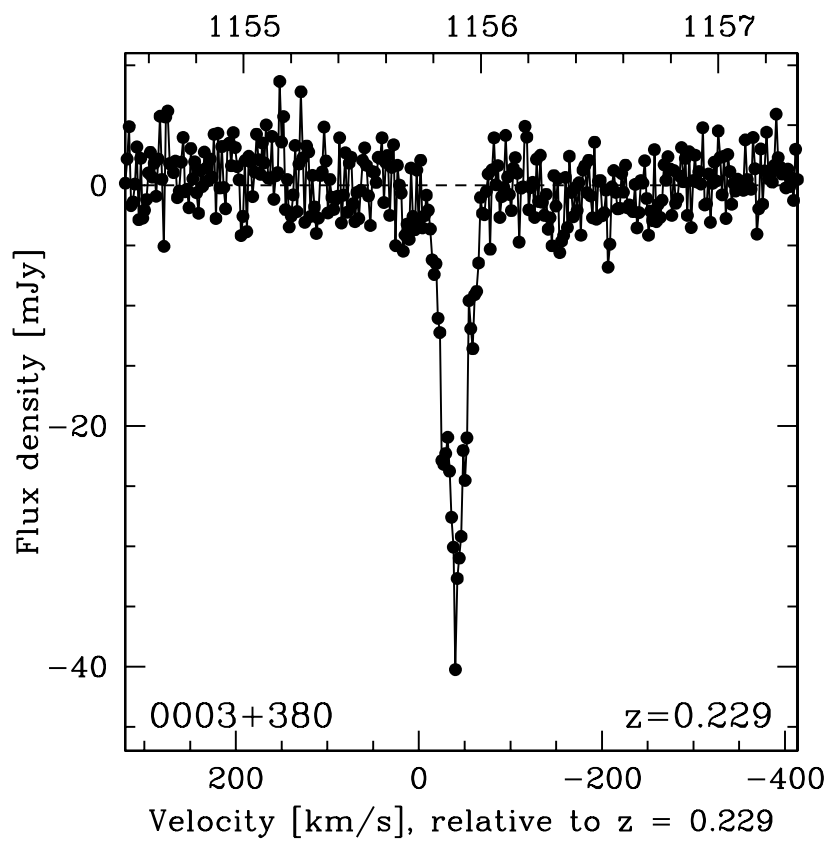


Figure 5.1: GMRT HI 21 cm absorption spectrum towards TXS 0003+380, at $z = 0.229$. The top axis indicates the frequency in MHz, while the bottom axis indicates velocity with respect to $z = 0.229$.

5.1.2 B3 1456+375, $z = 0.333$

B3 1456+375 is unresolved in the GMRT 1065 MHz image, and is extremely compact in the 5 GHz VLBI map (Helmboldt et al., 2007), with a largest linear size of ≈ 10 mas. The spectrum is very flat at low radio frequencies, with spectral index $\alpha = -0.02$ ($S \propto \nu^\alpha$) between 408 MHz and 1.4 GHz (Condon et al., 1998; Ficarra et al., 1985), steepening slightly to $\alpha = -0.27$ between 1.4 GHz and 5 GHz (Helmboldt et al., 2007). The source has been classified as a blazar in the literature, based on its optical and near-infrared properties (e.g. Davenport et al., 2015; Massaro et al., 2009). Our line-of-sight is hence likely to lie close to the direction of any jet emission. In addition, the optical to near-infrared continuum of the source falls steeply, with R-K = 5.14 mag, causing it to be classified as a “red” quasar by Glikman et al. (2012).

The GMRT HI 21 cm absorption spectrum towards B3 1456+375 is displayed in Figure 5.2. The absorption profile appears blueshifted from the AGN redshift ($z = 0.33343 \pm 0.00017$; Schneider et al., 2005), with the deepest absorption blueshifted by -62 km s $^{-1}$. However, it should be noted that the uncertainty in the source redshift means that the velocity offset is consistent with 0 km/s within 2σ significance. The spectrum does not show any signatures of disturbed kinematical features, and the absorption is quite narrow, with a width of ≈ 19 km s $^{-1}$ between the 20% points. The HI column density associated with the absorption feature is $(6.98 \pm 0.15) \times 10^{20}$ cm $^{-2}$, assuming $T_s = 100$ K. Given that the line-of-sight appears aligned with the jet direction, the detected HI 21 cm absorption is likely to arise either against the core or against beamed emission from the radio jet. In either case, since the viewing angle is small, the absorbing gas is likely to lie above the plane of the dusty torus.

For red quasars, the high extinction at optical wavebands is believed to be caused by dust extinction (e.g. Webster et al., 1995). However, it has also been suggested in the literature that not all red quasars are necessarily dusty systems (e.g. Benn et al., 1998). Carilli et al. (1998a) searched for HI 21 cm absorption in a small sample of radio-loud red quasars at intermediate redshifts ($z \sim 0.7$), to test whether the red AGNs are intrinsically red or are reddened by dust at the AGN redshift. Associated HI 21 cm absorption was detected towards 4 AGNs out of a sample of 5, which provided weak circumstantial evidence for dust-reddening of the AGNs. The current detection

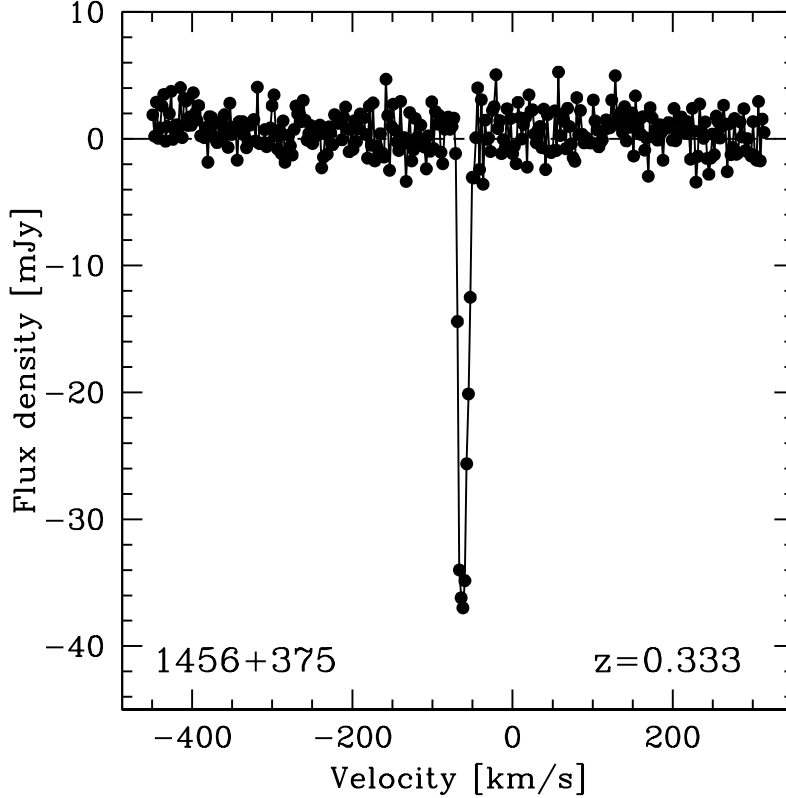


Figure 5.2: GMRT spectrum of HI 21 cm absorption towards B3 1456+375, at $z = 0.333$.

of associated HI 21 cm absorption towards the red quasar B3 1456+375, at $z = 0.333$, is consistent with the dust-reddening hypothesis.

5.1.3 TXS 1954+513, $z = 1.223$

The GMRT 640 MHz continuum image of TXS 1954+513, displayed in the top left panel of Figure 5.3 shows a central core and two emission components extended in the north and south directions. The two extended lobes can also be clearly seen in the 1.41 GHz image of Xu et al. (1995). The two extended sources have equal separations from the radio core, and hence the triple radio emission structure is likely to be in the plane of the sky. The total linear extent of the radio source is $\approx 20''$, which is ≈ 170 kpc at $z = 1.223$. A 3-component Gaussian model was fitted to the emission structure to measure the intensities of individual components, using the task JMFIT,

as described in Chapter 4. The integrated flux densities are (1254.1 ± 1.2) mJy (core), (403.4 ± 1.6) mJy (northern lobe) and (198.1 ± 1.3) mJy (southern lobe). The core emission is marginally resolved, with a peak flux of (1221.30 ± 0.69) mJy/Bm, the northern lobe is highly resolved, with a peak flux of (247.90 ± 0.66) mJy/Bm, while the southern lobe is also marginally resolved, with a peak flux of (184.00 ± 0.69) mJy/Bm. The emission from the core dominates the total intensity, with approximately 70% of the total source flux density of 1855.6 ± 2.4 mJy. The source has a spectral index of $\alpha = -0.2$ ($S = \nu^\alpha$) between 640 MHz (our GMRT estimate) and 1.41 GHz (Condon et al., 1998), which flattens to $\alpha = 0.01$ between 1.4 GHz and 4.8 GHz (Gregory and Condon, 1991).

Interestingly, Massaro et al. (2009) have found that TXS 1954+513 has the characteristics that are typical of a blazar; the optical spectrum shows broad emission lines, the source has a high X-ray luminosity of $\approx 10^{43}$ erg s⁻¹, and the radio spectrum between 1.4 GHz and 5 GHz is extremely flat. Recently, a few other authors (e.g. Healey et al., 2008; Xie et al., 2007) have also classified this source as a blazar. Blazars are known to have a dominant radio core, along with a flat radio spectrum. They are expected to be oriented towards the line-of-sight, with the core-jet emission enhanced due to beaming. As such, they are not expected to show extended lobe emission. It is puzzling that TXS 1954+513 shows characteristics of a blazar, since the radio images at 640 MHz and 1.4 GHz clearly show structures comprising a core and two radio lobes, that are oriented close to the plane of the sky.

However, the milli-arcsec scale VLBI map at 1.6 GHz (Xu et al., 1995), which resolves the central component of the GMRT 640 MHz emission, clearly shows a one-sided jet emanating from the core. The core-jet structure appears to be projected towards the east. The fact that a one-sided jet is seen suggests that the detected jet emission has been amplified by relativistic beaming, which would imply that the jet is oriented in our direction. Further, it is evident that there is a misalignment between the one-sided VLBI core-jet structure and the large-scale north-south lobes, detected in the 1.41 GHz and 640 MHz images. Such strong misalignments between the milli-arcsec-scale and the arc-sec scale radio structure have been detected earlier in a number of AGNs, mainly in BL Lac objects (Conway and Murphy, 1993; Pearson and Readhead, 1988; Wehrle et al., 1992), and recently in a few core-dominated triple radio structures (Marecki et al., 2006). There are different models in the literature that can account for

5. DETECTIONS

these misalignments; these include twisted radio jets that arise due to interaction with the ambient medium or due to the precession of the axis of the central supermassive black hole (Appl et al., 1996; Conway and Murphy, 1993), and restarted AGN activity accompanied by a flip in the spin of the central black hole, that has possibly arisen due to a galaxy merger event (Marecki et al., 2006).

TXS 1954+513 is only the fifth known associated HI 21 cm absorber at $z > 1$. The top-right panel in Figure 5.3 shows the HI 21 cm absorption spectrum obtained by taking a cut through the spectral cube at the location of the peak flux of the core emission in the 640 MHz GMRT continuum image (shown in the top left panel of the Figure 5.3). The two lower panels show spectra obtained by taking cuts through the locations of the peak flux of the two extended components; these show no evidence for HI 21 cm absorption. The peak of the absorption is blueshifted from the AGN redshift ($z = 1.2230 \pm 0.0001$; Lawrence et al., 1996) by $\approx 328 \text{ km s}^{-1}$. The full width between the 20% points is $\approx 40 \text{ km s}^{-1}$. The line width is quite narrow compared to the median line width of $\approx 166 \text{ km/s}$ between 20% points in the Vermeulen et al. (2003) and Geréb et al. (2015) samples.

The three panels of Figure 5.4 show the optical depth (in units of $1000 \times \tau$) plotted against velocity, in km s^{-1} , with respect to the AGN redshift. The left panel shows the spectrum at the location of the peak flux of the radio core, while the middle and right panels, respectively, show the spectra at the locations of the peak flux of the southern and northern lobes respectively. Note that the optical depth sensitivities of the spectra towards the peaks of the northern and southern lobes are sufficient to detect HI 21 cm absorption of the same strength as that of the main absorption component seen against the core, but not to detect the weaker absorption component. We can thus rule out the possibility that the cloud producing the strong HI 21 cm absorption covers both the core and either of the lobes, but cannot rule out the possibility that the gas producing the weaker HI 21 cm absorption might cover all three source components.

The blueshift of the peak of the HI 21 cm absorption from the AGN redshift of $z = 1.223$ indicates that this is a case of gas outflow from an AGN. The detected HI 21 cm absorption may arise against either the VLBI core, or the VLBI-scale eastward pointing radio jet. In either case, since the jet is likely to point close to our line-of-sight towards the core, the gas cloud appears to be moving in the direction of the radio jet and away from the core. The gas cloud may be being driven out by the ram pressure

5.1 Detections in the CJF sample

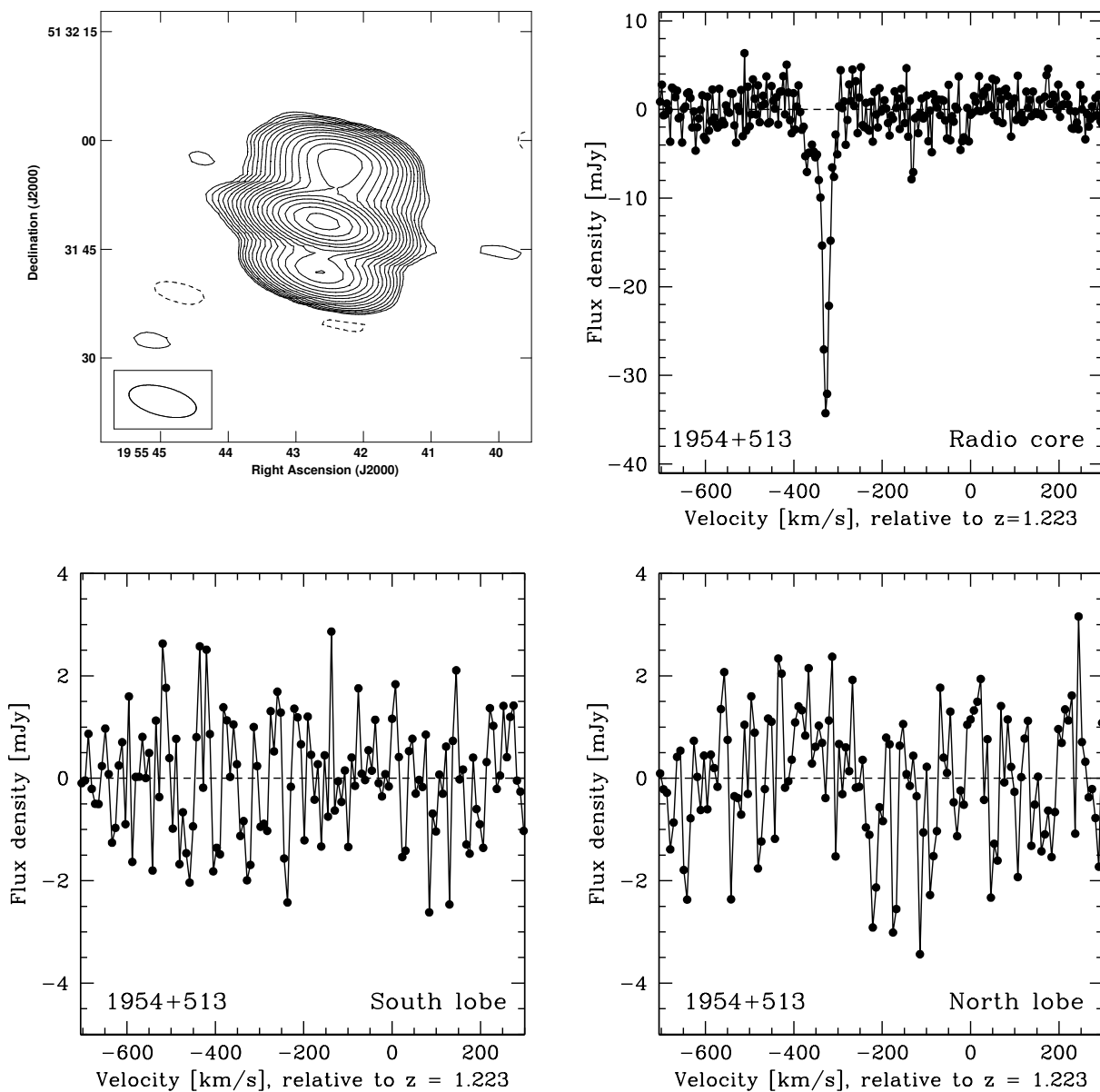


Figure 5.3: The top-left panel shows the continuum image at 640 MHz. The positive contour levels extend from 2.0 mJy/Bm to 1024.0 mJy/Bm, in steps of $\sqrt{2}$, while the single negative (dashed) contour is at -2.0 mJy/Bm. The top-right panel displays the HI 21 cm absorption spectrum towards the core component of the radio source. The bottom-left and bottom-right images display the absorption spectra towards the two lobes that are extended in the north and south directions.

5. DETECTIONS

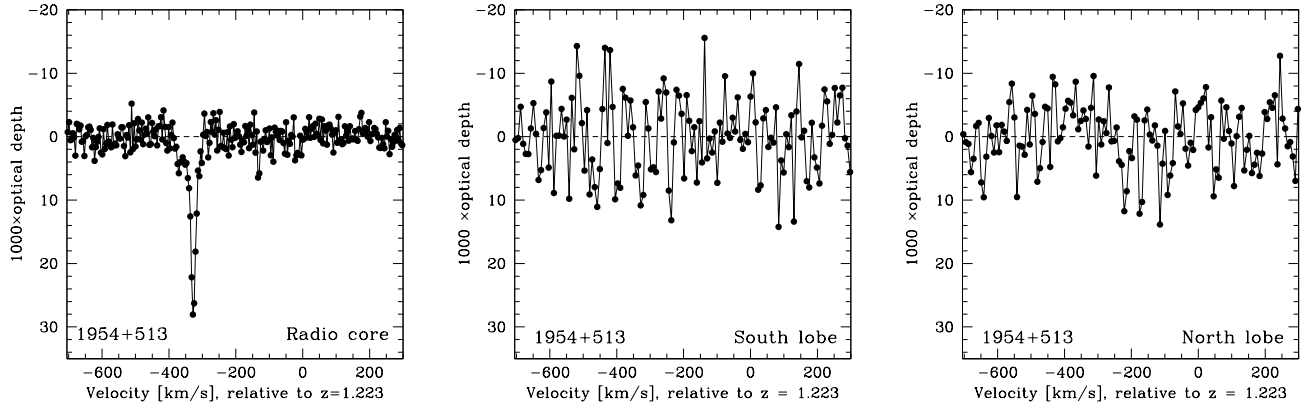


Figure 5.4: GMRT HI 21 cm absorption spectra towards (left panel) the radio core, (middle panel) the northern lobe, and (right panel) the southern lobe. In all three spectra, optical depth (in units of $1000 \times \tau$) is plotted against velocity, in km s^{-1} , relative to the AGN redshift of $z = 1.2230$. It is clear that the optical depth sensitivity towards the two lobes is sufficient to detect HI 21 cm absorption of the same strength as that seen towards the radio core.

of the jet, as suggested by recent numerical simulations (Wagner and Bicknell, 2011; Wagner et al., 2012).

We estimated the rest-frame UV (1216 \AA) luminosity of TXS 1954+513 by extrapolating from its measured R and B magnitudes (Monet et al., 2003) to infer its flux density at $1216 \times (1+z) \text{ \AA}$ ($z = 1.223$), and thence, its luminosity at this wavelength. Monet et al. (2003) obtained $R = 17.34$ and $B = 18.87$ from the second epoch of the USNO-B catalogue, with somewhat different values ($R = 17.47$ and $B = 18.44$) obtained in the first epoch. We have used the second-epoch magnitudes since the second-epoch R-band magnitude was obtained using a faint photometric standard, unlike the other measurements. This yielded $L_{UV} \approx 1.7 \times 10^{23} \text{ W Hz}^{-1}$, the highest UV luminosity at which associated HI 21 cm absorption has been detected at any redshift (Curran and Whiting, 2010; Curran et al., 2008). This is also the first case of detection of associated HI 21 cm absorption above the UV luminosity threshold of $L_{UV} = 10^{23} \text{ W Hz}^{-1}$, suggested by Curran and Whiting (2010). This shows that neutral hydrogen can indeed survive in AGN environments in high UV luminosities. We note that using the first-epoch R-band and B-band magnitudes of the USNO-B catalogue yields an even higher UV luminosity, $L_{UV} \approx 3.7 \times 10^{23} \text{ W Hz}^{-1}$, indicating that our conclusion that

TXS 1954+513 has a high rest-frame UV luminosity is not affected by the use of the second-epoch data.

5.1.4 TXS 0604+728, $z = 3.530$

Our tentative detection of HI 21 cm absorption at $z = 3.530$ towards TXS 0604+728 is shown in Figure 5.5. Unfortunately, follow-up GMRT observations of the source were repeatedly affected by RFI and we were hence unable to confirm the reality of the absorption line. If the detection is confirmed, this would be the highest redshift at which HI 21 cm absorption has ever been detected, surpassing the two absorbers at $z \approx 3.39$ towards TXS 0902+343 (Uson et al., 1991) and PKS 0201+113 (Kanekar et al., 2007).

The absorption feature appears symmetric around the AGN redshift, and is extremely wide, with a width of ≈ 850 km/s between the 20% points. For comparison, all the associated HI 21 cm absorbers in the samples of Vermeulen et al. (2003) and Geréb et al. (2015) have widths between 20% points $\lesssim 825$ km/s, with a median value of ≈ 166 km/s.

The radio source is unresolved in the GMRT 314 MHz image, but a complex core-jet morphology is visible in the milli-arcsecond-scale VLBI map at 5 GHz (Britzen et al., 2007) and the arcsecond-scale VLA image at 1.4 GHz (e.g. Taylor et al., 1996). The largest linear size of the radio source is ≈ 10 arcsecs. The source has a spectral index of $\alpha = -0.35$ ($S \propto \nu^\alpha$) between 1.4 GHz (Condon et al., 1998) and 4.8 GHz (Taylor et al., 1996), steepening marginally to $\alpha = -0.4$ at lower frequencies, between 314 MHz (our GMRT measurement) and 1.4 GHz. The wide absorption feature could arise against different radio source components in the core and the jets.

Finally, TXS 0604+728 also has a high estimated UV luminosity of $\approx 4.2 \times 10^{23}$ W Hz⁻¹. If the detection is confirmed, then it would be the second case of a detection of associated HI 21 cm absorption towards an AGN with a UV luminosity higher than the threshold of 10^{23} W Hz⁻¹, above which Curran et al. (2008) argue that HI 21 cm absorption should not be detected.

5. DETECTIONS

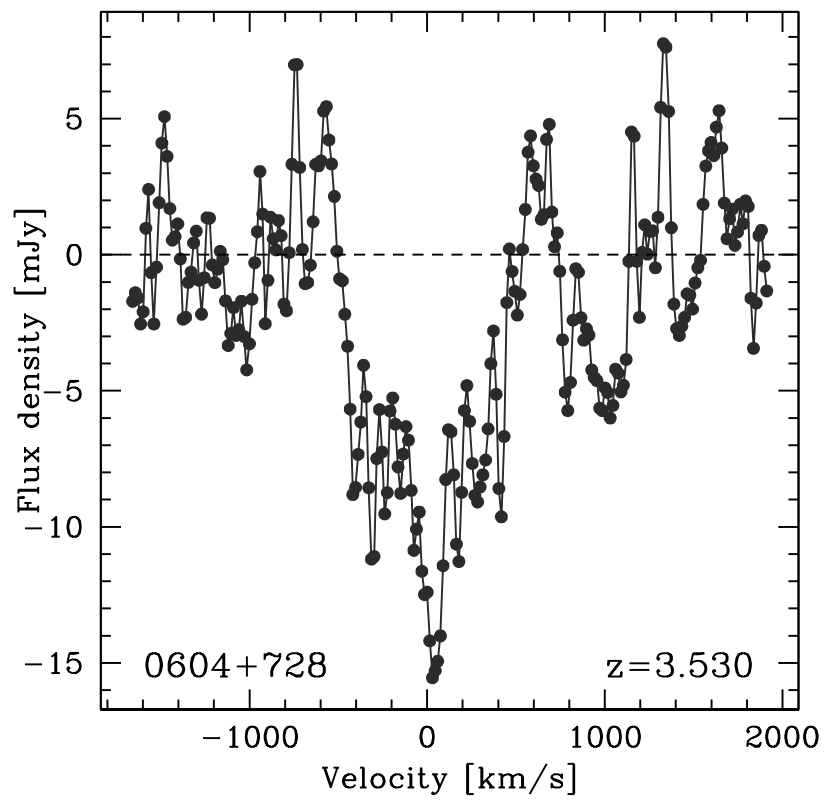


Figure 5.5: GMRT spectrum of HI 21 cm absorption towards TXS 0604+728, at $z = 3.530$.

5.2 HI 21 cm absorption detections in the GPS sample

5.2.1 TXS 1200+045, $z = 1.226$

TXS 1200+045 is unresolved in the GMRT 638 MHz continuum image, while the 1.6 GHz VLBI image shows a three-component structure (Liu et al., 2007). It is not clear whether the three VLBI emission components arise from a core and two lobes or from a one-sided core-jet structure. We note that component-A, which is by far the brightest of the three components detected in the 1.6 GHz VLBI image of Liu et al. (2007) lies at one end of the structure; this suggests that the source has a core-jet structure.

The GMRT HI 21 cm absorption spectrum towards TXS 1200+045 is displayed in Figure 5.6. The absorption is likely to arise against the strongest of the three components (component A) in the VLBI image of Liu et al. (2007) as the other two source components are quite weak implying a high HI 21 cm opacity to produce detectable HI 21 cm absorption.

The spectrum shows a narrow absorption with a line width of ≈ 125 km/s between 20% points, along with a wider and weaker absorption feature with a span of ≈ 500 km/s, extended towards the source redshift. The reality of both the narrow and wide absorption features has been confirmed through two GMRT observing runs (see Section 4.2.1). Interestingly, the deepest HI 21 cm absorption feature is significantly blueshifted from the AGN redshift of $z = 1.22597 \pm 0.00084$ (Hewett and Wild, 2010), by ≈ 2300 km/s. This suggests that the absorption arises in outflowing gas (at $z \approx 1.208$), perhaps pushed by the radio jet to high velocities. Also, the detection of the wider absorption feature indicates the presence of disturbed gas, that might indicate a jet-cloud interaction. Finally, the absorber towards TXS 1200+045 is the seventh known associated HI 21 cm absorber at $z > 1$.

5.2.2 TXS 1245-197, $z = 1.275$

The sample of GPS sources was selected based on the criterion that the sources have inverted spectra, with the peak frequency lying between 300 MHz and 5 GHz (e.g. Labiano et al., 2007). TXS 1245-197 has an observed turnover frequency of ≈ 400 MHz; the turnover frequency in the source rest-frame is ≈ 900 MHz. The inverted spectrum in a GPS source is believed to arise due to synchrotron self-absorption in a compact radio emission region, probably in the early stages of AGN evolution (see Section 2.3).

5. DETECTIONS

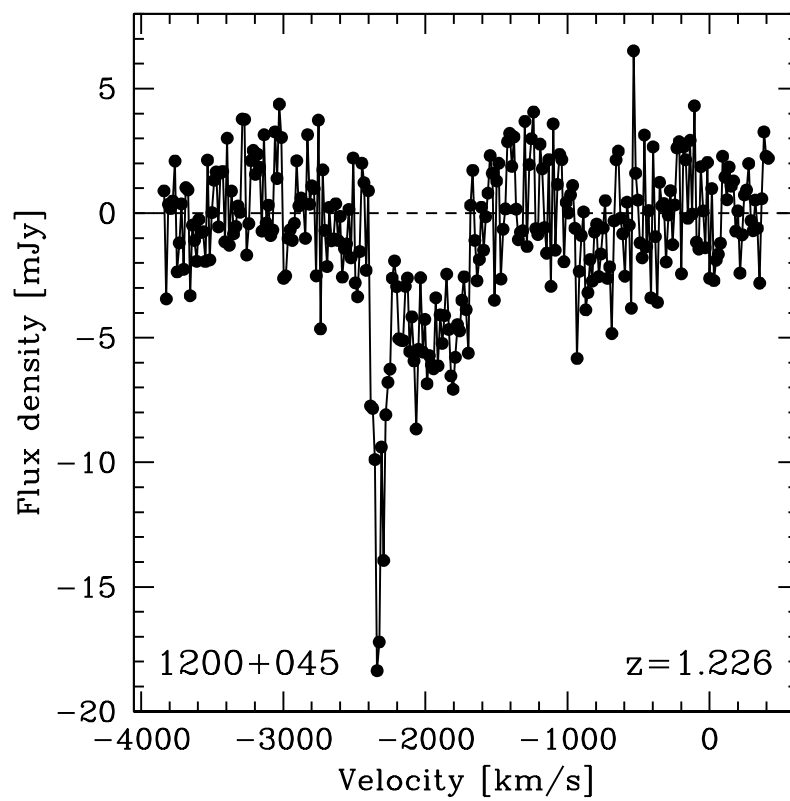


Figure 5.6: The GMRT HI 21 cm absorption spectrum towards TXS 1200+045, at $z = 1.226$.

5.2 HI 21 cm absorption detections in the GPS sample

However, the VLBI 2.3 GHz and 8.6 GHz images of TXS 1245-197 (e.g. Sokolovsky et al., 2011) show two prominent parsec-scale radio lobes, along with a fainter extended structure. Sokolovsky et al. (2011) found the two lobes to have comparable flux densities at both 2.3 and 8.6 GHz, and to have steep spectra between the two frequencies, with spectral indices of -0.72 and -0.59 . The authors hence classified the source as a Compact Symmetric Object (CSO), as the steep spectra make it unlikely that either source component arises from a compact core.

CSOs are powerful extragalactic radio sources that show emission on both sides of an AGN, and have sizes < 1 kpc (e.g. Wilkinson et al., 1994). Relativistic beaming is believed to be small or non-existent in these objects owing to their orientation close to the plane of the sky. Hence, the two brightest VLBI source components in TXS 1245-197 are likely to correspond to parsec-scale lobes at the ends of VLBI-scale jets, with the core remaining undetected at radio frequencies.

TXS 1245-197 is compact and unresolved in the GMRT 624 MHz continuum image, shown in the left panel of Figure 5.7, with a flux density of 8302.2 ± 0.6 mJy. If the steep spectra of the two compact components of the 2.3 GHz and 8.6 GHz VLBI images of Sokolovsky et al. (2011) extend to low frequencies, these components would dominate the 624 MHz flux density. The radio core is faint at 2.3 GHz and is likely to have an inverted or flat spectrum; it is hence unlikely to contribute significantly to the 624 MHz emission detected with the GMRT. As such, the detected HI 21 cm absorption (see the right panel of Figure 5.7) is likely to arise against one or both of the radio lobes detected in the VLBI image. The HI 21 cm absorption profile has a width of ≈ 325 km/s between 20% points, and has an extended wing that is blueshifted from the source redshift. The large velocity width could arise either due to absorption against both radio lobes, or possibly from disturbed gas that is interacting with the AGN jets (e.g. Geréb et al., 2015). Finally, the detection towards TXS 1245-197 is the sixth known associated HI 21 cm absorber at $z > 1$.

5. DETECTIONS

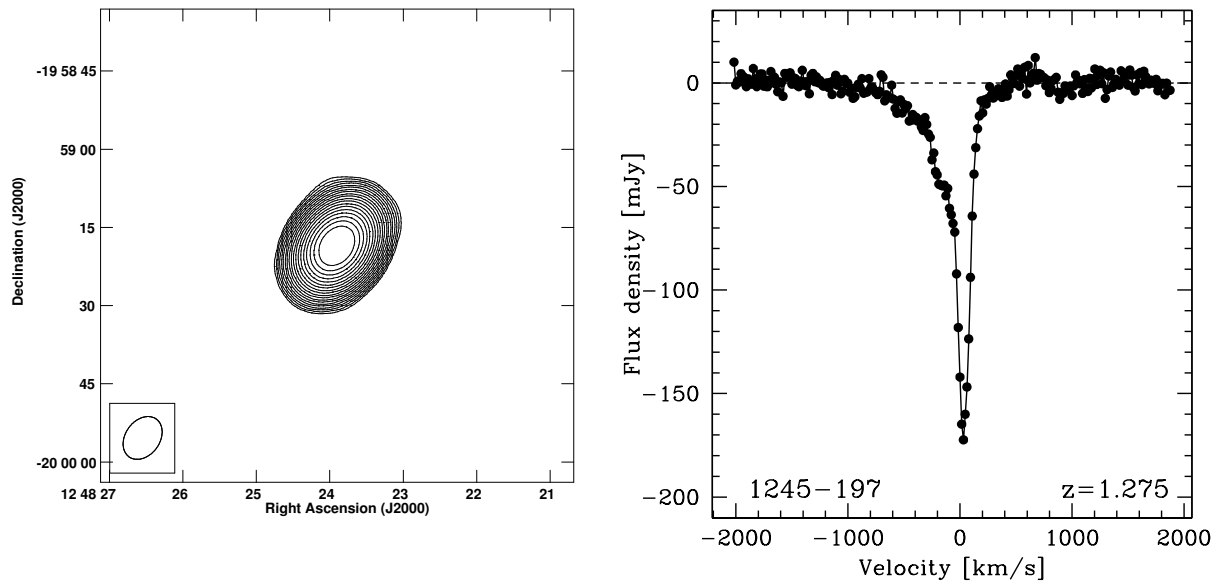


Figure 5.7: The left panel shows the GMRT continuum image of 1245-197 at 624 MHz. The contour levels extend from 9.0 mJy/Bm to 4608.0 mJy/Bm, in steps of $\sqrt{2}$. The panel at the right shows the GMRT HI 21 cm absorption spectrum towards TXS 1245-197, at $z = 1.275$.

6

Discussion

6.1 The Caltech-Jodrell Bank Flat-Spectrum sample

6.1.1 A uniformly-selected flat-spectrum sample

There are more than 50 detections of associated H I 21 cm absorption reported till now, with the vast majority of the absorbers detected at low redshifts, $z < 1$ (e.g. Curran and Whiting, 2010; Geréb et al., 2015; Gupta et al., 2006; Vermeulen et al., 2003). The typical reported detection fraction of H I 21 cm absorption in associated systems at low redshifts is $\gtrsim 30\%$ (e.g. Pihlström et al., 2003; Vermeulen et al., 2003). Conversely, as noted in Chapter 1, most of the searches for associated H I 21 cm absorption at high redshifts ($z > 1$) have been unsuccessful, with only four detections in the literature. With 25 searches available in the literature at $z > 1$ (e.g. Curran et al., 2013; Gupta et al., 2006), the detection rate is $16_{-8}^{+13}\%$, where the errors are from small number Poisson statistics (e.g. Gehrels, 1986). While the detection fraction of associated H I 21 cm absorption at $z > 1$ has only half the value at low redshifts, the difference between the two detection fractions is not statistically significant due to the large uncertainty in the high- z detection fraction. This is simply due to the fact that few high- z AGNs have so far been targetted in H I 21 cm absorption studies. Larger target samples are needed to test whether the detection rate of associated H I 21 cm absorption is indeed lower at high redshifts.

Moreover, most studies of associated H I 21 cm absorption (e.g. Curran et al., 2013; Gupta et al., 2006) have targetted highly heterogeneous AGN samples at all redshifts. The heterogeneity of the samples makes it difficult to distinguish between possible

6. DISCUSSION

redshift evolution in the AGN environment and differences in the AGN samples at different redshifts. For example, Gupta et al. (2006) carried out an analysis of 96 AGNs, mostly at low to intermediate redshifts, $z < 1$. They found little evidence for redshift evolution in either the detection rates of HI 21 cm absorption or in the distribution of the HI 21 cm optical depths. However, their sample was highly heterogeneous, consisting of 21 large radio galaxies, 13 flat-spectrum radio sources, 35 compact steep spectrum sources, and 27 GPS sources. The heterogeneity of the sample makes it difficult to reliably interpret the observational data.

An alternative explanation for the tentative result that the strength of associated HI 21 cm absorption may be weaker at high redshifts stems from the luminosity bias in most AGN samples used in such studies. High- z AGN samples typically contain more objects with higher rest-frame UV and radio luminosities. Curran et al. (2008) suggest that the high AGN luminosity in the UV and/or radio wavebands can lead to a lower HI 21 cm optical depth, either by ionizing the neutral hydrogen (and thus reducing the HI column density) or by altering the hyperfine level populations (and thus increasing the spin temperature; e.g. Field, 1959). Curran et al. (2008, 2013) have argued that the high luminosities of the high- z AGNs are the primary causes of the (tentative) low detection rate of the HI 21 cm absorption. We note, however, that the AGN samples of Curran et al. (2008, 2013) were also highly heterogeneous, containing all the AGNs that had been searched for HI 21 cm absorption in the literature.

We have hence put together a large sample of uniformly-selected sources, selected from the CJF sample, as described in chapter 2, to investigate the dependence of the HI 21 cm absorption strength on both redshift and AGN luminosity. Our full sample consists of 92 sources selected from the CJF sample, which includes 63 sources from our observations (the sources with usable spectra) and 29 from the literature. The sample contains 16 detections of HI 21 cm absorption (including our three confirmed detections towards TXS 0003+380, B3 1456+375, and TXS 1954+513, and our tentative detection towards TXS 0604+728) and 76 non-detections, yielding upper limits to the HI 21 cm optical depth. This is by far the largest sample of uniformly-selected AGNs that has been searched for associated HI 21 cm absorption. The sample covers a large redshift range, $0.01 \lesssim z \lesssim 3.6$, with a significant number of sources at $z > 1$. The sources from our GMRT observations are listed, in order of increasing redshift, in Table 6.1. The columns of this table are (1) the AGN name, (2) the AGN redshift, z , (3) the

6.1 The Caltech-Jodrell Bank Flat-Spectrum sample

integrated HI 21 cm optical depth or, for HI 21 cm non-detections, the 3σ upper limit to the HI 21 cm optical depth, in km s^{-1} , assuming a Gaussian line profile with a line FWHM of 100 km s^{-1} , (4) the logarithm of the AGN luminosity L_{UV} (in W Hz^{-1}) at a rest-frame wavelength of 1216 \AA , i.e. $L'_{UV} = \text{Log}[L_{UV}/(\text{W Hz}^{-1})]$, (5) the logarithm of the AGN luminosity $L_{1.4 \text{ GHz}}$ (in W Hz^{-1}) at a rest-frame frequency of 1.4 GHz, i.e. $L'_{1.4 \text{ GHz}} = \text{Log}[L_{1.4 \text{ GHz}}/(\text{W Hz}^{-1})]$, (6) the AGN spectral index around the redshifted HI 21 cm line frequency, $\alpha_{21 \text{ cm}}$, and (7) the AGN colour between the R- and K-bands, i.e. the difference between its measured R- and K-magnitudes, (8, 9) the two UV/optical wavebands, and the measured magnitudes therein that were used to infer the AGN's rest-frame 1216 \AA UV luminosity, (10) Ref. UV, the references for the measured optical and ultraviolet luminosities that were used to infer the rest-frame 1216 \AA luminosity (following the procedure of Curran and Whiting (2010)), and (11) Ref. RK, the references for the R- and K-band magnitude measurements.

The sources from the literature are listed in Table 6.2. The first 9 columns of this table are the same as those of Table 6.1. The remaining columns are (10) Ref. HI, the references for searches for associated HI 21 cm absorption in the literature, (11) Ref. UV, the references for the measured optical and ultraviolet luminosities that were used to infer the rest-frame 1216 \AA luminosity (following the procedure of Curran and Whiting (2010)), and (12) Ref. RK, the references for the R- and K-band magnitude measurements.

The luminosity at a rest-frame wavelength of 1216 \AA for each AGN was estimated by following the prescription of Curran and Whiting (2010). We first determined the flux density F_{UV} at the wavelength $1216 \times (1+z) \text{ \AA}$ for each AGN, by using a power-law spectrum to interpolate between its measured flux densities at two optical and/or UV wavebands in the literature. The luminosity at the rest-frame wavelength of 1216 \AA was then inferred from the expression $L_{UV} = 4\pi D_{AGN}^2 F_{UV}/(1+z)$, where D_{AGN} is the AGN's luminosity distance. For 5 AGNs, TXS 2021+614, TXS 0424+670, TXS 0600+442, TXS 1020+400 and TXS 2253+417, the flux density is known only at a single optical waveband, which is quite distant from the redshifted 1216 \AA wavelength. These systems hence do not have a listed rest-frame 1216 \AA luminosity in Table 6.1.

The radio spectral indices of the AGNs were computed from their flux densities at the redshifted HI 21 cm line frequency and at the nearest frequency with a flux density estimate in the literature. The latter frequency was usually 1.4 GHz, from the FIRST

6. DISCUSSION

or the NVSS surveys (Becker et al., 1995; Condon et al., 1998). Finally, the R-K colour could only be inferred for a total of 58 AGNs of the full sample of 92 systems; the remaining sources have information in the literature at only a single optical waveband.

In the following sections, we will examine the dependence of the HI 21 cm detection fractions and the distribution of HI 21 cm optical depths on redshift, radio spectral index, AGN radio and UV luminosities, and the (R-K) colour.

6.1.2 Redshift evolution

Figure 6.1 displays the velocity-integrated HI 21 cm optical depth, in logarithmic units, plotted as a function of redshift, for our full sample of 92 sources. It is clear that our GMRT observations, particularly at $1.1 < z < 1.5$, are sensitive enough that the 3σ upper limits on the integrated HI 21 cm optical depths of our non-detections are sufficiently stringent to rule out opacities that are comparable to those of the detections of HI 21 cm absorption. Further, it is clear from the figure that most of the detections are concentrated at low redshifts, $z < 1$, with 13 detections at $z < 1$, and just 3 detections at $z > 1$. On dividing the full sample at a median redshift of $z_{med} = 1.200$, the low- z sample has 13 detections and 33 non-detections, whereas the high- z sample has 3 detections (this includes the tentative detection at $z = 3.530$ towards TXS 0604+728) and 43 non-detections. The detection rates of HI 21 cm absorption are $28^{+10}_{-8}\%$ and $7^{+6}_{-4}\%$ for the $z < z_{med}$ and $z > z_{med}$ regimes, respectively (see Figure 6.2). The detection rate in the sample at $z > z_{med}$ is $4^{+6}_{-3}\%$ when the single tentative detection towards TXS 0604+728 is excluded from the sample. The errors on the detection fractions are computed using small-number Poisson statistics (e.g. Gehrels, 1986). Although the detection rate appears to be lower in the high- z sample, the difference in detection rates has only $\approx 2.1\sigma$ significance, once Poisson errors are taken into account. The difference in detection rates has a significance of $\approx 2.4\sigma$ when the tentative detection towards TXS 0604+728 is excluded from the sample.

Table 6.1: The 63 CJF sources observed using the GMRT, listed in order of increasing redshift. Note that $L'_{UV} = \text{Log}[L_{UV} / \text{W Hz}^{-1}]$ and $L'_{1.4 \text{ GHz}} = \text{Log}[L_{1.4 \text{ GHz}} / \text{W Hz}^{-1}]$.

Source	z	$\int \tau dv$ km s $^{-1}$	L'_{UV} ^a	$L'_{1.4 \text{ GHz}}$	$\alpha_{21 \text{ cm}}$ ^b	R-K ^c mag	Band 1 ^d mag	Band 2 ^d mag	Ref. ^e UV	Ref. ^f RK
TXS 0344+405	0.039	<6.3	21.34	23.23	1.70	0.6	NUV=20.1	B=14.0	1,2	2,3
TXS 0733+597	0.041	<0.67	19.69	24.24	-0.28	-1.8	FUV=20.9	NUV=20.5	1,1	2,3
S5 2116+81	0.084	<1.4	21.25	24.31	-0.67	1.5	NUV=17.8	B=14.8	1,2	2,3
TXS 1418+546	0.153	<1.5	21.71	25.48	0.58	4.7	FUV=18.7	NUV=18.0	1,1	4,3
S4 0749+54	0.200	<1.2	20.71	25.68	0.35	2.5	FUV=21.8	NUV=20.1	1,1	4,3
TXS 0003+380	0.229	1.943 ± 0.057	20.62	25.80	0.49	3.6	FUV=21.9	NUV=21.6	1,1	2,3
TXS 0010+405	0.255	<1.4	21.24	25.72	1.37	2.2	FUV=22.2	NUV=20.7	1,1	2,3
TXS 1719+357	0.263	<1.2	21.90	25.61	0.74	3.2	FUV=19.6	NUV=19.8	1,1	2,3
TXS 0424+670	0.324	<0.89	–	26.24	-0.46	–	–	–	–	–
B3 1456+375	0.333	3.834 ± 0.079	20.65	25.58	-0.41	5.1	FUV=23.7	NUV=21.3	1,1	2,6
S5 2007+77	0.342	<9.9	22.03	26.25	0.09	3.5	B=19.1	R=17.3	2,2	2,6
TXS 0035+367	0.366	<0.51	21.56	26.26	-0.17	2.4	FUV=21.3	NUV=20.8	1,1	2,3
TXS 0954+658	0.368	<5.8	21.96	26.55	0.01	3.3	FUV=20.4	NUV=19.7	1,1	2,3
CJ2 0925+504	0.370	<1.2	22.75	26.00	0.38	2.3	FUV=18.4	NUV=17.8	1,1	2,6
TXS 0110+495	0.389	<0.43	21.09	26.34	-0.01	2.4	NUV=21.5	R=17.8	1,2	2,3
TXS 1030+415	1.117	<0.69	23.32	27.30	-0.61	–	u=19.4	g=19.5	7,7	–
TXS 0600+442	1.136	<0.71	–	27.61	-0.37	–	–	–	–	–
S5 1044+71	1.150	<0.38	23.26	27.70	-0.97	4.7	NUV=19.8	R=17.5	1,2	2,3
TXS 2356+390	1.198	<0.42	22.36	27.36	-1.16	–	NUV=22.0	B=20.9	1,2	–
TXS 0821+394	1.216	<0.44	23.55	27.97	-0.75	3.0	NUV=19.2	u=18.5	1,7	2,3
TXS 1954+513	1.223	0.698 ± 0.036	23.23	27.75	0.06	2.4	B=17.9	R=17.3	2,2	2,3
TXS 1105+437	1.226	<0.70	23.04	27.18	-0.38	–	NUV=20.7	u=19.4	1,7	–
TXS 1015+359	1.228	<0.43	24.31	27.42	-0.02	–	FUV=20.5	NUV=18.1	1,1	–
TXS 1432+422	1.240	<0.95	22.62	27.04	0.10	–	NUV=21.9	u=20.4	1,7	–

continued on next page

Source	z	$\int \tau dv$ km s ⁻¹	L'_{UV} ^a	$L'_{1.4\text{ GHz}}$	$\alpha_{21\text{ cm}}$ ^b	R-K ^c mag	Band 1 ^d mag	Band 2 ^d mag	Ref. ^e UV	Ref. ^f RK
TXS 0945+408	1.249	<0.30	23.93	27.89	-0.46	2.5	FUV=19.4	NUV=18.3	1,1	2,3
S5 1150+81	1.250	<1.1	23.54	27.84	-0.33	3.3	FUV=20.7	NUV=19.3	1,1	2,3
TXS 1020+400	1.254	<0.51	–	27.77	-0.78	3.1	–	–	–	2,3
S5 1039+81	1.260	<1.5	23.90	27.46	0.01	2.9	B=19.7	R=17.5	2,2	2,3
TXS 0641+392	1.266	<0.68	22.64	27.22	0.79	–	B=20.5	R=19.4	2,2	–
TXS 0537+531	1.275	<0.32	22.84	27.46	0.01	2.7	NUV=18.7	B=18.8	1,2	2,3
TXS 1656+571	1.281	<0.74	23.56	27.77	-0.54	–	NUV=19.2	B=18.0	1,2	–
TXS 0707+476	1.292	<0.30	23.86	27.63	-0.15	1.4	NUV=18.4	B=17.0	1,2	2,3
TXS 0833+416	1.301	<0.63	24.06	27.26	-0.02	0.2	FUV=19.1	NUV=18.2	1,1	2,3
TXS 2319+444	1.310	<0.65	22.41	27.20	-0.05	–	NUV=22.2	R=19.2	1,2	–
TXS 0850+581	1.318	<0.37	23.53	27.63	-0.26	–	FUV=21.4	NUV=20.1	1,1	–
TXS 1240+381	1.318	<0.63	23.53	27.37	0.01	2.9	FUV=20.6	NUV=19.2	1,1	2,3
TXS 2007+659	1.325	<0.76	22.51	27.44	-0.26	–	NUV=22.0	R=20.3	1,2	–
S5 2353+81	1.344	<0.87	22.30	27.41	-0.53	2.9	NUV=22.9	B=19.9	1,2	2,8
JVAS J2236+7322	1.345	<0.97	22.64	27.08	-0.01	–	NUV=21.8	R=19.8	1,2	–
TXS 1342+663	1.351	<0.98	22.74	27.02	1.23	4.3	NUV=21.6	u=20.8	1,7	2,3
TXS 0035+413	1.353	<0.76	23.12	27.39	0.35	–	FUV=23.9	NUV=21.6	1,1	–
TXS 1739+522	1.375	<0.58	23.73	27.67	0.51	3.1	FUV=20.3	NUV=19.3	1,1	2,3
TXS 1442+637	1.380	<1.3	23.90	27.51	0.05	2.0	FUV=20.8	NUV=19.3	1,1	2,3
TXS 1030+611	1.401	<0.87	23.56	27.53	-0.37	5.3	NUV=19.1	u=19.3	1,7	2,3
TXS 1010+350	1.410	<0.67	23.94	27.41	-0.43	–	FUV=23.5	NUV=20.3	1,1	–
TXS 2229+695	1.413	<1.7	24.47	27.15	0.64	–	V=19.6	R=20.1	9,2	–
TXS 0820+560	1.418	<0.34	23.69	27.87	-0.26	–	FUV=20.5	NUV=19.5	1,1	–
TXS 0805+410	1.418	<0.69	23.32	27.40	-0.07	–	NUV=20.5	u=19.3	1,7	–
TXS 0804+499	1.436	<0.95	23.45	27.54	0.31	–	NUV=19.9	u=21.2	1,7	–
TXS 0145+386	1.442	<1.2	23.54	27.02	0.58	1.7	NUV=19.8	R=17.5	1,2	2,3

continued on next page

Source	z	$\int \tau dv$ km s ⁻¹	L'_{UV} ^a	$L'_{1.4 \text{ GHz}}$	$\alpha_{21 \text{ cm}}$ ^b	R-K ^c mag	Band 1 ^d mag	Band 2 ^d mag	Ref. ^e UV	Ref. ^f RK
TXS 0917+624	1.446	<0.79	23.22	27.70	0.23	3.2	NUV=20.9	u=19.6	1,7	2,3
JVAS J2311+4543	1.447	<2.2	22.82	26.90	0.76	–	NUV=21.7	R=19.1	1,2	–
S5 1058+72	1.460	<0.31	24.27	27.89	-0.21	1.9	FUV=18.6	NUV=17.8	1,1	2,3
TXS 0859+470	1.470	<0.43	23.54	28.17	-0.23	–	u=19.4	g=19.3	7,7	–
TXS 2253+417	1.476	<0.71	–	27.82	0.30	–	–	–	–	–
TXS 0340+362	1.484	<3.0	22.75	27.19	0.35	–	B=20.8	R=19.7	2,2	–
B3 1746+470	1.484	<4.5	23.43	27.00	0.54	–	NUV=19.8	R=19.1	1,2	–
TXS 1427+543	3.013	<0.44	23.77	28.66	-0.60	–	u=21.8	g=20.2	7,7	–
TXS 0800+618	3.033	<1.2	23.67	28.22	-0.05	–	NUV=20.1	R=19.6	1,2	–
TXS 0642+449	3.396	<2.9	24.47	27.86	0.72	2.9	B=19.5	V=18.5	5,5	2,3
TXS 0620+389	3.469	<0.20	24.28	28.50	-0.16	2.4	B=20.9	V=19.1	10, 10	2,11
TXS 0604+728	3.530	4.29 ± 0.28	23.96	28.64	-0.38	–	NUV=22.4	B=20.9	1,2	–
TXS 0749+426	3.589	<0.76	24.60	28.14	0.16	2.4	g=18.8	r=17.8	7,7	2,11

^aThe column shows the inferred rest-frame 1216 Å AGN luminosity, obtained by extrapolating from measurements in two nearby optical and/or ultraviolet bands. For some AGNs (indicated by a “–” in this column), the UV luminosity could not be obtained as the AGN flux density is only available at a single optical waveband in the literature.

^b $\alpha_{21 \text{ cm}}$ is the AGN spectral index at frequencies around the redshifted AGN H_I 21 cm line frequency.

^cFor sources with “–” entries, the flux density is not known in the K-band; the (R-K) colour hence could not be obtained.

^dThe two UV/optical bands and the measured magnitudes therein, that were used to infer the rest-frame 1216 Å UV luminosity.

^{e,f}References for the ultraviolet, optical and infrared band measurements, which were used to obtain the inferred 1216 Å UV luminosities (following the procedure of Curran and Whiting (2010)), and the (R-K) colour : (1) Bianchi et al. (2014), (2) Monet et al. (2003), (3) Cutri et al. (2003), (4) Urry et al. (2000), (5) Fedorov et al. (2011), (6) Chen et al. (2005) (7) Abazajian et al. (2009), (8) Cutri et al. (2013), (9) Véron-Cetty and Véron (2010), (10) Souchay et al. (2015), (11) Kuhn (2004).

^eThe first and second entries correspond to the 1st and 2nd UV/optical bands, respectively.

^fThe first and second entries correspond to the R and K bands, respectively.

Note: The typical uncertainties on the measurements in the different wavebands are (1) 0.1 mag (NUV), (2) 0.2 mag (FUV), (3) 0.05 mag (u), (4) 0.3 mag (B), (5) 0.02 mag (g), (6) 0.2 mag (V), (7) 0.01 (r), (8) 0.3 mag (R), (9) 0.07 mag (K).

6. DISCUSSION

However, it appears from Figure 6.1 that the measured integrated HI 21 cm optical depths in the sub-sample at low redshifts are higher than the typical upper limits in the high- z sub-sample. Hence, to test whether there is indeed a difference in the distribution of HI 21 cm optical depths in the two sub-samples, we used the Astronomical Survival analysis package, ASURV (Isobe et al., 1986). The two-sample tests in ASURV take into account the possibility that some of the measurements may be censored, i.e. may be upper or lower limits, as is the case with our integrated HI 21 cm optical depths. Within ASURV, a Peto-Prentice generalized Wilcoxon test finds evidence with 3σ significance that the low- z and high- z sub-samples (again separated at the median redshift) are drawn from different distributions. When the tentative detection towards TXS 0604+728 is excluded from the sample, the hypothesis that the two samples are drawn from the same distribution is excluded at 3.4σ significance. This is the first statistically significant evidence for redshift evolution in the HI 21 cm optical depths associated with AGN environments from a uniformly-selected sample.

We thus find that high- z AGNs have significantly weaker associated HI 21 cm absorption than low- z AGNs. This could arise due to a variety of reasons: (1) lower gas contents in high- z AGN environments, implying lower HI column densities, (2) higher gas spin temperatures in high- z environments, as has been seen for intervening galaxies towards AGNs, the damped Lyman- α systems (e.g. Kanekar et al., 2014), or (3) lower covering factors in the high- z AGN sample. Unfortunately, in the case of associated AGNs, we do not have direct estimates of the HI column density, and hence cannot estimate the gas spin temperature. Hence, while it is possible that the neutral gas in AGN environments indeed mainly consists of the warm neutral medium (as has been shown to be the case for damped systems; e.g. Kanekar and Chengalur (2003); Kanekar et al. (2014)), it is difficult to directly test this hypothesis. We will initially consider the low covering factor hypothesis to account for the low detection rate of HI 21 cm absorption, before investigating the low gas content and high spin temperature possibilities.

Table 6.2: The 29 CJF sources with HI 21 cm absorption searches available in the literature, listed in order of increasing redshift. Note that $L'_{UV} = \text{Log}[L_{UV} / \text{W Hz}^{-1}]$ and $L'_{1.4 \text{ GHz}} = \text{Log}[L_{1.4 \text{ GHz}} / \text{W Hz}^{-1}]$.

Source	z	$\int \tau dv$ km s ⁻¹	L'_{UV} ^a	$L'_{1.4 \text{ GHz}}$	$\alpha_{21 \text{ cm}}$ ^b	R-K ^c mag	Band 1 ^d mag	Band 2 ^d mag	Ref. ^e HI	Ref. ^f UV	Ref. ^g RK
TXS 1146+596	0.011	5.3 ± 1.8	20.30	23.09	0.26	2.3	NUV=19.7	u=14.6	1	1,7	2,3
TXS 0316+413	0.018	1.3	20.61	25.13	1.05	-0.2	FUV=16.3	NUV=15.5	2	1,1	2,3
B3 0651+410	0.022	<0.82	18.69	23.35	0.60	-1.0	FUV=20.5	NUV=19.6	3	1,1	2,3
TXS 1101+384	0.030	<0.63	21.28	24.18	0.17	-1.7	B=13.3	V=12.9	4	14, 14	14,3
TXS 1744+557	0.030	<1.2	19.53	24.02	0.22	-3.1	FUV=20.1	NUV=18.8	5	1,1	2,3
TXS 1652+398	0.034	<2.4	21.58	24.56	-0.12	-1.3	FUV=15.7	NUV=15.2	4	1,1	2,3
TXS 1254+571	0.042	33.9 ± 3.8	20.51	24.06	-0.57	6.1	u=15.2	g=13.9	12	7,7	2,3
TXS 1807+698	0.051	<1.6	20.91	25.00	1.05	0.2	FUV=18.0	NUV=17.0	4	1,1	2,3
TXS 0402+379	0.055	0.98 ± 0.11	19.88	25.31	-0.29	3.6	B=19.2	R=17.2	7	2,2	2,8
TXS 1144+352	0.063	<1.1	20.26	24.75	0.54	-0.9	FUV=20.2	NUV=19.3	5	1,1	2,3
TXS 2200+420	0.069	<0.95	20.30	25.78	-0.14	2.0	B=15.9	V=14.7	4	21, 20	19,6
TXS 1946+708	0.101	15.8 ± 4.6	18.60	25.35	-0.33	1.3	B=18.3	R=16.4	8	2,2	2,3
TXS 0309+411	0.134	<0.92	18.48	25.23	0.08	1.5	B=18.0	R=16.8	5	2,2	2,3
IVS B1622+665	0.201	<1.7	20.00	25.24	0.53	2.9	B=18.1	R=16.4	3	2,2	2,3
S5 1826+79	0.224	<15	21.28	25.57	0.59	2.1	FUV=20.8	NUV=21.2	9	1,1	2,3
TXS 2021+614	0.227	<0.21	–	26.43	0.07	3.3	–	–	9	–	2,3
TXS 2352+495	0.238	1.7	20.84	26.46	-0.09	2.9	B=21.1	V=19.6	9	16, 16	2,3
TXS 0831+557	0.241	0.58	21.39	27.03	-0.15	0.3	FUV=20.7	NUV=22.1	9	1,1	2,3
TXS 1943+546	0.263	2.9	20.85	26.46	-0.45	1.4	NUV=21.6	B=19.6	9	1,2	2,8
TXS 1031+567	0.459	<0.76	19.90	26.96	-0.20	–	u=23.9	g=22.8	9	7,7	–
TXS 1355+441	0.646	19	20.60	26.94	-0.34	–	NUV=24.6	u=22.2	9	1,7	–
S4 0108+38	0.669	46 ± 7	21.63	26.95	1.16	–	NUV=22.2	R=20.2	10	1, 17	–
TXS 1504+377	0.672	27.20 ± 0.04	20.30	26.95	-0.21	–	u=24.3	g=22.5	13	7,7	–
TXS 0923+392	0.695	<0.54	23.47	27.49	-0.38	1.7	FUV=19.2	NUV=17.5	9	1,1	17,3

continued on next page

Source	z	$\int \tau dv$ km s ⁻¹	L'_{UV} ^a	$L'_{1.4 GHz}$	$\alpha_{21 cm}$ ^b	R-K ^c mag	Band 1 ^d mag	Band 2 ^d mag	Ref. ^e H α	Ref. ^f UV	Ref. ^g RK
S5 0950+74	0.695	<1.4	21.65	27.15	0.92	–	B=19.5	R=18.6	9	2,2	–
TXS 1642+690	0.751	<0.69	22.66	27.34	0.03	–	B=19.1	R=18.6	9	2,2	–
S4 1843+35	0.764	<6.0	24.66	27.55	-0.03	–	B=17.2	R=16.5	9	2,2	–
TXS 1543+480	1.277	9.69 \pm 0.53	22.08	27.36	-0.23	6.3	NUV=22.8	u=22.6	11	1,7	7,3
TXS 0248+430	1.311	<1.4	23.10	27.84	0.22	-0.9	NUV=21.0	V=17.6	1	1,18	2,3

Notes:

^aThe column shows the inferred rest-frame 1216 Å AGN luminosity, obtained by extrapolating from measurements in two nearby optical and/or ultraviolet bands. For some AGNs (indicated by a “–” in this column), the UV luminosity could not be obtained as the AGN flux density is only available at a single optical waveband in the literature.

^b $\alpha_{21 cm}$ is the AGN spectral index at frequencies around the redshifted AGN H α 21 cm line frequency.

^cFor the sources with “–” entries, the flux density is not known in the K-band; the (R-K) colour hence could not be obtained.

^dThe two UV/optical bands and the measured magnitudes therein, that were used to infer the rest-frame 1216 Å UV luminosity.

^eReferences for associated H α 21 cm absorption searches : (1)Gupta et al. (2006); (2)De Young et al. (1973); (3)Orienti et al. (2006); (4)van Gorkom et al. (1989); (5)Chandola et al. (2013); (6)Dickey (1982); (7)Morganti et al. (2009); (8)Peck et al. (1999); (9)Vermeulen et al. (2003); (10)Carilli et al. (1998b); (11)Curran et al. (2013); (12) Gallimore et al. (1999); (13) Kanekar and Chengalur (2008).

^{f,g} References for the ultraviolet, optical and infrared waveband measurements, which were used to obtain the inferred 1216 Å UV luminosities (following the procedure of Curran and Whiting (2010)), and the (R-K) colour: (1) Bianchi et al. (2014), (2) Monet et al. (2003), (3) Cutri et al. (2003), (4) Urry et al. (2000), (5) Fedorov et al. (2011), (6) Chen et al. (2005) (7) Abazajian et al. (2009), (8) Cutri et al. (2013), (9) Véron-Cetty and Véron (2010), (10) Souchay et al. (2015), (11) Kuhn (2004), (12) Qi et al. (2015), (13) Zacharias et al. (2015), (14) Massaro et al. (2004), (15) Röser et al. (2008), (16) Zacharias et al. (2004), (17) Healey et al. (2008), (18) Rao et al. (2006), (19) Howard et al. (2004), (20) O’Dell et al. (1978), (21) Raiteri et al. (2009).

^f The first and second entries correspond to the 1st and 2nd UV/optical bands, respectively.

^gThe first and second entries correspond to the R and K bands, respectively.

Note: The typical uncertainties on the measurements in the different wavebands are (1) 0.1 mag (NUV), (2) 0.2 mag (FUV), (3) 0.05 mag (u), (4) 0.3 mag (B), (5) 0.02 mag (g), (6) 0.2 mag (V), (7) 0.3 mag (R), (8) 0.07 mag (K).

6.1.3 Dependence on the radio spectral index

A possible reason for the lower strength of associated HI 21 cm absorption in the high- z AGNs is that the low-frequency radio emission in the latter is dominated by extended structure. Although our target sources have been chosen from the CJF sample, with flat spectral indices, $\alpha \geq -0.5$ (Taylor et al., 1996), the CJF spectral index criterion is based on the flux densities at relatively high frequencies, 1.4 GHz and 4.85 GHz. It is hence possible that the radio emission at the low redshifted HI 21 cm absorption frequency is dominated by steep-spectrum extended structure, rather than by the flat- or inverted-spectrum radio core.

Such a scenario can be tested by estimating the covering factor from the fraction of the total radio flux density measured in high-resolution Very Long Baseline Interferometry (VLBI) continuum images at or near the redshifted HI 21 cm line frequency (e.g. Kanekar et al., 2009, 2014). Unfortunately, VLBI observations at frequencies below 1 GHz are technically challenging and are hence not available for most of the sources of our sample, especially for the systems at $z \gtrsim 1$. We will hence instead use the spectral index $\alpha_{21\text{ cm}}$ at the redshifted HI 21 cm frequency as a proxy for compactness of the AGN. A flat or inverted spectrum at low radio frequencies would indicate a core-dominated source, and a relatively high covering factor ($f \approx 1$), whereas a steep spectrum would indicate extended radio structure and a possible low covering factor ($f \ll 1$). If the integrated HI 21 cm optical depths indeed depend on the spectral index, or if the high- z sample has a systematically steeper spectral index than the low- z sample, it would suggest that a low covering factor may be the cause of the lower HI 21 cm optical depths at high redshifts.

Figure 6.3 shows the integrated optical depths of the 92 CJF sources plotted against the low-frequency spectral index, $\alpha_{21\text{ cm}}$. Clearly, there are a few sources which have $\alpha_{21\text{ cm}} < -0.5$, but the majority of the sources have flat radio spectra, with indices close to 0. In addition, the median spectral index, $\alpha_{21\text{ cm}} = -0.015$, is also very close to zero, indicating that the sample is dominated by compact objects, with $\alpha_{21\text{ cm}} > -0.5$.

Finally, a Peto-Prentice two-sample test finds that the two sub-samples, separated at the median $\alpha_{21\text{ cm}}$, are consistent (within $\approx 1.3\sigma$ significance) with being drawn from the same distribution. Excluding the tentative detection towards TXS 0604+728 has little effect on this result; the two sub-samples remain consistent (now within $\approx 1.1\sigma$

6. DISCUSSION

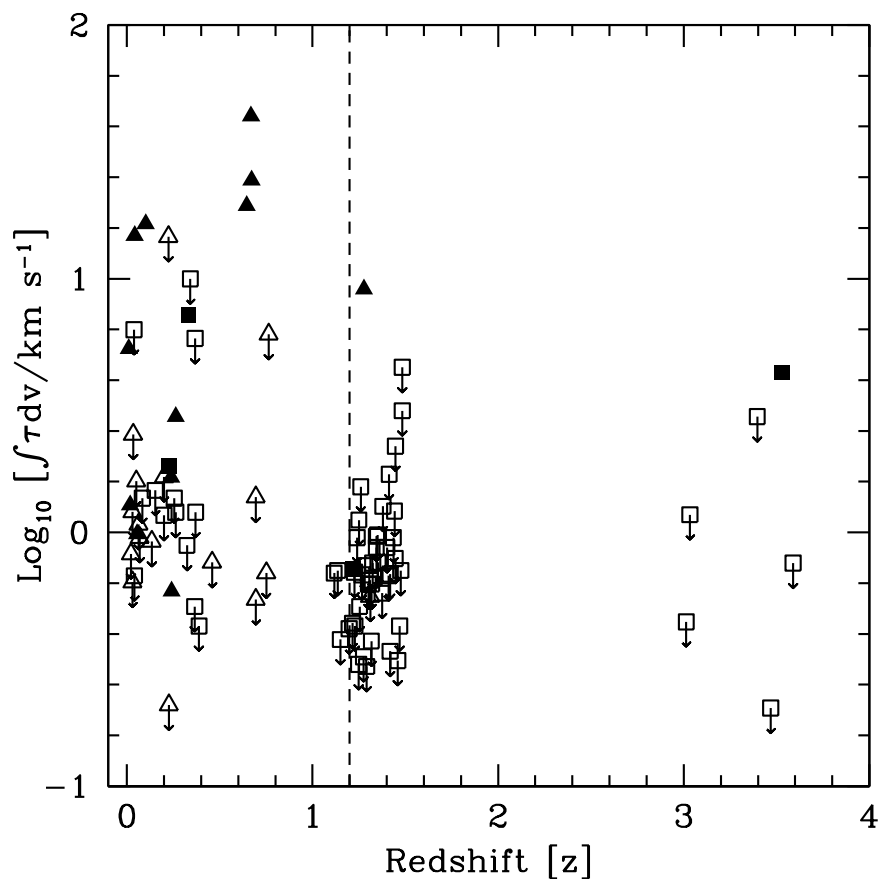


Figure 6.1: The integrated HI 21 cm optical depths of the full sample of 92 CJF sources, plotted as a function of redshift. The 63 sources observed by us using the GMRT are represented by squares, and the 29 literature sources are represented by triangles. Filled symbols indicate detections of HI 21 cm absorption, while open symbols indicate upper limits on the HI 21 cm optical depths. The dashed vertical line indicates the median redshift of the sample, $z_{med} = 1.2$.

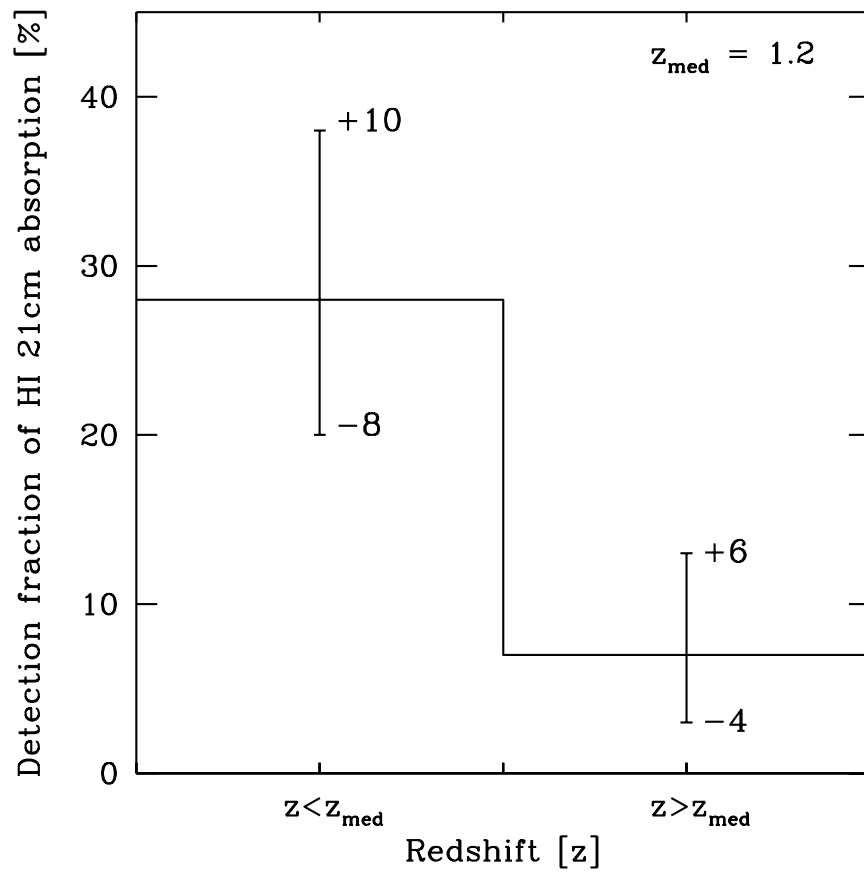


Figure 6.2: The detection rates of HI 21 cm absorption for the sub-samples with $z < z_{med}$ and $z > z_{med}$.

6. DISCUSSION

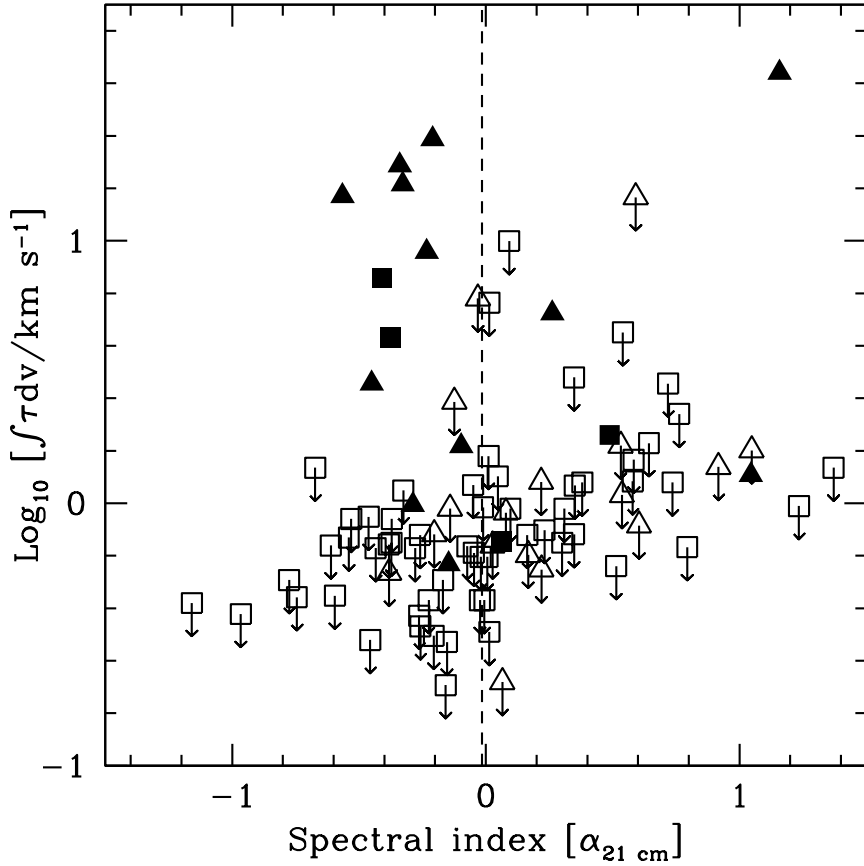


Figure 6.3: The integrated HI 21 cm optical depth of the 92 CJF sources plotted against the low-frequency spectral index, $\alpha_{21 \text{ cm}}$. The spectral indices are computed at frequencies near the redshifted HI 21 cm line frequency. The 29 literature sources are shown as triangles, and the 63 sources from our observations are shown as squares. Filled symbols represent detections, whereas open symbols represent upper limits on the integrated HI 21 cm optical depth. The dashed vertical line indicates the median low-frequency spectral index of the sample, $\alpha_{21 \text{ cm}, \text{med}} = -0.015$.

6.1 The Caltech-Jodrell Bank Flat-Spectrum sample

significance) with being drawn from the same distribution. Hence, we conclude that there is no significant evidence that the apparent low strength of HI 21 cm absorption in the high- z sample has arisen due to the low-frequency radio emission being dominated by extended, steep-spectrum structure, and hence, a low AGN covering factor. We will further consider the possibility that all low- z AGNs have high covering factors, while high- z AGNs have low covering factors, in Section 6.1.5.

6.1.4 Dependence on ultraviolet and radio luminosity

As discussed in Section 6.1.1, the lower strength of the associated HI 21 cm absorption in the high- z AGN sample could arise due to these AGNs having higher UV and/or radio luminosities (Curran et al., 2008). A high UV/radio luminosity could reduce the amount of neutral gas in the AGN environment and/or increase its spin temperature. Figures 6.4 and 6.5 show, respectively, the rest-frame 1216 Å UV and the rest-frame 1.4 GHz radio luminosities of the CJF sample plotted against redshift. It is apparent from the figures that the high redshift AGNs are biased towards higher ultraviolet and radio luminosities. Again, upon dividing the full sample at a median redshift of $z_{med} = 1.2$, a Gehan-Wilcoxon test finds that the null hypothesis that the rest-frame UV luminosities of the two sub-samples are drawn from the same distribution is rejected at $\approx 7.7\sigma$ significance. Similarly, the test also finds that the null hypothesis that the rest-frame 1.4 GHz radio luminosities of the high- z and low- z samples are drawn from the same distribution is rejected at $\approx 7.8\sigma$ significance. Hence, we conclude that there is a strong bias in our target sample towards high ultraviolet and radio luminosities for the systems at high redshifts. Finally, we also find that the rest-frame 1216 Å UV luminosities and the rest-frame 1.4 GHz radio luminosities of the sources in our sample are strongly correlated (see Figure 6.6), with a Kendall-tau value of ≈ 0.64 ($\approx 9\sigma$ significance).

We hence examine the possibility that the apparent redshift evolution in the HI 21 cm optical depths could have arisen due to the above luminosity bias. Figure 6.7 shows the integrated HI 21 cm optical depths of the AGNs of our sample, plotted against their rest-frame 1216 Å UV luminosities, while Figure 6.8 shows the integrated optical depths plotted against the rest-frame 1.4 GHz radio luminosities (with all quantities in logarithmic units). The dashed vertical lines in the two figures indicate the median UV and radio luminosities, $L_{UV,med} = 10^{22.64} W Hz^{-1}$ and $L_{1.4 GHz,med} = 10^{27.17} W Hz^{-1}$,

6. DISCUSSION

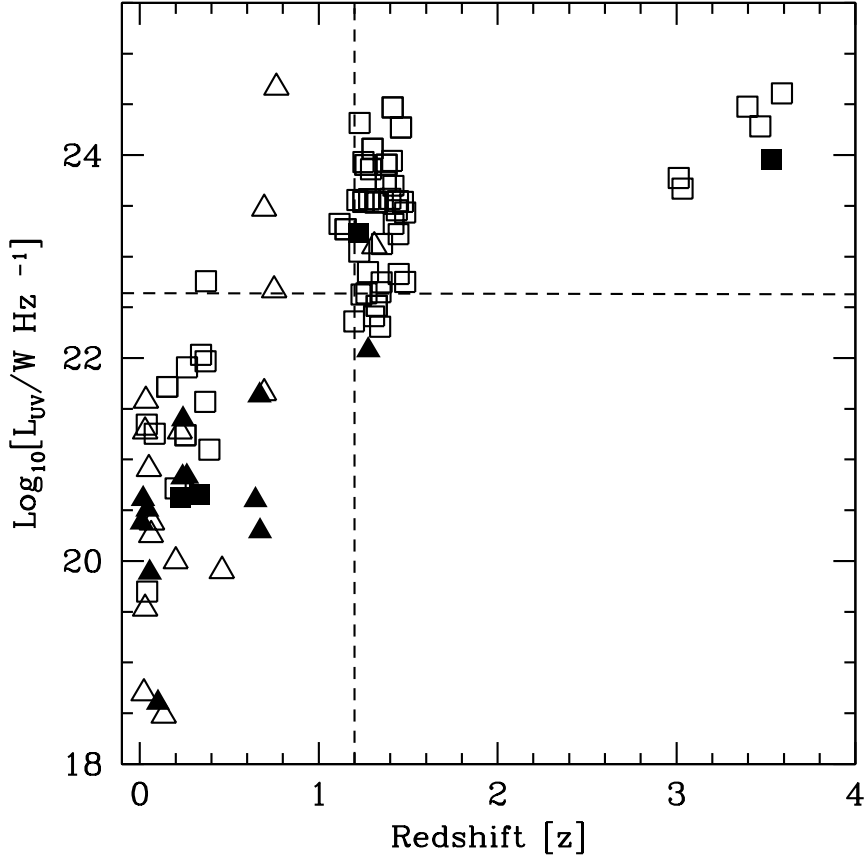


Figure 6.4: The rest-frame 1216 Å UV luminosities of 87 CJF sources of the sample plotted, in logarithmic units, against the AGN redshifts. The dashed horizontal line indicates the median UV luminosity, $L_{UV,med} = 10^{22.64} W Hz^{-1}$, and the dashed vertical line indicates the median redshift, $z_{med} = 1.2$. The squares and triangles represent the sources from our observations and the sources from the literature, respectively. Filled and open symbols represent detections and upper limits on the integrated H I 21 cm optical depths, respectively.

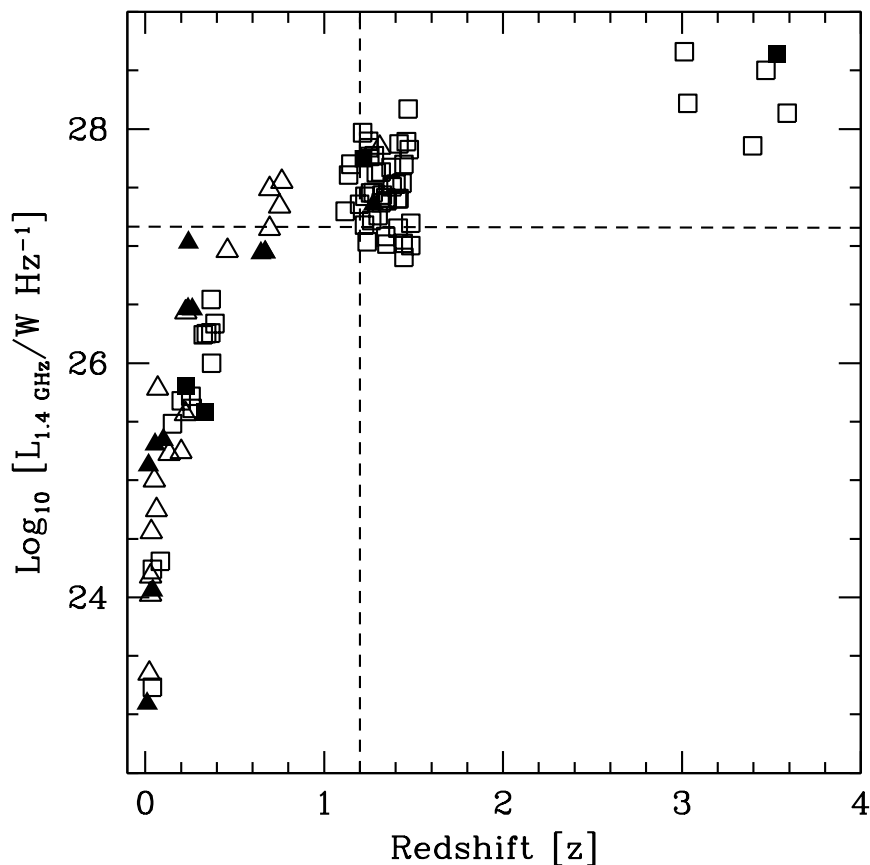


Figure 6.5: The rest-frame 1.4 GHz radio luminosities of the full sample of 92 CJB sources plotted, in logarithmic units, against the AGN redshifts. The dashed horizontal line indicates the median radio luminosity, $L_{1.4 \text{ GHz}, med} = 10^{27.17} \text{ W Hz}^{-1}$, and the dashed vertical line indicates the median redshift, $z_{med} = 1.2$. The squares and triangles represent the sources from our observations and the sources from the literature, respectively. Filled and open symbols represent detections and upper limits on the integrated HI 21 cm optical depths, respectively.

6. DISCUSSION

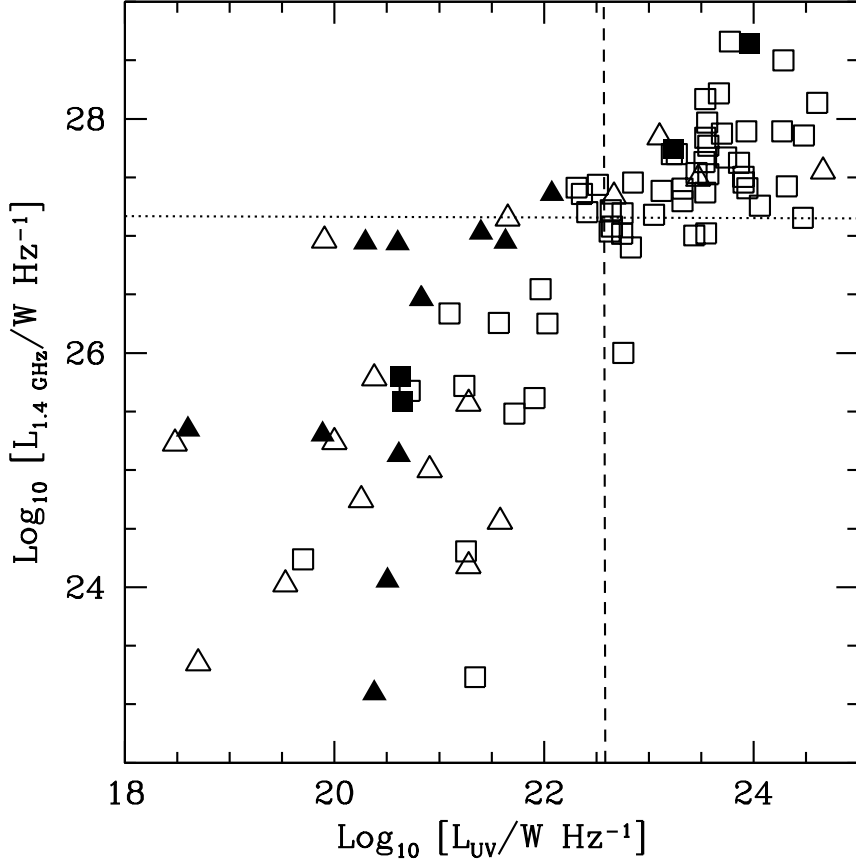


Figure 6.6: The rest-frame 1.4 GHz radio luminosities of 87 CJF sources of the sample plotted, in logarithmic units, against the rest-frame 1216 Å UV luminosities, in logarithmic units. The dashed vertical line indicates the median UV luminosity, $L_{UV,med} = 10^{22.64} W \text{ Hz}^{-1}$, and the dotted horizontal line indicates the median radio luminosity of $L_{1.4 \text{ GHz}} = 10^{27.17} W \text{ Hz}^{-1}$. The squares and triangles represent the sources from our observations and the sources from the literature, respectively. Filled and open symbols represent detections and upper limits on the integrated H α 21 cm optical depths, respectively.

6.1 The Caltech-Jodrell Bank Flat-Spectrum sample

respectively. It is clear from both figures that most detections of HI 21 cm absorption lie in the low-luminosity regions. Also, it appears that the measured integrated HI 21 cm optical depths of sources with low luminosities are higher than the typical 3σ upper limits of those with high luminosities. A Peto-Prentice two-sample test for censored data finds that the null hypothesis that the HI 21 cm optical depth distributions of low- and high-luminosity sub-samples are drawn from the same distribution is rejected at 3.6σ significance for the rest-frame 1216\AA UV luminosity, while it is rejected at 3.3σ significance for the rest-frame 1.4 GHz radio luminosity. When the single tentative detection towards TXS 0604+728 is excluded from the sample, the hypotheses are rejected at 3.9σ and 3.6σ significance, respectively.

We thus find that there is statistically significant evidence for a dependence of the strength of associated HI 21 cm absorption in our target sample on redshift, rest-frame 1216\AA ultraviolet luminosity, and rest-frame 1.4 GHz radio luminosity, but not on the low-frequency radio spectral index. Weaker HI 21 cm absorption is obtained at higher redshifts and higher radio and/or UV luminosities. Unfortunately, most of the luminous AGNs of our sample are also located at high redshifts (see Figures 6.4 and 6.5), implying that it is currently not possible to break the degeneracy between the three possibilities and identify the primary cause, if any, for the weakness in the HI 21 cm absorption. Searches for HI 21 cm absorption in either a low-luminosity AGN sample at high redshifts, or a high-luminosity sample at low redshifts would be required to break the degeneracy.

6.1.5 Effects of varying covering factor

In Section 6.1.3, we found no evidence for the hypothesis that the weaker HI 21 cm absorption in the high- z AGN sample might arise due to extended (and steep-spectrum) radio emission and hence, a low covering factor. However, a critical assumption in computing the integrated optical depths in the present analysis is that the gas covering factor is unity for all the systems. Such an assumption could lead to a large difference between the apparent and true optical depth, particularly for certain classes of AGNs with extended emission structures. For example, in Fanaroff-Riley type-II (FR-II) radio galaxies, the radio emission is dominated by large-scale radio lobes (e.g. O’Dea, 1998). It is possible that the neutral gas is concentrated near the AGN core, and hence does not extend to the large-scale lobes. As a result, the neutral gas would not

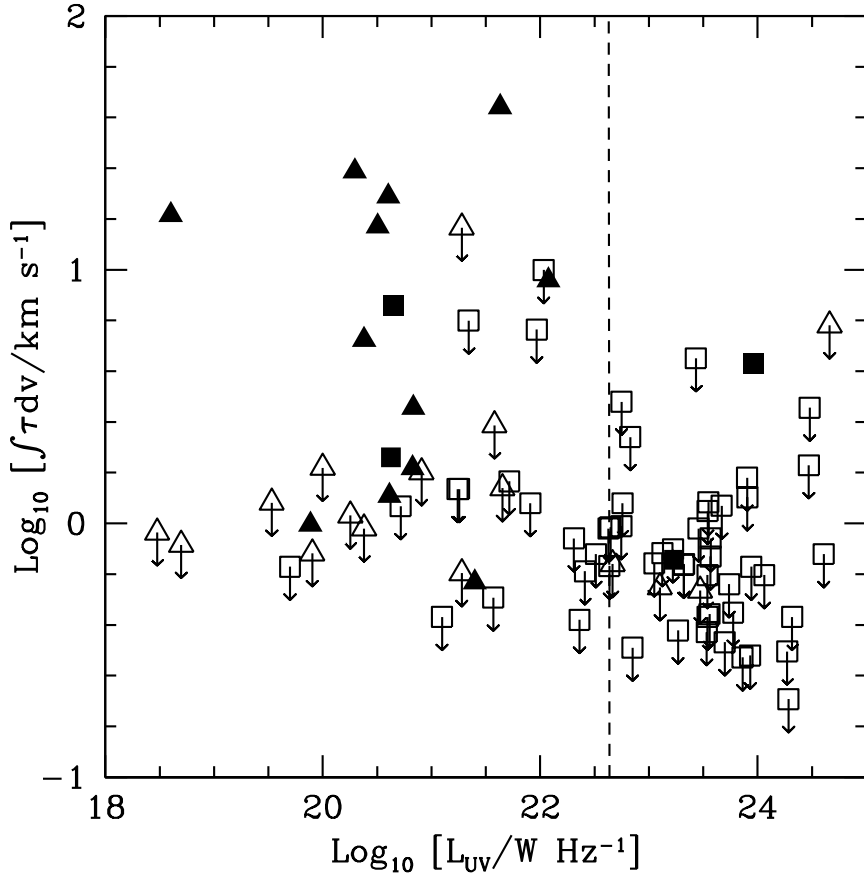


Figure 6.7: The integrated HI 21 cm optical depths of 87 sources of the CJF sample plotted against the rest-frame 1216 Å UV luminosities. The dashed vertical line indicates the median UV luminosity, $L_{UV,med} = 10^{22.64} W \text{ Hz}^{-1}$. The sources from our observations and from the literature are represented by squares and triangles, respectively. Filled and open symbols represent detections and upper limits on the HI 21 cm optical depth, respectively.

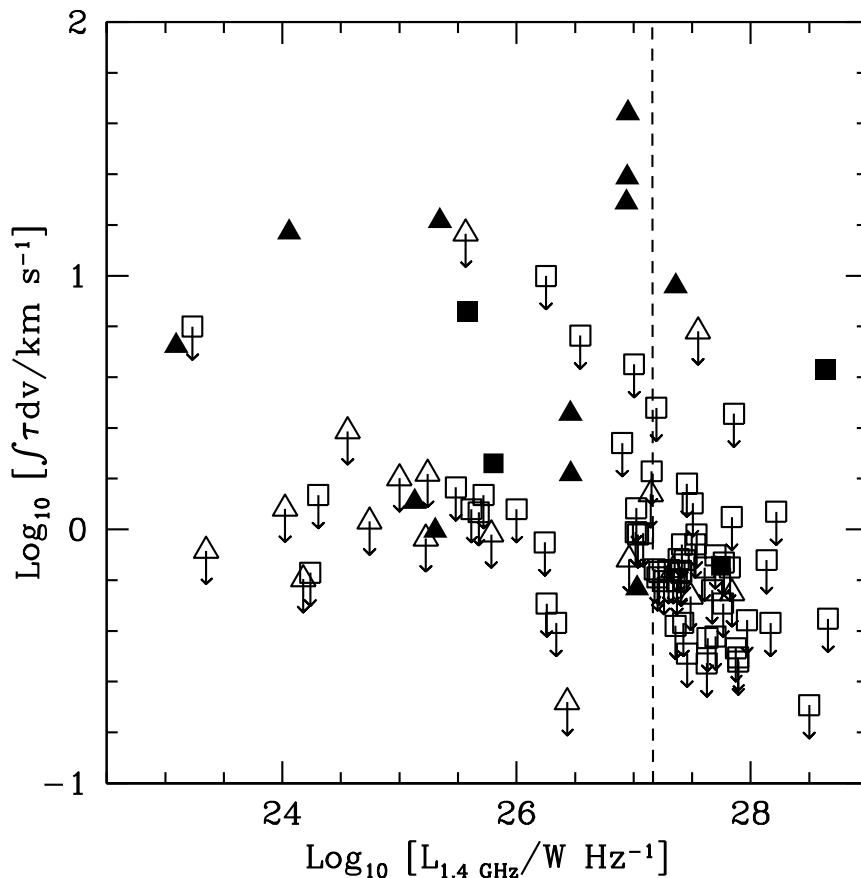


Figure 6.8: The integrated HI 21 cm optical depths of the full CJF sample of 92 sources plotted against the rest-frame 1.4 GHz radio luminosities. The dashed vertical line indicates the median radio luminosity, $L_{1.4 \text{ GHz}, med} = 10^{27.17} W \text{ Hz}^{-1}$. The sources from our observations and from the literature are represented by squares and triangles, respectively. Filled and open symbols represent detections and upper limits on the HI 21 cm optical depth, respectively.

6. DISCUSSION

obscure a significant fraction of the total radio flux density, yielding a low covering factor and hence a low apparent HI 21 cm optical depth. In this section, we consider the possibility that the covering factor may be very different in different AGNs, with values significantly different from unity.

We note, at the outset, that our results that suggest either redshift evolution and/or AGN luminosity dependence in the HI 21 cm optical depth are unchanged if *all* the AGNs have low covering factors. Further, if only the low- z AGNs have low covering factors, then their HI 21 cm optical depths would have been under-estimated due to the assumption of $f = 1$. Low covering factors for the low- z AGNs would hence *increase* the significance of the observed redshift evolution and AGN luminosity dependence of the HI 21 cm optical depth. We hence consider three other possibilities: (1) AGNs at all redshifts have random covering factors, uniformly distributed between 0 and unity, (2) low- z AGNs have high covering factors, $f \approx 1$, while high- z AGNs have random covering factors, uniformly distributed between 0 and unity, and (3) low- z AGNs have high covering factors, $f \approx 1$, while high- z AGNs have systematically low covering factors, $f \approx 0.1$.

In the first scenario, in which AGNs at all redshifts have random covering factors lying between 0 and 1, a Peto-Prentice test finds that the null hypothesis that the low- z and high- z sub-samples are drawn from the same distribution is rejected at 3.0σ significance, while it is rejected at 3.3σ significance when the tentative detection towards TXS 0604+728 is excluded from the full sample. These results are very similar to the case in which a uniform covering factor of unity is assumed for all the sources. Further, a Peto-Prentice test finds that the hypotheses that the two sub-samples in the low and high UV luminosity regimes are drawn from the same distribution are rejected at 3.5σ (retaining TXS 0604+728) and 3.8σ (excluding TXS 0604+728) significance. Similarly, the test also rejects the hypotheses that the two sub-samples at low and high 1.4 GHz radio luminosities are drawn from the same distribution at 3.2σ (retaining TXS 0604+728) and 3.5σ (excluding TXS 0604+728) significance. Hence, it is clear that there is no significant change in the results if random covering factors, lying between 0 and 1, are assumed for the AGNs instead of a uniform value of unity.

In the second scenario, we assume random covering factors between 0 and 1 for the AGNs at high redshifts, at $z > 1$, while the low- z AGNs are assumed to have a high covering factor, $f \approx 1$. Here, the null hypotheses that the low- z and high- z sub-samples

6.1 The Caltech-Jodrell Bank Flat-Spectrum sample

are drawn from the same distribution are rejected at 2.2σ (retaining TXS 0604+728) and 2.3σ (excluding TXS 0604+728) significance. The hypotheses are rejected at 3.0σ (retaining TXS 0604+728) and 3.1σ (excluding TXS 0604+728) significance for the high and low UV luminosity sub-samples. Finally, for the sub-samples at low and high radio luminosities, the hypotheses are rejected at 2.5σ (retaining TXS 0604+728) and 2.6σ (excluding TXS 0604+728) significance. While the statistical significance at which the null hypotheses are rejected is somewhat lower than for the case of unity covering factors, it appears clear that the results here are not significantly different.

Finally, in the third scenario, we assume $f \approx 1$ for all low- z AGNs, and $f \approx 0.1$ (i.e. a low covering factor) for all high- z AGNs. Here, the null hypotheses that the low- and high- z sub-samples are drawn from the same underlying distribution are rejected at far lower statistical significance, 0.8σ (retaining TXS 0604+728) and 1.0σ (excluding TXS 0604+728) significance. Similarly, in the case of UV luminosity sub-samples, the hypotheses are rejected at $\approx 1.9\sigma$ and $\approx 2.0\sigma$ significance, when retaining and excluding TXS 0604+728, respectively. Finally, in the case of radio luminosity sub-samples, the hypotheses are rejected at $\approx 1.2\sigma$ and $\approx 1.4\sigma$ significance, when retaining and excluding TXS 0604+728, respectively. Thus, if the high- z AGNs indeed have systematically lower covering factors than the low- z AGNs, the evidence for redshift evolution and UV/radio luminosity dependence in the HI 21 cm optical depths is not statistically significant.

Hence, to test if the high redshift AGNs indeed have low covering factors, we have examined the distribution of low-frequency spectral indices, $\alpha_{21\text{ cm}}$, computed around the redshifted HI 21 cm line frequencies (see Section 6.1.3), as a function of redshift. We assume that the low-frequency spectral index can be treated as a proxy for the covering factor: AGNs with extended radio structure would typically have $\alpha_{21\text{ cm}} < -0.5$, while compact AGNs would have $\alpha_{21\text{ cm}} \gtrsim 0$. Figure 6.9 plots the low-frequency spectral index $\alpha_{21\text{ cm}}$ against redshift, for the 92 sources of our sample. If the high- z AGNs systematically have extended radio structure and hence, low covering factors, the spectral indices at high redshifts should typically be $\lesssim -0.5$. However, no such bias is apparent in the figure. In fact, when the low- z and high- z sub-samples are separated at the median redshift of $z = 1.2$, the null hypothesis that they are drawn from the same distribution is ruled out at only $\approx 1.2\sigma$ significance by a Gehan-Wilcoxon two-sample test. The spectral indices of the high- z and low- z sub-samples thus appear consistent

6. DISCUSSION

with being drawn from the same underlying distribution. It hence appears unlikely that the high- z AGNs of our sample have systematically lower covering factors than their low- z counterparts.

In summary, our results suggesting that the HI 21 cm optical depths depend on the AGN redshift and/or the radio/UV luminosity appear to be robust in the two cases where we have assumed random covering factors for all sources, and random covering factors for the high- z sample, with $f = 1$ for the low- z systems. The sole scenario in which the null hypothesis that the AGN sub-samples are drawn from the same distribution is not rejected at $\gtrsim 3\sigma$ significance is one in which the high- z AGNs have systematically (and significantly) lower covering factors than the low- z AGNs. However, this scenario appears quite unlikely since there is no significant difference between the low-frequency spectral indices of the low- z and high- z sub-samples, which is likely to have arisen if the two sub-samples indeed had very different covering factors. We hence conclude that our results do not appear to strongly depend on the assumption that the AGNs of our sample have a uniform covering factor of unity.

6.1.6 Dependence on the R-K colour

As discussed earlier in Section 5.1.2, Webster et al. (1995) have pointed out that, for red quasars, the redder colours seen in the optical wavebands as compared to the near-infrared ones could be caused by dust extinction. However, it has also been noted in the literature that not all red quasars are dusty systems (e.g. Benn et al., 1998). While Carilli et al. (1998a) detected associated HI 21 cm absorption in four red quasars out of a target sample of five, providing support for the dust reddening hypothesis, their sample size is very small and limited to intermediate redshifts, $z \approx 0.7$. We have hence obtained the (R-K) colours (see Tables 6.1 and 6.2) of the AGNs in our CJF sample, to test the dust reddening hypothesis. Unfortunately, near-infrared data were available for only 58 of the 92 systems of the sample, and our analysis is hence limited to these 58 systems.

Figure 6.10 shows the integrated HI 21 cm optical depth plotted versus (R-K) colour for the above 58 AGNs. Of the 12 AGNs with HI 21 cm detections, five have relatively red colours, $(R-K) > 3$. Further, 3 of these five systems lie at the top right of the figure, indicating both red colours and high integrated HI 21 cm optical depths: for

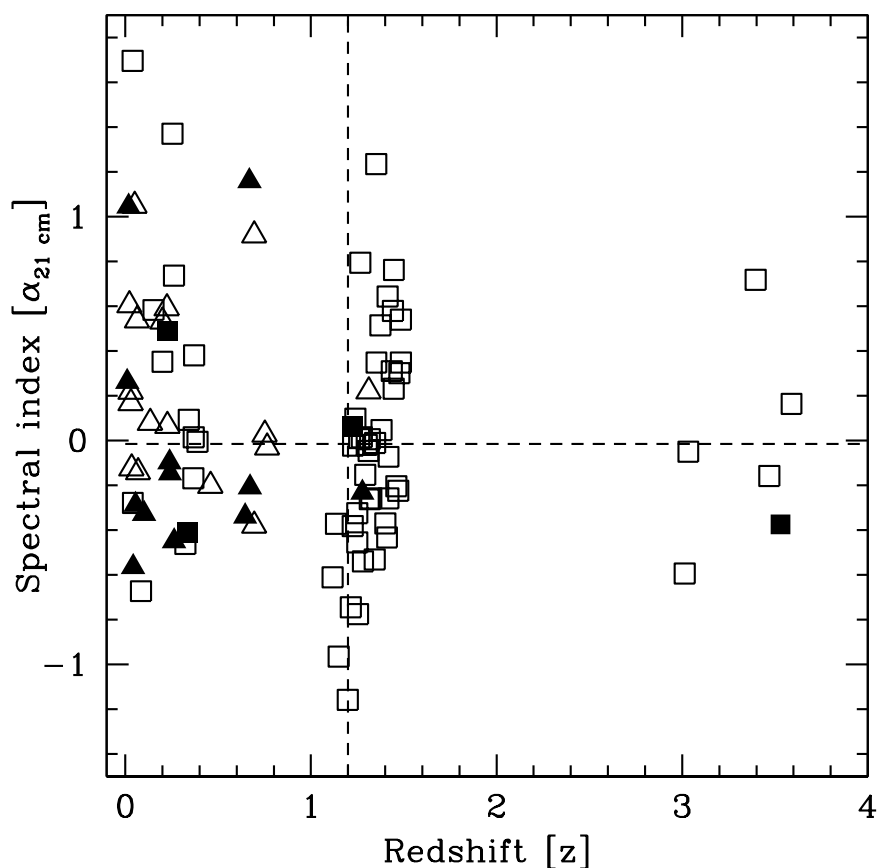


Figure 6.9: The low-frequency spectral index $\alpha_{21\text{ cm}}$, computed around the redshifted HI 21 cm line frequency, plotted as a function of redshift. The 63 sources from our observations and the 29 sources from the literature are plotted as squares and triangles, respectively. The dashed vertical line indicates the median redshift, $z_{med} = 1.2$, and the dashed horizontal line indicates the median spectral index, $\alpha_{21\text{ cm}} = -0.015$.

6. DISCUSSION

these systems, the red colours are likely to arise due to the presence of high columns of gas and associated dust at the AGN redshift.

To test the dependence of the strength of the HI 21 cm absorption on the (R-K) colour, we divided the sample of 58 systems at the median (R-K) value of 2.38, and carried out two-sample tests on the high-(R-K) and low-(R-K) sub-samples. A Peto-Prentice two-sample test for censored data finds that the null hypothesis that the sub-samples are drawn from the same underlying distribution is rejected at only 1.4σ significance. The two sub-samples are thus consistent with being drawn from the same distribution, and we find no statistically significant evidence for a dependence of the strength of HI 21 cm absorption on the (R-K) colour of the AGN. Our results based on the CJF sample thus do not provide support for the dust-reddening hypothesis. We will return to this issue at the end of this chapter, carrying out the same analysis on the combined CJF and GPS samples.

6.2 The Gigahertz Peaked Spectrum sample

As mentioned in Chapter 2, besides the primary survey in flat-spectrum sources, we also undertook a secondary survey for associated HI 21 cm absorption in GPS sources. We constructed a sample of 58 GPS sources, of which 23 sources had previous searches for HI 21 cm absorption available in the literature. As described in Chapter 3, we searched 12 GPS sources for associated HI 21 cm absorption using GMRT; seven of these yielded usable HI 21 cm spectra.

Table 6.3 gives the relevant details of our 7 GMRT targets; the columns of this table are (1) the AGN name, (2) the AGN redshift, (3) the integrated HI 21 cm optical depth, or, for non-detections, the 3σ upper limit to this quantity, assuming a Gaussian profile with a line FWHM of 100 km s^{-1} , (4) the logarithm of the AGN luminosity L_{UV} (in $W \text{ Hz}^{-1}$) at a rest-frame wavelength of 1216 \AA , i.e. $L'_{\text{UV}} = \text{Log}[L_{\text{UV}}/(W \text{ Hz}^{-1})]$, (5) the logarithm of the AGN luminosity $L_{1.4 \text{ GHz}}$ (in $W \text{ Hz}^{-1}$) at a rest-frame frequency of 1.4 GHz , i.e. $L'_{1.4 \text{ GHz}} = \text{Log}[L_{1.4 \text{ GHz}}/(W \text{ Hz}^{-1})]$, (6) the low-frequency spectral index of the AGN, between the redshifted HI 21 cm line frequency and the nearest frequency with a flux density estimate in the literature (usually 1.4 GHz , from the FIRST or NVSS surveys; Becker et al. (1995); Condon et al. (1998)), (7) the AGN colour (R-K) between the R- and the K-bands, (8, 9) the two UV/optical wavebands

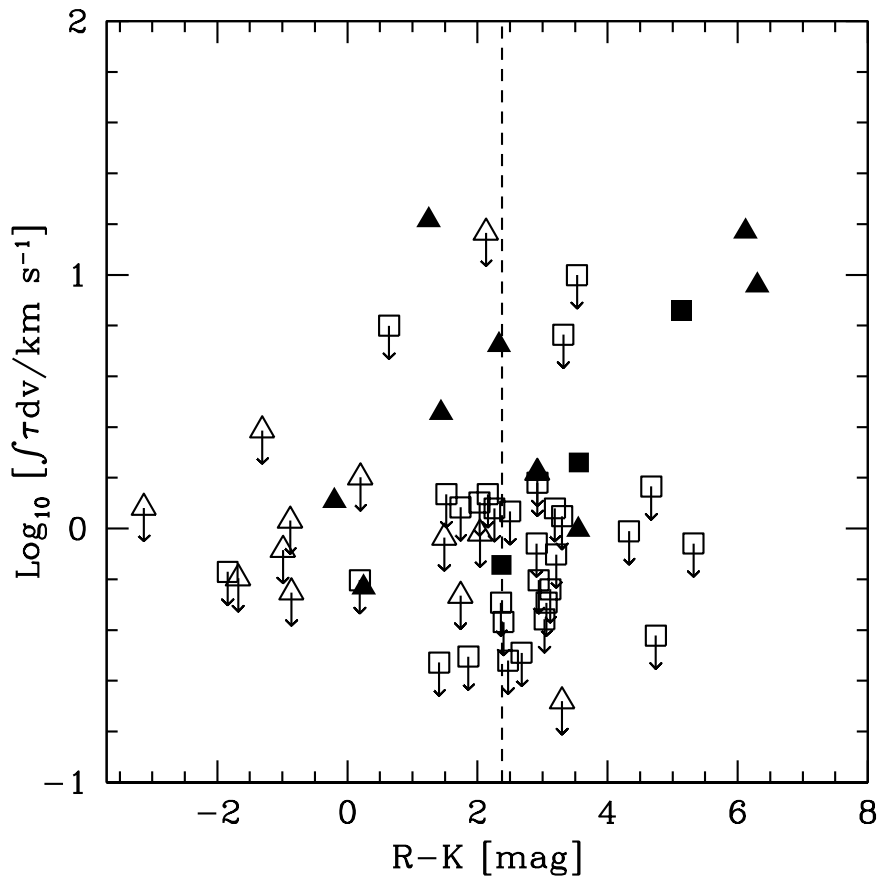


Figure 6.10: The HI 21 cm optical depth, in logarithmic units, plotted against (R-K) colour. The dashed vertical line indicates the median colour of 2.38. The sources from our observations are represented as squares, while those from the literature are represented as triangles. The HI 21 cm absorption detections are shown as filled symbols and non-detections as open symbols.

6. DISCUSSION

and the measured magnitudes therein, that were used to infer the AGN rest-frame 1216 Å UV luminosity, (10) Ref. UV, the references for the optical/UV luminosities that were used to infer the rest-frame 1216 Å luminosity, and (11) Ref. RK, the references for the R- and K-band magnitude measurements. Similar details for the 23 sources of the literature are listed in Table 6.4; here, the first nine columns are the same as in Table 6.3. The remaining columns are (12) Ref. HI, the references for searches for associated HI 21 cm absorption in the literature, (13) Ref. UV, the references for the optical/UV luminosities that were used to infer the rest-frame 1216 Å luminosity, and (14) Ref. RK, the references for the R- and K-band magnitude measurements.

While the sample of GPS sources with HI 21 cm absorption studies is relatively small, just 30 systems, we examined the sample for trends with redshift, UV/radio luminosity, and low-frequency spectral index. Figure 6.11 plots the integrated HI 21 cm optical depth of the 30 GPS sources against redshift. It is clear that the bulk of the sample is at very low redshifts; indeed, the median redshift of the GPS sample is $z_{med} = 0.23$. Using this median redshift to divide the sample into low- z and high- z sub-samples, a Peto-Prentice two-sample test finds that the null hypothesis that the two sub-samples are drawn from the same distribution is rejected at only $\approx 1.6\sigma$ significance. We thus find no significant evidence for redshift evolution; this is perhaps not surprising, given the fact that most of the targets are at very low redshifts (22 of the 30 AGNs have $z \leq 0.42$). We also do not find statistically significant evidence that the HI 21 cm optical depths depend on either the rest-frame 1216 Å UV or rest-frame 1.4 GHz radio luminosities. Dividing the sample at the median UV and radio luminosities into low- and high-luminosity sub-samples (see Figures 6.12 and 6.13), the null hypothesis that the two sub-samples are drawn from the same underlying distribution is rejected at $\approx 1.3\sigma$ (UV) and $\approx 0.9\sigma$ (radio) significance. We thus do not find significant evidence that the strength of the HI 21 cm absorption in GPS sources depends on the AGN UV/radio luminosity. Again, we emphasize that our present GPS sample is dominated by low-redshift, low-luminosity AGNs, and is also relatively small; it is hence not best-suited to probe the dependence of the strength of HI 21 cm absorption on redshift or luminosity.

Table 6.3: The sample of 7 GPS sources searched for HI 21 cm absorption using the GMRT, listed in order of increasing redshift. Note that $L'_{UV} = \text{Log}[L_{UV} / \text{W Hz}^{-1}]$ and $L'_{1.4 \text{ GHz}} = \text{Log}[L_{1.4 \text{ GHz}} / \text{W Hz}^{-1}]$.

Source	z	$\int \tau dv^a$ km s $^{-1}$	L'_{UV}^b	$L'_{1.4 \text{ GHz}}^c$	$\alpha_{21 \text{ cm}}^d$	R-K ^e mag	Band 1 ^f mag	Band 2 ^f mag	Ref. ^g UV	Ref. ^h RK
B3 0801+437	0.123	<0.58	19.70	25.13	0.61	1.4	NUV=22.7	B=17.8	1,2	2,7
TXS 1819+671	0.221	<0.85	20.60	25.67	-0.27	0.7	NUV=22.1	B=18.9	1,2	2,7
TXS 1108+201	0.299	<0.44	19.90	26.48	0.38	2.9	u=21.8	g=20.9	4,4	2,7
TXS 0507+179	0.416	<0.41	21.56	26.31	-0.70	–	B=20.2	R=19.0	2,2	–
TXS 2121-014	1.158	<0.38	21.53	27.84	-0.39	–	NUV=23.9	R=23.3	1,5	–
TXS 1200+045	1.226	2.52 ± 0.12	23.21	27.80	-0.15	2.7	NUV=20.4	u=18.9	1,3	5,8
TXS 1245-197	1.275	4.530 ± 0.062	22.44	28.52	-0.43	–	NUV=22.1	B=21.8	1,6	–

Notes:

^aThe column shows the integrated HI 21 cm optical depth or, for HI 21 cm non-detections, the 3σ limit to the HI 21 cm optical depth, in km s $^{-1}$, assuming a line FWHM of 100 km s $^{-1}$.

^bThe column shows the inferred 1216 Å UV luminosities, obtained by extrapolating from measurements in two nearby optical bands (following the procedure of Curran and Whiting (2010)).

^cThe column shows the rest-frame 1.4 GHz radio luminosities.

^d $\alpha_{21 \text{ cm}}$ is the AGN spectral index at frequencies around the redshifted AGN HI 21 cm line frequency.

^eFor sources with “–” entries, flux densities are not known in the infrared waveband; the (R-K) colour hence could not be obtained.

^fThe measurements at the two UV/optical bands that were used to infer the 1216 Å UV luminosities.

^{g,h}References for the ultraviolet, optical and infrared band measurements, that were used to obtain the inferred 1216 Å UV luminosities (following the procedure of Curran and Whiting (2010)), and the R-K magnitudes : (1) Bianchi et al. (2014), (2) Monet et al. (2003), (3) Abazajian et al. (2005), (4) Adelman-McCarthy et al. (2008), (5) de Vries et al. (2007), (6) Flesch (2015), (7) Cutri et al. (2013), (8) Lawrence et al. (2007).

^gThe first and second entries correspond to the 1st and 2nd UV/optical bands, respectively.

^hThe first and second entries correspond to the R and K bands respectively.

Note: The typical uncertainties on measurements in the different UV, optical and near-IR wavebands are (1) 0.1 mag (NUV), (2) 0.2 mag (FUV), (3) 0.05 mag (u), (4) 0.3 mag (B), (5) 0.2 mag (V), (6) 0.3 mag (R).

6. DISCUSSION

Further, we find no evidence for the dependence of HI 21 cm absorption strength on the low-frequency spectral index, $\alpha_{21\text{ cm}}$. Figure 6.14 plots the integrated HI 21 cm optical depth of the 30 GPS sources against $\alpha_{21\text{ cm}}$. Upon dividing the sample at the median spectral index of $\alpha_{21\text{ cm}} = 0.0$, the null hypothesis that the two sub-samples, separated at the median $\alpha_{21\text{ cm}}$, are drawn from the same distribution is rejected at $\approx 0.7\sigma$ significance. Also, we do not find any bias in the distribution of $\alpha_{21\text{ cm}}$ as a function of redshift, in our GPS sample. Figure 6.15 plots the low-frequency spectral index, $\alpha_{21\text{ cm}}$, as a function of redshift, for the 30 GPS sources. When the low- z and the high- z sub-samples are separated at the median redshift of $z = 0.23$, the null hypothesis that they are drawn from the same distribution is ruled out at only $\approx 1.6\sigma$ significance by a Gehan-Wilcoxon two-sample test. Hence, we conclude that we find neither significant evidence for the dependence of the strength of HI 21 cm absorption on the low-frequency spectral index, nor a redshift bias in the low-frequency spectral index, for our sample of 30 GPS sources.

Finally, we also do not find any significant evidence for the dependence of HI 21 cm absorption strength on the (R-K) colour of the GPS sources of our sample. Figure 6.16 plots the integrated HI 21 cm optical depth as a function of (R-K) colour, for the 30 GPS sources. Dividing the sample at the median (R-K) colour of 2.0, the null hypothesis that the low-(R-K) and high-(R-K) sub-samples are drawn from the same underlying distribution is rejected at $\approx 1.9\sigma$ significance. Hence, the two sub-samples appear consistent with being drawn from the same underlying distribution. We note, however, that it is difficult to test the above hypothesis with the present, rather small, GPS sample.

Table 6.4: The 23 GPS sources with HI 21 cm absorption searches available in the literature, listed in order of increasing redshift. Note that $L'_{UV} = \text{Log}[L_{UV} / \text{W Hz}^{-1}]$ and $L'_{1.4 \text{ GHz}} = \text{Log}[L_{1.4 \text{ GHz}} / \text{W Hz}^{-1}]$.

Source	z	$\int \tau dv^a$ km s $^{-1}$	L'_{UV}^b	$L'_{1.4 \text{ GHz}}^c$	$\alpha_{21 \text{ cm}}^d$	R-K ^e mag	Band 1 ^f mag	Band 2 ^f mag	Ref. ^g HI	Ref. ^h UV	Ref. ⁱ RK
TXS 0116+319	0.060	5.92 ± 0.13	18.85	25.29	-0.22	-2.1	NUV=20.5	B=16.7	5	1,2	2,2
B3 1315+415	0.066	2.10 ± 0.33	19.08	24.38	0.51	-1.6	NUV=21.7	u=20.1	4	1,5	2,3
TXS 1404+286	0.077	0.84 ± 0.16	20.34	24.98	1.05	-1.7	FUV=20.2	NUV=18.4	7	1,1	2,3
TXS 0902+468	0.085	4.10 ± 0.51	19.00	24.65	-0.07	0.1	u=18.5	g=16.6	4	7,7	2,3
TXS 1946+708 ^j	0.101	15.8 ± 4.6	19.75	25.29	0.60	1.3	B=18.3	R=16.4	10	2,2	2,4
TXS 0729+562	0.104	<0.59	19.30	24.90	-0.20	-0.4	B=16.3	R=13.4	4	2,2	2,3
GB6 J1247+6723	0.107	3.70 ± 0.27	19.78	24.78	0.72	0.5	FUV=22.9	NUV=22.6	2	1,1	2,3
TXS 1345+125	0.122	1.66 ± 0.09	20.30	26.26	-0.39	2.0	NUV=19.7	B=17.0	7	1,8	10, 3
TXS 1601-222	0.141	<1.8	18.99	25.59	-0.03	2.6	B=20.8	R=18.8	7	2,2	10, 12
PKS 1934-63	0.181	0.03 ± 0.01	21.56	26.95	0.63	1.3	NUV=21.8	B=17.2	6	1,2	11,11
PKS 0428+20	0.219	2.0	20.74	26.59	0.20	3.4	B=20.4	R=18.6	1	2,2	2, 12
TXS 2021+614 ^j	0.230	<0.21	20.40	26.34	0.57	3.3	B=19.3	R=17.5	1	2,2	2,3
TXS 0941-080	0.228	<0.69	20.90	26.55	-0.40	2.1	FUV=21.8	NUV=21.6	1	1,1	10,3
TXS 0554-026	0.235	<3.4	20.60	25.92	0.43	4.4	B=18.3	R=16.5	1	2,2	2,3
TXS 2352+495 ^j	0.240	1.7	21.32	26.53	0.05	2.9	B=18.3	V=17.7	1	13,13	2,3
TXS 2050+364	0.354	4.2	22.08	27.10	0.55	-0.2	B=18.0	R=17.2	1	2,2	2,14
TXS 1117+146	0.362	<0.33	18.01	26.92	-0.28	3.3	u=23.9	g=21.8	1	5,5	2,12
TXS 1323+321	0.368	0.41	18.50	27.24	-0.35	4.9	u=22.9	g=20.5	1	5,5	2,3
8C 2342+821	0.735	<0.41	21.36	27.77	-0.27	–	B=21.4	R=20.0	1	2,2	–
TXS 2149+056	0.740	<9.3	22.27	26.86	0.68	–	NUV=22.4	R=20.2	9	1,10	–
TXS 1518+046	1.296	<0.35	21.76	28.17	0.13	4.4	u=23.2	g=23.1	7	9,9	2,12
TXS 2055+055	1.381	<0.78	22.16	28.02	-0.83	–	NUV=23.2	R=23.4	7	1,10	–
TXS 1351-018	3.707	<0.014	23.93	27.98	0.46	–	g=20.2	r=19.3	8	5,5	–

Notes:

^aThe column shows the integrated HI 21 cm optical depth or, for HI 21 cm non-detections, the 3σ limit to the HI 21 cm optical depth, in km s^{-1} , assuming a line FWHM of 100 km s^{-1} .

^bThe column shows the inferred 1216 \AA UV luminosities, obtained by extrapolating from measurements in two nearby optical bands (following the procedure of Curran and Whiting (2010)).

^cThe column shows the rest-frame 1.4 GHz radio luminosities.

^d $\alpha_{21 \text{ cm}}$ is the AGN spectral index at frequencies around the redshifted AGN HI 21 cm line frequency.

^eFor sources with “–” entries, flux densities are not known in the infrared waveband; the (R-K) colour hence could not be obtained.

^fThe measurements at the two UV/optical wavebands that were used to infer the 1216 \AA UV luminosities.

^gReferences for associated HI 21 cm absorption searches: (1) Vermeulen et al. (2003); (2) Saikia et al. (2007); (3) Pihlström et al. (2003); (4) Chandola et al. (2011); (5) van Gorkom et al. (1989); (6) Véron-Cetty et al. (2000); (7) Gupta et al. (2006); (8) Curran et al. (2008); (9) Carilli et al. (1998b); (10) Peck et al. (1999).

^{h,i}References for the ultraviolet, optical and infrared band measurements, that were used to obtain the inferred 1216 \AA luminosities (following the procedure of Curran and Whiting (2010)), and the R-K magnitudes : (1) Bianchi et al. (2014), (2) Monet et al. (2003), (3) Cutri et al. (2003), (4) Fedorov et al. (2011), (5) Abazajian et al. (2009), (6) Healey et al. (2008), (7) Abazajian et al. (2005), (8) Surace and Sanders (2000), (9) Adelman-McCarthy et al. (2008), (10) de Vries et al. (2007), (11) Qi et al. (2015), (12) Lawrence et al. (2007), (13) Zacharias et al. (2004), (14) Lucas et al. (2008), (15) Ellison et al. (2005).

^hThe first and second entries correspond to the 1st and 2nd UV/optical bands, respectively.

ⁱThe first and second entries correspond to the R and K bands respectively.

^jThese sources are also part of our CJF sample.

Note: The typical uncertainties on measurements in the different UV, optical and near-IR wavebands are (1) 0.1 mag (NUV), (2) 0.2 mag (FUV), (3) 0.05 mag (u), (4) 0.3 mag (B), (5) 0.2 mag (V), (6) 0.01 (r), (7) 0.3 mag (R).

6.3 The combined sample of 119 compact AGNs

The primary criterion for selecting the target sources of our CJF and GPS samples was source compactness. In the earlier sections of this chapter, we provided results for the two samples separately. In the present section, we combine the two samples to construct a large (albeit not complete) sample of compact sources with searches for associated HI 21 cm absorption. Our full sample then consists of 119 AGNs, 92 from the CJF sample and 27 from the GPS sample (taking into account the fact that 3 sources are common to the two samples). This is by far the largest sample of compact AGNs that has been searched for associated HI 21 cm absorption so far.

Figure 6.17 displays the integrated HI 21 cm optical depth, in logarithmic units, plotted as a function of redshift. The CJF sources are represented as squares, while the GPS sources are represented as triangles. Filled symbols represent detections of HI 21 cm absorption, while open symbols represent upper limits on the HI 21 cm optical depth. Upon dividing the full sample at the median redshift of $z_{med} = 0.7$, indicated by the dashed vertical line in the plot, a Peto-Prentice two-sample test for censored data finds that the hypothesis that the low- z and high- z sub-samples are drawn from the same underlying distribution is rejected at 4.1σ significance. If the tentative detection of absorption at $z = 3.530$ towards TXS 0604+728 is excluded, the same null hypothesis is rejected at $\approx 4.4\sigma$ significance. This is the strongest evidence so far for redshift evolution in the strength of HI 21 cm absorption in AGN environments.

However, it is again clear, from Figures 6.18 and 6.19, that the AGNs of the high- z sub-sample have significantly higher rest-frame UV and radio luminosities than those of the low- z sub-sample. Separating the data into two sub-samples by the median redshift, $z_{med} = 0.70$, a Gehan-Wilcoxon two-sample test finds the null hypothesis that the two sub-samples are drawn from the same distribution to be rejected at $\approx 9.7\sigma$ significance (UV) and $\approx 10.3\sigma$ significance (radio). It is thus clear that there is a strong bias in the high- z sample towards higher UV and radio luminosities.

Figures 6.20 and 6.21 plot the integrated HI 21 cm optical depths of the AGNs of the sample versus their rest-frame 1216 Å UV and 1.4 GHz radio luminosities, respectively, with the dashed vertical line in each figure indicating the median UV or radio luminosity ($L_{UV,med} = 10^{22.0} W Hz^{-1}$ and $L_{1.4GHz,med} = 10^{27.0} W Hz^{-1}$). A Peto-Prentice two-sample test finds the null hypothesis that the low-luminosity and

6. DISCUSSION

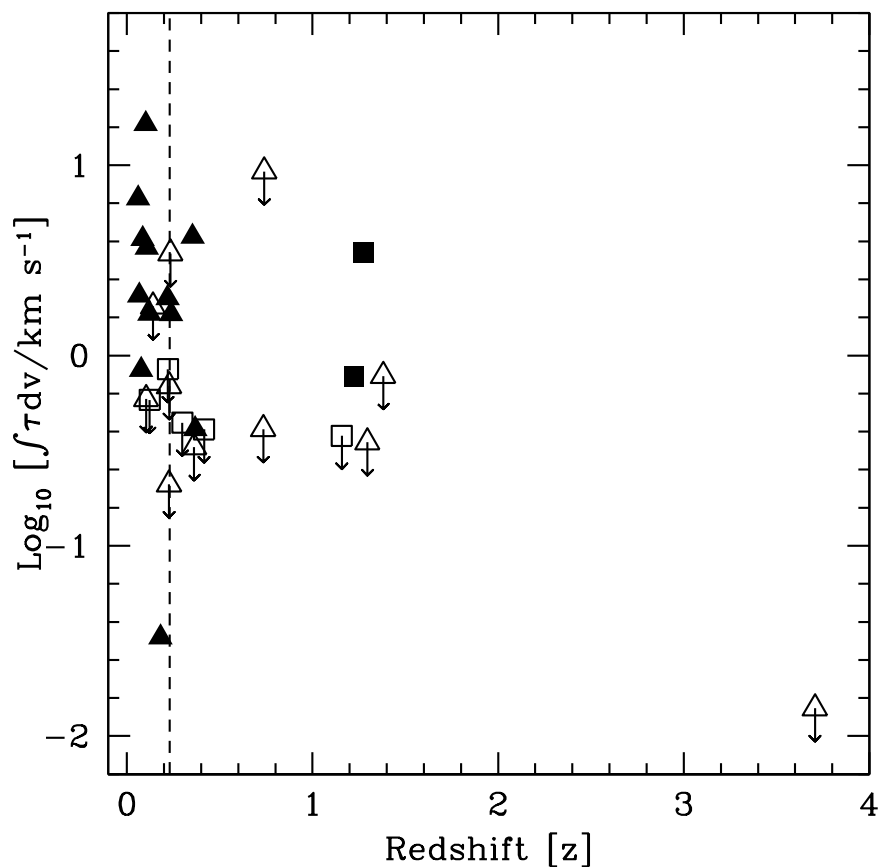


Figure 6.11: The integrated HI 21 cm optical depths of the sample of 30 GPS sources, plotted as a function of redshift. The 7 sources observed by us using the GMRT are represented by squares, and the 23 literature sources are represented by triangles. Filled symbols indicate detections of HI 21 cm absorption, while open symbols indicate upper limits on the HI 21 cm optical depth. The dashed vertical line indicates the median redshift of the sample, $z_{med} = 0.23$.

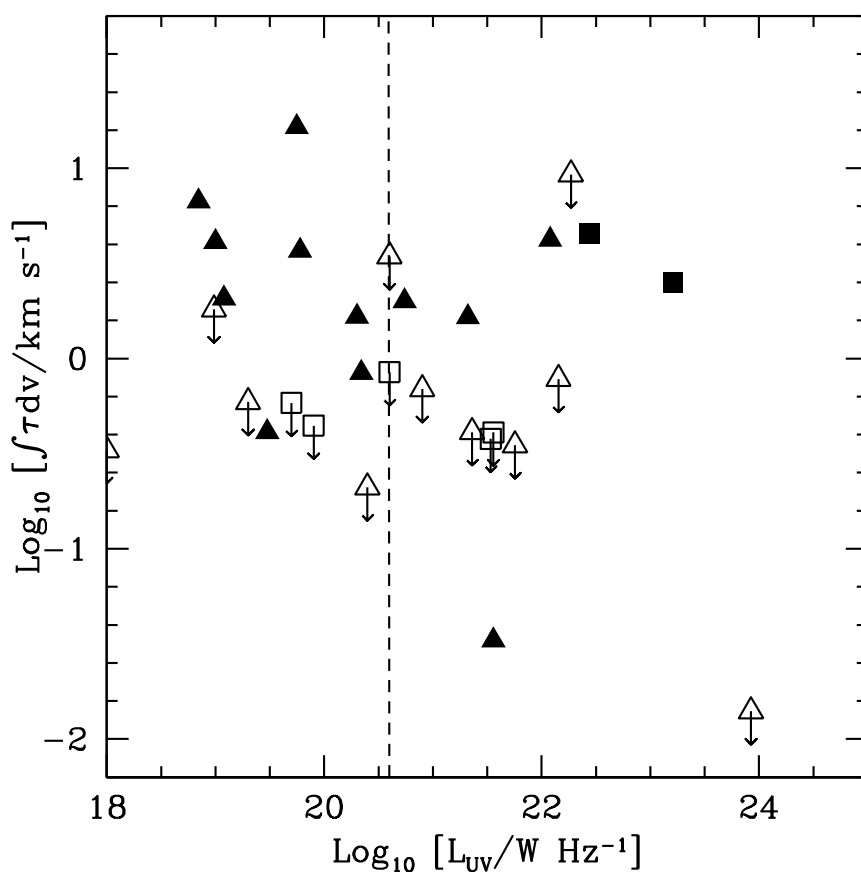


Figure 6.12: The integrated HI 21 cm optical depths plotted against rest-frame 1216 Å UV luminosities, for the sample of 30 GPS sources. The dashed vertical line represents the median UV luminosity of $L_{UV,med} = 10^{20.6} W \text{ Hz}^{-1}$. The squares and triangles in the plots represent the sources from our observations and the sources from the literature, respectively. Filled and open symbols represent detections and upper limits on the integrated HI 21 cm optical depths, respectively.

6. DISCUSSION

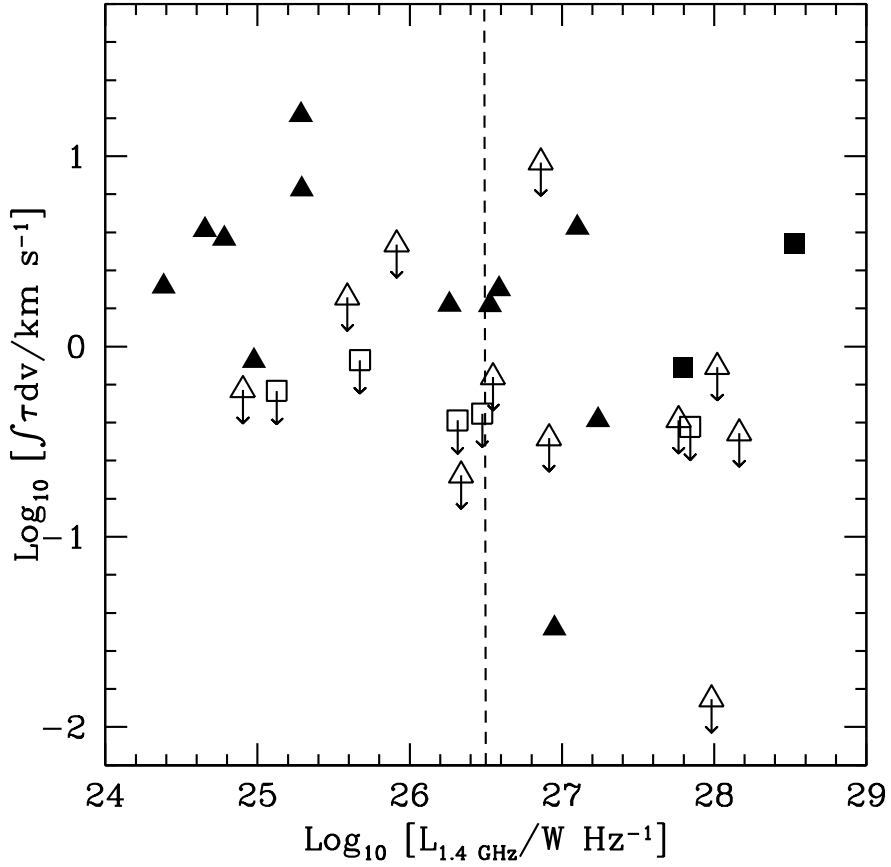


Figure 6.13: The integrated HI 21 cm optical depths plotted against rest-frame 1.4 GHz radio luminosities, for the sample of 30 GPS sources. The dashed vertical line represents the median radio luminosity of $L_{1.4 \text{ GHz}, \text{med}} = 10^{26.5} W \text{ Hz}^{-1}$. The squares and triangles in the plots represent the sources from our observations and the sources from the literature, respectively. Filled and open symbols represent detections and upper limits on the integrated HI 21 cm optical depths, respectively.

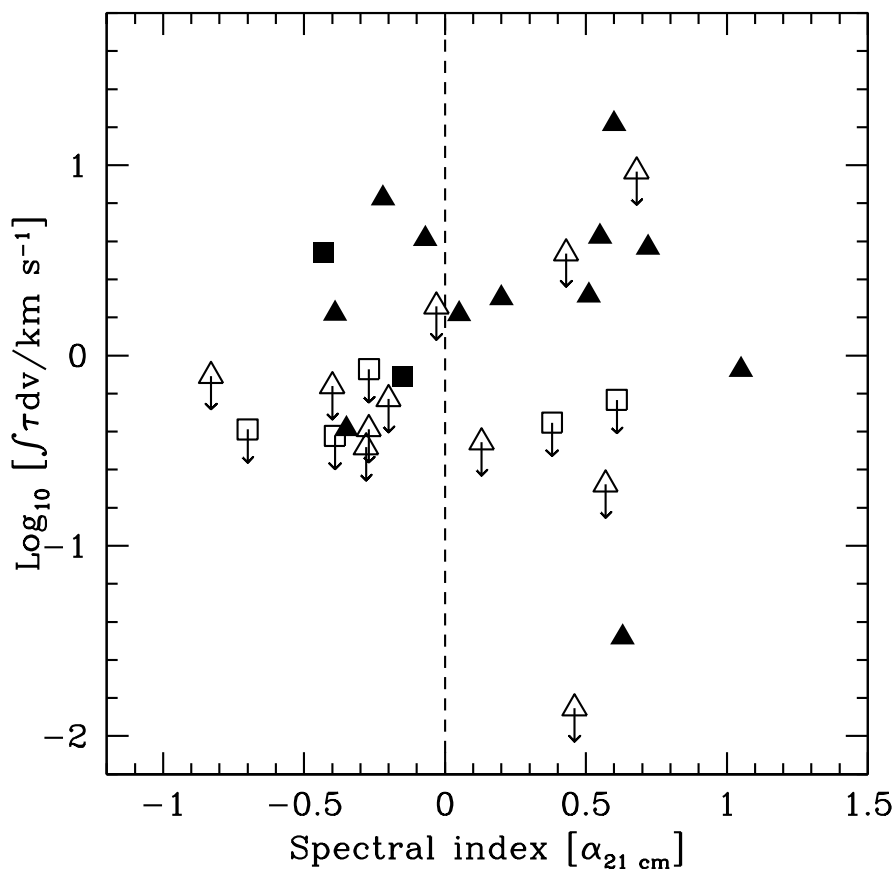


Figure 6.14: The integrated HI 21 cm optical depths, in logarithmic units, plotted against the low-frequency spectral indices, for the sample of 30 GPS sources. The dashed vertical line represents the median spectral index of $\alpha_{21\text{ cm}} = 0.0$. The squares and triangles in the plots represent the sources from our observations and the sources from the literature, respectively. Filled and open symbols represent detections and upper limits on the integrated HI 21 cm optical depths, respectively.

6. DISCUSSION

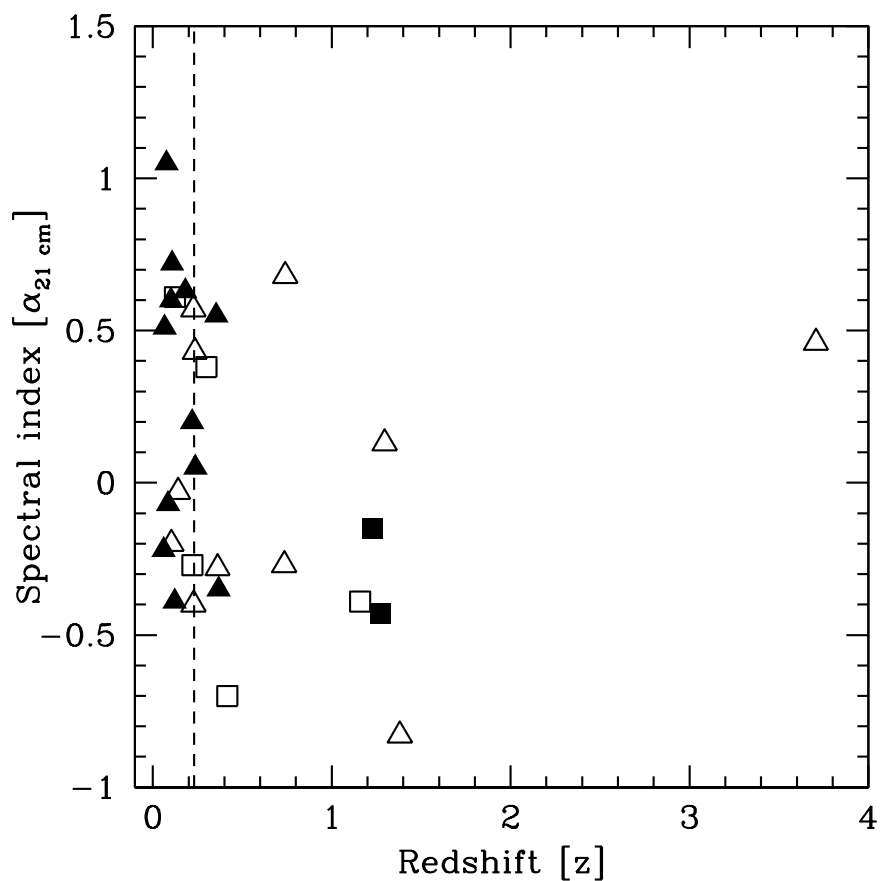


Figure 6.15: The low-frequency spectral index, $\alpha_{21 \text{ cm}}$, plotted as a function of redshift, for the 30 GPS sources. The dashed vertical line represents the median redshift of $z = 0.23$. The squares and triangles in the plots represent the sources from our observations and the sources from the literature, respectively. Filled and open symbols represent detections and upper limits on the integrated H I 21 cm optical depths, respectively.

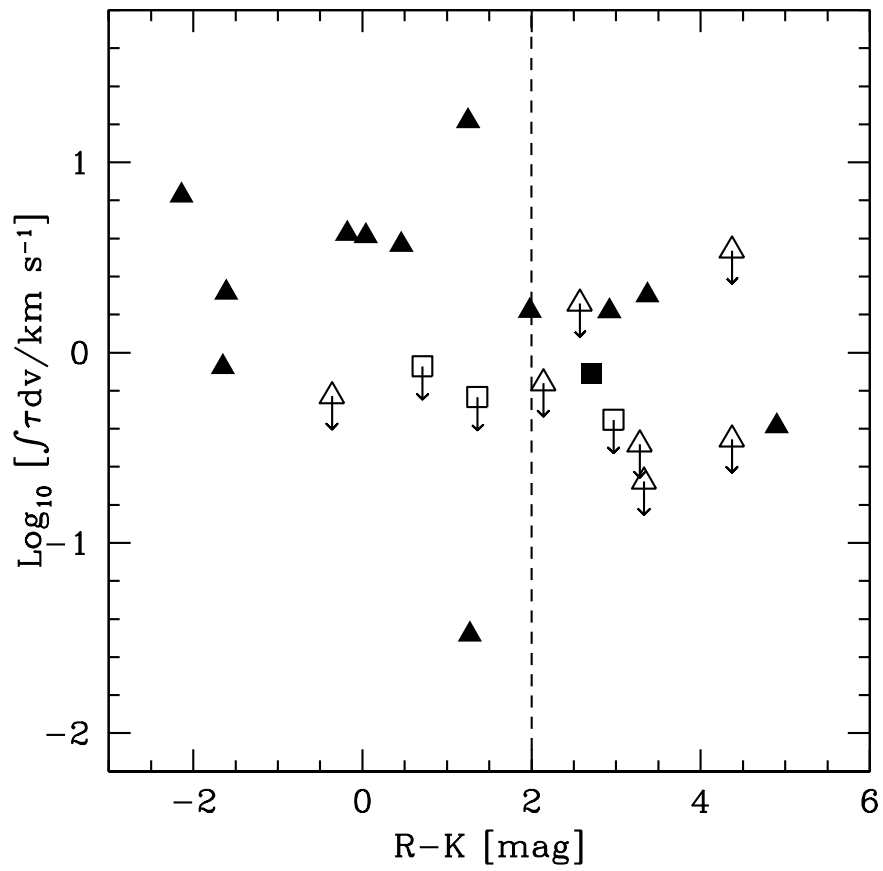


Figure 6.16: The HI 21 cm optical depth, in logarithmic units, plotted against (R-K) colour. The dashed vertical line indicates the median colour of 2.0. The sources from our observations are represented as squares, while those from the literature are represented as triangles. The HI 21 cm absorption detections are shown as filled symbols and non-detections as open symbols.

6. DISCUSSION

high-luminosity sub-samples are drawn from the same distribution to be rejected at $\approx 3.4\sigma$ significance (UV) and $\approx 3.3\sigma$ significance (radio). Excluding the tentative detection towards TXS 0604+728, the null hypothesis in both cases is rejected at $\approx 3.6\sigma$ significance.

Next, the integrated optical depth, in logarithmic units, is plotted against the low radio frequency spectral index, $\alpha_{21\text{ cm}}$, in Figure 6.22. The low radio frequency spectral index acts as a proxy for compactness of the AGN, as discussed in Section 6.1.3. Dividing the full sample at a median spectral index of $\alpha_{21\text{ cm}} = -0.023$, the null hypothesis that the low- $\alpha_{21\text{ cm}}$ and high- $\alpha_{21\text{ cm}}$ sub-samples are drawn from the same distribution is rejected at $\approx 0.9\sigma$ significance. When the single tentative detection towards TXS 0604+728 is excluded from the sample, the null hypothesis is rejected at $\approx 0.7\sigma$ significance. Hence, the two sub-samples are consistent at being drawn from the same underlying distribution. Thus, we find no evidence that the strength of the HI 21 cm absorption depends on the low-frequency radio spectral index. It is thus unlikely that the lower strength of HI 21 cm absorption in the high- z sample has arisen due to the high- z sample being dominated by AGNs with low covering factors. Further, Figure 6.23 plots the low-frequency spectral index against redshift, for the sample of 119 compact AGNs. Dividing the full sample at the median redshift of $z = 0.7$, a Gehan-Wilcoxon two-sample test finds that the null hypothesis that the low- z and high- z sub-samples are drawn from the same distribution is rejected at $\approx 1.9\sigma$ significance. Hence, we do not find strong evidence for a bias in the distribution of the spectral indices as a function of redshift. We conclude that it is unlikely that the high- z AGNs of our sample have systematically lower covering factors than their low- z counterparts.

Finally, Figure 6.24 plots the integrated HI 21 cm optical depth, in logarithmic units, as a function of (R-K) colour for the 78 compact AGNs of our sample for which this colour could be obtained (the near-IR data were not available for the remaining 41 sources). Dividing the sample at the median (R-K) colour of 2.36, the null hypothesis that the low-(R-K) and high-(R-K) sub-samples are drawn from the same distribution is rejected at $\approx 0.9\sigma$ significance. Our results for the full sample of compact AGNs thus do not support the dust-reddening hypothesis.

We thus find that the strength of HI 21 cm absorption in the full sample of 119 compact AGNs shows a statistically significant dependence on redshift, the AGN rest-frame 1216 Å UV luminosity, and the AGN rest-frame 1.4 GHz radio luminosity. While

6.3 The combined sample of 119 compact AGNs

the statistical significance of the redshift dependence is marginally stronger than that of the dependence on the two luminosities, the strong correlation between redshift and luminosity in the present sample means that it is not possible to break the degeneracy between the two possibilities of redshift evolution and high AGN luminosity as the primary cause of the lower strength of associated HI 21 cm absorption in high- z active galactic nuclei.

6. DISCUSSION

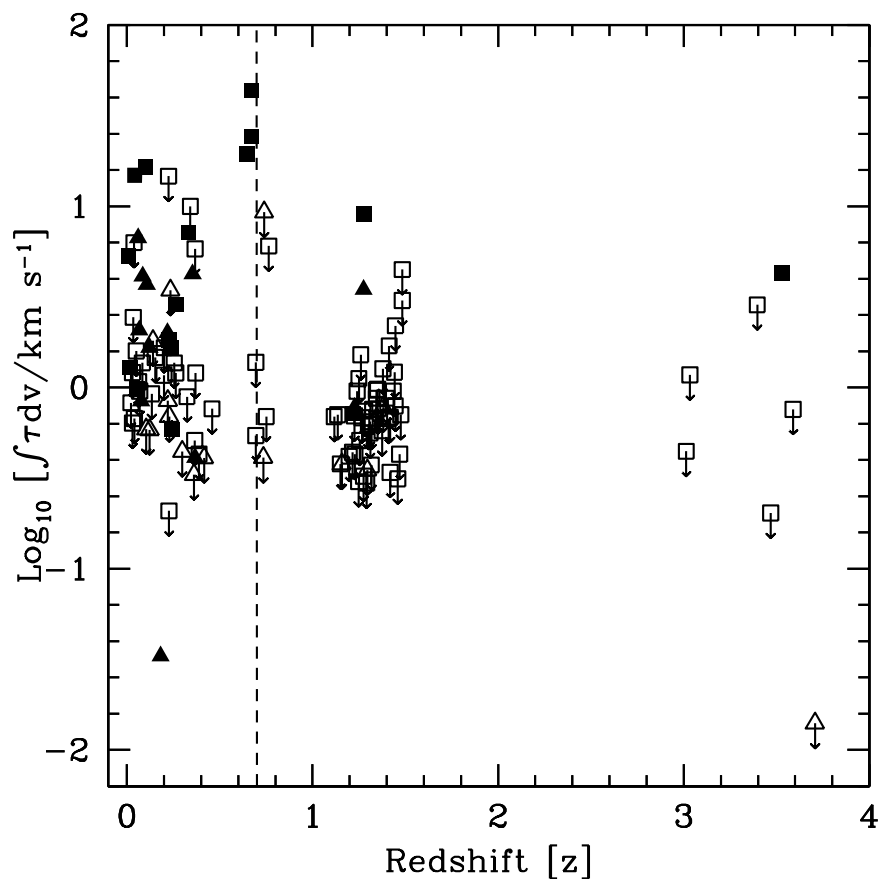


Figure 6.17: The integrated HI 21 cm optical depths of the sample of 119 sources, which includes 92 CJF sources and 27 GPS sources, plotted as a function of redshift. The CJF sources are represented by squares, while the GPS sources are represented as triangles. Filled symbols indicate detections of HI 21 cm absorption, while open symbols indicate upper limits on the HI 21 cm optical depths. The dashed vertical line indicates the median redshift of the sample, $z_{med} = 0.7$.

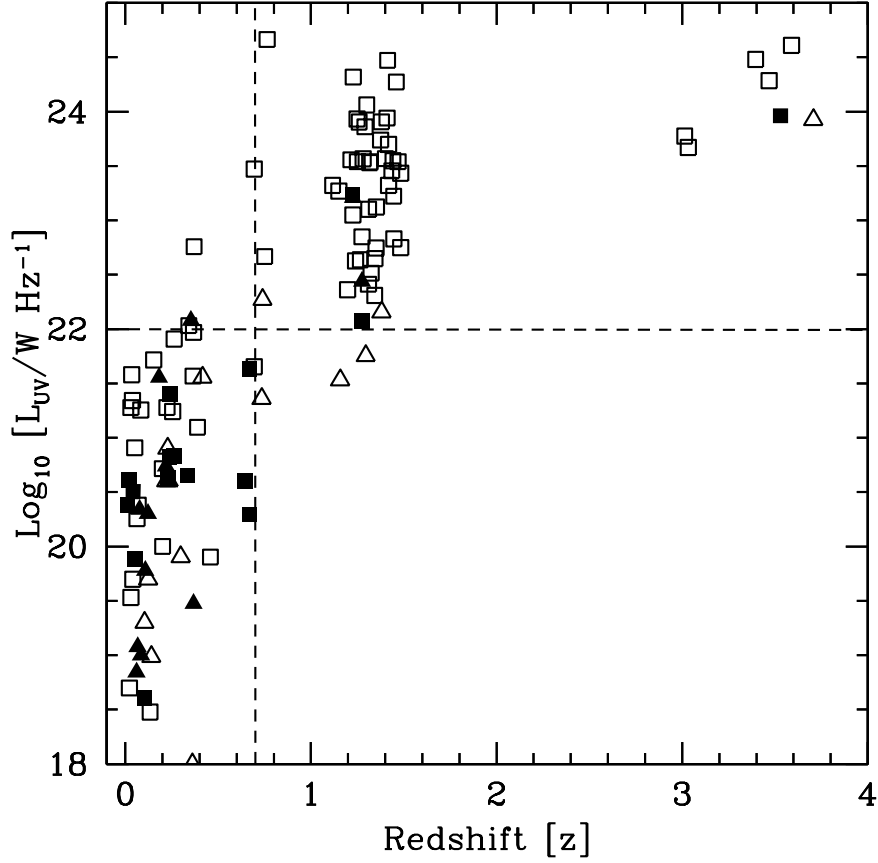


Figure 6.18: The rest-frame 1216 Å UV luminosities of 114 compact sources of the full sample plotted, in logarithmic units, against the AGN redshift. The dashed horizontal line indicates the median UV luminosity, $L_{UV,med} = 10^{22.0} W \text{ Hz}^{-1}$, and the dashed vertical line indicates the median redshift, $z_{med} = 0.7$. The squares and triangles in the plots represent the sources from our observations and the sources from the literature, respectively. Filled and open symbols represent detections and upper limits on the integrated HI 21 cm optical depths, respectively.

6. DISCUSSION

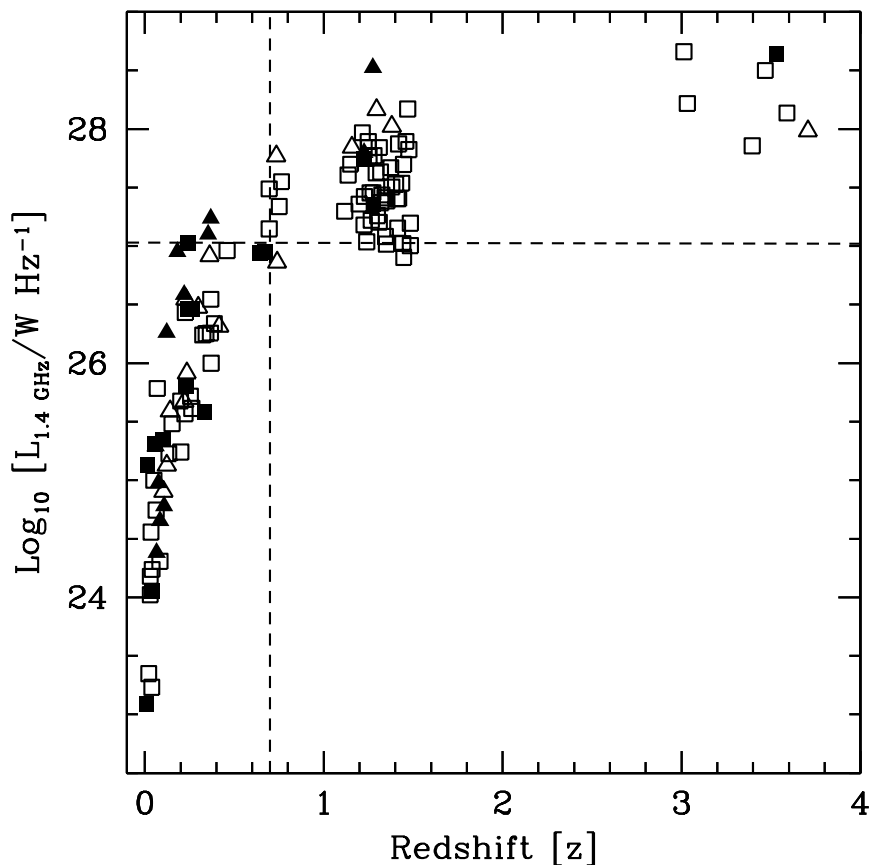


Figure 6.19: The rest-frame 1.4 GHz radio luminosity of the full sample of 119 compact sources, plotted against the redshift. The dashed horizontal line indicates the median radio luminosity, $L_{1.4 \text{ GHz}, med} = 10^{27.03} W \text{ Hz}^{-1}$, and the dashed vertical line indicates the median redshift of $z_{med} = 0.7$. The squares and triangles in the plots represent the sources from our observations and the sources from the literature, respectively. Filled and open symbols represent detections and upper limits on the integrated HI 21 cm optical depths, respectively.

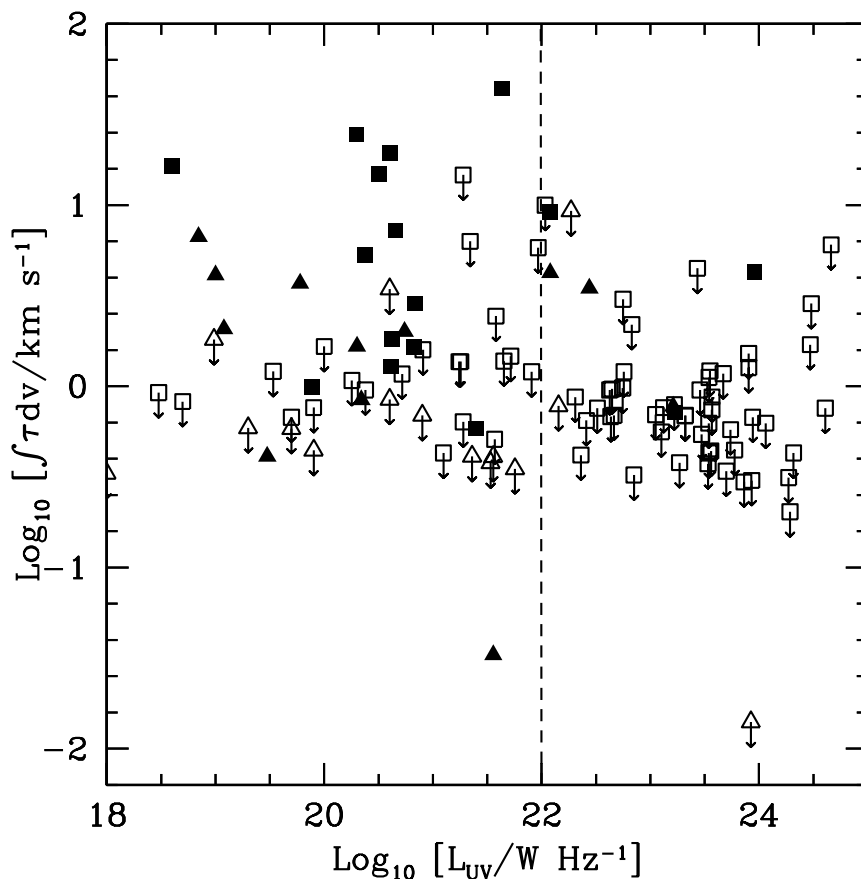


Figure 6.20: The integrated HI 21 cm optical depths of the 114 compact AGNs of our full sample, which includes 87 CJF sources and 27 GPS sources, plotted against their rest-frame 1216Å UV luminosities. The CJF sources are represented by squares, while the GPS sources are represented as triangles. Filled symbols indicate detections of HI 21 cm absorption, while open symbols indicate upper limits on the HI 21 cm optical depth. The dashed vertical line indicates the median UV luminosity of the sample, $L_{UV,med} = 10^{22.0} W Hz^{-1}$.

6. DISCUSSION

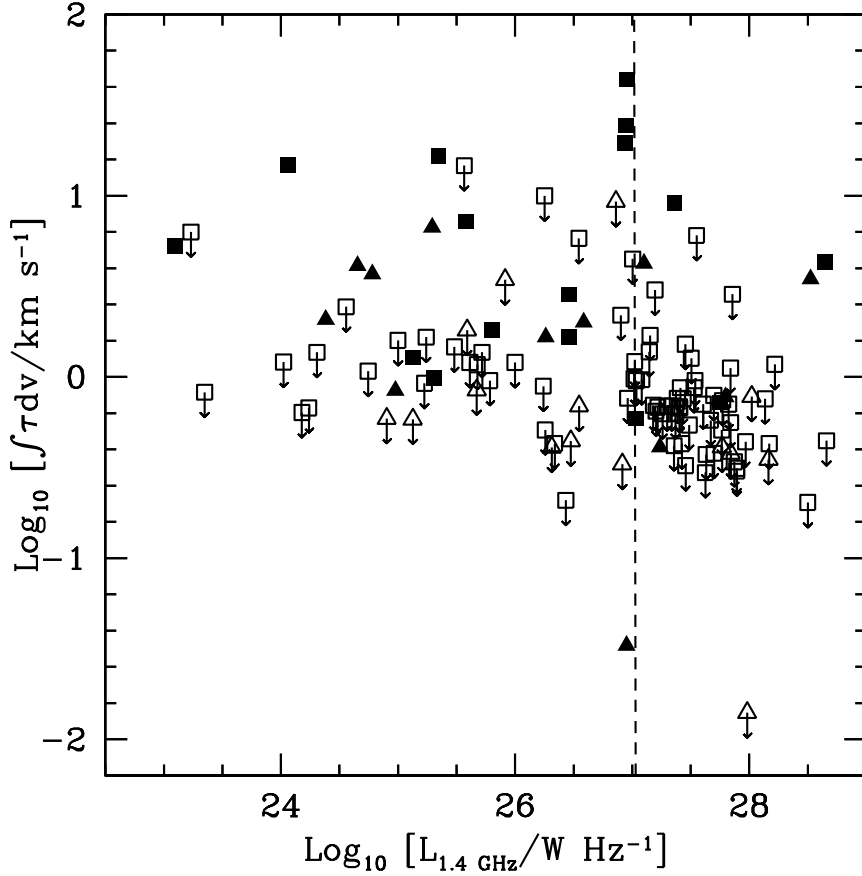


Figure 6.21: The integrated HI 21 cm optical depths of the 119 compact AGNs of our full sample, which includes 92 CJKF sources and 27 GPS sources, plotted against their rest-frame 1.4 GHz radio luminosities. The CJKF sources are represented by squares, while the GPS sources are represented as triangles. Filled symbols indicate detections of HI 21 cm absorption, while open symbols indicate upper limits on the HI 21 cm optical depth. The dashed vertical line indicates the median radio luminosity of the sample, $L_{1.4 \text{ GHz}, \text{med}} = 10^{27.03} W \text{ Hz}^{-1}$.

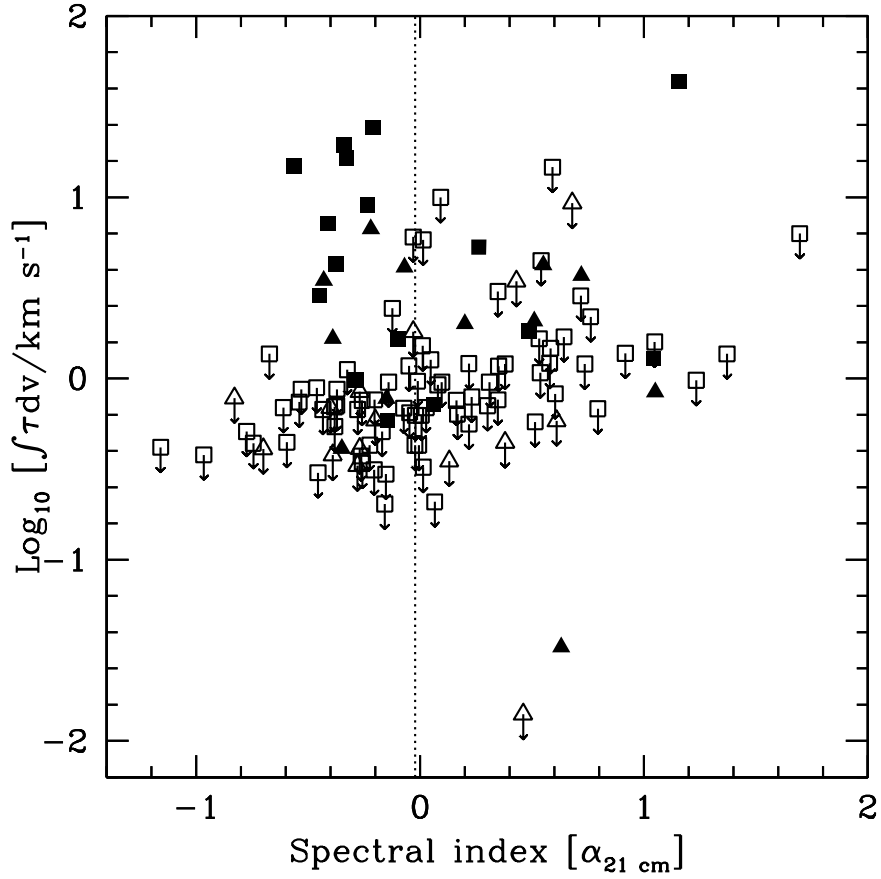


Figure 6.22: The integrated HI 21 cm optical depth plotted as a function of low-frequency spectral index, $\alpha_{21 \text{ cm}}$, for the sample of 119 sources. The CJKF sources are represented by squares, while the GPS sources are represented as triangles. Filled symbols indicate detections of HI 21 cm absorption, while open symbols indicate upper limits on the HI 21 cm optical depth. The dashed vertical line indicates the median spectral index of the sample, $\alpha_{21 \text{ cm}} = -0.023$.

6. DISCUSSION

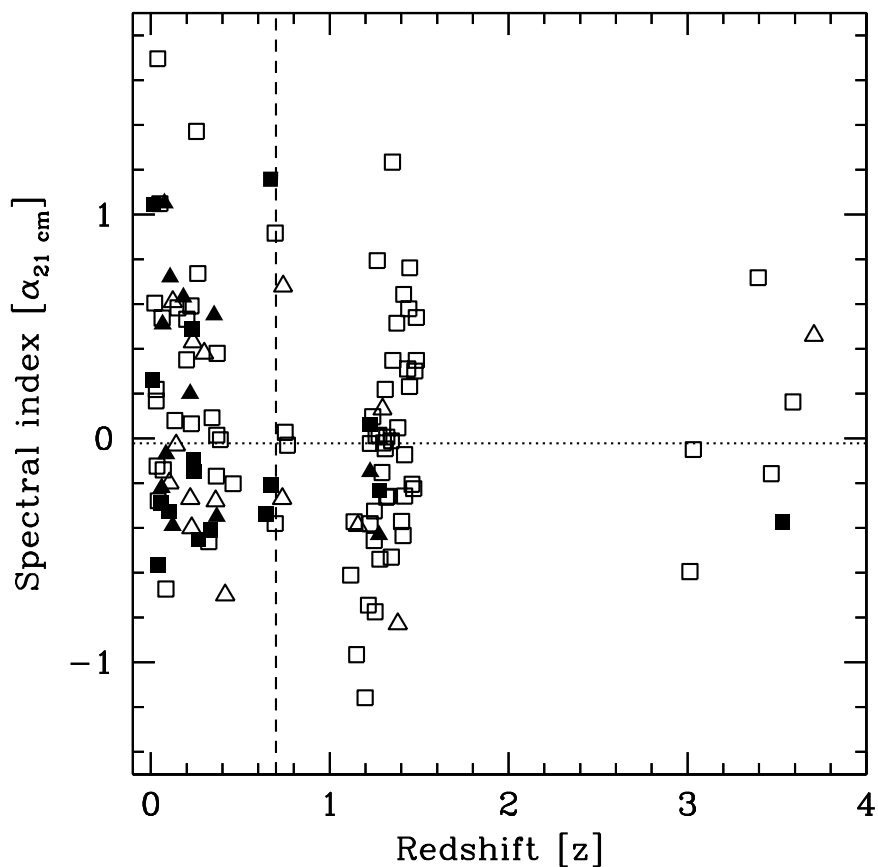


Figure 6.23: The low-frequency spectral index, $\alpha_{21\text{ cm}}$, plotted as a function of redshift for the sample of 119 sources. The CJF sources are represented by squares, while the GPS sources are represented as triangles. Filled symbols indicate detections of HI 21 cm absorption, while open symbols indicate non-detections. The dashed vertical line indicates the median redshift of the sample, $z = 0.7$, while the dotted horizontal line indicates the median low-frequency spectral index of the sample, $\alpha_{21\text{ cm}} = -0.023$

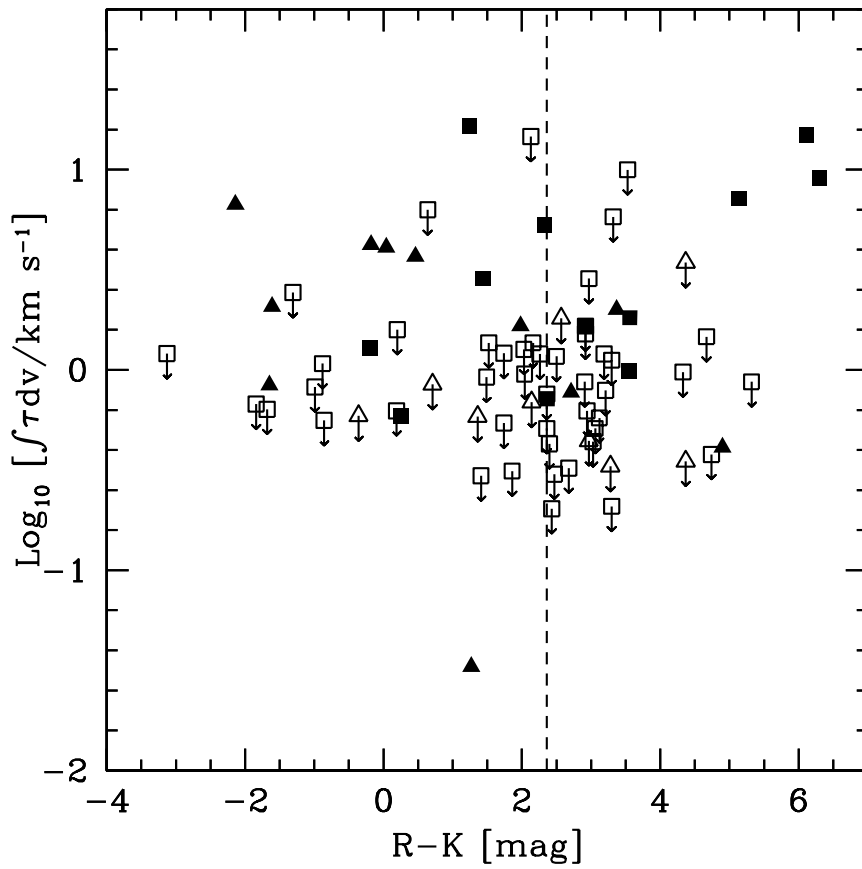


Figure 6.24: The integrated HI 21 cm optical depth, in logarithmic units, plotted against (R-K) colour. The CJF sources are represented by squares, while the GPS sources are represented as triangles. Filled symbols indicate detections of HI 21 cm absorption, while open symbols indicate upper limits on the HI 21 cm optical depth. The dashed vertical line indicates the median (R-K) colour of 2.36.

6. DISCUSSION

7

Summary and Future Work

In this chapter, we provide a summary of the observations carried out, and the new results obtained, during the course of this thesis. We will also discuss new avenues for future research that are indicated by our results.

7.1 GMRT surveys for associated HI 21 cm absorption

This thesis is based on GMRT searches for redshifted associated HI 21 cm absorption in two samples of compact AGNs at a wide range of redshifts. Radio source compactness was used as the primary criterion to select our target sources as gas lying towards compact sources is more likely to cover the background source and hence, to have a higher covering factor, and a higher apparent HI 21 cm optical depth. All searches were carried out using the 1420 MHz, 610 MHz and 325 MHz receivers of the GMRT.

Our primary survey for associated HI 21 cm absorption was of a sample of 74 flat-spectrum AGNs, selected from the Caltech-Jodrell Bank Flat-spectrum (CJF) sample. The CJF sample is a nearly complete sample, with all sources having flux densities ≥ 350 mJy at 4850 MHz and flat radio spectra, with $\alpha \geq 0.5$ (where $S_\nu \propto \nu^\alpha$) at low radio frequencies. The flat-spectrum criterion implies that our target sources are likely to be compact. 21 AGNs of our sample are at low redshifts, $z < 0.4$, 46 at high redshifts $1.1 < z < 1.5$, and 7 at very high redshifts, $3.0 < z < 3.6$. Besides our 74 targets, there are 29 CJF sources with HI 21 cm absorption searches in the literature, yielding a full sample consisting of more than 100 sources. This is the first survey for associated HI 21 cm absorption in a large and uniformly-selected AGN sample.

7. SUMMARY AND FUTURE WORK

Our second survey for associated HI 21 cm absorption targetted Gigahertz-peaked spectrum (GPS) sources, which are also known to be extremely compact, with sizes $\lesssim 1$ kpc. Our sample of 12 GPS sources consisted of 9 AGNs at $z < 0.4$, and 3 at $1.1 < z < 1.5$. 23 other GPS sources were found to have searches for HI 21 cm absorption in the literature, yielding an initial GPS source sample of 35 sources.

We used the AIPS software package to analyse all our GMRT data. Standard procedures of low-frequency imaging and spectroscopy were followed in analysing the data. The data on 11 sources of the CJF sample and 5 sources of the GPS sample were found to be affected by RFI; these sources were hence excluded from our analysis. We obtained clean spectra for 63 sources of the CJF sample, which include 3 confirmed detections, one tentative detection and 59 non-detections of redshifted HI 21 cm absorption. We obtained clean spectra for 7 sources of the GPS sample, which include 2 confirmed detections and 5 non-detections. For the non-detections, the typical optical depth RMS noise is ≈ 0.004 per ~ 30 km s $^{-1}$ channel for the CJF sample, while it is ≈ 0.002 per ~ 15 km s $^{-1}$ channel for the GPS sample. Of the six new detections, three confirmed detections are at $z \approx 1.2$, while the single tentative detection is at $z \approx 3.5$. We have thus roughly doubled the number of detections of associated HI 21 cm absorption at $z > 1$ in this thesis. Further, if confirmed, the tentative detection at $z = 3.530$ would have the highest redshift of any detection of HI 21 cm absorption.

7.2 AGNs with detections of HI 21 cm absorption

We have obtained a total of five new confirmed detections and one new tentative detection of associated HI 21 cm absorption, from our two surveys of the CJF and the GPS samples. Out of these, 2 detections, towards TXS 0003+380 and B3 1456+375, are at $z \approx 0.3$. The absorption profiles towards both AGNs are narrow, with full width between the 20% points < 100 km s $^{-1}$; further, in both cases, the HI 21 cm absorption is blueshifted relative to the AGN. The optical spectra of both AGNs show blazar characteristics (e.g. Davenport et al., 2015; Massaro et al., 2009). In both sources, the HI 21 cm absorption may arise against either the AGN core or beamed emission from the radio jet. The source B3 1456+375 is classified as a red quasar (e.g. Glikman et al., 2012); our detection of associated HI 21 cm absorption towards this source is consistent with the hypothesis that the red AGN colour is due to reddening by foreground dust.

7.2 AGNs with detections of HI 21 cm absorption

Our three new detections of associated HI 21 cm absorption at $z \approx 1.2$ are towards TXS 1954+513 (from the CJF sample), and TXS 1200+045 and TXS 1245-197 (both from the GPS sample). Of these, while TXS 1954+513 is classified as a blazar (e.g. Healey et al., 2008; Massaro et al., 2009; Xie et al., 2007), the GMRT image shows a core-dominated triple structure, with the two radio lobes aligned nearly perpendicular to the VLBI-scale core-jet structure (Xu et al., 1995). This misalignment may arise either due to a twisted radio jet or due to restarted AGN activity with a spin-flip of the central SMBH. The HI 21 cm absorption towards this source is likely to arise against either the milli-arcsec scale core or the milli-arcsec scale radio jet. The absorption is blueshifted from the blazar redshift of $z = 1.2230$, consistent with a scenario in which the HI “cloud” that gives rise to the absorption is being driven out by the radio jet that is aligned close to our line-of-sight. The AGN has a high intrinsic rest-frame 1216 Å UV luminosity, $\approx (1.7 - 3.7) \times 10^{23} \text{ W Hz}^{-1}$. Our detection of HI 21 cm absorption in this source demonstrates that neutral hydrogen can survive in AGN environments in the presence of high UV luminosities, contrary to recent suggestions in the literature.

The second of our detections at $z \approx 1.2$, TXS 1200+045, is compact in the GMRT 638 MHz image, whereas the 1.6 GHz VLBI image (Liu et al., 2007) shows a three-component structure. The three VLBI emission components may arise from either a core and two lobes, or a one-sided core-jet structure. The HI 21 cm absorption could arise against any of the three VLBI components. The absorption is significantly blueshifted from the AGN redshift of $z = 1.226$, by $\approx 2300 \text{ km s}^{-1}$. A weak extended absorption feature, with a span of $\approx 600 \text{ km s}^{-1}$, is also visible in the spectrum, indicating the presence of disturbed gas. The wide absorption profile as well as the large blueshift from the AGN suggest that the absorption may arise in outflowing gas that is being pushed by the radio jets to high velocities.

The third of our $z \approx 1.2$ detections, TXS 1245-197, has two prominent parsec-scale radio lobes in the 2.3 GHz VLBI image (Sokolovsky et al., 2011). Both lobes have steep radio spectra, with comparable flux densities. The source is classified as a Compact Symmetric Object, as it appears unlikely that the radio core might give rise to such steep-spectrum emission. The HI 21 cm absorption profile has a width of $\approx 325 \text{ km s}^{-1}$ between 20% points, with a wide weak wing extending blueward from the AGN redshift. The large velocity width could arise either due to absorption against both radio lobes,

7. SUMMARY AND FUTURE WORK

or possibly from disturbed gas that is interacting with the AGN jets (e.g. Geréb et al., 2015).

Finally, we obtained a tentative detection of HI 21 cm absorption towards TXS 0604+728, at $z = 3.530$. The putative HI 21 cm absorption is extremely wide, with a spread of $\approx 850 \text{ km s}^{-1}$ between the 20% points. The radio source has a complex core-jet structure, on angular scales ranging from milli-arcsecs to ≈ 10 arcsecs (Britzen et al., 2007; Taylor et al., 1996). The wide absorption could arise against different radio source components in the core and the radio jets. Unfortunately, we have so far not been able to confirm the tentative detection since the data from the later runs were corrupted by RFI. If confirmed, this would be the highest redshift at which HI 21 cm absorption has ever been detected.

7.3 Redshift evolution and AGN luminosity dependence

Our GMRT observations of 74 CJF sources gave 63 sources with usable HI 21 cm absorption spectra. A further 29 CJF sources have searches for associated HI 21 cm absorption in the literature, yielding a full sample of 92 uniformly-selected flat-spectrum sources. Dividing the sample at its median redshift $z_{med} = 1.2$, we find that the low- z sample has 13 detections and 33 non-detections, while the high- z sample has 3 detections and 43 non-detections; these imply HI 21 cm detection rates of $28_{-8}^{+10}\%$ and $7_{-4}^{+6}\%$, respectively. Although the detection rate appears lower in the high- z sample, the difference between the two detection rates has only $\approx 2\sigma$ significance, due to the large Poisson errors. However, a Peto-Prentice two-sample test on the integrated HI 21 cm optical depths of the AGNs of the two sub-samples finds that the low- z and high- z AGN sub-samples are unlikely to be drawn from the same distribution, at $\approx 3\sigma$ significance, with the high- z AGN sample having a weaker strength of HI 21 cm absorption. This is the first statistically significant evidence for redshift evolution in the strength of HI 21 cm absorption in AGN environments, obtained from a uniformly-selected sample.

We find no evidence that the lower strength of HI 21 cm absorption in the high- z sub-sample might arise due to the lower-frequency radio emission being dominated by extended, steep-spectrum radio structure, and hence a lower AGN covering factor. Further, we also find no significant difference in the low-frequency spectral indices of the low- z and high- z sub-samples, implying that it is unlikely that the high- z AGNs in

7.3 Redshift evolution and AGN luminosity dependence

our sample have systematically steeper spectral indices, and hence low covering factors. We also find that our results do not depend strongly on the assumption that all the AGNs in our sample have a uniform covering factor of unity.

However, we find that there is a significant bias in the intrinsic AGN luminosities in our sample, with the high redshift AGNs having higher rest-frame 1216 Å UV and 1.4 GHz radio luminosities. A Peto-Prentice two-sample test finds that the integrated HI 21 cm optical depths in the low- and high-luminosity sub-samples are unlikely to be drawn from the same parent distribution at $\approx 3.5\sigma$ significance. The strength of the HI 21 cm absorption is higher in the AGNs with low rest-frame 1216 Å UV and/or 1.4 GHz radio luminosities. We thus find from our sample of 92 CJF sources that there is statistically significant evidence for a dependence of the strength of the HI 21 cm absorption on redshift, and rest-frame 1216 Å UV and 1.4 GHz radio luminosity, with the absorption weaker at high redshifts and high luminosities. The fact that most of the high-luminosity AGNs of our sample lie at high redshifts means that it is currently not possible to break the degeneracy between the effects of redshift evolution and high intrinsic luminosity, to identify the primary cause for the weaker HI 21 cm absorption in high- z , high-luminosity active galactic nuclei.

We have combined our GPS sample of 27 sources, including 7 from our observations and 20 from the literature, with our CJF sample, to construct a sample of 119 compact AGNs with searches for redshifted associated HI 21 cm absorption. This is by far the largest sample of compact AGNs that has been searched for associated HI 21 cm absorption till now. We continue to find that the strength of the HI 21 cm absorption shows a strong dependence on both redshift and AGN luminosity, with weaker HI 21 cm absorption in AGNs at high redshift and high UV/radio luminosity. Unfortunately, the pattern that most of the high-luminosity AGNs are at high redshifts persists in this sample. Thus, although we have formally established that the strength of HI 21 cm absorption depends on both redshift and AGN luminosity, our current samples do not allow us to break the degeneracy between these two possible causes of the weakening of the HI 21 cm absorption.

In summary, this thesis has demonstrated that uniformly-selected AGNs with high UV/radio luminosities, and located at high redshifts, show weaker associated HI 21 cm absorption, than similarly-selected AGNs with low UV/radio luminosities and located at low redshifts. The possible causes of the weaker absorption in high- z , high-luminosity

7. SUMMARY AND FUTURE WORK

AGNs are (1) lower amounts of neutral gas in high- z AGN environments, due to either lower amounts of gas in galaxy environments at high redshifts, or ionization of the neutral gas by the UV photons from the AGN, and (2) higher spin temperatures in high- z AGN environments, due to either a preponderance of warm gas in high- z galaxies (similar to the situation in high- z DLAs; Kanekar et al., 2014) or a higher spin temperature (different from the kinetic temperature), due to the high AGN UV/radio luminosity. Unfortunately, the luminosity bias in our sample, with the higher-luminosity AGNs located at higher redshifts, implies that the present dataset does not allow us to distinguish between the above possibilities, and identify the primary cause, if any, of the decline in the strength of the HI 21 cm absorption in the high- z , high-luminosity sample; this will be the focus of future studies.

7.4 Future Work

This thesis has made progress in both finding new associated HI 21 cm absorbers at high redshifts (where we have doubled the number of detections of absorption at $z > 1$), and showing clearly that the strength of HI 21 cm absorption depends on the AGN redshift and the AGN UV/radio luminosity. However, much work remains to be done in both these areas. First, the typical current upper limits on the HI 21 cm column density for the non-detections are $\approx 2 \times 10^{20} \text{ cm}^{-2} \times (T_s/100 \text{ K})$ (see Tables 4.1 and 4.2). While these appear to be extremely tight limits, ruling out the presence of HI 21 cm column densities similar to those seen in high- z DLAs, this is true only for an assumed spin temperature of 100 K. If the gas spin temperature is indeed $\approx 1000 \text{ K}$, due to either more warm gas in high- z galaxies or higher spin temperatures due to the AGN UV/radio luminosity, the limits would be much less constraining, $\approx \text{few} \times 10^{21} \text{ cm}^{-2}$. It would hence be interesting to carry out extremely deep GMRT searches for HI 21 cm absorption in a sub-sample of bright high- z AGNs, to rule out the possibility of high HI column densities even for high gas spin temperatures.

Next, breaking the degeneracy between redshift evolution and AGN UV/radio luminosity is clearly critical for our understanding of AGN environments and evolution. There are two direct ways of addressing this issue, via HI 21 cm absorption studies of either (1) a sample of low-luminosity AGNs at high redshifts $z \gtrsim 1$, or (2) a sample of high-luminosity AGNs at low redshifts, $z \lesssim 1$. The first of these possibilities

would require very deep integrations to achieve good HI 21 cm optical depth sensitivity on low-luminosity AGNs; the second approach, identifying AGNs with high UV/radio luminosity at $z \lesssim 1$, is hence likely to be more fruitful. We have hence compiled a sample of 38 AGNs, again selected from the CJF sample, at redshifts $0.65 < z < 1.1$, all of which have UV luminosities $\geq 10^{22.64} \text{ W Hz}^{-1}$, i.e. greater than or equal to the median rest-frame 1216 Å UV luminosity of our present sample. We have already carried out Green Bank Telescope HI 21 cm spectroscopy of 19 systems of the sample, at $0.65 < z < 1.0$. The data analysis will be completed shortly and should yield some insight on the primary dependence of the strength of HI 21 cm absorption. We also plan to use the new 550 – 900 MHz receivers of the upgraded GMRT to carry out a search for associated HI 21 cm absorption in all 38 high-luminosity AGNs of this sample, which should provide enough statistical leverage to clearly distinguish between the two possibilities of redshift evolution and luminosity dependence.

Finally, poor low-frequency coverage in today’s radio telescopes and strong RFI have meant that there is a large hole at $z \approx 1.5 - 3.0$ in the redshift coverage of searches for associated HI 21 cm absorption. The new 250 – 500 MHz band of the upgraded GMRT will, for the first time, allow deep absorption surveys of large AGN samples in this redshift range. We have already used these receivers to carry out a search for HI 21 cm absorption in 13 GPS sources at $1.8 < z < 3.0$, and plan to carry out a detailed survey of all CJF and GPS sources that lie in this redshift range in the future. This will enable us to trace the distribution of the neutral hydrogen in AGN environments all the way out to very high redshifts, $z \approx 4$, using a uniformly-selected sample of compact active galactic nuclei.

7. SUMMARY AND FUTURE WORK

Appendix A

We have used three statistical tests for data analysis in this thesis; these are the Peto-Prentice two-sample test, the Gehan-Wilcoxon test, and the generalized Kendall's tau rank correlation test. All these three tests can be performed using the tools that are available in the Astronomical Survival Analysis (ASURV) software package (Isobe et al., 1986). In the following, I will briefly introduce the ASURV package, and further, I will describe the characteristics of these three tests.

Astronomers often search for a particular property in a sample of celestial objects, and end up failing to detect the property in all the objects. In such a case, the observed data consist of both detections and non-detections. Standard statistical tests cannot be employed in the data analysis in such situations. However, certain statistical analysis techniques, called 'survival analysis', have been developed which deal with these issues. The non-detections are labelled as 'censored' data points, i.e. upper or lower limits, in these techniques.

ASURV is a software package consisting of various statistical techniques from survival analysis, that are relevant to many situations in astronomy. This package can be operated independently of other computer softwares, and can be run by selecting options from a menu. The various tools that the package provides are the maximum-likelihood estimator of a censored distribution, several two-sample tests, correlation tests and linear regressions (Feigelson and Nelson, 1985; Isobe et al., 1986).

The package mainly uses non-parametric methods that make no assumptions about the distribution from which the sample is drawn. Maximum-likelihood techniques are frequently used to characterize the distribution. Such non-parametric techniques are particularly suitable for astronomical studies since the underlying distribution of the data sample is usually unknown. Further, the tools in the package are broadly classified

as ‘univariate’ and ‘bivariate’. In univariate methods, only a single variable of a sample is involved. These methods determine the distribution from which the censored sample is drawn, as well as compare it with another censored sample. Bivariate methods test whether a censored variable is correlated with another variable of the data and, if so, measure the empirical relation between the two variables.

The Peto-Prentice and Gehan-Wilcoxon tests are univariate methods that test whether two samples are drawn from the same distribution. While the Peto-Prentice test compares two censored samples, the Gehan-Wilcoxon test compares two uncensored samples. These tests return a test statistic and a ‘p’ value, that are used to reject the null hypothesis that the two samples are drawn from the same distribution. Both of these tests are generalizations of the well-known Wilcoxon and logrank two-sample tests for uncensored data. Among all the two-sample tests provided in the package, the Peto-Prentice test is known to be least affected by differences in the patterns of the censored variable in the two samples.

Apart from the above mentioned univariate methods, we have also used the bivariate Kendall’s tau test in this thesis. A tau test is a non-parametric technique that is used to test the statistical dependence of two variables in a sample, by using a tau coefficient. The Kendall’s tau coefficient is a test statistic that is used to measure the ordinal association between two variables. That is, the coefficient is a measure of the similarity of the orderings of ranked data. Labelling the relative positions of the measurements within the variable is called ranking. The Kendall’s tau coefficient lies in the range $-1 \leq \tau \leq 1$. The value will be high, $\tau \approx 1$, when the measurements of the two variables have a similar rank, $\tau \approx 0$ when the two variables are independent, and low, $\tau \approx -1$, when the measurements of the two variables have opposite ranks.

Bibliography

K. Abazajian, et al., J. K. Adelman-McCarthy, M. A. Agüeros, S. S. Allam, K. S. J. Anderson, S. F. Anderson, J. Annis, N. A. Bahcall, I. K. Baldry, S. Bastian, A. Berlind, M. Bernardi, M. R. Blanton, J. J. Bochanski, Jr., W. N. Boroski, H. J. Brewington, J. W. Briggs, J. Brinkmann, R. J. Brunner, T. Budavári, L. N. Carey, F. J. Castander, A. J. Connolly, K. R. Covey, I. Csabai, J. J. Dalcanton, M. Doi, F. Dong, D. J. Eisenstein, M. L. Evans, X. Fan, D. P. Finkbeiner, S. D. Friedman, J. A. Frieman, M. Fukugita, B. Gillespie, K. Glazebrook, J. Gray, E. K. Grebel, J. E. Gunn, V. K. Gurbani, P. B. Hall, M. Hamabe, D. Harbeck, F. H. Harris, H. C. Harris, M. Harvanek, S. L. Hawley, J. Hayes, T. M. Heckman, J. S. Hendry, G. S. Hennessy, R. B. Hindsley, C. J. Hogan, D. W. Hogg, D. J. Holmgren, J. A. Holtzman, S.-i. Ichikawa, T. Ichikawa, Ž. Ivezić, S. Jester, D. E. Johnston, A. M. Jorgensen, M. Jurić, S. M. Kent, S. J. Kleinman, G. R. Knapp, A. Y. Kniazev, R. G. Kron, J. Krzesinski, D. Q. Lamb, H. Lampeitl, B. C. Lee, H. Lin, D. C. Long, J. Loveday, R. H. Lupton, E. Mannery, B. Margon, D. Martínez-Delgado, T. Matsubara, P. M. McGehee, T. A. McKay, A. Meiksin, B. Ménard, J. A. Munn, T. Nash, E. H. Neilsen, Jr., H. J. Newberg, P. R. Newman, R. C. Nichol, T. Nicinski, M. Nieto-Santisteban, A. Nitta, S. Okamura, W. O'Mullane, R. Owen, N. Padmanabhan, G. Pauls, J. Peoples, J. R. Pier, A. C. Pope, D. Pourbaix, T. R. Quinn, M. J. Raddick, G. T. Richards, M. W. Richmond, H.-W. Rix, C. M. Rockosi, D. J. Schlegel, D. P. Schneider, J. Schroeder, R. Scranton, M. Sekiguchi, E. Sheldon, K. Shimasaku, N. M. Silvestri, J. A. Smith, V. Smolčić, S. A. Snedden, A. Stebbins, C. Stoughton, M. A. Strauss, M. SubbaRao, A. S. Szalay, I. Szapudi, P. Szkody, G. P. Szokoly, M. Tegmark, L. Teodoro, A. R. Thakar, C. Tremonti, D. L. Tucker, A. Uomoto, D. E. Vanden Berk, J. Vandenberg, M. S. Vogeley, W. Voges, N. P. Vogt, L. M. Walkowicz, S.-i. Wang, D. H. Weinberg, A. A. West, S. D. M. White, B. C. Wilhite, Y. Xu, B. Yanny, N. Yasuda, C.-W.

BIBLIOGRAPHY

- Yip, D. R. Yocum, D. G. York, I. Zehavi, S. Zibetti, and D. B. Zucker. The Third Data Release of the Sloan Digital Sky Survey. *AJ*, 129:1755–1759, March 2005. doi: 10.1086/427544.
- K. N. Abazajian, J. K. Adelman-McCarthy, M. A. Agüeros, S. S. Allam, C. Allende Prieto, D. An, K. S. J. Anderson, S. F. Anderson, J. Annis, N. A. Bahcall, and et al. The Seventh Data Release of the Sloan Digital Sky Survey. *ApJS*, 182:543-558, June 2009. doi: 10.1088/0067-0049/182/2/543.
- J. K. Adelman-McCarthy, M. A. Agüeros, S. S. Allam, C. Allende Prieto, K. S. J. Anderson, S. F. Anderson, J. Annis, N. A. Bahcall, C. A. L. Bailer-Jones, I. K. Baldry, J. C. Barentine, B. A. Bassett, A. C. Becker, T. C. Beers, E. F. Bell, A. A. Berlind, M. Bernardi, M. R. Blanton, J. J. Bochanski, W. N. Boroski, J. Brinchmann, J. Brinkmann, R. J. Brunner, T. Budavári, S. Carliles, M. A. Carr, F. J. Castander, D. Cinabro, R. J. Cool, K. R. Covey, I. Csabai, C. E. Cunha, J. R. A. Davenport, B. Dilday, M. Doi, D. J. Eisenstein, M. L. Evans, X. Fan, D. P. Finkbeiner, S. D. Friedman, J. A. Frieman, M. Fukugita, B. T. Gänsicke, E. Gates, B. Gillespie, K. Glazebrook, J. Gray, E. K. Grebel, J. E. Gunn, V. K. Gurbani, P. B. Hall, P. Harding, M. Harvanek, S. L. Hawley, J. Hayes, T. M. Heckman, J. S. Hendry, R. B. Hindsley, C. M. Hirata, C. J. Hogan, D. W. Hogg, J. B. Hyde, S.-i. Ichikawa, Ž. Ivezić, S. Jester, J. A. Johnson, A. M. Jorgensen, M. Jurić, S. M. Kent, R. Kessler, S. J. Kleinman, G. R. Knapp, R. G. Kron, J. Krzesinski, N. Kuropatkin, D. Q. Lamb, H. Lampeitl, S. Lebedeva, Y. S. Lee, R. French Leger, S. Lépine, M. Lima, H. Lin, D. C. Long, C. P. Loomis, J. Loveday, R. H. Lupton, O. Malanushenko, V. Malanushenko, R. Mandelbaum, B. Margon, J. P. Marriner, D. Martínez-Delgado, T. Matsubara, P. M. McGehee, T. A. McKay, A. Meiksin, H. L. Morrison, J. A. Munn, R. Nakajima, E. H. Neilsen, Jr., H. J. Newberg, R. C. Nichol, T. Nicinski, M. Nieto-Santisteban, A. Nitta, S. Okamura, R. Owen, H. Oyaizu, N. Padmanabhan, K. Pan, C. Park, J. Peoples, Jr., J. R. Pier, A. C. Pope, N. Purger, M. J. Raddick, P. Re Fiorentin, G. T. Richards, M. W. Richmond, A. G. Riess, H.-W. Rix, C. M. Rockosi, M. Sako, D. J. Schlegel, D. P. Schneider, M. R. Schreiber, A. D. Schwobe, U. Seljak, B. Sesar, E. Sheldon, K. Shimasaku, T. Sivarani, J. Allyn Smith, S. A. Snedden, M. Steinmetz, M. A. Strauss, M. SubbaRao, Y. Suto, A. S. Szalay, I. Szapudi, P. Szkody, M. Tegmark, A. R. Thakar, C. A. Tremonti, D. L. Tucker,

- A. Uomoto, D. E. Vanden Berk, J. Vandenberg, S. Vidrih, M. S. Vogeley, W. Voges, N. P. Vogt, Y. Wadadekar, D. H. Weinberg, A. A. West, S. D. M. White, B. C. Wilhite, B. Yanny, D. R. Yocum, D. G. York, I. Zehavi, and D. B. Zucker. The Sixth Data Release of the Sloan Digital Sky Survey. *ApJS*, 175:297-313, April 2008. doi: 10.1086/524984.
- S. W. Allen, R. J. H. Dunn, A. C. Fabian, G. B. Taylor, and C. S. Reynolds. The relation between accretion rate and jet power in X-ray luminous elliptical galaxies. *MNRAS*, 372:21–30, October 2006. doi: 10.1111/j.1365-2966.2006.10778.x.
- R. Antonucci. Unified models for active galactic nuclei and quasars. *ARA&A*, 31: 473–521, 1993. doi: 10.1146/annurev.aa.31.090193.002353.
- S. Appl, H. Sol, and L. Vicente. Misalignment and curvature effects in extragalactic radio sources. *A&A*, 310:419–437, June 1996.
- J. N. Bahcall and R. D. Ekers. On the Possibility of Detecting Redshifted 21-CM Absorption Lines in the Spectra of Quasi-Stellar Sources. *ApJ*, 157:1055, September 1969. doi: 10.1086/150135.
- J. A. Baldwin. Broad Emission Lines in Active Galactic Nuclei. In B. M. Peterson, F.-Z. Cheng, and A. S. Wilson, editors, *IAU Colloq. 159: Emission Lines in Active Galaxies: New Methods and Techniques*, volume 113 of *Astronomical Society of the Pacific Conference Series*, page 80, 1997.
- B. Balmaverde, R. D. Baldi, and A. Capetti. The accretion mechanism in low-power radio galaxies. *A&A*, 486:119–130, July 2008. doi: 10.1051/0004-6361:200809810.
- P. D. Barthel. Is every quasar beamed? *ApJ*, 336:606–611, January 1989. doi: 10.1086/167038.
- R. H. Becker, R. L. White, and D. J. Helfand. The FIRST Survey: Faint Images of the Radio Sky at Twenty Centimeters. *ApJ*, 450:559, September 1995. doi: 10.1086/176166.
- C. R. Benn, M. Vigotti, R. Carballo, J. I. Gonzalez-Serrano, and S. F. Sánchez. Red quasars not so dusty. *MNRAS*, 295:451, April 1998. doi: 10.1046/j.1365-8711.1998.t01-2-01327.x.

BIBLIOGRAPHY

- P. N. Best, C. R. Kaiser, T. M. Heckman, and G. Kauffmann. AGN-controlled cooling in elliptical galaxies. *MNRAS*, 368:L67–L71, May 2006. doi: 10.1111/j.1745-3933.2006.00159.x.
- L. Bianchi, A. Conti, and B. Shiao. The ultraviolet sky: An overview from the GALEX surveys. *Advances in Space Research*, 53:900–912, March 2014. doi: 10.1016/j.asr.2013.07.045.
- J. Binney. The physics of dissipational galaxy formation. *ApJ*, 215:483–491, July 1977. doi: 10.1086/155378.
- R. Braun and R. A. M. Walterbos. Physical properties of neutral gas in M31 and the Galaxy. *ApJ*, 386:120–138, February 1992. doi: 10.1086/170998.
- S. Britzen, R. C. Vermeulen, G. B. Taylor, R. M. Campbell, T. J. Pearson, A. C. S. Readhead, W. Xu, I. W. A. Browne, D. R. Henstock, and P. Wilkinson. A multi-epoch VLBI survey of the kinematics of CJF sources. I. Model-fit parameters and maps. *A&A*, 472:763–771, September 2007. doi: 10.1051/0004-6361:20052677.
- A. M. Brooks, F. Governato, T. Quinn, C. B. Brook, and J. Wadsley. The Role of Cold Flows in the Assembly of Galaxy Disks. *ApJ*, 694:396–410, March 2009. doi: 10.1088/0004-637X/694/1/396.
- G. Canalizo, N. Bennert, B. Jungwiert, A. Stockton, F. Schweizer, M. Lacy, and C. Peng. Spectacular Shells in the Host Galaxy of the QSO MC2 1635+119. *ApJ*, 669:801–809, November 2007. doi: 10.1086/521721.
- C. L. Carilli, E. S. Perlman, and J. T. Stocke. Discovery of neutral hydrogen 21 centimeter absorption at redshift 0.25 toward PKS 1413+135. *ApJL*, 400:L13–L15, November 1992. doi: 10.1086/186637.
- C. L. Carilli, K. M. Menten, M. J. Reid, M. P. Rupen, and M. S. Yun. Redshifted Neutral Hydrogen 21 Centimeter Absorption toward Red Quasars. *ApJ*, 494:175–182, February 1998a. doi: 10.1086/305191.
- C. L. Carilli, J. M. Wrobel, and J. S. Ulvestad. A Subkiloparsec Disk in Markarian 231. *AJ*, 115:928–937, March 1998b. doi: 10.1086/300253.

- Y. Chandola, S. K. Sirothia, and D. J. Saikia. H I absorption towards nearby compact radio sources. *MNRAS*, 418:1787–1795, December 2011. doi: 10.1111/j.1365-2966.2011.19607.x.
- Y. Chandola, N. Gupta, and D. J. Saikia. Associated 21-cm absorption towards the cores of radio galaxies. *MNRAS*, 429:2380–2391, March 2013. doi: 10.1093/mnras/sts499.
- P. S. Chen, H. W. Fu, and Y. F. Gao. 2MASS observation of BL Lac objects. *NewA*, 11:27–42, October 2005. doi: 10.1016/j.newast.2005.05.004.
- J. J. Condon, W. D. Cotton, E. W. Greisen, Q. F. Yin, R. A. Perley, G. B. Taylor, and J. J. Broderick. The NRAO VLA Sky Survey. *AJ*, 115:1693–1716, May 1998. doi: 10.1086/300337.
- J. E. Conway and D. W. Murphy. Helical jets and the misalignment distribution for core-dominated radio sources. *ApJ*, 411:89–102, July 1993. doi: 10.1086/172809.
- W. D. Cotton, J. J. Wittels, I. I. Shapiro, J. Marcaide, F. N. Owen, S. R. Spangler, A. Rius, C. Angulo, T. A. Clark, and C. A. Knight. The very flat radio spectrum of 0735 plus 178 - A cosmic conspiracy. *ApJL*, 238:L123–L128, June 1980. doi: 10.1086/183271.
- D. J. Croton, V. Springel, S. D. M. White, G. De Lucia, C. S. Frenk, L. Gao, A. Jenkins, G. Kauffmann, J. F. Navarro, and N. Yoshida. The many lives of active galactic nuclei: cooling flows, black holes and the luminosities and colours of galaxies. *MNRAS*, 365:11–28, January 2006. doi: 10.1111/j.1365-2966.2005.09675.x.
- S. J. Curran and M. T. Whiting. H I 21 cm Absorption and Unified Schemes of Active Galactic Nuclei. *ApJ*, 712:303–317, March 2010. doi: 10.1088/0004-637X/712/1/303.
- S. J. Curran, M. T. Whiting, T. Wiklind, J. K. Webb, M. T. Murphy, and C. R. Purcell. A survey for redshifted molecular and atomic absorption lines - II. Associated HI, OH and millimetre lines in the $z > 3$ Parkes quarter-Jansky flat-spectrum sample. *MNRAS*, 391:765–784, December 2008. doi: 10.1111/j.1365-2966.2008.13925.x.

BIBLIOGRAPHY

- S. J. Curran, M. T. Whiting, E. M. Sadler, and C. Bignell. A survey for the missing hydrogen in high-redshift radio sources. *MNRAS*, 428:2053–2063, January 2013. doi: 10.1093/mnras/sts171.
- R. M. Cutri, M. F. Skrutskie, S. van Dyk, C. A. Beichman, J. M. Carpenter, T. Chester, L. Cambresy, T. Evans, J. Fowler, J. Gizis, E. Howard, J. Huchra, T. Jarrett, E. L. Kopan, J. D. Kirkpatrick, R. M. Light, K. A. Marsh, H. McCallon, S. Schneider, R. Stiening, M. Sykes, M. Weinberg, W. A. Wheaton, S. Wheelock, and N. Zacarias. *2MASS All Sky Catalog of point sources*. June 2003.
- R. M. Cutri, E. L. Wright, T. Conrow, J. W. Fowler, P. R. M. Eisenhardt, C. Grillmair, J. D. Kirkpatrick, F. Masci, H. L. McCallon, S. L. Wheelock, S. Fajardo-Acosta, L. Yan, D. Benford, M. Harbut, T. Jarrett, S. Lake, D. Leisawitz, M. E. Ressler, S. A. Stanford, C. W. Tsai, F. Liu, G. Helou, A. Mainzer, D. Gettings, A. Gonzalez, D. Hoffman, K. A. Marsh, D. Padgett, M. F. Skrutskie, R. P. Beck, M. Papin, and M. Wittman. Explanatory Supplement to the AllWISE Data Release Products. Technical report, November 2013.
- D. Dallacasa, C. Stanghellini, M. Centonza, and G. Furnari. High frequency peakers. *NewAR*, 46:299–302, May 2002. doi: 10.1016/S1387-6473(01)00198-1.
- J. R. A. Davenport, J. J. Ruan, A. C. Becker, C. L. Macleod, and R. M. Cutri. SDSS J14584479+3720215: a Benchmark JHK_S Blazar Light Curve from the 2Mass Calibration Scans. *ApJ*, 803:2, April 2015. doi: 10.1088/0004-637X/803/1/2.
- N. de Vries, I. A. G. Snellen, R. T. Schilizzi, M. D. Lehnert, and M. N. Bremer. Complete identification of the Parkes half-Jansky sample of GHz peaked spectrum radio galaxies. *A&A*, 464:879–883, March 2007. doi: 10.1051/0004-6361:20066506.
- W. H. de Vries, R. Morganti, H. J. A. Rottgering, Renee C. Vermeulen, W. van Breugel, R. Rengelink, and M. J. Jarvis. Deep westerbork 1.4 ghz imaging of the bootes field. *Astron. J.*, 123:1784–1800, 2002. doi: 10.1086/338906.
- D. S. De Young, M. S. Roberts, and W. C. Saslaw. Detection of 21-CENTIMETER Hydrogen Absorption in the High-Velocity Component of the Radio Galaxy Perseus a. *ApJ*, 185:809–816, November 1973. doi: 10.1086/152456.

- P. Di Matteo, F. Combes, A. L. Melchior, and B. Semelin. Old stellar counter-rotating components in elliptical-spiral mergers: exploring the GalMer database. *ASP Conf. Ser.*, 396:265, 2008.
- J. M. Dickey. VLA observations of H I absorption in the nuclei of Seyfert and active galaxies. *ApJ*, 263:87–93, December 1982. doi: 10.1086/160482.
- J. M. Dickey. Measuring Spin Temperatures in Other Galaxies: The Mixture of Interstellar Phases. In A. Ferrara, C. F. McKee, C. Heiles, and P. R. Shapiro, editors, *The Physics of the Interstellar Medium and Intergalactic Medium*, volume 80 of *Astronomical Society of the Pacific Conference Series*, page 357, 1995.
- J. N. Douglas, F. N. Bash, F. A. Bozyan, G. W. Torrence, and C. Wolfe. The Texas Survey of Radio Sources Covering -35.5 degrees $<$ declination $<$ 71.5 degrees at 365 MHz. *AJ*, 111:1945, May 1996. doi: 10.1086/117932.
- B. T. Draine. *Physics of the Interstellar and Intergalactic Medium*. 2011.
- A. C. Edge, G. Pooley, M. Jones, K. Grainge, and R. Saunders. GPS Sources with High Peak Frequencies. In J. A. Zensus, G. B. Taylor, and J. M. Wrobel, editors, *IAU Colloq. 164: Radio Emission from Galactic and Extragalactic Compact Sources*, volume 144 of *Astronomical Society of the Pacific Conference Series*, page 187, 1998.
- R. D. Ekers. Radio observations of active and normal nuclei. 17:171–173, March 1978. doi: 10.1088/0031-8949/17/3/007.
- S. L. Ellison, P. B. Hall, and P. Lira. The Optical-Infrared Colors of CORALS QSOs: Searching for Dust Reddening Associated with High-Redshift Damped Ly α Systems. *AJ*, 130:1345–1357, October 2005. doi: 10.1086/444537.
- B. H. C. Emonts, R. Morganti, C. Struve, T. A. Oosterloo, G. van Moorsel, C. N. Tadhunter, J. M. van der Hulst, E. Brogt, J. Holt, and N. Mirabal. Large-scale HI in nearby radio galaxies - II. The nature of classical low-power radio sources. *MNRAS*, 406:987–1006, August 2010. doi: 10.1111/j.1365-2966.2010.16706.x.
- H. I. Ewen and E. M. Purcell. Observation of a Line in the Galactic Radio Spectrum: Radiation from Galactic Hydrogen at 1,420 Mc./sec. *Nature*, 168:356, September 1951. doi: 10.1038/168356a0.

BIBLIOGRAPHY

- A. C. Fabian. Observational Evidence of Active Galactic Nuclei Feedback. *ARA&A*, 50:455–489, September 2012. doi: 10.1146/annurev-astro-081811-125521.
- C. Fanti, R. Fanti, D. Dallacasa, R. T. Schilizzi, R. E. Spencer, and C. Stanghellini. Are compact steep-spectrum sources young? *A&A*, 302:317, October 1995.
- P. N. Fedorov, V. S. Akhmetov, and V. V. Bobylev. Residual rotation of the Hipparcos/Tycho-2 system as determined from the data of the XPM catalogue. *MNRAS*, 416:403–408, September 2011. doi: 10.1111/j.1365-2966.2011.19045.x.
- E. D. Feigelson and P. I. Nelson. Statistical methods for astronomical data with upper limits. I - Univariate distributions. *ApJ*, 293:192–206, June 1985. doi: 10.1086/163225.
- L. Ferrarese and D. Merritt. A Fundamental Relation between Supermassive Black Holes and Their Host Galaxies. *ApJL*, 539:L9–L12, August 2000. doi: 10.1086/312838.
- A. L. Fey and P. Charlot. VLBA Observations of Radio Reference Frame Sources. III. Astrometric Suitability of an Additional 225 Sources. *ApJS*, 128:17–83, May 2000. doi: 10.1086/313382.
- A. Ficarra, G. Grueff, and G. Tomassetti. A new Bologna sky survey at 408 MHz. *A&AS*, 59:255–347, February 1985.
- G. B. Field. The Spin Temperature of Intergalactic Neutral Hydrogen. *ApJ*.
- G. B. Field. Excitation of the Hydrogen 21-CM Line. *Proceedings of the IRE*, 46: 240–250, January 1958. doi: 10.1109/JRPROC.1958.286741.
- E. W. Fleisch. The Half Million Quasars (HMQ) Catalogue. *PASA*, 32:e010, March 2015. doi: 10.1017/pasa.2015.10.
- J. S. Gallagher, G. R. Knapp, S. M. Faber, and B. Balick. Neutral hydrogen in the normal elliptical galaxy NGC 4278. *ApJ*, 215:463–473, July 1977. doi: 10.1086/155376.

- J. F. Gallimore, S. A. Baum, C. P. O’Dea, A. Pedlar, and E. Brinks. Neutral Hydrogen (21 Centimeter) Absorption in Seyfert Galaxies: Evidence for Free-Free Absorption and Subkiloparsec Gaseous Disks. *ApJ*, 524:684–706, October 1999. doi: 10.1086/307853.
- K. Gebhardt, R. Bender, G. Bower, A. Dressler, S. M. Faber, A. V. Filippenko, R. Green, C. Grillmair, L. C. Ho, J. Kormendy, T. R. Lauer, J. Magorrian, J. Pinkney, D. Richstone, and S. Tremaine. A Relationship between Nuclear Black Hole Mass and Galaxy Velocity Dispersion. *ApJL*, 539:L13–L16, August 2000. doi: 10.1086/312840.
- N. Gehrels. Confidence limits for small numbers of events in astrophysical data. *ApJ*, 303:336–346, April 1986. doi: 10.1086/164079.
- K. Geréb, F. M. Maccagni, R. Morganti, and T. A. Oosterloo. The HI absorption ”Zoo”. *A&A*, 575:A44, March 2015. doi: 10.1051/0004-6361/201424655.
- G. Ghisellini, P. Padovani, A. Celotti, and L. Maraschi. Relativistic bulk motion in active galactic nuclei. *ApJ*, 407:65–82, April 1993. doi: 10.1086/172493.
- E. Glikman, T. Urrutia, M. Lacy, S. G. Djorgovski, A. Mahabal, A. D. Myers, N. P. Ross, P. Petitjean, J. Ge, D. P. Schneider, and D. G. York. FIRST-2MASS Red Quasars: Transitional Objects Emerging from the Dust. *ApJ*, 757:51, September 2012. doi: 10.1088/0004-637X/757/1/51.
- A. W. Graham and S. P. Driver. A Log-Quadratic Relation for Predicting Supermassive Black Hole Masses from the Host Bulge Sérsic Index. *ApJ*, 655:77–87, January 2007. doi: 10.1086/509758.
- P. C. Gregory and J. J. Condon. The 87GB catalog of radio sources covering delta between 0 and + 75 deg at 4.85 GHz. *ApJS*, 75:1011–1291, April 1991. doi: 10.1086/191559.
- J. E. Gunn. *Feeding the monster - Gas discs in elliptical galaxies*, pages 213–225. 1979.
- N. Gupta, C. J. Salter, D. J. Saikia, T. Ghosh, and S. Jeyakumar. Probing radio source environments via HI and OH absorption. *MNRAS*, 373:972–992, December 2006. doi: 10.1111/j.1365-2966.2006.11064.x.

BIBLIOGRAPHY

- N. Häring and H.-W. Rix. On the Black Hole Mass-Bulge Mass Relation. *ApJL*, 604: L89–L92, April 2004. doi: 10.1086/383567.
- S. E. Healey, R. W. Romani, G. Cotter, P. F. Michelson, E. F. Schlafly, A. C. S. Readhead, P. Giommi, S. Chaty, I. A. Grenier, and L. C. Weintraub. CGRaBS: An All-Sky Survey of Gamma-Ray Blazar Candidates. *ApJS*, 175:97-104, March 2008. doi: 10.1086/523302.
- T. M. Heckman, E. P. Smith, S. A. Baum, W. J. M. van Breugel, G. K. Miley, G. D. Illingworth, G. D. Bothun, and B. Balick. Galaxy collisions and mergers - The genesis of very powerful radio sources? *ApJ*, 311:526–547, December 1986. doi: 10.1086/164793.
- D. S. Heeschen. Flickering of extragalactic radio sources. *AJ*, 89:1111–1123, August 1984. doi: 10.1086/113608.
- J. F. Helmboldt, G. B. Taylor, S. Tremblay, C. D. Fassnacht, R. C. Walker, S. T. Myers, L. O. Sjouwerman, T. J. Pearson, A. C. S. Readhead, L. Weintraub, N. Gehrels, R. W. Romani, S. Healey, P. F. Michelson, R. D. Blandford, and G. Cotter. The VLBA Imaging and Polarimetry Survey at 5 GHz. *ApJ*, 658:203–216, March 2007. doi: 10.1086/511005.
- D. R. Henstock, I. W. A. Browne, P. N. Wilkinson, G. B. Taylor, R. C. Vermeulen, T. J. Pearson, and A. C. S. Readhead. The Second Caltech–Jodrell Bank VLBI Survey. II. Observations of 102 of 193 Sources. *ApJS*, 100:1, September 1995. doi: 10.1086/192206.
- D. R. Henstock, I. W. A. Browne, P. N. Wilkinson, and R. G. McMahon. Redshifts for flat-spectrum radio sources in the second Caltech–Jodrell Bank VLBI sample. *MNRAS*, 290:380–400, September 1997. doi: 10.1093/mnras/290.2.380.
- P. C. Hewett and V. Wild. Improved redshifts for SDSS quasar spectra. *MNRAS*, 405: 2302–2316, July 2010. doi: 10.1111/j.1365-2966.2010.16648.x.
- E. K. S. Hicks, R. I. Davies, M. A. Malkan, R. Genzel, L. J. Tacconi, F. Müller Sánchez, and A. Sternberg. The Role of Molecular Gas in Obscuring Seyfert Active Galactic Nuclei. *ApJ*, 696:448–470, May 2009. doi: 10.1088/0004-637X/696/1/448.

- P. F. Hopkins, L. Hernquist, T. J. Cox, T. Di Matteo, P. Martini, B. Robertson, and V. Springel. Black Holes in Galaxy Mergers: Evolution of Quasars. *ApJ*, 630:705–715, September 2005. doi: 10.1086/432438.
- P. F. Hopkins, L. Hernquist, T. J. Cox, B. Robertson, and E. Krause. An Observed Fundamental Plane Relation for Supermassive Black Holes. *ApJ*, 669:67–73, November 2007. doi: 10.1086/521601.
- P. F. Hopkins, E. Quataert, and N. Murray. Stellar feedback in galaxies and the origin of galaxy-scale winds. *MNRAS*, 421:3522–3537, April 2012. doi: 10.1111/j.1365-2966.2012.20593.x.
- E. S. Howard, J. R. Webb, J. T. Pollock, and R. E. Stencel. Microvariability and Long-Term Variability of Four Blazars. *AJ*, 127:17–23, January 2004. doi: 10.1086/380216.
- C. H. Ishwara-Chandra, K. S. Dwarkanath, and K. R. Anantharamaiah. GMRT Detection of HI 21 cm Associated Absorption towards the $z = 1.2$ Red Quasar 3C 190. *Journal of Astrophysics and Astronomy*, 24:37, March 2003. doi: 10.1007/BF03012190.
- T. Isobe, E. D. Feigelson, and P. I. Nelson. Statistical methods for astronomical data with upper limits. II - Correlation and regression. *ApJ*, 306:490–507, July 1986. doi: 10.1086/164359.
- W. Jaffe, K. Meisenheimer, H. J. A. Röttgering, C. Leinert, A. Richichi, O. Chesneau, D. Fraix-Burnet, A. Glazeborg-Kluttig, G.-L. Granato, U. Graser, B. Heijligers, R. Köhler, F. Malbet, G. K. Miley, F. Paresce, J.-W. Pel, G. Perrin, F. Przygodda, M. Schoeller, H. Sol, L. B. F. M. Waters, G. Weigelt, J. Woillez, and P. T. de Zeeuw. The central dusty torus in the active nucleus of NGC 1068. *Nature*, 429:47–49, May 2004. doi: 10.1038/nature02531.
- Shardha Jogee. The Fueling and evolution of AGN: Internal and external triggers. *Lect. Notes Phys.*, 693:143, 2006. doi: 10.1007/3-540-34621-X_6.
- N. Kanekar and F. H. Briggs. 21-cm absorption studies with the Square Kilometer Array. *NewAR*, 48:1259–1270, December 2004. doi: 10.1016/j.newar.2004.09.030.

BIBLIOGRAPHY

- N. Kanekar and J. N. Chengalur. A deep search for 21-cm absorption in high redshift damped Lyman-alpha systems. *A&A*, 399:857–868, March 2003. doi: 10.1051/0004-6361:20021922.
- N. Kanekar and J. N. Chengalur. Outflowing atomic and molecular gas at $z \sim 0.67$ towards 1504 + 377. *MNRAS*, 384:L6–L10, February 2008. doi: 10.1111/j.1745-3933.2007.00410.x.
- N. Kanekar, J. X. Prochaska, A. Smette, S. L. Ellison, E. V. Ryan-Weber, E. Momjian, F. H. Briggs, W. M. Lane, J. N. Chengalur, T. Delafosse, J. Grave, D. Jacobsen, and A. G. de Bruyn. The spin temperature of high-redshift damped Lyman α systems. *MNRAS*.
- N. Kanekar, J. N. Chengalur, and W. M. Lane. HI 21-cm absorption at $z \sim 3.39$ towards PKS 0201+113. *MNRAS*, 375:1528–1536, March 2007. doi: 10.1111/j.1365-2966.2007.11430.x.
- N. Kanekar, W. M. Lane, E. Momjian, F. H. Briggs, and J. N. Chengalur. The covering factor of high-redshift damped Lyman- α systems. *MNRAS*, 394:L61–L65, March 2009. doi: 10.1111/j.1745-3933.2008.00610.x.
- N. Kanekar, J. X. Prochaska, A. Smette, S. L. Ellison, E. V. Ryan-Weber, E. Momjian, F. H. Briggs, W. M. Lane, J. N. Chengalur, T. Delafosse, J. Grave, D. Jacobsen, and A. G. de Bruyn. The spin temperature of high-redshift damped Lyman α systems. *MNRAS*, 438:2131–2166, March 2014. doi: 10.1093/mnras/stt2338.
- N. Katz, D. H. Weinberg, and L. Hernquist. Cosmological Simulations with TreeSPH. *ApJS*, 105:19, July 1996. doi: 10.1086/192305.
- T. Kaufmann, L. Mayer, J. Wadsley, J. Stadel, and B. Moore. Cooling flows within galactic haloes: the kinematics and properties of infalling multiphase gas. *MNRAS*, 370:1612–1622, August 2006. doi: 10.1111/j.1365-2966.2006.10599.x.
- K. I. Kellermann and F. N. Owen. *Radio galaxies and quasars*, pages 563–602. 1988.
- K. I. Kellermann and I. I. K. Pauliny-Toth. The Spectra of Opaque Radio Sources. *ApJL*, 155:L71, February 1969. doi: 10.1086/180305.

- K. I. Kellermann and I. I. K. Pauliny-Toth. Compact radio sources. *ARA&A*, 19: 373–410, 1981. doi: 10.1146/annurev.aa.19.090181.002105.
- K. I. Kellermann, R. Sramek, M. Schmidt, D. B. Shaffer, and R. Green. VLA observations of objects in the Palomar Bright Quasar Survey. *AJ*, 98:1195–1207, October 1989. doi: 10.1086/115207.
- D. Kereš and L. Hernquist. Seeding the Formation of Cold Gaseous Clouds in Milky Way-Size Halos. *ApJL*, 700:L1–L5, July 2009. doi: 10.1088/0004-637X/700/1/L1.
- D. Kereš, N. Katz, D. H. Weinberg, and R. Davé. How do galaxies get their gas? *MNRAS*, 363:2–28, October 2005. doi: 10.1111/j.1365-2966.2005.09451.x.
- F. J. Kerr. *Radio-Line Emission and Absorption by the Interstellar Gas*, page 575. the University of Chicago Press, January 1968.
- J. Kormendy and K. Gebhardt. Supermassive black holes in galactic nuclei. In J. C. Wheeler and H. Martel, editors, *20th Texas Symposium on relativistic astrophysics*, volume 586 of *American Institute of Physics Conference Series*, pages 363–381, October 2001. doi: 10.1063/1.1419581.
- J. Kormendy and D. Richstone. Inward Bound—The Search For Supermassive Black Holes In Galactic Nuclei. *ARA&A*, 33:581, 1995. doi: 10.1146/annurev.aa.33.090195.003053.
- C. G. Kotanyi and R. D. Ekers. Radio galaxies with dust lanes. *A&A*, 73:L1–L3, March 1979.
- O. P. Kuhn. Rest-frame optical continua of $L^*_{L^*}$, $z > 3$ quasars: probing the faint end of the high- z quasar luminosity function. *MNRAS*, 348:647–660, February 2004. doi: 10.1111/j.1365-2966.2004.07386.x.
- A. Labiano, P. D. Barthel, C. P. O’Dea, W. H. de Vries, I. Pérez, and S. A. Baum. GPS radio sources: new optical observations and an updated master list. *A&A*, 463: 97–104, February 2007. doi: 10.1051/0004-6361:20066183.
- A. Lawrence, S. J. Warren, O. Almaini, A. C. Edge, N. C. Hambly, R. F. Jameson, P. Lucas, M. Casali, A. Adamson, S. Dye, J. P. Emerson, S. Foucaud, P. Hewett,

BIBLIOGRAPHY

- P. Hirst, S. T. Hodgkin, M. J. Irwin, N. Lodieu, R. G. McMahon, C. Simpson, I. Smail, D. Mortlock, and M. Folger. The UKIRT Infrared Deep Sky Survey (UKIDSS). *MNRAS*, 379:1599–1617, August 2007. doi: 10.1111/j.1365-2966.2007.12040.x.
- C. R. Lawrence, J. R. Zucker, A. C. S. Readhead, S. C. Unwin, T. J. Pearson, and W. Xu. Optical Spectra of a Complete Sample of Radio Sources. I. The Spectra. *ApJS*.
- J. P. Leahy, T. W. B. Muxlow, and P. W. Stephens. 151-MHz and 1.5-GHz observations of bridges in powerful extragalactic radio sources. *MNRAS*, 239:401–440, July 1989.
- D. N. C. Lin, J. E. Pringle, and M. J. Rees. The link between tidal interaction and nuclear activity in galaxies. *ApJ*, 328:103–110, May 1988. doi: 10.1086/166272.
- H. Liszt. The spin temperature of warm interstellar H I. *A&A*, 371:698–707, May 2001. doi: 10.1051/0004-6361:20010395.
- X. Liu, L. Cui, W.-F. Luo, W.-Z. Shi, and H.-G. Song. VLBI observations of nineteen GHz-peaked-spectrum radio sources at 1.6 GHz. *A&A*, 470:97–104, July 2007. doi: 10.1051/0004-6361:20077265.
- K. Y. Lo. Mega-Masers and Galaxies. *ARA&A*, 43:625–676, September 2005. doi: 10.1146/annurev.astro.41.011802.094927.
- A. Loeb and S. R. Furlanetto. *The First Galaxies in the Universe*. 2013.
- P. W. Lucas, M. G. Hoare, A. Longmore, A. C. Schröder, C. J. Davis, A. Adamson, R. M. Bandyopadhyay, R. de Grijs, M. Smith, A. Gosling, S. Mitchison, A. Gáspár, M. Coe, M. Tamura, Q. Parker, M. Irwin, N. Hambly, J. Bryant, R. S. Collins, N. Cross, D. W. Evans, E. Gonzalez-Solares, S. Hodgkin, J. Lewis, M. Read, M. Riello, E. T. W. Sutorius, A. Lawrence, J. E. Drew, S. Dye, and M. A. Thompson. The UKIDSS Galactic Plane Survey. *MNRAS*, 391:136–163, November 2008. doi: 10.1111/j.1365-2966.2008.13924.x.
- J. Magorrian, S. Tremaine, D. Richstone, R. Bender, G. Bower, A. Dressler, S. M. Faber, K. Gebhardt, R. Green, C. Grillmair, J. Kormendy, and T. Lauer. The

- Demography of Massive Dark Objects in Galaxy Centers. *AJ*, 115:2285–2305, June 1998. doi: 10.1086/300353.
- P. R. Maloney, D. J. Hollenbach, and A. G. G. M. Tielens. X-Ray-irradiated Molecular Gas. I. Physical Processes and General Results. *ApJ*, 466:561, July 1996. doi: 10.1086/177532.
- A. Marconi and L. K. Hunt. The Relation between Black Hole Mass, Bulge Mass, and Near-Infrared Luminosity. *ApJL*, 589:L21–L24, May 2003. doi: 10.1086/375804.
- A. Marconi, G. Risaliti, R. Gilli, L. K. Hunt, R. Maiolino, and M. Salvati. Local supermassive black holes, relics of active galactic nuclei and the X-ray background. *MNRAS*, 351:169–185, June 2004. doi: 10.1111/j.1365-2966.2004.07765.x.
- A. Marecki, P. Thomasson, K.-H. Mack, and M. Kunert-Bajraszewska. Signatures of restarted activity in core-dominated, triple radio sources selected from the FIRST survey. *A&A*, 448:479–487, March 2006. doi: 10.1051/0004-6361:20053994.
- E. Massaro, M. Perri, P. Giommi, and R. Nesci. Log-parabolic spectra and particle acceleration in the BL Lac object Mkn 421: Spectral analysis of the complete BeppoSAX wide band X-ray data set. *A&A*, 413:489–503, January 2004. doi: 10.1051/0004-6361:20031558.
- E. Massaro, P. Giommi, C. Leto, P. Marchegiani, A. Maselli, M. Perri, S. Piranomonte, and S. Scavi. Roma-BZCAT: a multifrequency catalogue of blazars. *A&A*, 495: 691–696, February 2009. doi: 10.1051/0004-6361:200810161.
- D. L. Meier, S. Koide, and Y. Uchida. Magnetohydrodynamic Production of Relativistic Jets. *Science*, 291:84–92, January 2001. doi: 10.1126/science.291.5501.84.
- A. Merloni and S. Heinz. A synthesis model for AGN evolution: supermassive black holes growth and feedback modes. *MNRAS*, 388:1011–1030, August 2008. doi: 10.1111/j.1365-2966.2008.13472.x.
- H. Mo, F. C. van den Bosch, and S. White. *Galaxy Formation and Evolution*.
- D. G. Monet, S. E. Levine, B. Canzian, H. D. Ables, A. R. Bird, C. C. Dahn, H. H. Guetter, H. C. Harris, A. A. Henden, S. K. Leggett, H. F. Levison, C. B. Luginbuhl,

BIBLIOGRAPHY

- J. Martini, A. K. B. Monet, J. A. Munn, J. R. Pier, A. R. Rhodes, B. Riepe, S. Sell, R. C. Stone, F. J. Vrba, R. L. Walker, G. Westerhout, R. J. Brucato, I. N. Reid, W. Schoening, M. Hartley, M. A. Read, and S. B. Tritton. The USNO-B Catalog. *AJ*, 125:984–993, February 2003. doi: 10.1086/345888.
- C. B. Moore, C. L. Carilli, and K. M. Menten. Neutral Hydrogen 21 CM Absorption at Redshift 2.6365 toward the Gravitational Lens MG J0414+0534. *ApJL*, 510:L87–L90, January 1999. doi: 10.1086/311818.
- R. Morganti. *Using HI Absorption to Trace Outflows from Galaxies and Feeding of AGN*, page 31. 2012. doi: 10.1007/978-3-642-22795-0_4.
- R. Morganti, T. A. Oosterloo, G. van Moorsel, C. N. Tadhunter, and N. Killeen. HI absorption in radio galaxies. *ArXiv Astrophysics e-prints*, June 2000.
- R. Morganti, T. A. Oosterloo, C. N. Tadhunter, G. van Moorsel, N. Killeen, and K. A. Wills. HI absorption in radio galaxies: effect of orientation or interstellar medium? *MNRAS*, 323:331–342, May 2001. doi: 10.1046/j.1365-8711.2001.04153.x.
- R. Morganti, C. N. Tadhunter, and T. A. Oosterloo. Fast neutral outflows in powerful radio galaxies: a major source of feedback in massive galaxies. *A&A*, 444:L9–L13, December 2005. doi: 10.1051/0004-6361:200500197.
- R. Morganti, A. B. Peck, T. A. Oosterloo, G. van Moorsel, A. Capetti, R. Fanti, P. Parma, and H. R. de Ruiter. Is cold gas fuelling the radio galaxy NGC 315? *A&A*, 505:559–567, October 2009. doi: 10.1051/0004-6361/200912605.
- R. Morganti, J. Fogasy, Z. Paragi, T. Oosterloo, and M. Orienti. Radio Jets Clearing the Way Through a Galaxy: Watching Feedback in Action. *Science*, 341:1082–1085, September 2013. doi: 10.1126/science.1240436.
- C. A. Muller and J. H. Oort. Observation of a Line in the Galactic Radio Spectrum: The Interstellar Hydrogen Line at 1,420 Mc./sec., and an Estimate of Galactic Rotation. *Nature*, 168:357–358, September 1951. doi: 10.1038/168357a0.
- M. Nenkova, M. M. Sirocky, R. Nikutta, Ž. Ivezić, and M. Elitzur. AGN Dusty Tori. II. Observational Implications of Clumpiness. *ApJ*, 685:160–180, September 2008. doi: 10.1086/590483.

- C. P. O’Dea. The Compact Steep-Spectrum and Gigahertz Peaked-Spectrum Radio Sources. *PASP*, 110:493–532, May 1998. doi: 10.1086/316162.
- S. L. O’Dell, J. J. Puschell, W. A. Stein, and J. W. Warner. The changes in spectral-flux distribution during variability of extragalactic nonthermal sources, 0.36 to 3.5 microns. *ApJS*, 38:267–286, November 1978. doi: 10.1086/190557.
- M. Orienti, R. Morganti, and D. Dallacasa. H I absorption in high-frequency peaker galaxies. *A&A*, 457:531–536, October 2006. doi: 10.1051/0004-6361:20064820.
- T. J. Pearson and A. C. S. Readhead. The milliarcsecond structure of a complete sample of radio sources. II - First-epoch maps at 5 GHz. *ApJ*, 328:114–142, May 1988. doi: 10.1086/166274.
- A. B. Peck and G. B. Taylor. Evidence for a Circumnuclear Disk in 1946+708. *ApJL*, 554:L147–L150, June 2001. doi: 10.1086/321699.
- A. B. Peck, G. B. Taylor, and J. E. Conway. Obscuration of the Parsec-Scale Jets in the Compact Symmetric Object 1946+708. *ApJ*, 521:103–111, August 1999. doi: 10.1086/307535.
- J. E. G. Peek, M. E. Putman, and J. Sommer-Larsen. Ongoing Galactic Accretion: Simulations and Observations of Condensed Gas in Hot Halos. *ApJ*, 674:227–236, February 2008. doi: 10.1086/524374.
- R. A. Perley and B. J. Butler. An Accurate Flux Density Scale from 1 to 50 GHz. *ApJS*, 204:19, February 2013. doi: 10.1088/0067-0049/204/2/19.
- B. M. Peterson. *An Introduction to Active Galactic Nuclei*.
- B. M. Peterson. *An Introduction to Active Galactic Nuclei*. February 1997.
- Y. M. Pihlström, J. E. Conway, and R. C. Vermeulen. The presence and distribution of H I absorbing gas in sub-galactic sized radio sources. *A&A*, 404:871–881, June 2003. doi: 10.1051/0004-6361:20030469.
- A. G. Polatidis, P. N. Wilkinson, W. Xu, A. C. S. Readhead, T. J. Pearson, G. B. Taylor, and R. C. Vermeulen. The First Caltech–Jodrell Bank VLBI Survey. I. $\lambda = 18$ Centimeter Observations of 87 Sources. *ApJS*, 98:1, May 1995. doi: 10.1086/192152.

BIBLIOGRAPHY

- G. C. Privon. Modeling the Infrared Emission from Cygnus A. *ArXiv e-prints*, August 2009.
- Z. Qi, Y. Yu, B. Bucciarelli, M. G. Lattanzi, R. L. Smart, A. Spagna, B. J. McLean, Z. Tang, H. R. A. Jones, R. Morbidelli, L. Nicastro, and A. Vecchiato. Absolute Proper Motions Outside the Plane (APOP)—A Step Toward the GSC2.4. *AJ*, 150:137, October 2015. doi: 10.1088/0004-6256/150/4/137.
- D. Raine and E. Thomas. *Black Holes: a Student Text (3RD Edition)*. World Scientific Press, September 2014. doi: 10.1142/p947.
- C. M. Raiteri, M. Villata, A. Capetti, M. F. Aller, U. Bach, P. Calcidese, M. A. Gurwell, V. M. Larionov, J. Ohlert, K. Nilsson, A. Strigachev, I. Agudo, H. D. Aller, R. Bachev, E. Benítez, A. Berdyugin, M. Böttcher, C. S. Buemi, S. Buttiglione, D. Carosati, P. Charlot, W. P. Chen, D. Dultzin, E. Forné, L. Fuhrmann, J. L. Gómez, A. C. Gupta, J. Heidt, D. Hiriart, W.-S. Hsiao, M. Jelínek, S. G. Jorstad, G. N. Kimeridze, T. S. Konstantinova, E. N. Kopatskaya, A. Kostov, O. M. Kurtanidze, A. Lähteenmäki, L. Lanteri, L. V. Larionova, P. Leto, G. Latev, J.-F. Le Campion, C.-U. Lee, R. Ligustri, E. Lindfors, A. P. Marscher, B. Mihov, M. G. Nikolashvili, Y. Nikolov, E. Ovcharov, D. Principe, T. Pursimo, B. Ragozzine, R. M. Robb, J. A. Ros, A. C. Sadun, R. Sagar, E. Semkov, L. A. Sigua, R. L. Smart, M. Sorcia, L. O. Takalo, M. Tornikoski, C. Trigilio, K. Uckert, G. Umana, A. Valcheva, and A. Volvach. WEBT multiwavelength monitoring and XMM-Newton observations of $\text{J}0140+6130$ BL Lacertae in 2007-2008. Unveiling different emission components. *A&A*, 507:769–779, November 2009. doi: 10.1051/0004-6361/200912953.
- K. E. Randall, A. M. Hopkins, R. P. Norris, and P. G. Edwards. An unbiased sample of bright southern compact steep spectrum and gigahertz peaked spectrum sources. *MNRAS*, 416:1135–1151, September 2011. doi: 10.1111/j.1365-2966.2011.19116.x.
- S. M. Rao, D. A. Turnshek, and D. B. Nestor. Damped Ly α Systems at $z < 1.65$: The Expanded Sloan Digital Sky Survey Hubble Space Telescope Sample. *ApJ*, 636: 610–630, January 2006. doi: 10.1086/498132.

- A. C. S. Readhead, G. B. Taylor, T. J. Pearson, and P. N. Wilkinson. Compact Symmetric Objects and the Evolution of Powerful Extragalactic Radio Sources. *ApJ*, 460:634, April 1996. doi: 10.1086/176997.
- M. J. Rees. Black Hole Models for Active Galactic Nuclei. *ARA&A*, 22:471–506, 1984. doi: 10.1146/annurev.aa.22.090184.002351.
- S. N. Reeves, E. M. Sadler, J. R. Allison, B. S. Koribalski, S. J. Curran, and M. B. Pracy. H I emission and absorption in nearby, gas-rich galaxies. *MNRAS*, 450: 926–942, June 2015. doi: 10.1093/mnras/stv504.
- R. B. Rengelink, Y. Tang, A. G. de Bruyn, G. K. Miley, M. N. Bremer, H. J. A. Roettgering, and M. A. R. Bremer. The Westerbork Northern Sky Survey (WENSS), I. A 570 square degree Mini-Survey around the North Ecliptic Pole. *A&AS*, 124, August 1997. doi: 10.1051/aas:1997358.
- N. Roche and S. A. Eales. Optical/ultraviolet morphology and alignment of low-redshift radio galaxies. *MNRAS*, 317:120–140, September 2000. doi: 10.1046/j.1365-8711.2000.03684.x.
- S. Röser, E. Schilbach, H. Schwan, N. V. Kharchenko, A. E. Piskunov, and R.-D. Scholz. PPM-Extended (PPMX) - a catalogue of positions and proper motions. *A&A*, 488: 401–408, September 2008. doi: 10.1051/0004-6361:200809775.
- D. J. Saikia, N. Gupta, and C. Konar. HI gas in rejuvenated radio galaxies: Giant Metrewave Radio Telescope observations of the DDRG J1247+6723. *MNRAS*, 375: L31–L35, February 2007. doi: 10.1111/j.1745-3933.2006.00269.x.
- E. Schinnerer, A. Eckart, L. J. Tacconi, R. Genzel, and D. Downes. Bars and Warps Traced by the Molecular Gas in the Seyfert 2 Galaxy NGC 1068. *ApJ*, 533:850–868, April 2000. doi: 10.1086/308702.
- D. P. Schneider, P. B. Hall, G. T. Richards, D. E. Vanden Berk, S. F. Anderson, X. Fan, S. Jester, C. Stoughton, M. A. Strauss, M. SubbaRao, W. N. Brandt, J. E. Gunn, B. Yanny, N. A. Bahcall, J. C. Barentine, M. R. Blanton, W. N. Boroski, H. J. Brewington, J. Brinkmann, R. Brunner, I. Csabai, M. Doi, D. J. Eisenstein, J. A. Frieman, M. Fukugita, J. Gray, M. Harvanek, T. M. Heckman, Ž. Ivezić, S. Kent,

BIBLIOGRAPHY

- S. J. Kleinman, G. R. Knapp, R. G. Kron, J. Krzesinski, D. C. Long, J. Loveday, R. H. Lupton, B. Margon, J. A. Munn, E. H. Neilsen, H. J. Newberg, P. R. Newman, R. C. Nichol, A. Nitta, J. R. Pier, C. M. Rockosi, D. H. Saxe, D. J. Schlegel, S. A. Snedden, A. S. Szalay, A. R. Thakar, A. Uomoto, W. Voges, and D. G. York. The Sloan Digital Sky Survey Quasar Catalog. III. Third Data Release. *AJ*.
- F. Shankar, P. Salucci, G. L. Granato, G. De Zotti, and L. Danese. Supermassive black hole demography: the match between the local and accreted mass functions. *MNRAS*, 354:1020–1030, November 2004. doi: 10.1111/j.1365-2966.2004.08261.x.
- F. Shu. *Physics of Astrophysics: Volume I Radiation*.
- F. Shu. *Physics of Astrophysics: Volume I Radiation*. University Science Books, 1991.
- E. P. Smith and T. M. Heckman. Multicolor surface photometry of powerful radio galaxies. II - Morphology and stellar content. *ApJ*, 341:658–678, June 1989. doi: 10.1086/167524.
- I. A. G. Snellen, R. T. Schilizzi, G. K. Miley, A. G. de Bruyn, M. N. Bremer, and H. J. A. Röttgering. On the evolution of young radio-loud AGN. *MNRAS*, 319: 445–456, December 2000. doi: 10.1046/j.1365-8711.2000.03935.x.
- K. V. Sokolovsky, Y. Y. Kovalev, A. B. Pushkarev, P. Mimica, and M. Perucho. VLBI-selected sample of compact symmetric object candidates and frequency-dependent position of hotspots. *A&A*, 535:A24, November 2011. doi: 10.1051/0004-6361/201015772.
- R. S. Somerville and J. R. Primack. Semi-analytic modelling of galaxy formation: the local Universe. *MNRAS*, 310:1087–1110, December 1999. doi: 10.1046/j.1365-8711.1999.03032.x.
- J. Souchay, A. H. Andrei, C. Barache, T. Kalewicz, C. Gattano, B. Coelho, F. Taris, S. Bouquillon, and O. Becker. The third release of the Large Quasar Astrometric Catalog (LQAC-3): a compilation of 321 957 objects. *A&A*, 583:A75, November 2015. doi: 10.1051/0004-6361/201526092.
- L. Spitzer, Jr. Diffuse matter in space. *Interscience Tracts on Physics and Astronomy*, 28, 1968.

- V. Springel and L. Hernquist. The history of star formation in a Λ cold dark matter universe. *MNRAS*, 339:312–334, February 2003. doi: 10.1046/j.1365-8711.2003.06207.x.
- V. Springel, T. Di Matteo, and L. Hernquist. Modelling feedback from stars and black holes in galaxy mergers. *MNRAS*, 361:776–794, August 2005. doi: 10.1111/j.1365-2966.2005.09238.x.
- C. Stanghellini, C. P. O’Dea, D. Dallacasa, S. A. Baum, R. Fanti, and C. Fanti. A complete sample of GHz-peaked-spectrum radio sources and its radio properties. *A&AS*, 131:303–315, August 1998. doi: 10.1051/aas:1998270.
- M. Stickel and H. Kuehr. An update of the optical identification status of the S4 radio source catalogue. *A&AS*, 103, February 1994.
- C. Struve, T. A. Oosterloo, R. Morganti, and L. Saripalli. Centaurus A: morphology and kinematics of the atomic hydrogen. *A&A*, 515:A67, June 2010. doi: 10.1051/0004-6361/201014355.
- J. A. Surace and D. B. Sanders. Imaging of Ultraluminous Infrared Galaxies in the Near-Ultraviolet. *AJ*, 120:604–620, August 2000. doi: 10.1086/301491.
- C. Tasse, P. N. Best, H. Röttgering, and D. Le Borgne. Radio-loud AGN in the XMM-LSS field. II. A dichotomy in environment and accretion mode? *A&A*, 490:893–904, November 2008. doi: 10.1051/0004-6361:20079299.
- G. B. Taylor, R. C. Vermeulen, A. C. S. Readhead, T. J. Pearson, D. R. Henstock, and P. N. Wilkinson. A Complete Flux-Density–limited VLBI Survey of 293 Flat-Spectrum Radio Sources. *ApJS*, 107:37, November 1996. doi: 10.1086/192354.
- K. R. W. Tristram, D. Raban, K. Meisenheimer, W. Jaffe, H. Röttgering, L. Burtscher, W. D. Cotton, U. Graser, T. Henning, C. Leinert, B. Lopez, S. Morel, G. Perrin, and M. Wittkowski. Parsec-scale dust distributions in Seyfert galaxies. Results of the MIDI AGN snapshot survey. *A&A*, 502:67–84, July 2009. doi: 10.1051/0004-6361/200811607.
- C. Urry. AGN Unification: An Update. In G. T. Richards and P. B. Hall, editors, *AGN Physics with the Sloan Digital Sky Survey*, volume 311 of *Astronomical Society of the Pacific Conference Series*, page 49, June 2004.

BIBLIOGRAPHY

- C. M. Urry and P. Padovani. Unified Schemes for Radio-Loud Active Galactic Nuclei. *PASP*, 107:803, September 1995. doi: 10.1086/133630.
- C. M. Urry, R. Scarpa, M. O’Dowd, R. Falomo, J. E. Pesce, and A. Treves. The Hubble Space Telescope Survey of BL Lacertae Objects. II. Host Galaxies. *ApJ*, 532:816–829, April 2000. doi: 10.1086/308616.
- J. M. Uson, D. S. Bagri, and T. J. Cornwell. Radio detections of neutral hydrogen at redshift $Z=3.4$. *Physical Review Letters*, 67:3328–3331, 1991. doi: 10.1103/PhysRevLett.67.3328.
- G. van der Wolk, P. D. Barthel, R. F. Peletier, and J. W. Pel. Dust tori in radio galaxies. *A&A*, 511:A64, February 2010. doi: 10.1051/0004-6361/200912435.
- J. H. van Gorkom, G. R. Knapp, R. D. Ekers, D. D. Ekers, R. A. Laing, and K. S. Polk. *AJ*, 97:708, 1989.
- R. van Ojik, H. J. A. Roettgering, G. K. Miley, and R. W. Hunstead. The gaseous environments of radio galaxies in the early Universe: kinematics of the Lyman α emission and spatially resolved H I absorption. *A&A*, 317:358–384, January 1997.
- R. C. Vermeulen, Y. M. Pihlström, W. Tschager, W. H. de Vries, J. E. Conway, P. D. Barthel, S. A. Baum, R. Braun, M. N. Bremer, G. K. Miley, C. P. O’Dea, H. J. A. Röttgering, R. T. Schilizzi, I. A. G. Snellen, and G. B. Taylor. Observations of H I absorbing gas in compact radio sources at cosmological redshifts. *A&A*, 404:861–870, June 2003. doi: 10.1051/0004-6361:20030468.
- M.-P. Véron-Cetty and P. Véron. A catalogue of quasars and active nuclei: 13th edition. *A&A*, 518:A10, July 2010. doi: 10.1051/0004-6361/201014188.
- M.-P. Véron-Cetty, L. Woltjer, L. Staveley-Smith, and R. D. Ekers. The nature of powerful compact radio galaxies. *A&A*, 362:426–434, October 2000.
- A. Y. Wagner and G. V. Bicknell. Relativistic Jet Feedback in Evolving Galaxies. *ApJ*, 728:29, February 2011. doi: 10.1088/0004-637X/728/1/29.
- A. Y. Wagner, G. V. Bicknell, and M. Umemura. Driving Outflows with Relativistic Jets and the Dependence of Active Galactic Nucleus Feedback Efficiency on Interstellar

- Medium Inhomogeneity. *ApJ*, 757:136, October 2012. doi: 10.1088/0004-637X/757/2/136.
- J. V. Wall and J. A. Peacock. Bright extragalactic radio sources at 2.7 GHz. III - The all-sky catalogue. *MNRAS*, 216:173–192, September 1985.
- D. E. P. Walsh, G. R. Knapp, J. M. Wrobel, and D.-W. Kim. Interstellar matter in early-type galaxies. III - Radio emission and star formation. *ApJ*, 337:209–229, February 1989. doi: 10.1086/167098.
- R. L. Webster, P. J. Francis, B. A. Petersont, M. J. Drinkwater, and F. J. Masci. Evidence for a large undetected population of dust-reddened quasars. *Nature*, 375: 469–471, June 1995. doi: 10.1038/375469a0.
- A. E. Wehrle, M. H. Cohen, S. C. Unwin, H. D. Aller, M. F. Aller, and G. Nicolson. The milliarcsecond structure of highly variable radio sources. *ApJ*, 391:589–607, June 1992. doi: 10.1086/171373.
- S. D. M. White and C. S. Frenk. Galaxy formation through hierarchical clustering. *ApJ*, 379:52–79, September 1991. doi: 10.1086/170483.
- P. N. Wilkinson, A. G. Polatidis, A. C. S. Readhead, W. Xu, and T. J. Pearson. Two-sided ejection in powerful radio sources: The compact symmetric objects. *ApJL*, 432: L87–L90, September 1994. doi: 10.1086/187518.
- H. Wu, Z. L. Zou, X. Y. Xia, and Z. G. Deng. A statistical study of the spectra of very luminous IRAS galaxies. II. Spectral and environmental analysis. *A&AS*, 132: 181–193, October 1998. doi: 10.1051/aas:1998443.
- G. Z. Xie, H. Dai, and S. B. Zhou. The Connections between Accretion, Jets, and Blazar Unification. *AJ*, 134:1464, October 2007. doi: 10.1086/521552.
- W. Xu, A. C. S. Readhead, T. J. Pearson, A. G. Polatidis, and P. N. Wilkinson. The First Caltech–Jodrell Bank VLBI Survey. III. VLBI and MERLIN Observations at 5 GHz and VLA Observations at 1.4 GHz. *ApJS*, 99:297, August 1995. doi: 10.1086/192189.

BIBLIOGRAPHY

- B. A. York, N. Kanekar, S. L. Ellison, and M. Pettini. Discovery of 21-cm absorption in a $z_{abs} = 2.289$ damped Lyman α system towards TXS 0311+430: the first low spin temperature absorber at $z > 1$. *MNRAS*, 382:L53–L57, November 2007. doi: 10.1111/j.1745-3933.2007.00388.x.
- N. Zacharias, D. G. Monet, S. E. Levine, S. E. Urban, R. Gaume, and G. L. Wycoff. The Naval Observatory Merged Astrometric Dataset (NOMAD). In *American Astronomical Society Meeting Abstracts*, volume 36 of *Bulletin of the American Astronomical Society*, page 1418, December 2004.
- N. Zacharias, C. Finch, J. Subasavage, G. Bredthauer, C. Crockett, M. Divittorio, E. Ferguson, F. Harris, H. Harris, A. Henden, C. Kilian, J. Munn, T. Rafferty, A. Rhodes, M. Schultheiss, T. Tilleman, and G. Wieder. The First U.S. Naval Observatory Robotic Astrometric Telescope Catalog. *AJ*, 150:101, October 2015. doi: 10.1088/0004-6256/150/4/101.